LBL-35984
CONF-9310315
UC-414

Proceedings of the 9th High Energy Heavy Ion Study

October 25–29, 1993

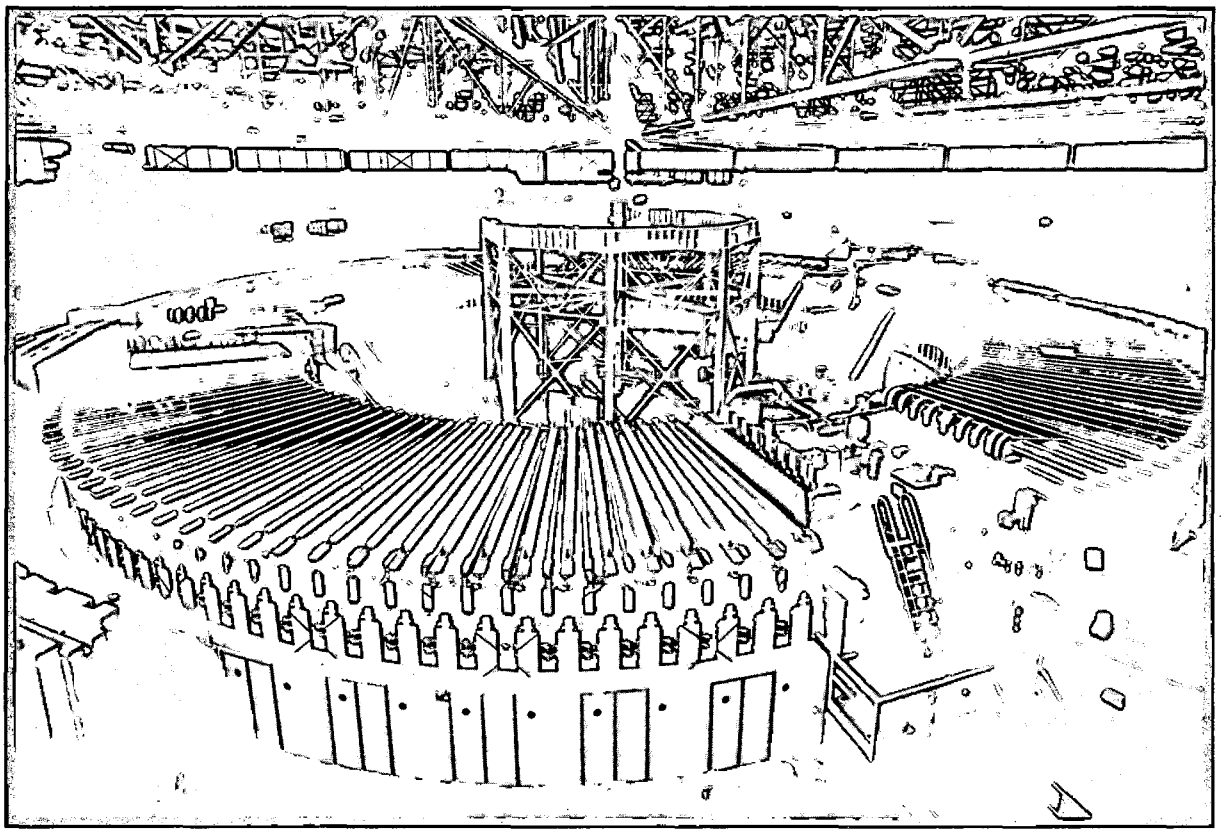

Lawrence Berkeley Laboratory • University of California

REFERENCE COPY
Does Not
Circulate
Bldg. 50 Library.
LBL-35984
Copy 1

Prepared for the U.S. Department of Energy under Contract No. DE-AC03-76SF00098

Front cover: Bevatron 9/6/55
Back cover: Bevatron shielding under construction 1/14/63

DISCLAIMER

This document was prepared as an account of work sponsored by the United States Government. Neither the United States Government nor any agency thereof, nor The Regents of the University of California, nor any of their employees, makes any warranty, express or implied, or assumes any legal liability or responsibility for the accuracy, completeness, or usefulness of any information, apparatus, product, or process disclosed, or represents that its use would not infringe privately owned rights. Reference herein to any specific commercial products process, or service by its trade name, trademark, manufacturer, or otherwise, does not necessarily constitute or imply its endorsement, recommendation, or favoring by the United States Government or any agency thereof, or The Regents of the University of California. The views and opinions of authors expressed herein do not necessarily state or reflect those of the United States Government or any agency thereof or The Regents of the University of California and shall not be used for advertising or product endorsement purposes.

This report has been reproduced directly from the best available copy.

Available to DOE and DOE Contractors
from the Office of Scientific and Technical Information
P.O. Box 62, Oak Ridge, TN 37831
Prices available from (615) 576-8401, FTS 626-8401

Available to the public from the
National Technical Information Service
U.S. Department of Commerce
5285 Port Royal Road, Springfield, VA 22161

Lawrence Berkeley Laboratory is an equal opportunity employer.

DISCLAIMER

This document was prepared as an account of work sponsored by the United States Government. While this document is believed to contain correct information, neither the United States Government nor any agency thereof, nor the Regents of the University of California, nor any of their employees, makes any warranty, express or implied, or assumes any legal responsibility for the accuracy, completeness, or usefulness of any information, apparatus, product, or process disclosed, or represents that its use would not infringe privately owned rights. Reference herein to any specific commercial product, process, or service by its trade name, trademark, manufacturer, or otherwise, does not necessarily constitute or imply its endorsement, recommendation, or favoring by the United States Government or any agency thereof, or the Regents of the University of California. The views and opinions of authors expressed herein do not necessarily state or reflect those of the United States Government or any agency thereof or the Regents of the University of California.

LBL-35984

Proceedings of the 9th High Energy Heavy Ion Study

Lawrence Berkeley Laboratory
October 25–29 1993

Jointly sponsored by

Nuclear Science Division
Lawrence Berkeley Laboratory
University of California
Berkeley, CA 94720
USA

and

Gesellschaft für Schwerionenforschung MBH
Planckstraße 1
D-6100 Darmstadt
Germany

Edited by

A.D. Chacon
M. Justice
H.G. Ritter

Organizing Committee

R. Bock, GSI
E. Grosse, GSI
J. Randrup, LBL
H.G. Ritter, Chair
R. Scharenberg, Purdue
L.S. Schroeder, LBL

This work was supported by the Director, Office of Energy Research, Office of High Energy and Nuclear Physics, U.S. Department of Energy under Contract No. DE-AC03-76SF00098.

Preface

The 9th High Energy Heavy Ion Study was again jointly sponsored by the Nuclear Science Division of the Lawrence Berkeley Laboratory and the Gesellschaft für Schwerionenforschung in Darmstadt, Germany. Over 75 scientists from six countries attended.

Since the last workshop we have seen great changes in the field. The SIS accelerator at GSI is now fully operational with an exciting set of experiments. The Bevalac, on the other hand, has been shut down. During this workshop the complete GSI program and the last Bevalac experiments were presented side by side for the first time, creating an atmosphere of stimulating, friendly competition.

The first day of the week was devoted to a celebration of the scientific achievements of the Bevatron in particle physics, nuclear physics, space science, medicine, and biology. Lee Schroeder put together an exciting program with distinguished speakers.

This workshop was made possible by the work of many people. Mollie Field and Del Thomas from LBL's Conference Coordination Group made the arrangements for lodging, local transportation, and logistics. Their experience and devotion made this workshop possible. Joy Lofdahl helped with travel arrangements. A. Dean Chacon and Marvin Justice, with the help of Julie McCullough, did an excellent job editing the Proceedings.

Hans Georg Ritter
Chair, Organizing Committee

CONTENTS

Preface iii

Di-Lepton Production

Dielectron Measurements in p+p and p+d Collisions from 1.0 to 5.0 GeV Kinetic Beam Energy

W.K. Wilson, S. Beedoe, M. Bougteb, J. Cailiu, J. Carroll, W. Christie, W.G. Gong, T. Hallman, L. Heilbronn, H.Z. Huang, G. Igo, P. Kirk, G. Krebs, A. Letessier-Selvon, L. Madansky, F. Manso, H.S. Matis, D. Miller, J. Miller, C. Naudet, R.J. Porter, G. Roche, L.S. Schroeder, P. Seidl, M. Toy, Z.F. Wang, R. Welsh, and A. Yegneswaran 1

Recent Measurements of Dielectron Production in A+A Collisions at 1.05 GeV/nucleon

R.J. Porter 6

Dilepton Production in Proton+Nucleon Collisions

K. Haglin 11

Dilepton Production in Heavy-Ion Collisions

C.M. Ko 16

Di-lepton Experiments at CERN Energies

H. Specht ..... *

Neutral Mesons Measured with TAPS

R. Simon ..... *

HADES — a High Acceptance Di-lepton Spectrometer

W. Koenig ..... *

Multifragmentation

Multifragmentation Measured with the Miniball

B. Tsang ..... *

Studying Multifragmentation Dynamics at Intermediate Energies Using Two-Fragment Correlations

T.C. Sangster, H.C. Britt, and M.N. Namboodiri 25

Determining Critical Exponents in Small Systems

A.S. Hirsch 34

*No manuscript submitted

Multifragmentation: the Success of Statistical Models

M. Begemann-Blaich, J.C. Adloff, P. Bouissou, T. Hofmann, J. Hubele, G. Imme, I. Iori, P. Kreutz, G.J. Kunde, S. Leray, V. Lindenstruth, Z. Liu, U. Lynen, R.J. Meijer, U. Milkau, A. Moroni, W.F.J. Müller, C. Ngô, C.A. Ogilvie, J. Pochodzalla, G. Raciti, G. Rudolf, H. Sann, A. Schüttauf, W. Seidel, L. Stuttge, W. Trautmann, A. Tucholski, and A. Wörner 44

Multifragmentation at Intermediate Energies

G. Wozniak ..... *

Dynamical Aspects of Multifragmentation

V. Lindenstruth, J. Pochodzalla, J.C. Adloff, M. Begemann-Blaich, P. Bouissou, J. Hubele, G. Imme, I. Iori, P. Kreutz, G.J. Kunde, S. Leray, Z. Liu, U. Lynen, R.J. Meijer, U. Milkau, A. Moroni, W.F.J. Müller, C. Ngô, C.A. Ogilvie, G. Raciti, G. Rudolf, H. Sann, A. Schüttauf, W. Seidel, L. Stuttge, W. Trautmann, and A. Tucholski 53

Production of Neutron Deficient Nuclei by Fragmentation of Xe Isotopes

J. Reinhold, J. Friese, H.J. Körner, R. Schneider, K. Zeitelhack, H. Geissel, A. Magel, G. Münzenberg, and K. Sümmerer 58

Collective Effects and Flow

Collective Effects in Au + Au (FOPI)

N. Herrmann ..... *

Collective Phenomena at the EOS TPC

D. Keane, S. Albergo, F. Bieser, F.P. Brady, Z. Caccia, D.A. Cebra, A.D. Chacon, J.L. Chance, Y. Choi, S. Costa, J. Elliott, M. Gilkes, J.A. Hauger, A. Hirsch, E.L. Hjort, A. Insolia, M. Justice, V. Lindenstruth, H.S. Matis, M. McMahan, C. McParland, W.F.J. Müller, , D.L. Olson, M. Partlan, N. Porile, R. Potenza, G. Rai, J. Rasmussen, H.G. Ritter, J. Romanski, J.L. Romero, G.V. Russo, H. Sann, R. Scharenberg, A. Scott, Y. Shao, B. Srivastava, T.J.M. Symons, M. Tincknell, C. Tuvè, S. Wang, P. Warren, D. Weerasundara, H.H. Wieman, and K.L. Wolf 63

Fragment Flow (FOPI)

F. Rami ..... *

Fragment–Fragment Correlations

G. Peilert, T.C. Sangster, M.N. Namboodiri, and H.C. Britt 74

Neutron Squeeze-out Observed in ^{197}Au + ^{197}Au Collisions

Y. Leifels, Th. Blaich, J. Keller and D. Lambrecht 84

Azimuthal Asymmetry of Neutral Pion Emission in Au+Au Reactions at 1 GeV/u

H. Löhner, A.E. Raschke, R.H. Siemssen, M. Sumbera, L.B. Venema, and H.W. Wilschut 91

Pion Production and Absorption in Relativistic Nucleus–Nucleus Collisions

P. Senger and the KaoS Collaboration 96

Multifragmentation of Gold by 1- and 3.6 GeV/A Helium

E. Norbeck, W. Bauer, V. Lips, R. Barth, H. Oeschler, S.P. Avdeyev, V.A. Karnaukhov, W.D. Kuznetsov, L.A. Petrov, O.V. Bochkarev, L.V. Chulkov, E.A. Kuzmin, W. Karcz, and W. Neubert 102

Fragmentation of Hot Nuclear Systems Formed in Xe-Induced Reactions at E_{beam}=60 MeV/nucleon

W. Skulski, K. Tso, N. Colonna, G.J. Wozniak, L.G. Moretto, D.R. Bowman, M. Chartier, C.K. Gelbke, W.C. Hsi, M.A. Lisa, W.G. Lynch, G.F. Peaslee, L. Phair, C. Schwarz, and M.B. Tsang 107

Beam and Radioactive Beam Studies

Measurement of Electron Capture from Electron–Positron Pair Production

H. Gould, A. Belkacem, B. Feinberg, and R. Bossingham 113

How Well Do We Understand the Dripline?

I. Tanihata ..... *

Radioactive Beam Studies at SIS

K. Sümmerer 117

Neutron Halo Nuclei Studied at GSI

W. Schwab 127

Scattering and Particle Production

The Disappearance of Flow, Critical Behavior, and the Onset of Multifragmentation

G.D. Westfall 133

Particle Production from Compressed Nuclear Matter

E. Grosse ..... *

High-Energy Pions: A Probe for the Hot and Dense Collision Zone?

C. Müntz for the KaoS Collaboration 143

Subthreshold Kaon, Antikaon and Antiproton Production at Bevalac/SIS Energies

G.Q. Li, C.M. Ko, X.S. Fang, and Y.M. Zheng 148

"Collective Effects" of Mesons at SIS-Energies

S.A. Bass, C. Hartnack, R. Mattiello, H. Stöcker, and W. Greiner 153

Proton and Pion Production in the Target Rapidity Region

H.H. Gutbrod, B. Roters, C. Blume, and H.R. Schmidt 161

Lifetime Effects in Two-Proton Correlations in Heavy Ion Collisions

M.A. Lisa, C.K. Gelbke, W. Gong, S. Pratt, N. Carlin, P. Decowski, R.T. deSouza, E. Gualtieri, S. Hannuschke, Y.D. Kim, R. Lacey, T. Li, W.G. Lynch, T. Murakami, G. Peaslee, G. Poggi, T. Reposeur, M.B. Tsang, A.M. Vander Molen, G.D. Westfall, H.M. Xu, J. Yee, S.J. Yennello, K. Kwiatkowski, and V.E. Viola, Jr. 171

Pion "Flow" in Relativistic Heavy-Ion Collisions

B.-A. Li 177

Summary and Epilogue

Heavy Ion Collisions between 1 Gev/N and 10 GeV/N

J. Aichelin 183

Quo Vadis, Bevalac Physics?

W. Bauer 198

List of Participants 211

Di-Lepton Production

Dielectron Measurements in p+p and p+d Collisions from 1.0 TO 5.0 GeV Kinetic Beam Energy

(The DLS Collaboration)
W.K. Wilson[a1], S. Beedoe[b 2], M. Bougteb[c], J. Cailiu[a 3], J. Carroll[b], W. Christie[d 4], W.G. Gong[a], T. Hallman[d 5], L. Heilbronn[a], H.Z. Huang[a 6], G. Igo[b], P. Kirk[e], G. Krebs[a], A. Letessier-Selvon[a 7], L. Madansky[d], F. Manso[c], H.S. Matis[a], D. Miller[f] J. Miller[a], C. Naudet[a8], R.J. Porter[a], G. Roche[a,c], L.S. Schroeder[a], P. Seidl[a], M. Toy[b], Z.F. Wang[e], R. Welsh[d], A. Yegneswaran[a 9]

[a] *Lawrence Berkeley Laboratory, University of California, Berkeley, CA 94720, USA*
[b] *University of California at Los Angeles, CA 90024, USA*
[c] *Université Blaise Pascal/IN2P3, 63177 Aubière Cedex, France*
[d] *The Johns Hopkins University, Baltimore, MD 21218, USA*
[e] *Louisiana State University, Baton Rouge, LA 70803, USA*
[f] *Northwestern University , Evanston, IL 60201, USA*

ABSTRACT

The first measurements of dielectron production in p+p and p+d interactions at incident kinetic energies from 1.0-4.9 GeV are summarized. The beam energy and invariant mass dependence of the dielectron yield in p+d interactions relative to the yield in p+p interactions are presented. The ratio of the yield in p+d to that in p+p interactions decreases from nearly 9 at 1.0 GeV to ≈ 2 at 4.9 GeV. The large ratio at 1.0 GeV suggests that dielectron production in the p+d system is dominated by a p+n process. The beam energy dependence of the ratio indicates that this p+n contribution decreases with respect to the other dielectron sources as the incident energy is increased.

This talk will summarize the first results of the DLS (Dilepton Spectrometer) proton beam and hydrogen target program at the Bevatron[1,2,3]. One of the goals of the DLS collaboration is to use dielectrons as probes of the hot, compressed nuclear matter formed in the early stages of relativistic nuclear collisions. The heavy-ion physics motivation for the proton beam program is to provide measurements which will quantify the contributions of the various processes leading to dielectron production. Only when we understand dilepton production in "simple" nucleon-nucleon collisions can we proceed on to untangle the complex dielectron spectra produced in heavy-ion reactions.

[1]Present address: Wayne State University, Detroit Michigan, 48201, USA.
[2]Present address: Hampton University, Hampton, Virginia 23668, USA.
[3]Present address: Beijing High Energy Institute, China.
[4]Present address: Brookhaven National Laboratory, Upton, New York 11973, USA.
[5]Present address: University of California at Los Angeles, California 90024, USA.
[6]Present address: Physics Dept. Purdue University, W. Lafayette, Indiana 47906 USA.
[7]Present address: Université de Paris VI et VII, LPNHE 75252 Paris Cedex 05, France.
[8]Present address: Jet Propulsion Laboratory, Pasadena California 91109, USA.
[9]Present address: CEBAF, Newport News, Virginia 23606, USA.

1. Introduction

Dileptons are useful probes of the hot, compressed nuclear matter produced in the early stages of heavy-ion collisions due to their low interaction cross sections with the nuclear medium[4]. Compared to hadrons, electro-magnetic probes such as dileptons leave the collision zone relatively undisturbed and therefore carry direct information about the conditions within the nuclear fireball. However, the initial measurements of electron pairs produced in Ca+Ca and Nb+Nb collisions for beam kinetic energies from 1-2 GeV/nucleon[5] have proven difficult to interpret due to a lack of knowledge of the fundamental nucleon-nucleon cross sections for the many processes[6,7] which contribute to the dielectron yield. The most commonly cited processes fall into three main categories: the production of virtual photons through p+n bremsstrahlung, direct and dalitz decay of hadrons, and pion annihilation. A fourth category, soft parton annihilation, has also been proposed by some authors[8]. Soft parton annihilation and pion annihilation will not be discussed here.

Bremsstrahlung is the radiation of photons from charges which are accelerated during a collision. Any process which generates a real photon can instead produce a massive virtual photon which decays to an electron-positron pair, so bremsstrahlung produces dielectrons as well as real photons[9]. Until recently, it was expected that the bremsstrahlung contribution would be primarily via the pn channel[10]. If this were so, one could gauge the possible pn bremsstrahlung contribution by comparing the dielectron yield in pd and pp collisions.

Similarly, all of the hadrons which decay into gamma rays can produce virtual photons which then decay to dielectrons. The ρ and the ω vector mesons decay directly into electron-positron pairs, giving rise to (overlapping) peaks in the mass spectra. Other hadrons, such as the η and the Δ resonance undergo three body "Dalitz" decays which lead to dielectrons with continuum mass spectra. In the pp system, we have the ability to go above and below the absolute energy threshold for the creation of several hadrons, allowing us the possibility of isolating their contribution to the shape of the mass spectrum.

2. Experimental Setup and Analysis

Proton beams of 1.03, 1.26, 1.60, 1.85, 2.07, and 4.9 GeV kinetic energy were provided by the Lawerence Berkeley Laboratory Bevatron. Electron pairs were detected using the DLS, a twin arm magnetic dipole spectrometer. Dielectrons are difficult to use as probes of nuclear collisions due to their low production cross sections relative to hadrons. The detector system must be designed to be sensitive to the rare dielectron signal while withstanding a barrage of hadrons. The DLS uses threshold Ĉerenkov gas radiators to preferentially trigger on electrons. For details of the DLS hardware and performance, please see Ref. 11. In the DLS liquid target program, the solid target described in the reference was replaced by a 12.7 cm long cylinder which was filled with liquid hydrogen or deuterium for the pp and pd runs respectively. Like-sign pairs are used to estimate the combinatoric background within the opposite-sign sample. The "true" pair yield is given by subtracting the combinatoric background from the opposite-sign pairs. The yields were normalized by the total number of incident protons in each projectile-target combination and by the densities of the liquid hydrogen and deuterium targets. No correction for the DLS acceptance was applied to the data presented in this talk. Dilepton production cross sections corrected for the DLS acceptance will appear in subsequent papers.

3. The p+d To p+p Dielectron Yield Ratio

The ratio of the pd to pp dielectron yields (pd/pp ratio) should clearly indicate the relative importance of hadronic decay with respect to pn bremsstrahlung. If bremsstrahlung is the dominant source of dielectrons, the pd/pp ratio [taken as (pn+pp)/pp] would thus be 10 or larger. On the other hand, if most dielectrons are produced through hadronic decays, the pd/pp ratio would have a value closer to 2-4 since hadron production cross sections in pn interactions are typically no more than 3 times larger than those of pp reactions in this energy regime[12].

From an experimental point of view, the pd/pp ratio is a particularly clean observable since the detector efficiency is the same for both systems and thus cancels out of the ratio. We also found that the dielectron mass, transverse momentum, and rapidity distributions were similar enough to cancel the acceptance out of the pd/pp ratio to within the statistical uncertainty of these measurements.

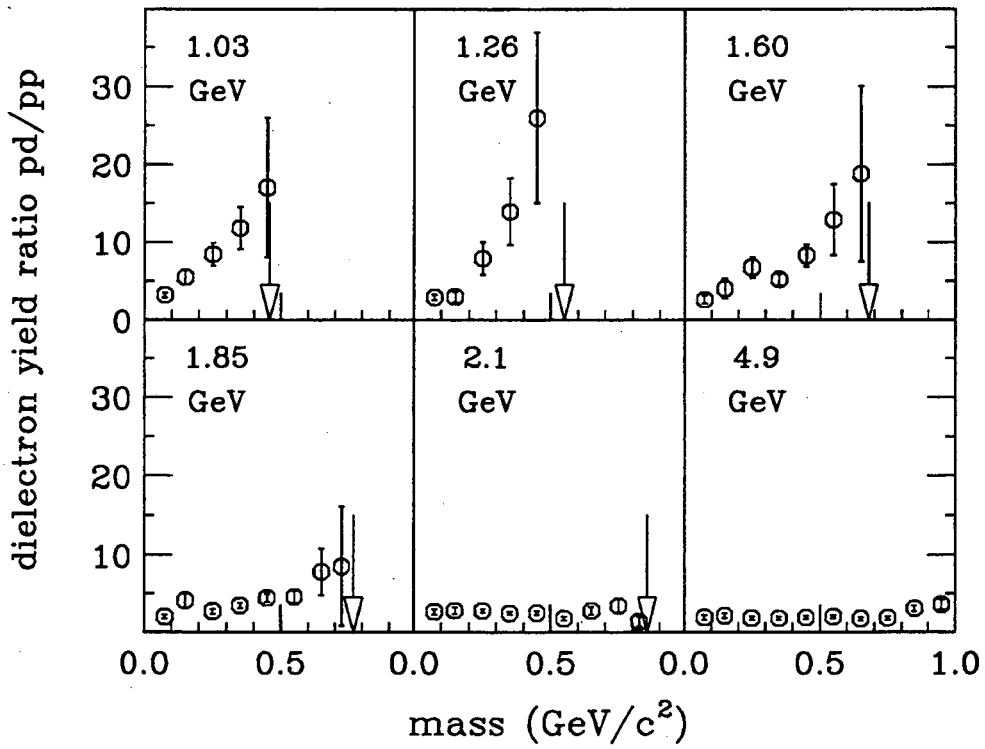

Fig. 1: The pd/pp ratio as a function of the invariant mass of the electron pair.The maximum dielectron mass kinematically allowed in pp collisions is indicated by an arrow for each beam energy except 4.9 GeV, where the limit, m=1.7 GeV/c^2, is off-scale.

The pd/pp ratio is plotted in Fig. 1 as a function of the invariant mass of the electron pair. Note that in the data for beam energies from 1.0-1.6 GeV, the ratio increases with pair mass. Some of this trend may be due to Fermi motion contributions to the collision energy in the pd system. At a fixed incident energy, the pd system can create dilepton pairs of greater mass than the pp system, so we would expect an increasing pd/pp ratio when the pair mass approaches the kinematical limit. The arrows in the figure indicate the upper limits on the

dielectron masses for pp interactions. However, the mass dependence may also reflect the contributions of different dilepton production mechanisms in pd and pp interactions[7].

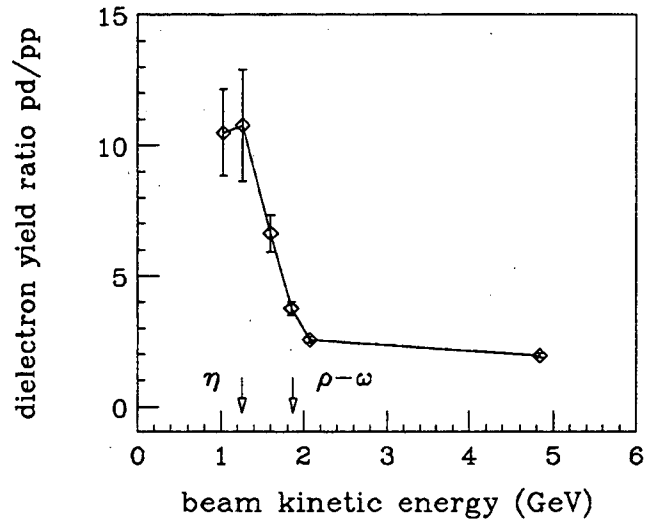

Fig. 2: The pd/pp ratio as a function of the beam energy for pairs with m>0.15 GeV/c^2. The error bars are smaller than the plotting symbols for the 2.1 and 4.9 GeV data. The beam energy thresholds for η and ρ-ω meson production are indicated by the two arrows. The lines are only to guide the eye.

Dielectrons with mass less than the pion mass are dominantly produced by the Dalitz decay of neutral pions. The pd/pp ratio in the m$\geq$0.15 GeV/c^2 region, displayed in Fig. 2, is largest at 1.0 GeV incident energy. At this energy, pn bremsstrahlung and Δ Dalitz decay have been predicted to be the dominant sources of dielectrons with masses greater than the pion mass.[13,14] Since the expected cross sections for Δ^+ and Δ^o resonance excitation[12] provide a pd/pp ratio of only 2.7, there must be an additional pn dielectron source such as bremsstrahlung.

Another possible cause of the large pd/pp ratio at the lower beam energies is subthreshold η production. Preliminary reports from the PINOT spectrometer at SATURNE[15] indicate that the pn/pp ratio for η production may be 4-8 near threshold. Together with the knowledge of the Δ production cross sections, the comparison of the PINOT η measurements with our pd/pp ratio data should pin down the role of pn bremsstrahlung production of dielectrons at the lower beam energies.

Note that the data displayed in Fig. 2 indicate that the pd/pp ratio of the dielectron yield decreases dramatically with increasing energy. This trend could be due to increasingly important hadronic decay contributions, or an unexpectedly large pp bremsstrahlung contribution at the higher beam energies[10]. Full details of the pd/pp ratio measurements may be found in Ref. 2 by Wilson et al.

4. Conclusions

We have measured the ratios of the pd to pp dielectron yields for incident kinetic energies from 1.0-4.9 GeV. The ratio for pairs with invariant masses greater than that of the pion

decreases from 8.9±1.5 at 1.0 GeV to 2.14±0.14 at 4.9 GeV. The large pd/pp ratio of the dielectron yield at 1.0 GeV indicates a significant pn contribution to the dielectron yield in pd collisions.

We have also found that the dielectron yield in pp interactions at 4.9 GeV cannot be accounted for using only the known hadronic decays with their most probable production cross sections. Full details of this calculation may be found in Ref. 3 by Huang et al.

As the analysis of this data set proceeds, the dielectron cross sections which will be extracted as a function of the mass, transverse momentum, and rapidity of the pair will allow more quantitative statements to be made about the sources of dielectrons in these interactions. At the very least, they will provide input into cascade calculations which can then be compared to dielectron measurements in heavy-ion collisions.

Nucleon-nucleon dielectron production is interesting in its own right apart from its applications to electron pair production in heavy-ion collisions. For example, virtual photon bremsstrahlung may provide access to the time-like electromagnetic form factor of the proton in the so called "unphysical" region. The low photon mass region ($<2m_p$) is called unphysical because it is forbidden in p-$\bar{p}$ interactions by energy conservation. In pp bremsstrahlung, one of the protons must go off mass shell in order to emit a massive photon, so the photon mass can take on any value. The most widely accepted theoretical picture of the form factor is the VDM (vector dominance model) which predicts a strong enhancement in virtual photon production in the ρ-ω mass region. It is our hope that analysis of our measurements in the vector meson mass region will yield constraints on VDM.

5. References

[1] H.Z. Huang et al., *Phys. Rev. C* in press (1994).
[2] W.K. Wilson et al., *Phys. Lett. B* ? (1993).
[3] H.Z. Huang et al., *Phys. Lett. B* **297**, 233 (1992).
[4] C. Gale and J. Kapusta, *Phys. Rev. C* **35**, 2107 (1987); L.H. Xia et al., *Nucl. Phys. A* **485**, 721 (1988).
[5] G. Roche et al., *Phys. Lett. B* **226**, 228 (1989); S. Beedoe et al., *Phys. Rev. C.* **47**, 2840 (1993).
[6] Gy. Wolf et al., *Nucl. Phys. A* **517**, 615 (1990).
[7] V.D. Toneev et al., *GSI Preprint* GSI-92-05, (1992).
[8] P. Lichard and J.A. Thomson, *Phys. Rev. D* **44**, 668 (1991).
[9] M. Schäfer et al., *Phys. Lett. B* **221**, 1 (1989); K. Haglin et al., *Phys. Lett. B* **224**, 433 (1989).
[10] See also the contribution by K. Haglin et al. to these proceedings.
[11] A. Yegneswaran et al., *Nucl. Instr. and Meth. A* **290**, 61 (1990).
[12] B.J. VerWest, R.A. Arndt, *Phys. Rev. C* **25**, 1979 (1992).
[13] L. Xiong et al., *Phys. Rev. C* **R1355**, 41 (1990).
[14] Gy. Wolf et al., *Giessen preprint* UGI-92-5 (1992).
[15] The PINOT Collaboration, *News from SATURNE* **16**, 37 (1992).

Recent Measurements of Dielectron Production in A+A Collisions at 1.05 Gev/nucleon

R. Jeff Porter
Lawrence Berkeley Laboratory and University of California, Davis
for the Dilepton Spectrometer Collaboration

Abstract

In late 1992 and early 1993, the DLS collaboration performed measurements in several A+A systems at a beam kinetic energy of 1.05 GeV/nucleon. Although the analysis of the data sets from Ca+Ca, He+Ca, C+C, and d+Ca systems are still preliminary, a brief discussion of this experimental program as well as the pair statistics from these measurements will be given in this report.

Dielectron pairs produced in A+A collisions offer physicists a unique probe into the dynamics of the heavy-ion collision. Once created, the electron-positron pair suffer little rescattering within the surrounding hadronic medium and can thus retain information about their production mechanism. Some current estimates of the principle sources for dielectron production in the 1-2 GeV/nucleon collision energy range indicate that hadronic mechanisms such as Δ and η Dalitz decays and $\pi^+\pi^-$ annihilation play dominant roles in the pair yield [1][2]. Hence, the invariant mass distribution from the dielectron signal may provide information about the important contributions the baryon resonances and meson states make to the collision dynamics.

The first measurements of dielectron pairs in A+A interactions at Bevalac energies were performed by the Dilepton Spectrometer (DLS) collaboration during a period of from 1987 to 1989 [3][4]. The pair samples from these data sets, shown in table 1, established the DLS capability in providing measurements of this signal while the corresponding mass spectra prompted theoretical interpretations of the

Reaction	E/A (GeV)	True Pairs	Date	Status
Ca + Ca	2.10	49±12	May87	Published
Ca + Ca	1.05	255±35	Jan88	Published
Ca + Ca	2.10	202±43	May89	Analyzed
Nb + Nb	1.05	54±13	May89	Published

Table 1. Original DLS measurements of dielectron production in A+A systems.

data. For example, the experimental mass spectrum for the Ca+Ca system at 1.05 GeV/nucleon and a model's description of the spectrum is shown in figure 1. In this model by Wolf et al.[1], the sources for the yield for pair masses below about 0.5 GeV are a combination of pn Bremsstrahlung, and Dalitz decays of the Δ resonance and the η meson. For larger pair masses, the $\pi^+\pi^-$ annihilation contribution to the spectrum dominates. As discussed by these authors and others (e.g. [5]), effects from the dense nuclear medium in the interaction could alter the signal from the $\pi^+\pi^-$ annihilation process and would be reflected in the dielectron mass spectrum. However, these cited theoretical projections predict that such effects on the mass spectrum are too subtle to be distinguished by this original data.

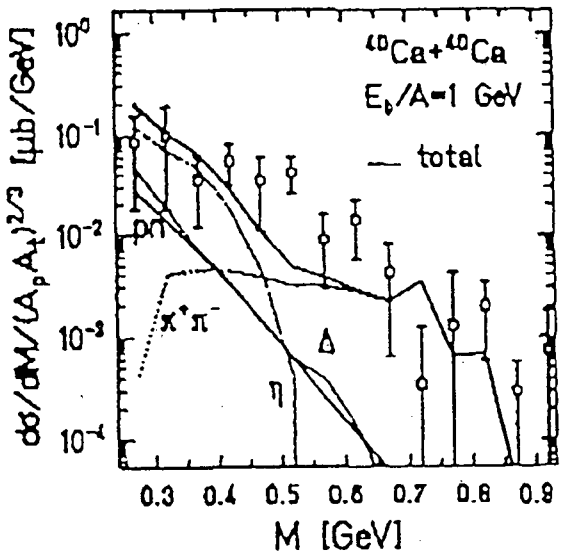

Figure 1. The e^+e^- invariant mass spectrum from Ca+Ca interactions at 1.05 GeV/nucleon. The data is from the 1987 DLS measure while the theoretical model is from publication of Wolf et. al. [1].

As discussed by Ken Wilson in these proceedings, the DLS undertook an extensive experimental program to identify the primary nucleon+nucleon source components of the dielectron signal at these energies via measurements in p+p and p+d systems. This series of experiments concluded in July of 1992 and the DLS returned to measurements in A+A systems. Recognizing the deficiency of the initial data as noted above, the primary goal of the DLS was to obtain a statistically large pair sample in a single A+A system. Our experience with the analysis of the Nb+Nb at 1.05 GeV/nucleon and the Ca+Ca at 2.1 GeV/nucleon pointed

out the difficulties of maintaining control of the systematic problems encountered in measuring dielectron pairs in high multiplicity environments. Also, the then impending shutdown of the Bevalac brought the realization that the DLS would have only one sufficiently long running period to obtain the desired goal. Thus to ensure a good likelihood of success, the system of Ca+Ca at 1.05 GeV/nucleon was chosen for the measurement. The result of this experimental run, which lasted for a five week period in September and October of 1992, was a pair sample more than a factor of 10 larger than previous measurements. With this factor of 3 decrease in the size of the statistical uncertainty, the data promises to have an impact on identifying potential effects of the interaction medium on the hadronic participants of the collision.

As an experimental aid in deciphering the physics content of the dielectron probe, the DLS Multiplicity Array was developed and installed prior to the 1989 heavy-ion running. This detector is a set of 96 scintillator slats which surround the scattering chamber in which the beam-target interaction occurs. A full description of this detector can be found in ref [4] where the first results of the correlation between dielectron pairs and the event multiplicity is reported. This correlation is shown in figure 2 as the pair yield's associated multiplicity distribution normalized

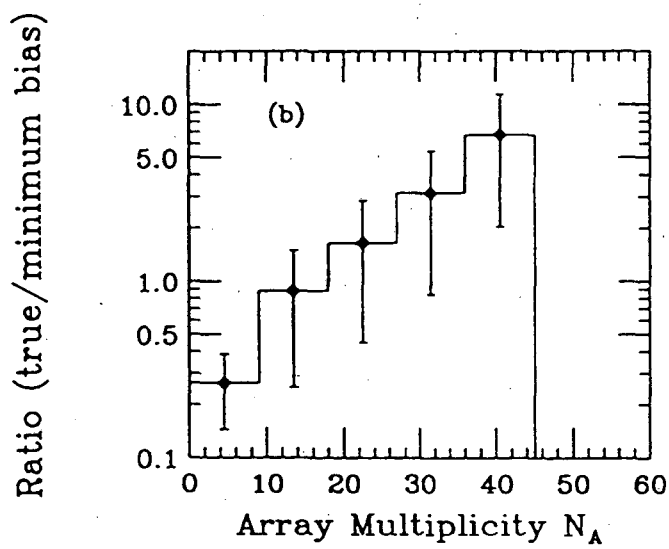

Figure 2. The e^+e^- multiplicity dependence from Nb+Nb interactions at 1.05 GeV/nucleon taken as the event multiplicity associated with the pair yield relative to a Monte Carlo minimum bias multiplicity distribution.

by a Monte Carlo minimum bias interaction multiplicity distribution is plotted. Although the correlation of increasing relative yield to increasing multiplicities is clear, the statistically small sample in this measurement did not allow for a definite parameterization of this dependence nor a detailed investigation into correlations between the event multiplicity and the mass spectrum. The Multiplicity Array and scattering chamber were removed for the liquid target program but reinstalled for the Ca+Ca measurement. A similar correlation between pair yield and event multiplicity in the Ca+Ca measurement has been observed. With this large data sample, the multiplicity dependence in the dielectron yield can be specified and the investigation into the multiplicity dependences in the invariant mass spectrum will be pursued.

The DLS was allotted a separate three week experimental run in January of 1993 very near the end of the Bevatron's operation. Since this time period was not sufficiently long enough to greatly enhance the statistics in the Ca+Ca measurement by a return to this system and with the expressed desire to shut down the Hilac operation prior to our running period, choices for the systems in which to measure dielectron production were made on the basis of complementing the Ca+Ca measurement. One goal of these investigations was to provide an experimental measurement to indicate the level of contribution which Fermi momentum in the target and projectile nuclei has on the mass spectrum in the mass region projected as dominated by the $\pi^+\pi^-$ annihilation process. For this reason, it was determined that a measurement in He+Ca interactions at 1.05 GeV/nucleon would provide specific insight into the Ca+Ca data. That is, while the average Fermi momentum per nucleon is quite similar in the two systems, the level of compression of the nuclear matter achieved during the interaction will be quite different in the He+Ca system as compared with a small impact parameter Ca+Ca collision. As a second goal, there was an interest in performing a series of measurements to indicate the $A_p \cdot A_t$ dependence in the cross section. As this dependence may change in different regions of the mass spectrum, these measurements may identify mechanisms in which the rescattering of either participant nucleons or produced secondaries is important to the production process. During this January 1993 period, the measurement of dielectron production in the He+Ca system was performed followed by measurements in C+C and d+Ca collisions at this same energy. The C+C system was of interest as a symmetric system with a similar $A_p \cdot A_t$ value as the He+Ca system. The d+Ca system provides another $A_p \cdot A_t$ point of reference in an interaction domain in which nucleon+nucleon processes should dominate the production mechanisms. Although the mass spectra from these measurements are

too preliminary for release at this time, the currently measured pair samples for the complete set of new A+A system measurements are shown in table 2.

Reaction	E/A (GeV)	True Pairs	Date	Status
Ca + Ca	1.05	3117±124	Sep92	Preliminary
He + Ca	1.05	1148±44	Jan93	Preliminary
d + Ca	1.05	1250±42	Jan93	Preliminary
C + C	1.05	2168±70	Jan93	Preliminary

Table 2. Recent DLS measurements of dielectron production in A+A systems.

In summary, once the experimental goals of providing measures for dielectron production in a purely nucleon+nucleon picture was realized with the liquid target program, the DLS returned to measurements in A+A systems. The results of the program include a statistically large sample of dielectron pairs from Ca+Ca collisions at 1.05 GeV/nucleon with an associated event multiplicity measurement. Further augmentation of this data is provided by data obtained in He+Ca, C+C, and d+Ca systems, all at this same beam energy. These final data sets may provide physicists with a means of investigating and distinguishing potential medium effects envisioned to occur during the heavy-ion collision.

References

[1] G. Wolf et al.,*Nuclear Phys.* **A545**, (1992)
[2] V.D. Toneev et al.,*GSI Preprint* GSI-92-05, (1992)
[3] G. Roche et al.,*Phys. Rev. Lett.* **61**, 1069 (1988)
[4] S. Beedoe et al.,*Phys. Rev. C* **47(6)**, 2840 (1993)
[5] C. M. Ko et al., "Relativistic Aspects of Nuclear Physics", ed. T. Kodama et al., World Scientific Publ. (1992) (See also contribution by C. M. Ko to these proceedings)

DILEPTON PRODUCTION IN PROTON+NUCLEON COLLISIONS

Kevin Haglin
National Superconducting Cyclotron Laboratory, Michigan State University
East Lansing, Michigan 48824

ABSTRACT

We calculate dielectron production from proton-proton and proton-neutron reactions for energies above hadronic inelastic thresholds. Simple bremsstrahlung from proton-proton scattering is not small compared with proton-neutron at these energies. This shows a clear breakdown of the dipole approximation. The many-pion final states are shown to radiate even more strongly than simple bremsstrahlung. We add the total bremsstrahlung contribution to Dalitz decay of the η, radiative decay of the Δ and to two-pion annihilation and compare with proton-proton inclusive cross sections and ratios of pd/pp yields from the Dilepton Spectrometer.

1. Introduction

It has been argued over and over that the dipole approximation of proton-nucleon bremsstrahlung is a good one, even for Bevalac energies. This means that one would argue that np bremsstrahlung is a much stronger contributor to e^+e^- production than pp. If this were true one would expect the pd/pp ratio to be something not too small. The np component allowed by the target deuteron would clearly dominate—pushing this ratio to something large. How then can we understand the experimentally observed ratio of 10 at 1.0 GeV with monotonic decrease to nearly 2 at 4.9 GeV[1,2]? The answer to this question becomes apparent upon careful re-examination of simple nucleon-nucleon bremsstrahlung calculations for these energies as well as a serious examination of bremsstrahlung beyond two-to-two hadronic reactions. We investigate the effects of pions in the final state since the energies of interest are clearly above pion production thresholds. We find their effect to be most important.

2. Soft-Photon Approximation

We start with a completely general hadronic reaction $a+b \rightarrow 1+2+\ldots+n$. Accelerating charged particles can radiate real or virtual photons. The radiation can originate from any of the $n+2$ external lines carrying charge, from any three-hadron vertex, or from exchanged charged mesons. In the soft-photon limit, the scattering amplitude for radiation off the external lines diverges since the half off shell hadron approaches its mass shell. All the rest, dubbed internal radiation, stay finite. To a good approximation, they can be neglected. This is the approach we take, since we intend to handle general many particle final states, it is a first step toward a complete calculation. The matrix element for soft-photon production simplifies to the purely hadronic counterpart times a multiplicative function describing the complicated electrodynamics of the reaction[3]. Partially correcting for phase space and insisting on energy conservation at the photon-dilepton vertices, the differential cross section for pure hadronic scattering (elastic or inelastic)

while at the same time producing a virtual photon (electron-positron pair) of invariant mass M and energy q_0 is

$$\frac{d\sigma^{e^+e^-}}{dM} = \frac{\alpha^2}{4\pi^4}\frac{\widehat{\sigma}(s)}{Mq_0^2}\int \delta(q^2-M^2)\delta^4\left(q-(p_+ + p_-)\right)d^4q\frac{d^3p_+d^3p_-}{E_+E_-}\frac{R_n(s')}{R_n(s)}, \qquad (1)$$

where R_n is n-body phase space[4], $s' = s + M^2 - 2\sqrt{s}\,q_0$, and

$$\widehat{\sigma}(s) \equiv \int \prod_{i=1}^{n} d^3p_i \left[\frac{d^{3n}\sigma}{\prod_{i=1}^{n} d^3p_i}\right]\left(q_0^2\,|\epsilon\cdot J|^2\right). \qquad (2)$$

The bracketed expression in Eq. (2) is the purely hadronic cross section and $q_0^2|\epsilon\cdot J|^2$ is the dimensionless electromagnetic *weighting* representing a coherent sum of all radiating external lines in the diagrams. The function $q_0^2|\epsilon\cdot J|^2$ is ultimately responsible for our earlier claim that pp bremsstrahlung is not small as compared with np at Bevalac energies. It has been evaluated for the general case and appears in the literature[5]. We show in Fig. 1 this electromagnetic *weighting* as a function of center-of-mass scattering angle for simple np and pp reactions at four different energies.

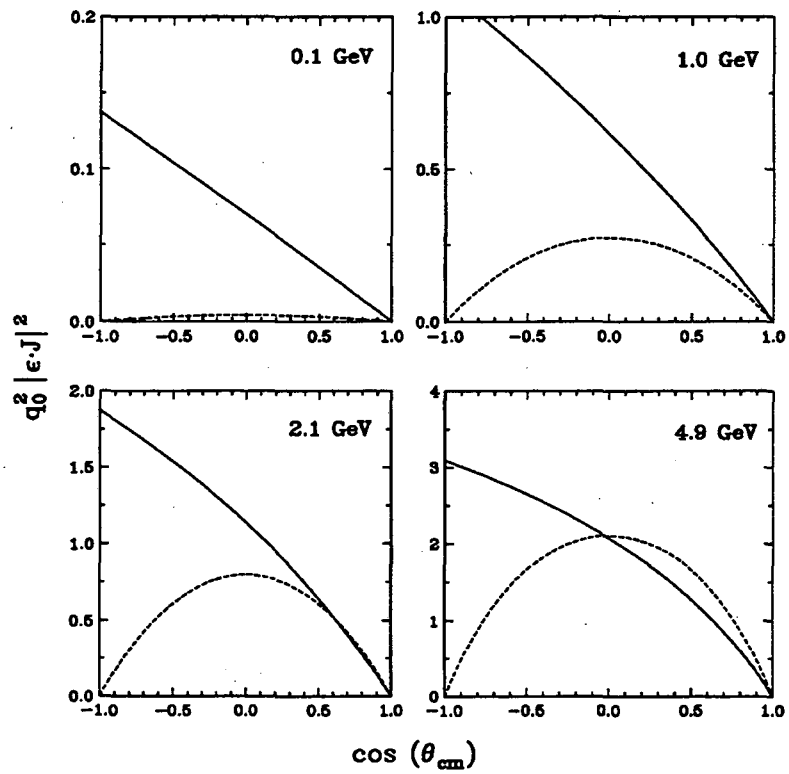

Fig. 1. Electromagnetic *weighting* for np (solid curves) and pp (dashed curves) processes versus center-of-mass scattering angle.

One can see that the dipole approximation is excellent at 100 MeV, but already at 1.0 GeV it starts to fail. At 2.1 GeV as well as 4.9 GeV, it is completely invalid.

3. Simple Nucleon-Nucleon Bremsstrahlung

Hadronic cross sections are input for the soft-photon calculations we are discussing. Precise forms we take for differential np and pp cross sections have been published elsewhere[6], so we do not reproduce them here. But we stress the importance of choosing parametrizations that account for observed angular dependences of the cross sections. Upon integrating Eq. (1) with the DLS acceptance version 2.0 included, we arrive at a cross section. An absolute comparison can be made with the experimental results[7] which we show in Fig. 2.

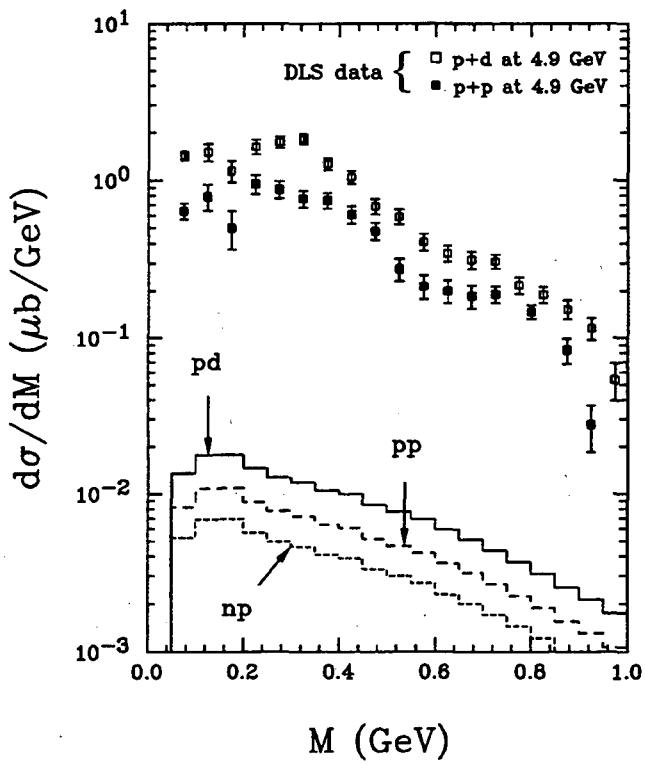

Fig. 2. Invariant mass distribution of dielectrons from experiment as compared with simple pp bremsstrahlung (long-dashed histogram), with np bremsstrahlung (short-dashed histogram) and from an approximate $pd \approx pp + np$ bremsstrahlung (solid histogram).

4. Many-Body Final-State Bremsstrahlung

We parametrize the single, double and triple pion final state cross sections according to relativistic Breit-Wigner forms. Again, the forms we take have been published elsewhere[6], so for brevity, we do not present them here. Including the experimental acceptance, we preform the necessary integration over many-body phase space to arrive at cross sections (mass distributions) for the individual processes $NN \to NN\pi e^+e^-$, $NN \to NN\pi\pi e^+e^-$ and $NN \to NN\pi\pi\pi e^+e^-$. In Fig. 3a we show the one-pion

channels' contributions in pp scattering as compared with simple bremsstrahlung. The double pion channels are intermediate between these and simple bremsstrahlung, but fall faster with increasing mass due to phase space. Finally, the three pion channels contribute roughly the same as the two-pion channels at very low mass, but phase space cuts them off even faster. When all the channels are added together we arrive at the total pp bremsstrahlung shown in Fig. 3b as open squares. One concludes that bremsstrahlung is indeed the largest source of dielectrons and that it comes from many-body bremsstrahlung. Also included in Fig. 3b are results from η Dalitz, radiative Δ decay and an estimate of $\pi^+\pi^-$ annihilation[8]. Details can be found in Ref. 6.

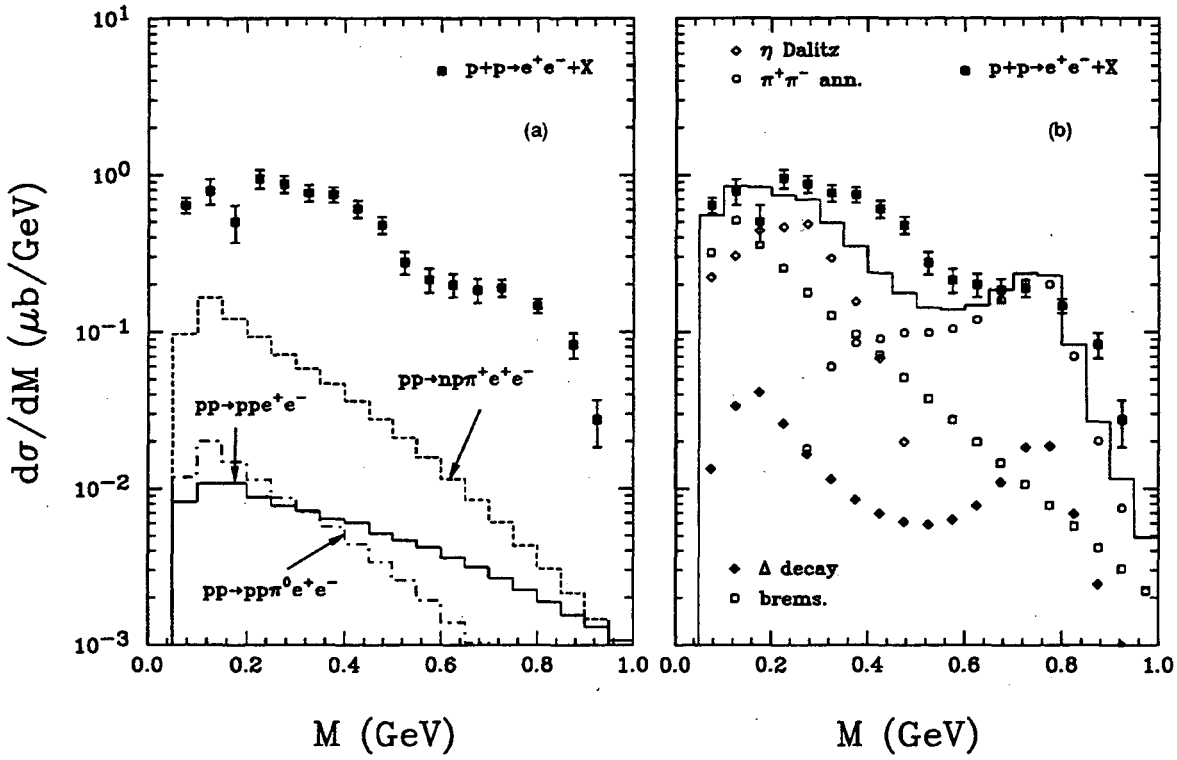

Fig. 3. Invariant mass distribution from single pion channels (a) and from several different sources (b) as compared with inclusive pp results at 4.9 GeV from the Bevalac. Solid histogram in (b) is the sum of all four sources.

5. Ratios

With all processes included (annihilation only included at 4.9 GeV), we construct the ratio pd/pp for four different energies. We use simple $pd = np + pp$ approximations; it must be pointed out that a more complete treatment of the deuteron must be done—one that accounts for Fermi motion—but this is a simple first step. In Fig. 4 we show the ratios as compared with the DLS experimental results[2]. The lower energies' results do not fit the data as well as the higher but the general trends are right. The monotonic rise with increasing mass at the lower energies in our calculation is because simple bremsstrahlung dominates. For masses near the kinematic limit and using a velocity vector for a massive photon in the current, simple pp bremsstrahlung is strongly suppressed as compared with np. At higher energies, the agreement is quite satisfactory.

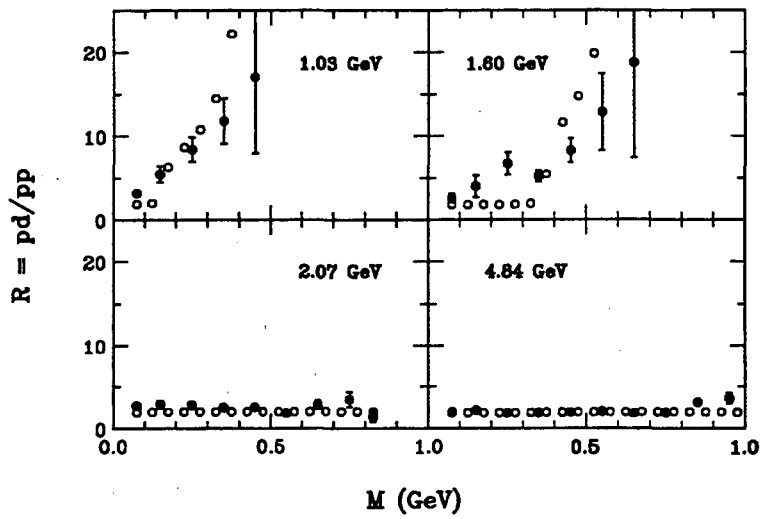

Fig. 4. Ratio of *pd/pp* cross sections as a function of invariant mass. Experimental DLS data[2] are the solid circles and our calculations are the open circles.

6. Concluding Remarks

Proton-proton bremsstrahlung is as strong or stronger than proton-neutron at Bevalac energies. Hadronically inelastic channels, i.e. single and double pion channels, are more important to low-mass dielectron production than simple bremsstrahlung and even η Dalitz decays. Observed *pd/pp* dielectron production ratios can be understood by including simple and many-body bremsstrahlung, Dalitz and radiative decays and two-pion annihilation. A more detailed study of the ratios properly incorporating the target deuteron and also isospin differences in η production (and therefore Dalitz decays) must be done.

7. Acknowledgements

I am grateful to Charles Gale and Subal Das Gupta for their financial support through the Natural Sciences and Engineering Research Council of Canada and the FCAR fund of the Quebec government while I was a postdoc at McGill University where much of this work was completed. This work was supported by the National Science Foundation under grant number PHY-9017077.

8. References

1. H. Z. Huang, *et al.*, Phys. Lett. **B** 297, 233 (1992).
2. W. K. Wilson, *et al.* Phys. Lett. **B** 316 (1993).
3. L. Heller, in *Soft Lepton Pair and Photon Production*, edited by J. A. Thompson (Nova Science, 1992), p. 1.
4. E. Byckling and K. Kajantie, *Particle Kinematics* (John Wiley & Sons, 1973).,
5. K. Haglin, V. Emely'anov and C. Gale, Phys. Rev. **D 47**, 973 (1993).
6. K. Haglin and C. Gale, Phys. Rev. **C**, in press.
7. H. Z. Huang, *et al.*, Phys. Rev. **C**, in press.
8. J. Kapusta and P. Lichard, Phys. Rev. C **40**, R1574 (1989).

DILEPTON PRODUCTION IN HEAVY-ION COLLISIONS

Che Ming Ko
Cyclotron Institute and Department of Physics
Texas A&M University, College Station, Texas 77843, USA

1. Introduction

According to the transport model for heavy-ion collisions at the Bevalac/SIS energies of around 1 GeV/nucleon, a nuclear matter with a density of 2-3 times the normal nuclear matter density can be created [1, 2, 3]. This dense matter is also highly excited, with a delta to nucleon ratio reaching about 30% [4]. Decays of these deltas give rise to an appreciable number of pions in the matter. Rho mesons can then be formed from pion-pion interactions. Heavy-ion collisions thus offer the possibility to study both the properties of dense matter and the in-medium properties of hadrons.

There are already some indications that medium effects play an important role in understanding the experimental data. For example, the observation of an enhanced yield of pions with low transverse kinetic energies in heavy-ion experiments [5, 6] has led to the suggestion that this may be due to the softening of the pion dispersion relation in the dense matter formed in the collision [7]. Also, deltas through their interactions with other hadrons have been shown to be largely responsible for the production of kaons, antikaons, and antiprotons from heavy-ion collisions at energies that are below their production threshold in the nucleon-nucleon interaction in free space. Furthermore, it has been demonstrated in the relativistic transport model that the reduction of kaon, antikaon, and antiproton masses due to the attractive scalar field in the dense matter can account for the observed enhancement of their yields as a result of the reduced production threshold [8].

Because of the relatively weak interactions with other particles, dileptons created from a dense matter, unlike hadrons mentioned in the above, do not suffer final-state interactions and are thus expected to carry more direct information about the properties of dense matter and the in-medium properties of hadrons [9, 10]. In this talk, I shall review the present theoretical understandings of dilepton production from heavy-ion collisions and the possible medium effects that one can learn from dilepton experiments.

2. Dileptons from heavy-ion collisions

Since the probability for dilepton production in heavy-ion collisions is small, perturbative treatments can be used. Based on transport models, perturbative calculations of dilepton production, including contributions from the proton-neutron bremsstrahlung, the pion-nucleon interaction, delta and eta decays, and the pion-pion annihilation, have been carried out by the Giessen group [11] and the Texas A&M group [12]. A typical result from

the latter group is shown in Fig. 1 in which the experimental data from the DLS collaboration at Bevalac [13, 14] are also shown. It is seen that dileptons with small invariant masses are mainly from proton-neutron bremsstrahlungs and delta decays while dileptons with large invariant masses are dominated by pion-pion annihilation. The contribution from eta decays, that was neglected in ref. [12], turns out to be very important at invariant masses below about 500 MeV [15]. Nevertheless, the eta has a width of only 1.08 KeV and decays thus outside of the matter, its contribution to dilepton production can in principle be subtracted out if its spectrum is also measured.

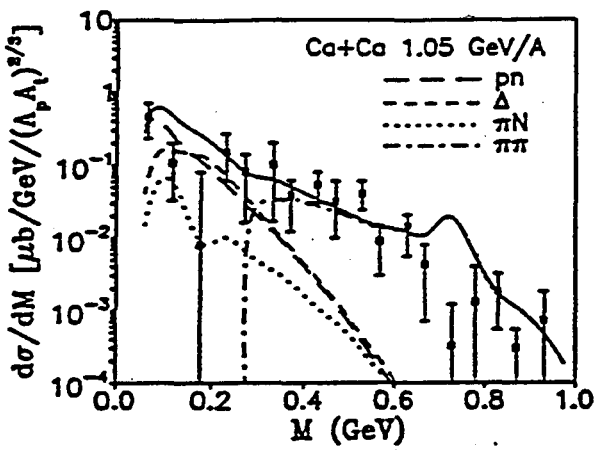

Fig. 1 The dilepton invariant mass spectrum from Ca+Ca collisions at 1.05 GeV/nucleon. The experimental data of refs. [13, 14] are given by solid squares while the theoretical total yield is given by the solid curve.

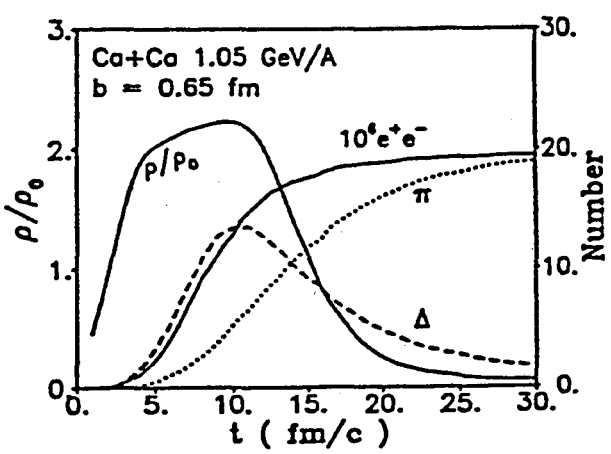

Fig. 2 The time dependence of the dilepton, pion, delta numbers and the central density.

We also see clearly the rho meson contribution to dilepton production from the pion-

pion annihilation as a result of the dominance of rho meson in the pion electromagnetic from factor. Because of the large uncertainty in experimental data, no definite conclusions can be drawn from this comparison. Although most dileptons are produced in the early stage of the collision when the central density is high, those from pion-pion annihilation have substantial contributions also from lower densities [15]. This is so as most pions in the transport model do not appear until the expansion stage of the collision when the density decreases. This is illustrated in Fig. 2 where the time dependence of the dilepton, pion, delta numbers and the central density for a central Ca+Ca collision is shown.

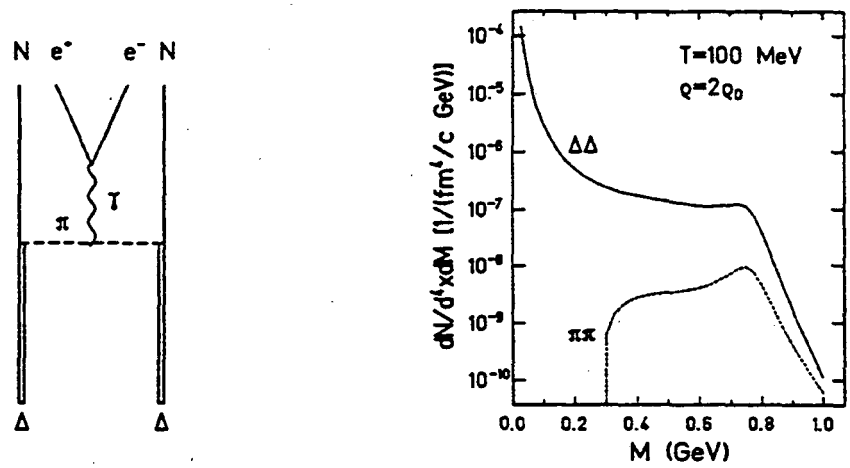

Fig. 3 Left: Dilepton production from a delta-delta interaction. Right: Dilepton production rate in a fireball from pion-pion and delta-delta interactions.

However, the contribution to dilepton production from the annihilation of two virtual pions in a delta-delta interaction as shown in Fig. 3 has not been included in these studies. In a fireball model, it has been found that this contribution, shown also in Fig. 3, is more important than that from the annihilation of two real pions [16]. As seen in Fig. 2, the delta number at the high density stage is larger than the pion number, dilepton production from delta-delta interactions is likely to be more important than that from pion-pion annihilation. Since the total number of deltas and pions in a heavy-ion collision remains essentially constant after initial compression, we expect that the contribution to dilepton production from both real and virtual pion-pion annihilation will be mainly from the high density stage of the collision. The study of dilepton production from heavy-ion collisions will thus provide information on the properties of both pion and rho meson in a dense matter.

3. Medium effects on dilepton production

3.1. The pion dispersion relation in a medium

Medium effects on dilepton production were first studied by Gale and Kapusta in connection with the pion dispersion relation in a medium [17]. Because of the strong attractive

p-wave interaction of the pion with a nucleon, its dispersion relation is expected to be softened in the nuclear medium. Using a schematic in-medium pion dispersion relation, they found that dileptons produced from the pion-pion annihilation are enhanced at invariant masses around twice the pion mass. This effect was treated more consistently by Xia *et al.* [18] who had used the delta-hole model to describe the pion-nucleon interaction. The coupling to the delta-hole polarization in the nuclear medium leads to the following self-energy for a pion with momentum k and energy ω [19, 20],

$$\Pi_o(\mathrm{k},\omega) \approx \frac{9}{8}\left(\frac{f_\Delta}{m_\pi}\right)^2 \rho_N \frac{\omega_R}{\omega^2-\omega_R^2} k^2 e^{-2k^2/b^2}. \tag{1}$$

In the above, $f_\Delta \approx 1$ is the pion-nucleon-delta coupling constant, m_π is the pion mass, $b \approx 7m_\pi$ is the momentum cutoff, and ρ_N is the nuclear density. The delta-hole excitation energy is given by $\omega_R \approx m_\Delta - m_N + k^2/2m_\Delta$, with M_N and M_Δ being the nucleon and delta masses, respectively. The delta-hole short-range repulsive interaction described by the Migdal parameter $g' \approx 0.6$ modifies the pion self-energy to $\Pi = \Pi_0/(1 - g'\Pi_0/k^2)$. In Fig. 4, the pion dispersion relation, given by $\omega^2 = m_\pi^2 + k^2 + \Pi(\omega, k)$, is shown for different nuclear densities. Because of the interaction between the pion and the delta-hole state, the pion branch in the lower part of the figure is seen to become softened while the delta-hole branch in the upper part of the figure is stiffened.

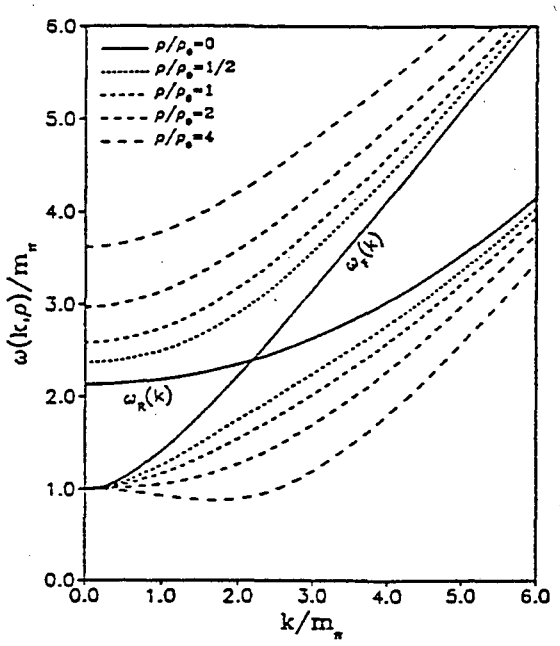

Fig. 4 The pion dispersion relation in a medium.

The dilepton invariant mass spectrum from the pion-pion annihilation in a fireball and with the dispersion relation of Fig. 4 is shown in Fig. 5 by the dashed curves for different total dilepton three momenta. Compared with the results using the free pion dispersion

relation given by the dotted curves, the enhancement at twice the pion mass is clearly seen. This calculation is, however, not gauge invariant as it neglects the vertex correction from the delta-hole polarization. As pointed out by Korpa and Pratt [21], for dileptons with zero three momentum the vertex correction would cancel exactly the enhancement due to the effect from the pion self-energy. This is shown in Fig. 5 by the solid curves. For dileptons with zero three momentum, the dilepton yield around twice the pion mass indeed vanishes. However, the cancellation is less complete for dileptons with finite three momenta as seen in Fig. 5 [22].

The results shown in Fig. 5 neglects the imaginary part of the pion self-energy, which is appreciable because of finite delta width and strong pion absorption in a nuclear medium. Including this effect leads to a less singular dilepton spectrum at smaller invariant masses and makes the medium effect more appreciable [23].

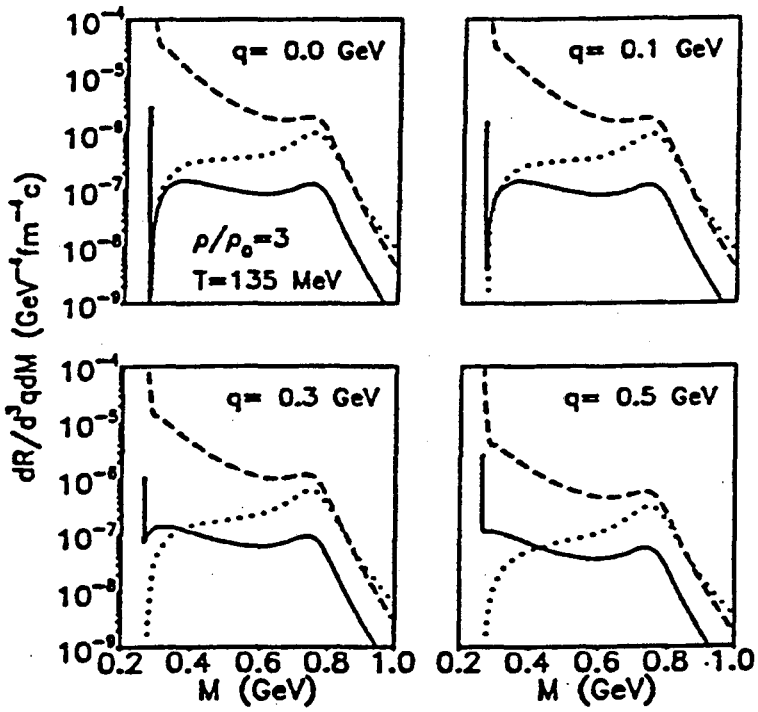

Fig. 5 The dilepton invariant mass spectra from the pion-pion annihilation for different three momenta. Dotted, dashed, and solid curves are results from, respectively, free pions, pions with self-energies, and pions with self-energies and vertex corrections.

3.2. Rho meson in dense matter

In above studies, the pion electromagnetic form factor, dominated by the rho meson, is assumed to be the same as that in free space. Chanfray *et al.* [24] showed, however, that the modification of pions in a medium also affects the properties of the rho meson, leading to an increase of both its mass and width in dense matter. This is followed by more

consistent studies by the GSI group [25] and the Texas A&M group [26] in the framework of the vector dominance model.

For the vector dominance model in a medium, the rho meson self-energy is given by the diagrams in Fig. 6, where both pions and the rho-pion vertices are dressed with the effect from the delta-hole polarization. The rho meson spectral function, obtained from the imaginary part of its propagator, is shown in Fig. 7a. One sees that as the nuclear density increases, the rho meson peak shifts to larger masses and at the same time its width becomes broader. Also seen in the spectral function is a peak around three times the pion mass, and it corresponds approximately to the sum of the pion mass and the energy of the delta-hole state. This peak is not seen in the less consistent study of ref. [24].

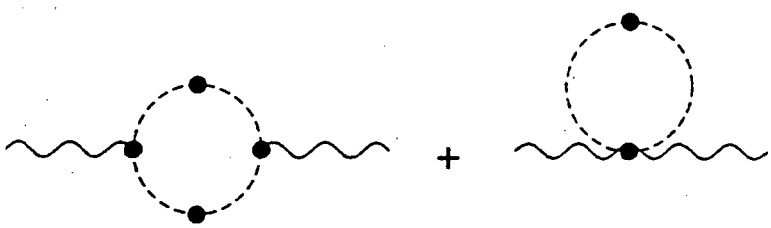

Fig. 6 The rho meson self-energy diagrams. Wavy and dashed lines denote rho meson and pion, respectively.

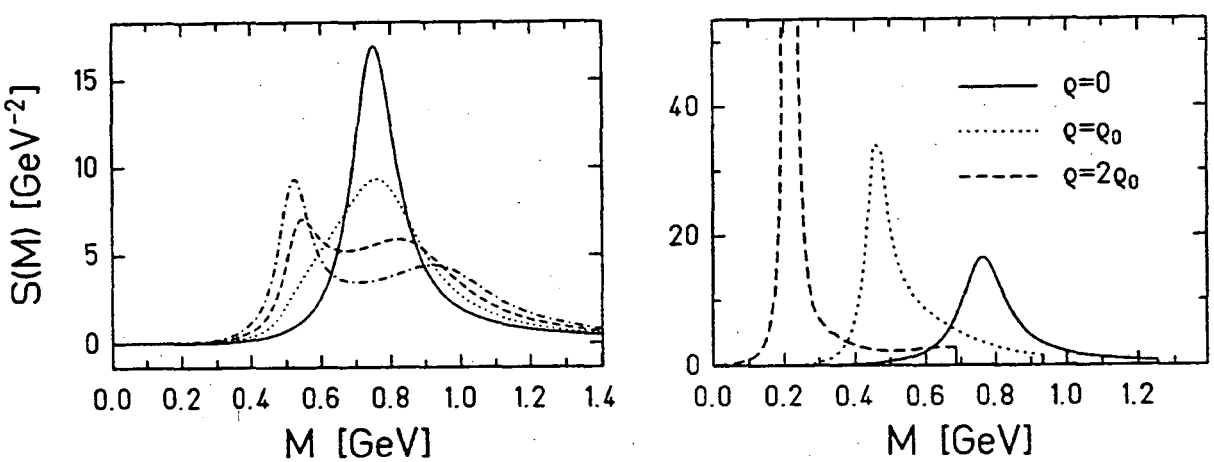

Fig. 7 The rho meson spectral function in a medium: (a) Vector dominance model and (b) QCD sum rules method.

The rho meson mass in a medium has also been studied in the QCD sum rules method [28]. In this approach, the rho meson mass is determined by various quark and gluon condensates in the QCD vacuum. As these condensates are modified in the nuclear medium, the rho meson mass is also affected. It turns out that the in-medium rho meson mass

decreases with density and is approximately given by

$$m^* \approx m_\rho \left(1 - \lambda \frac{\rho_N}{\rho_0}\right), \tag{2}$$

where ρ_0 is the normal nuclear matter density and $\lambda \approx 0.18$. This mass dependence of the rho meson mass is similar to the in-medium scaling law of Brown and Rho [27] deduced from the scaling property of QCD.

The difference between the results from the vector dominance model and the QCD sum rules calculation of ref. [28] can be qualitatively understood as follows. The rho meson is a mixture of a bare rho meson consisting of a quark-antiquark pair and a pion-pion resonance. In the vector dominance model, one includes only the medium effect on the pion-pion interaction but not on the internal quark structure of the bare rho meson. The opposite is the case in the QCD sum rules study of ref. [28]. To take into account the medium effect on both the pion-pion interaction and the quark structure of the rho meson, one can introduce the spectral function obtained from the vector dominance model into the QCD sum rules analysis [29]. It is then found that the effect due to the change of the QCD vacuum in the presence of the nuclear medium is much stronger than the medium effect on the pion-pion interaction. The resulting rho meson spectral function is shown in Fig. 7b. One sees that the rho meson peak moves to smaller masses as the density increases.

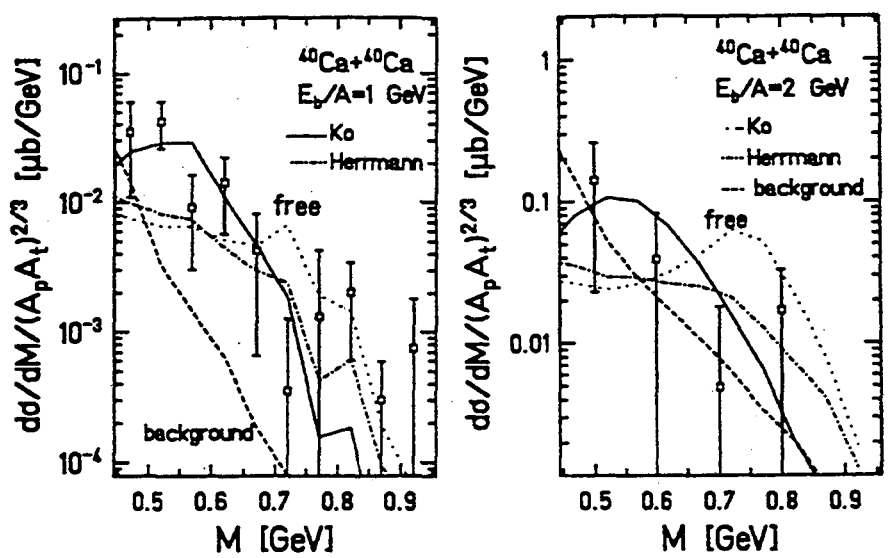

Fig. 8 Dilepton invariant mass spectra [15]. Dotted, dashed, and solid curves correspond, respectively, to calculations with the rho meson in free space, from the vector dominance model, and from the QCD sum rules. Data are from refs. [13, 14].

The effect of the modified rho meson properties in a dense matter on the dilepton invariant mass spectrum has been studied in the transport model by Wolf [30]. This is shown in Fig. 8. Dotted, dashed, and solid curves correspond, respectively, to calculations

with the rho meson in free space, from the vector dominance model of Hermann *et al.* [25], and from the QCD sum rules of ref. [29]. The difference among the three results are appreciable. Unfortunately, present data from the Bevalac shown in the figure are not accurate enough to allow us to draw definitive conclusions about the properties of a rho meson in dense matter. A similar study has also been carried out by Winckelmann [31].

4. Conclusions

Transport model studies of heavy-ion collisions at the Bevalac/SIS energies indicate that dilepton production from pion-pion interactions in the dense matter formed in the initial stage of the collisions is very important. The softening of the pion dispersion relation in the dense matter enhances the production of small invariant mass dileptons with finite three momenta. The change of rho meson properties in the dense matter affects dileptons with large invariant masses. To detect these effects requires, however, a better understanding of dileptons from the Dalitz decay of deltas and etas as well as from delta-delta interactions. Future experiments at SIS with the HADES detector [32] will provide more accurate data than those available from the DLS collaboration at Bevalac and will allow us to see more clearly the medium effects on dilepton production. The study of dileptons in heavy-ion collisions thus offers the exciting possibility to investigate the properties of hadrons in the dense matter.

This work was supported in part by the National Science Foundation under Grant No. PHY-9212209 and the Welch Foundation under Grant No. A-1110.

References

[1] H. Stöcker and W. Greiner, Phys. Rep. **137**, 278 (1986).
[2] W. Cassing, V. Metag, U, Mosel, and K. Niita, Phys. Rep. **188**, 363 (1990).
[3] J. Aichelin, Phys. Rep. **202**, 233 (1991).
[4] W. Ehehalt, W. Cassing, A. Engle, U. Mosel, and Gy. Wolf, Phys. Rev. **C47**, R2467 (1993).
[5] G. Odyniec *et al.*, in Proceedings of the 8th High Energy Heavy-Ion Study, edited by J. Harris and G. Woznick, LBL Report No. 24580, 1988, p. 215.
[6] O. Schwalb *et al.*, Phys. Lett **B**, in press.
[7] L. Xiong, C. M. Ko, and V. Koch, Phys. Rev. **C47**, 788 (1993).
[8] G. Q. Li and C. M. Ko, X. S. Fang, and Y. M. Zheng, in Proceedings of the 9th High-Energy Heavy-Ion Study, edited by H. G. Ritter, LBL Report, to appear.
[9] C. M. Ko, Z. G. Wu, and L. Xiong, in Proceedings of the Rio de Janeiro International Workshop on Relativistic Aspects of Nuclear Physics, edited by T. Kodama *et al.*, (World Scientific, Singapore, 1989), p. 309.
[10] C. M. Ko, in Proceedings of the Pittsburgh Workshop on Soft Lepton Pair and Photon Production, edited by J. A. Thompson, (Nova Science Publishers, Inc., 1990), p. 243.

[11] Gy. Wolf, G. Batko, T. S. Biro, W. Cassing, and U. Mosel, Nucl. Phys. **A512**, 772 (1990).
[12] L. Xiong, Z. G. Wu, C. M. Ko, and J. Q. Wu, Nucl. Phys. **A512**, 772 (1990).
[13] G. Roche *et al.*, Phys. Rev. Lett. **61**, 1069 (1988).
[14] C. Naudet *et al.*, Phys. Rev. Lett. **62**, 2652 (1988).
[15] Gy. Wolf, W. Cassing, and U. Mosel, Nucl. Phys. **A552**, 549 (1993).
[16] X. S. Fang, C. M. Ko, P. J. Siemens, and L. H. Xia, in Progress in Research, Cyclotron Institute, TAMU, 1992, p. 64 .
[17] C. Gale and J. Kapusta, Phys. Rev. **C35**, 2107 (1987).
[18] L. H. Xia, C. M. Ko, L. Xiong, and J. Q. Wu, Nucl. Phys. **A485**, 721 (1988).
[19] B. Friedmann, V. R. Pandharipandi, and Q. N. Usmani, Nucl. Phys. **A372**, 372 (1981).
[20] T. Ericson and W. Weise, *Pions and Nuclei*, Oxford University Press, New York, 1987.
[21] C. L. Korpa and S. Pratt, Phys. Rev. Lett. **64**, 1502 (1990).
[22] C. L. Korpa, L. Xiong, C. M. Ko, and P. J. Siemens, Phys. Lett. **B246**, 333 (1990).
[23] C. M. Ko, L. H. Xia, and P. J. Siemens, Phys. Lett. **B231**, 16 (1989).
[24] G. Chanfray, A. Aouissat, P. Schuck, and W. Nörenberg, Phys. Lett. **256**, 325 (1991).
[25] M. Hermann, B. L. Friman, and W. Nörenberg, Z. Phys. **A343**, 119 (1992).
[26] M. Asakawa, C. M. Ko, P. Lévai, and X. J. Qiu, Phys. Rev. **C46**, R1159 (1992).
[27] G. E. Brown and M. Rho, Phys. Rev. Lett. **66**, 2720 (1991).
[28] T. Hatsuda and S. H. Lee, Phys. Rev. **C46**, R34 (1992).
[29] M. Asakawa and C. M. Ko, Phys. Rev. **C48**, R526 (1993); Nucl. Phys. **A560**, 399 (1993).
[30] Gy. Wolf, private communications.
[31] L. Winckelmann, private communications.
[32] W. Kühn, private communications.

Multifragmentation

Studying Multifragmentation Dynamics at Intermediate Energies using Two-Fragment Correlations

T. C. Sangster, H. C. Britt and M. N. Namboodiri
Lawrence Livermore National Laboratory
Livermore, CA 94550

One of the most challenging topics in Nuclear Physics is the multifragmentation at moderate excitation energies in large nuclear systems. Although the idea that multifragmentation is analogous to a liquid-gas like phase transition is not new [1], it has only been recently that highly exclusive experimental measurements have been coupled with sophisticated theoretical models like QMD and BUU/VUU to explore reaction dynamics and the process of fragment formation. Indeed, much of what we know about multifragmentation has resulted from the study of complex correlations present in both the experimental data and theoretical calculations. One of the most crucial questions in the ongoing debate concerning the liquid-gas analogy is the differentiation between simultaneous and sequential fragment emission. Clearly, the phase transition analogy breaks down if fragments are emitted sequentially as in an evaporative process.

There have been a number of two-fragment correlation results published recently [2,3,4] (including those presented in this paper) which attempt to put limits on the emission timescale using three-body Coulomb trajectory calculations with explicit emission times for sequential decays from a fixed source density. These results have been generally consistent and indicate that intermediate mass fragment (IMF) emission is nearly simultaneous in medium energy heavy ion collisions. Only very recently have calculations been performed which approach this question from the other extreme: simultaneous emission from a variable density source [5] (see the contribution from G. Peilert for a summary of these results). The freeze-out density extracted from these calculations is remarkably consistent with the short emission times reported in Refs. [2,3,4]. When considered together, these results argue favorably for a simultaneous multifragmentation.

In this paper we present comprehensive results on two-fragment correlations for heavy systems at intermediate energies. The fragment emission timescale is estimated to be less than 500 fm/c by a direct comparison to correlation functions generated using the sequential three-body trajectory code MENEKA [6]. We also examine the influence of the fragment charge on the shapes of the relative velocity ($\mathbf{V}_{rel}$) and reduced velocity ($\mathbf{V}_{red} = \mathbf{V}_{rel}/\sqrt{Z_1+Z_2}$) correlation functions. Finally, we will look at two-dimensional correlation functions (the components of $\mathbf{V}_{rel}$ projected onto the pair center-of-momentum velocity, $\mathbf{V}_{pair}$) which show no preference for either longitudinal or transverse emission supporting the notion that fragment emission is simultaneous.

The data were obtained at the LBL Bevalac using the PAGODA detector array [7] and Fe beams at both E/A=50 and 100 MeV on targets of Ta, Au and Th. Fragments with velocities between 1.0 and 4.1 cm/ns (E/A=0.5 to 8.8 MeV) and charges between 5 and

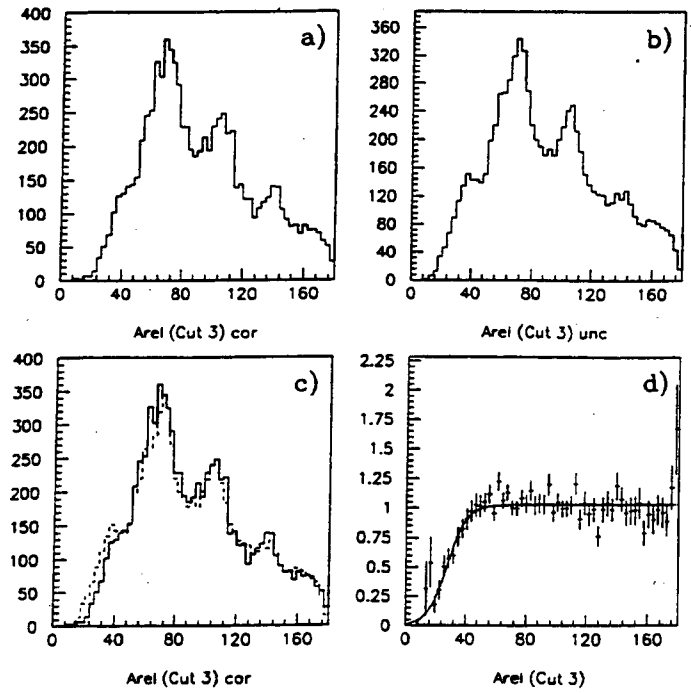

Fig. 1. Correlated (a) and background (b) relative angle distributions for the E/A=100 MeV Fe+Au reaction and the Coulomb product constraint $73 \leq Z_1 Z_2 \leq 110$. The normalized distributions are plotted together in c) and show the suppression at small relative angles due to the final state Coulomb repulsion; the correlation function (d) is obtained by taking the ratio of the normalized correlated and background distributions.

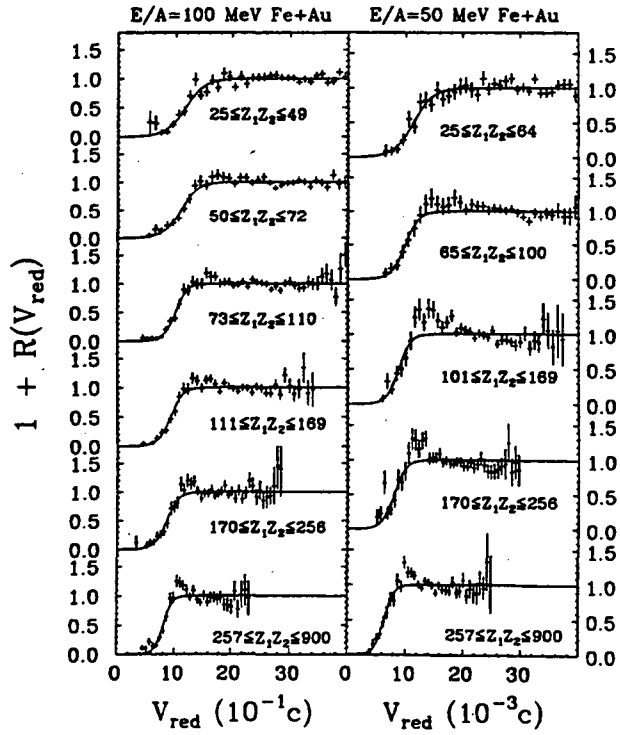

Fig 2. Reduced velocity correlation functions for both the E/A=50 and 100 MeV Fe+Au data sets. The curves through the data points are fits to a simple Fermi function as described in the text.

53 were exclusively measured in eight identical composite detector modules arranged cylindrically around the target between polar angles of 22° and 158° on centerlines of ±36°, ±72°, ±108° and ±144°. Each module subtended approximately ±13° in and out of the beam plane and provided an angular and velocity resolution of 0.25° and 0.05 cm/ns, respectively. A complete description of the fragment identification scheme as well as results on inclusive IMF distributions and binary fission systematics has already been published [8,9,10].

To extract the two-fragment data set used for the analysis in this paper, all coincidence combinations of two fragments were formed and binary fission pairs explicitly removed. Although the experimental setup was ideal for a broad range of inclusive fragment and binary fission measurements, there are certain features worth noting in the two-fragment data sample. The fragment identification algorithms allowed only a single IMF with charge greater than 4 in each module. Therefore, the minimum opening angle between any two fragments is the minimum angle between two adjacent modules, 10°. Additionally, this minimum opening angle can occur only at relatively large laboratory angles since the centerline between the most forward two modules is 54°. Finally, due to the planar geometry of the PAGODA array, there are two kinematically distinct classes of fragment pairs - pairs measured on the same side and pairs measured on opposite sides of the beam. Although opposite side pairs do not populate the low velocity portion of the relative velocity spectrum, there is considerable overlap between the two classes. Indeed, both classes are required to properly construct the V_{rel} correlation functions.

Correlation functions are constructed following the formalism of Ref. [11] where the two-particle coincidence spectrum is divided by a background distribution which contains all the details of the experimental acceptance and reaction dynamics except those associated with the final state Coulomb interaction. Such a background spectrum is constructed using the technique of event mixing in which two fragments from different, but kinematically similar, events are treated as an actual pair of coincident fragments. Since only fragments from true coincidences are used to construct the mixed-event background and all constraints applied to the true pairs are also applied to the background pairs, the mixed distribution essentially reflects the two-fragment phase space population of the detector array in the absence of any final state interaction.

Fig. 1a and 1b show the correlated (a) and background (b) relative angle distributions (θ_{rel} in degrees) for the E/A=100 MeV Fe+Au reaction and the Coulomb product constraint $73 \leq Z_1 Z_2 \leq 110$. The two distributions are remarkably similar despite considerable acceptance structure. When the two distributions are normalized and plotted together (Fig. 1c), the effect of the fragment-fragment Coulomb repulsion can be seen at small θ_{rel}. Relative to the background distribution, there is a distinct suppression of pairs with small relative angles. This suppression appears as a Coulomb hole in the θ_{rel} correlation function (the ratio of the two normalized distributions) shown in Fig. 1d.

In order to study the charge dependence of the various correlation functions (θ_{rel}, V_{rel} and V_{red}), the data were sorted according to constraints on the Coulomb product, $Z_1 Z_2$. Fig. 2 shows all of the V_{red} correlation functions generated for both the E/A=50 and 100 MeV Fe+Au data. The curves through the data points are fits to a simple Fermi distribution,

$$f(x) = \frac{a}{1.0+\exp[(b-x)/c]}.$$

To quantitatively assess the charge dependence of the correlation functions, we compare the half depth points (the value of x such that f(x)=a/2=b) as a function of

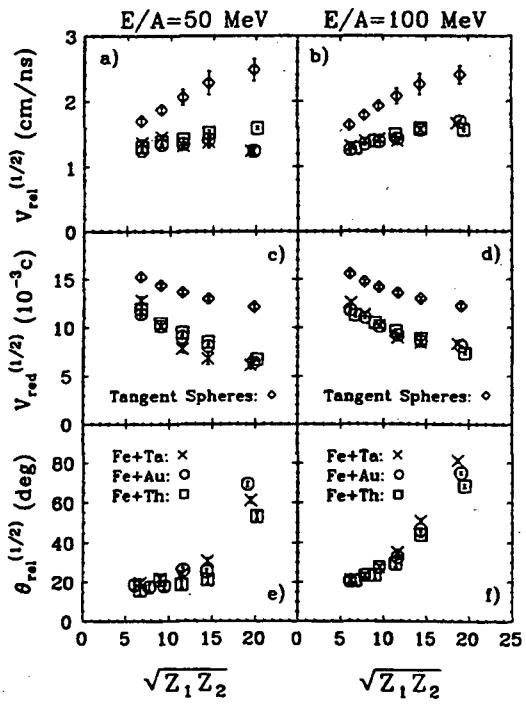

Fig. 3. The half depth points as a function of the Coulomb product for the relative velocity (a,b), the reduced velocity (c,d) and the relative angle (e,f) correlation functions. The diamonds show the means of a simple tangent spheres asymptotic relative velocity calculation as described in the text.

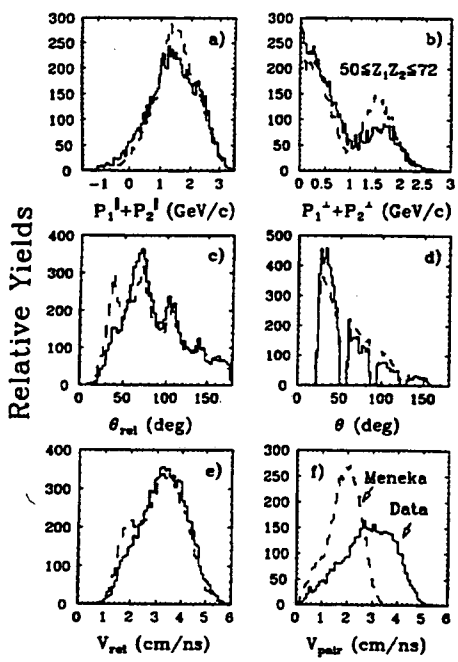

Fig. 4. A comparison of selected distributions from the MENEKA trajectory calculations passed through the PAGODA acceptance filter and compared with the appropriate data. The Fe+Au data are shown as the solid histograms while the acceptance filtered MENEKA results are the dashed histograms.

Z_1Z_2. The half depth point was chosen as the fiducial for comparison because it necessarily selects the subset of fragment pairs which are initially closest together in space-time.

Fig. 3 shows the half depth points as a function of the Coulomb product for the three different correlation functions generated and for all six systems studied. There is little difference between the two bombarding energies or among the three targets. The width of the θ_{rel} Coulomb holes (Fig. 3e and 3f) increases as expected with the Coulomb product. Indeed, it appears that the widths extrapolate smoothly to values consistent with binary fission for $\sqrt{Z_1Z_2} > 25$. Also as expected, the widths of the V_{rel} Coulomb holes (Fig. 3a and 3b) increase with increasing Z_1Z_2. It is for this reason that the reduced velocity has become the preferred parameter for studying two-fragment correlation functions: over a limited range of Z_{ij}, it has been shown [2] that V_{red} does eliminate much of the charge dependence inherent in the mixed-fragment (i.e., $Z_i \neq Z_j$) correlation functions. However, the width of the V_{red} Coulomb holes (Fig. 3c and 3d) clearly exhibits an equally strong dependence on the Coulomb product. Therefore, V_{red} does not appear to be a global scaling parameter.

The dependence of both the V_{rel} and V_{red} Coulomb hole widths is qualitatively similar to that displayed by a simple two-body tangent spheres calculation of the asymptotic relative velocity. The measured Z_{ij} in each Z_1Z_2 bin were used to calculate the tangent spheres asymptotic relative velocity using $r_0=1.4$ fm and the means of the corresponding V_{rel} and V_{red} distributions are shown by the diamonds in Fig. 3. Deep in the Coulomb hole, the effect of the residual source Coulomb field on the two-fragment systematics is minimized. Therefore, the similarity between the tangent spheres calculation and the half depths points is not surprising.

However, the influence of the residual Coulomb field of the source may have a significant influence when estimating the fragment emission timescale by comparing to model calculations. With the idea that the width of the Coulomb hole will depend on the relative fragment emission time, we have made an estimate of the emission timescale [3] by directly comparing the V_{red} correlation functions with the results of the classical three-body trajectory code MENEKA [6] which explicitly accounts for the Coulomb influence and recoil effects of the emitting source. The essential features of the code are isotropic surface emission from a spherical, compound source characterized by a unique radius parameter ($r_0=1.4$ for our calculation) with emission energies selected to reproduce the experimentally measured distributions and the distribution of time delays between fragment emission given by $e^{-\tau/t}$. Additional details of the calculation are given in Ref. [3,6].

In order to optimize the selection of the input parameters (most were fixed at values suggested by previous work), the two-fragment MENEKA output was passed through the PAGODA acceptance filter and the inclusive distributions were compared with the data. A selection of the quantities used for comparison is shown in Fig. 4. With the exception of V_{pair}, all of the quantities compare remarkably well with the data. Any discrepancies are caused by a slight excess of pairs on the same side of the beam in MENEKA. The significant difference in the V_{pair} spectra may simply arise due to the rather naive assumptions concerning the fragment source (e.g., no collective motion). Since no constraints were placed on V_{pair} when generating the correlation functions and all other dynamical quantities compare favorably, we feel that the comparison of correlation functions to extract the fragment emission timescale is entirely valid. It is worth noting, however, that such may not be the case at higher energies where collective effects become important.

Once the MENEKA input parameters were chosen, reduced velocity correlation functions were constructed for emission lifetimes of 50, 100, 250, 500, 1000 fm/c by treating the detector-accepted MENEKA pairs exactly like the data. Fig. 5 shows the

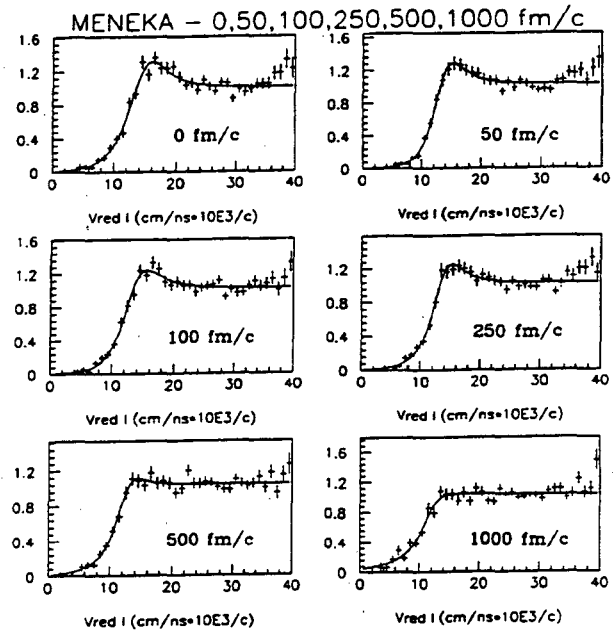

Fig. 5. The reduced velocity correlation functions generated with MENEKA for the Coulomb product constraint $50 \leq Z_1 Z_2 \leq 72$ and values of τ from 0 (upper left) to 1000 fm/c (lower right). Additional input parameters for the calculation correspond to the system E/A=100 MeV Fe+Au. The curves are fits to a modified Fermi distribution as described in the text.

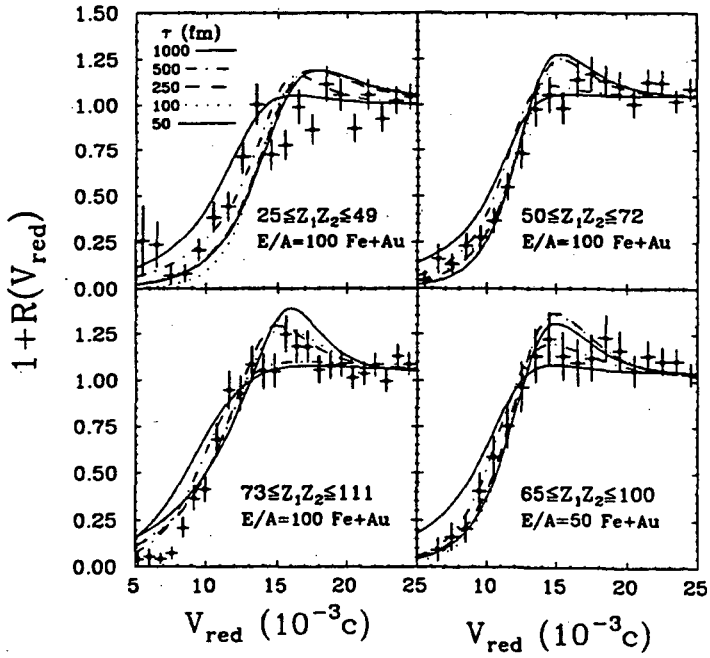

Fig. 6. Comparison of the fitted curves in Fig. 5 to the appropriate measured correlation functions. The emission lifetime appears to be less than 500 fm/c for both bombarding energies.

V_{red} correlation functions generated with MENEKA for the Coulomb product constraint $50 \leq Z_1 Z_2 \leq 72$. The curves through the data points are fits to a modified Fermi distribution,

$$f(x) = \frac{a(1.0+\exp[(d-x)/e])}{1.0+\exp[(b-x)/c]}.$$

We then compare these curves with the measured correlation functions in Fig. 6. The emission lifetime appears to be less than 500 fm/c for both bombarding energies and perhaps somewhat less at E/A=100 MeV than at E/A=50 MeV. There is very little sensitivity within the calculation for lifetimes less than about 250 fm/c. This is likely due to the fact that for such short emission times, the product of the average fragment velocity and the emission time is generally less than the source diameter. In other words, we may already be probing the limit at which the source geometry and the notion of an emission time become indistinguishable. The distinction between emission time and source geometry is addressed further in Ref. [5] and the contribution by Peilert.

When considering the emission of fragments it is instructive to look at whether a preferred emission orientation exists in the two fragment system. A preference for longitudinal emission may indicate a more time-like than space-like emission pattern which would suggest a finite emission time. In Fig. 7a and 7b we show the longitudinal and transverse components of the relative velocity (in cm/ns) projected onto the pair velocity for the Coulomb product constraint $Z_1 Z_2 \leq 200$ and the system E/A=100 MeV Fe+Au. The effect of the final state Coulomb interaction is clearly visible at small values of V_{per} and V_{par}. Fig. 7c and 7d show the ratio of these two distributions as a contour and lego plot, respectively. There is clearly a symmetric Coulomb hole showing no preference for longitudinal or transverse emission and the expected broad, featureless plateau at larger values of V_{per}. Fig. 8 shows the same set of results for the E/A=50 MeV Fe+Au system. As with the MENEKA comparisons, the lower energy two-dimensional correlation functions are virtually identical to those at the higher energy.

The observation of a Coulomb hole in two-fragment relative velocity correlation functions indicates that the lifetime of the emitting source must be quite short. By measuring complete two-fragment velocity systematics, we have been able to put limits on the source lifetime by comparing the data with the results of a classical three-body trajectory calculation in which the source lifetime is explicitly included. The comparison of reduced velocity correlation functions generated with the trajectory code MENEKA indicates that the emission lifetime is less than 500 fm/c and may be considerably less. In addition, two-dimensional correlation functions show no preference for either longitudinal or transverse emission in the two-fragment system suggesting that the emission is very nearly simultaneous. Furthermore, these results are consistent with those of calculations by Peilert [5] in which the source lifetime is identically zero and only the source density is used to optimize the space-time geometry for correlation function comparisons to data.

Acknowledgments:
This work was performed under the auspices of the U. S. Department of Energy by the Lawrence Livermore National Laboratory under Contract W-7405-ENG-48.

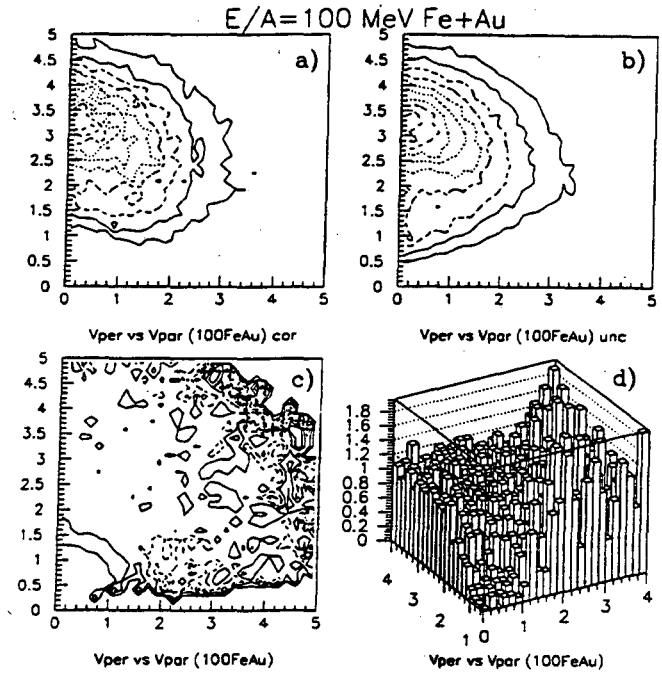

Fig. 7. Plots of the longitudinal vs. transverse components of the relative velocity projected onto the pair velocity, V_{pair} for the Coulomb product constraint $Z_1Z_2 \leq 200$ and the system E/A=100 MeV Fe+Au. a) shows the correlated and b) shows the background distributions; c) and d) show the two-dimensional correlation functions as both a contour and lego plot (these are simply the appropriately normalized ratio of a and b). A symmetric Coulomb hole is clearly visible indicating little preference for either longitudinal (time-like) or transverse (space-like) emission.

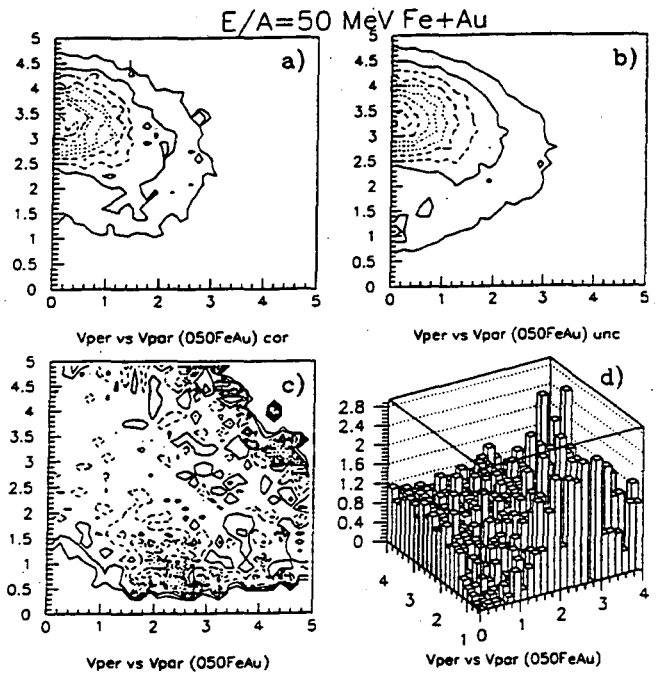

Fig. 8. Same as Fig. 7 except for the system E/A=50 MeV Fe+Au.

References:

1. R. W. Minich *et al.*, Phys. Lett. **118B**, 458 (1982); J. E. Finn *et al.*, Phys. Rev. Lett **49**, 1321 (1982).
2. Y. D. Kim *et al.*, Phys. Rev. Lett. **67,** 14 (1991); Phys. Rev. C **45**, 338 (1992); Phys. Rev. C **45**, 387 (1992).
3. T. C. Sangster *et al.*, Phys. Rev. C **47**, R2457 (1993).
4. D. Fox *et al.*, Phys. Rev. C **47**, R421 (1993).
5. G. Peilert, T. C. Sangster, M.N. Namboodiri and H. C. Britt, submitted to Phys. Rev. Lett.
6. A. Elmaani *et al.*, Nucl. Instrum. Methods **A313**, 401 (1992); Phys. Rev. C **43,** R2474 (1991).
7. M. M. Fowler *et al.*, Nucl. Instrum. and Methods. **A281**, 517 (1989).
8. M. Begemann-Blaich *et al.*, Phys. Rev. C **45**, 677 (1992).
9. Th. Blaich *et al.*, Phys. Rev. C **45**, 689 (1992).
10. T. C. Sangster *et al.*, Phys. Rev. C **46**, 404 (1992).
11. W. A. Zajc *et al.*, Phys. Rev. C **29**, 2173 (1984).

Determining Critical Exponents in Small Systems

A. S. Hirsch,
Purdue University
West Lafayette, IN 47907-1396

A. Introduction

The EOS Collaboration, consisting of groups from GSI, Kent State University, Lawrence Berkeley Laboratory, INFN Catania, Purdue University, Texas A&M, and U.C. Davis, has been interested in flow and multifragmentation for over ten years. The Purdue High Energy Nuclear Physics Group studies of proton-nucleus collisions using an internal gas jet target of heavy noble gases allowed us to accurately measure target fragment yields over a wide range of fragment mass, charge, and incident energies.[1] A high statistics study of the fragment yield in the limiting fragmentation regime provided evidence that heavy fragments come from the simultaneous disassembly of a system somewhat lighter than the original target nucleus and nearly at rest in the laboratory.[2] Complementary studies indicated that the missing nucleons were knocked out in a prompt first stage, leaving the excited target remnant to decay.[3]

With the development of time projection chambers (TPCs), it has become possible to reconstruct all of the charged fragments. I report here some preliminary results from the EOS Collaboration experiment in which we used reverse kinematics to study projectile fragmentation of 1 GeV/nucleon gold nuclei incident on a carbon target. The target resides just in front of the TPC. Behind the TPC sits a multiple-sampling ionization chamber (MUSIC II), followed by a 100 element two layer time-of-flight (TOF) wall. The TPC is capable of detecting charges one through eight, MUSIC II, seven through Z_{beam}, and TOF, charges one through Z_{beam}. For the preliminary analysis presented here, each detector covered an exclusive range: TPC, $1 \leq Z \leq 6$; MUSIC, $11 \leq Z \leq Z_{beam}$; TOF, $7 \leq Z \leq 10$. The total charge reconstructed from about 15,000 events is shown in Figure 1. The tail to the high multiplicity side of the peak is due to the lack of track matching between the TOF wall and the other two detectors. In what follows, we have accepted for analysis only those events with reconstructed charge 79 ± 3 shown as the two vertical lines in Figure 1.

At small excitation energies, the excited projectile remnant decays via emission of a few nucleons or light clusters. At high excitation energies, total vaporization of the remnant is observed. Somewhere in between, a wide range of intermediate mass fragments are made via a simultaneous disassembly of the excited remnant. See Figure 2. (Charges 1-3 have been omitted from this figure so that the yield of the heavier fragments is apparent.) From the point of view of the liquid drop model of the nucleus we might describe the three regimes as follows. At low excitation energies, we observe evaporation. At the highest excitation energies, the nucleus is vaporized into a gas of nucleons and light clusters. At intermediate excitation energies, the nucleus is torn between the liquid and the gas phases. The observation in inclusive studies of a power-law yield in the fragment

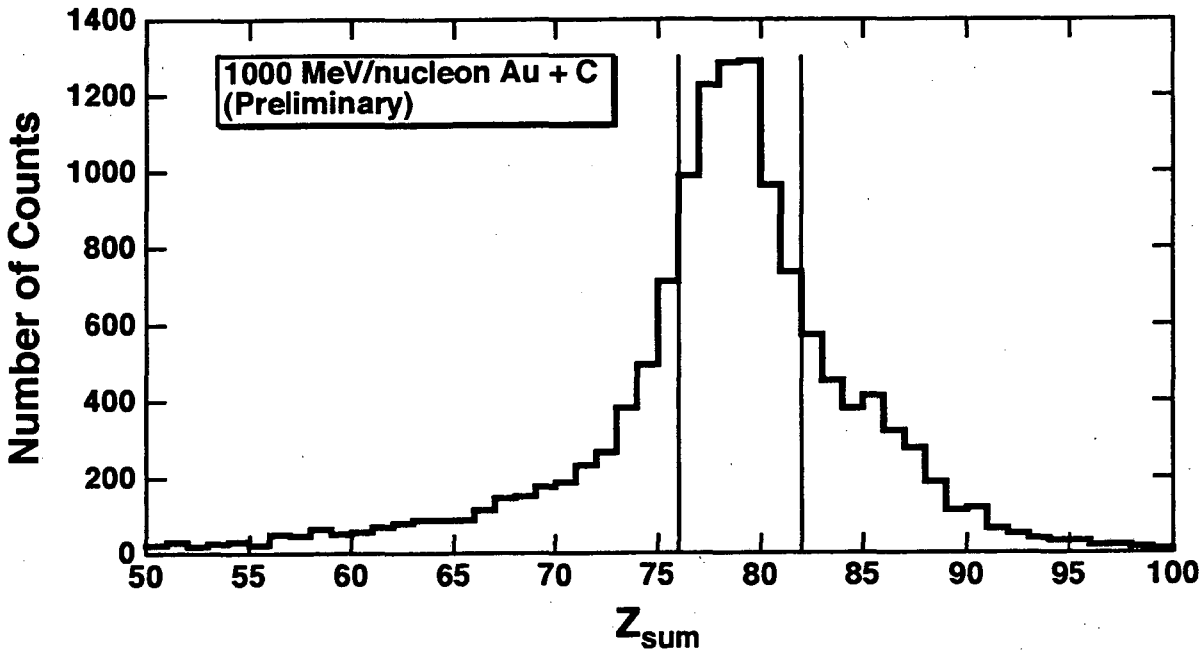

Figure 1 Total reconstructed charge, Z_{sum}. Vertical lines denote 79±3.

mass distribution led us to suggest that perhaps nuclear fragmentation was a critical phenomenon occurring in a small system.[4] From this point of view, fragments result from the density fluctuations that are characteristic of second order phase transitions. Subsequent experiments have confirmed that fragmentation is a multi-body, simultaneous breakup that occurs when deposited energy is of the order of the total binding energy of the nucleus. Of course, the observation of a power law in the mass yield, with an exponent in the range of two to three, is suggestive but not conclusive of critical behavior. Critical behavior is characterized by a finite number of critical exponents, so if indeed nuclear multifragmentation is a critical phenomenon, then it too should possess critical exponents.

B. Signatures of critical behavior

Fluctuations are the hallmark of a phase transition occurring near a critical point. These can be fluctuations in density in a fluid system, magnetization in a magnetic system, or cluster sizes in a percolation system. It is the fluctuations that we must examine to see whether a system is exhibiting critical behavior. These fluctuations are largest in the critical region and persist even with infinite statistics. Far from the critical region, fluctuations exist, but these are fluctuations that are indicative of the 'mean field'. A second hallmark of second order phase transitions is a finite number of critical exponents. These govern the power law behavior of various quantities as the critical point is approached. For example, the rate at which the isothermal compressibility diverges as T_c

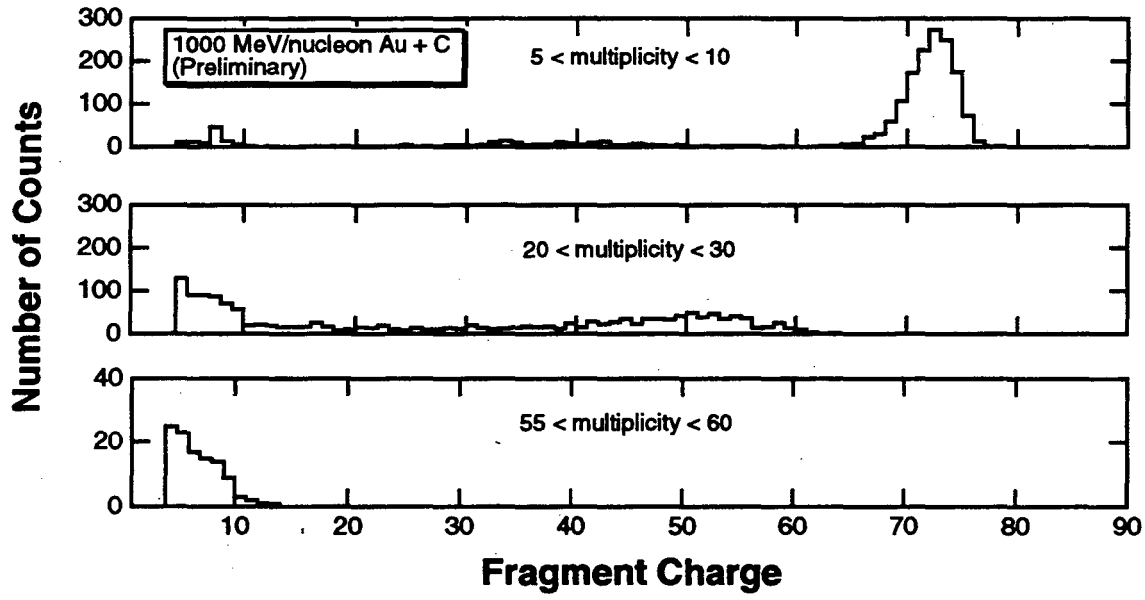

Figure 2 Fragment yields for different multiplicity regimes. Charges 1-3 have been omitted.

is approached from either side is given by $K_T \propto |T - T_c|^{-\gamma}$. The density of clusters of size s at T_c, is given by $\rho(s) \propto s^{-\tau}$. Only two of these critical exponents are independent and are related to the others via a sum rule. Every known second order phase transition has been shown to obey this rule.

As a prototypical system, we will use bond percolation on a cubic lattice of linear dimension L. We will use percolation as a testing ground for our techniques for analyzing exclusive multifragmentation data. In the last part of this talk, we will discuss our preliminary analysis of these data.

Let us first address the issue of what a second order phase transition looks like in a system of only 200 constituents. As Campi has addressed this issue and others in an important series of papers.[5] Quantities that diverge in macroscopic systems show peaking behavior as the constituent number of the system decreases. The critical point becomes a critical region and the location of the maximum is shifted somewhat from the location of the divergent behavior in the infinite system. In a fluid, we might examine the isothermal compressibility. The analogous percolation quantity is the second moment of the cluster distribution[6];

$$M_2 = \sum_s s^2 n_s(p) \tag{1}$$

where n_s is the number of clusters containing s sites and p is the probability that a bond is formed between neighboring sites. In the infinite system, percolation does indeed possess a critical 'point',

in that one never makes the infinite or spanning cluster below a particular value of $p = p_c$ (for bond forming percolation). In Figure 3 we show the behavior of $ln\ (M_2)$ versus reduced multiplicity, i.e. the number of clusters per lattice site formed, for three different sizes of percolation lattices. It is clear that a peak remains even as the system size grows quite small.

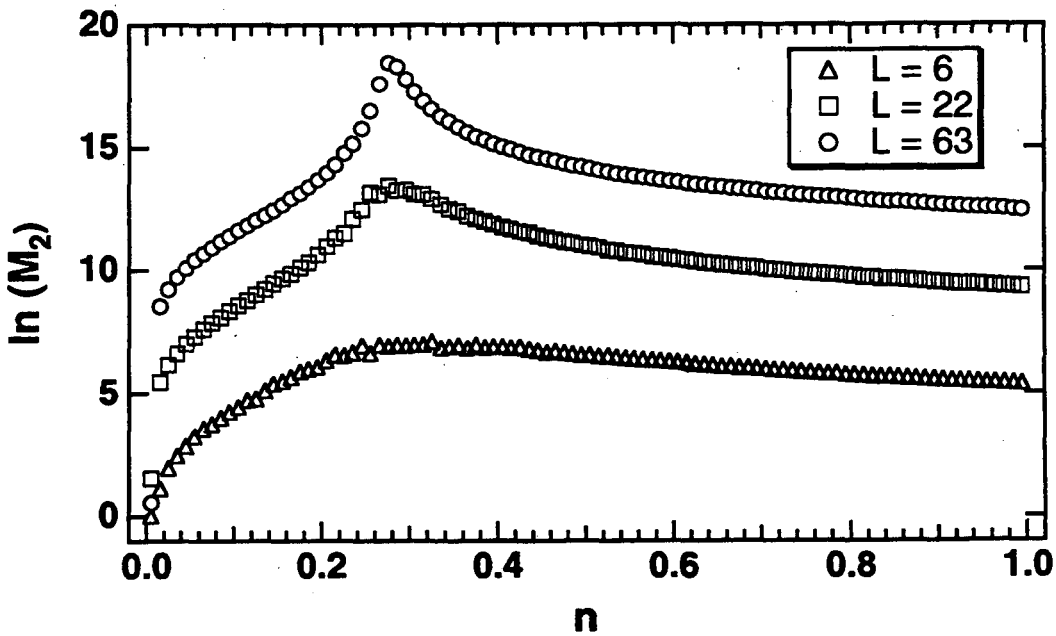

Figure 3 $ln(M_2)$ versus n for different lattice sizes.

Making an analogy to a liquid-gas system, we will label the region above p_c as the 'liquid' region, and below p_c as the 'gas' region. This gives us a more physical picture. It is understood that in the summation of equation (1) the largest cluster, S_{max}, is to be omitted whenever we are on the liquid side of p_c, since it represents what would be the infinite cluster if $L \rightarrow \infty$. In Figure 3 we have removed the largest cluster everywhere for display purposes. As $L \rightarrow \infty$ the 'singular' part of the moments exhibit power law behavior:

$$\left[\sum_s s^k n_s\right]_{singular} \sim |\varepsilon|^{\frac{-(1+k-\tau)}{\sigma}} \tag{2}$$

where $\varepsilon = p - p_c$, and τ and σ are critical exponents. Other critical exponents are defined by

$$M_2 \sim |\varepsilon|^{-\gamma} \tag{3}$$

$$S_{max} \sim |\varepsilon|^{\beta} \tag{4}$$

$$\text{and } n_s \propto s^{-\tau} \text{ at } \varepsilon = 0. \tag{5}$$

The behavior expressed in equations (3)-(5) holds only in the limit $L \rightarrow \infty$ and $s \rightarrow \infty$. The relations between exponents is:

$$\gamma + 2\beta = 2 - \alpha = \frac{\tau - 1}{\sigma} \tag{6}$$

$$\tau = 2 + \frac{\beta}{\beta + \gamma} \tag{7}$$

Of course, multifragmentation is not percolation on a lattice. If we wish to perform a cluster analysis in an effort to determine the exponents γ, β, and τ, we must find a suitable substitute for the percolation probability, p. Ideally we would like to use temperature, but since this is difficult to measure directly in our case, we will follow Campi's suggestion [5] and use charged particle multiplicity, m, or the reduced multiplicity, $n = m/79$, where 79 represents the charge of the gold projectile nucleus.

Fluctuations indicative of power law behavior are indeed present *in a particular multiplicity* interval. These are observed in the deviations of the largest fragment produced when plotted as a function of multiplicity as shown in Figure 4. For each multiplicity bin we find the average size of the largest fragment. We then compute the standard deviation about this mean and divide this deviation by the mean for normalization. The number of entries in each multiplicity bin of Figure 4 is approximately constant, so the peaking is *not* simply a matter of counting statistics. These fluctuations represent the density fluctuations that occur on all length scales at the critical point in a macroscopic system. It is significant that these deviations are similar to those in a percolation lattice of comparable size.

C. Determination of Critical Exponents

Having now some evidence for critical fluctuations, one would like to pursue the question of critical behavior further. We will do this by:

- determining in an independent manner three critical exponents, γ, β, and τ.
- determining whether these exponents obey the sum rule, equation (7).

We have used small percolation lattices in order to develop a method for extracting critical exponents from small systems. In what follows, I will describe this method using percolation and then apply it to the multifragmentation data.

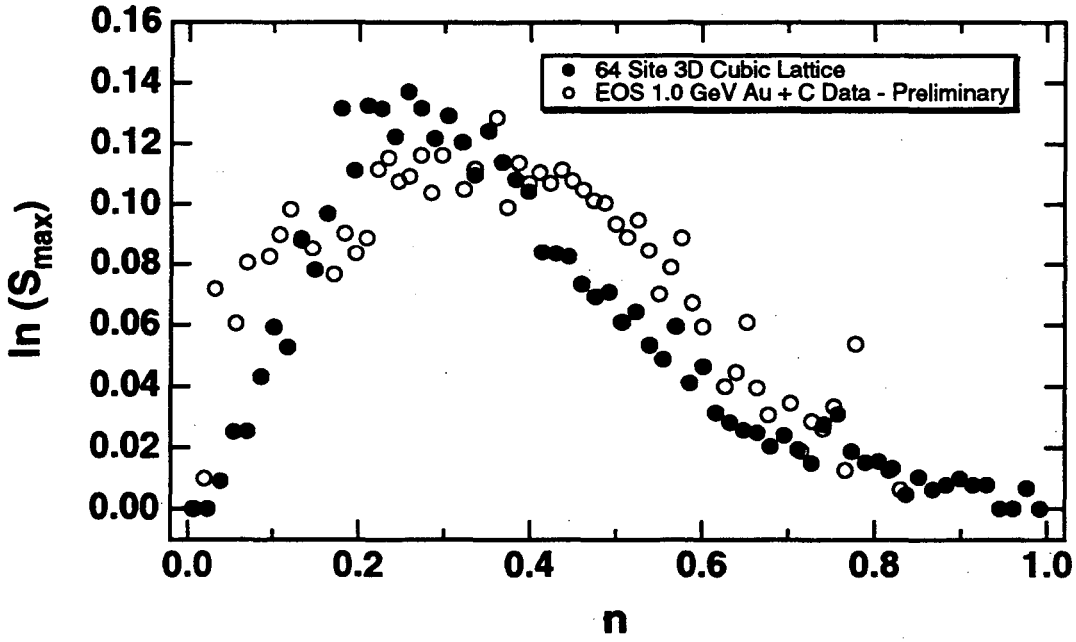

Figure 4 Fluctuations in the average size of the largest fragment versus multiplicity.

The key to determining critical exponents using a finite system is to find a region in probability where the power law behavior of equation (2) holds. This means that one cannot expect power law behavior too close to the peak in M_2, for example, because finite size effects dominate there. On the other hand, one cannot go too far from the peak, since here, one is in the so-called mean field regime, where fluctuations are small relative to the mean.

We now discuss the determination of the exponent γ. It is well known in percolation theory that the critical percolation probability, p_c, in a small lattice is different from that for an infinite lattice[6]. One can account for finite size effects in part by choosing a p_c that is lattice size dependent. Thus, the methods consists of the following steps:

- choose a trial value of p_c
- on the 'gas' side of p_c, plot $ln\ (M_2)$ versus $|p - p_c|$. Do the same for the 'liquid' side. This means choosing an appropriate fitting region for each side. This is determined by requiring the value of γ from the two regions to be the same. If one cannot find such a region, then adjust the value of p_c.

An example of this using a percolation lattice of $L = 63^3$ sites is shown in Figure 5. The extracted value is in excellent agreement with the canonical value of 1.80. We have also performed this same exercise on an $L = 6^3$ lattice with a similar result.

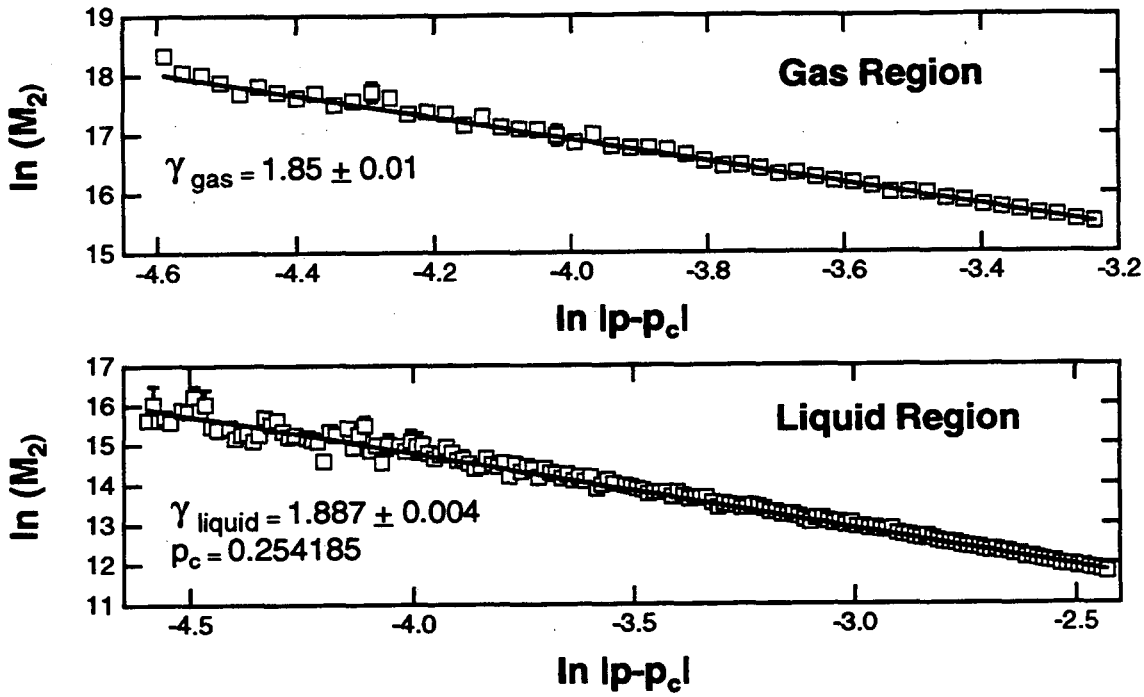

Figure 5 Determination of γ for percolation.

Having found both p_c and γ, we can now use the same p_c and fitting regions to determine β from equation (4).

As Campi pointed out [5], by plotting $ln\,(M_3)$ versus $ln\,(M_2)$, one can determine τ. This is because in an infinite system, the slope of this correlation is:

$$\frac{\Delta\,[ln\,(M_3)]}{\Delta\,[ln\,(M_2)]} = \frac{\tau-4}{\tau-3}. \tag{8}$$

In a small system, one must be careful to avoid the 'liquid' side of this correlation, since here we must remove the largest piece. The effect of removing this largest cluster is a large perturbation on a small lattice. On the 'gas' side, however, the largest piece is small, and it makes little difference whether it is removed or not. Thus, we use only the gas side to determine τ when using this correlation. An alternative method is to fit the cluster distribution at p_c as a function of cluster size, since according to equation (5) it should be a power law with exponent τ. Finite size effects once again enter in if one tries to extend the fit to clusters of too large a size. In fact, even in large lattices, one typically restricts the region of the power law fit to be about 1% of the maximum possible cluster size. If one adheres to this rule of thumb, one can obtain good agreement between the two methods.

We now apply this procedure to multifragmentation of Au nuclei at 1 GeV/nucleon. We will use multiplicity, since we don't know, on an event-by-event basis, the temperature. We first make

an estimate of the critical multiplicity, m_c. The critical fluctuations shown in Figure 4 give us a first guess. After some trial and error, we determine that $m_c = 27$ gives good agreement on both the liquid and gas sides of M_2. The fits to the data are shown in Figure 6. We then use this value of m_c

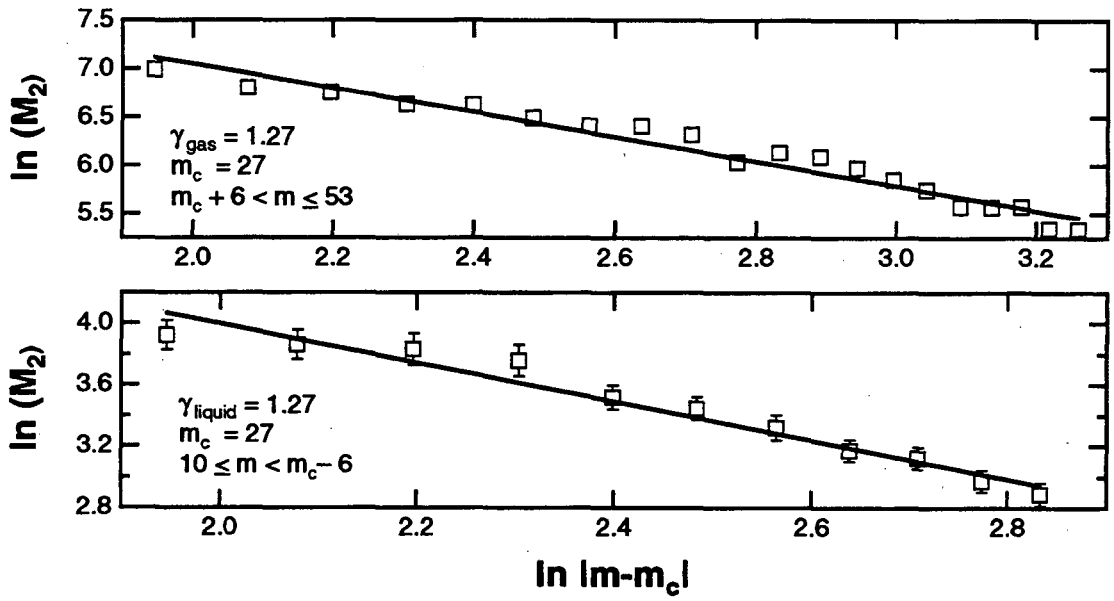

Figure 6 Determination of γ for Au multifragmentation.

in our determination of β, Figure 7. Finally, using the correlation between M_3 and M_2 we can determine τ. This is shown in Figure 8.

We summarize our results in the table below. We list values for three-dimensional percolation lattices, real fluids, mean field theory and our fragmentation data. The uncertainty in the exponent values for the data are about 10-15%. These are due to the different values one can obtain by varying the choice of m_c and fitting region. The significant point is that we were unable to find a set of values that was consistent with either the percolation or the mean field values. The similarity between nuclear matter values and those for fluid systems is very striking. Most remarkable is the fact that the sum rule is obeyed for the nuclear matter exponents. If this preliminary analysis is correct,

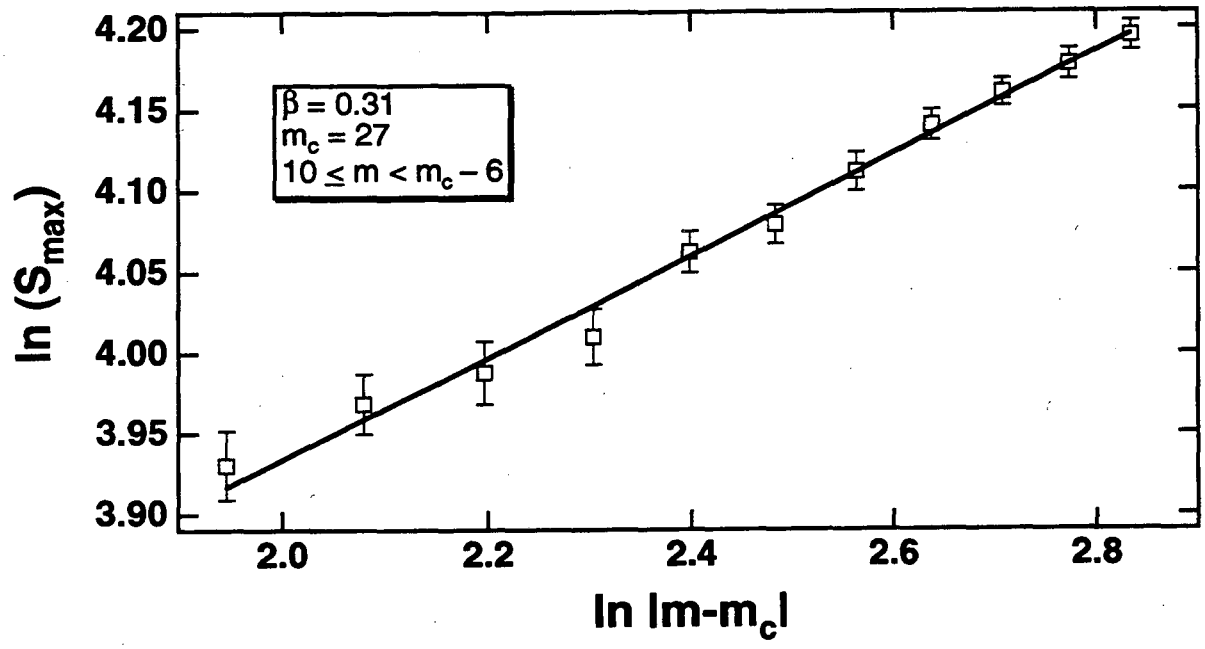

Figure 7 Determination of β for Au multifragmentation.

then we have directly measured the approach of the equation of state of nuclear matter to the critical point using small samples (finite nuclei). The implication is that the fragmenting system has had sufficient time to approximate thermal equilibrium. In a small system, the approach occurs over a considerable range of excitation energy, temperature, and density. It remains to determine these quantities from the data. This analysis is underway.

As a final word, the Purdue group would like to give a special thank you to Lee Schroeder who, when he was our DOE contract officer, suggested that we explore using the EOS-TPC to pursue our interest in multifragmentation.

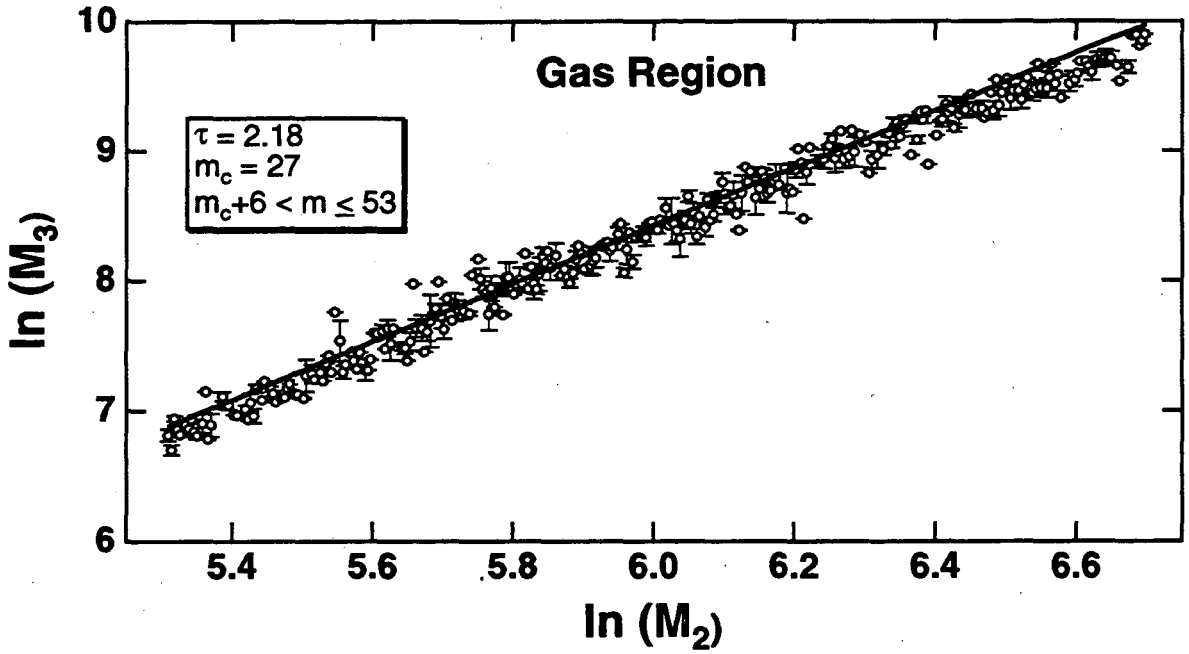

Figure 8 Determination of τ for Au multifragmentation.

Table 1: Critical Exponents for Various Systems

System	γ	β	τ	$2+\beta/(\gamma+\beta)$
3D Percolation	1.80	0.45	2.20	2.20
Fluid	1.24	0.33	2.21	2.21
Mean Field Theory	1.0	0.5	2.33	2.33
Au+C fragmentation	1.27	0.31	2.18	2.20

References

[1] B. C. Stringfellow, et al., Nucl Instrum. Methods, A **251**, 242 (1986).
[2] J. A. Gaidos, et al., Phys. Rev. Lett. **42**, 82 (1979).
[3] K. Nakai et al., Phys. Lett. B **121**, 373 (1983).
[4] J. E. Finn, et al., Phys. Rev. Lett. **49**, 1321 (1982): R. W. Minich, et al., Phys. Lett. B **118**, 458 (1982).
[5] X. Campi, J. Phys. A **19**, L917 (1986); X. Campi, Phys. Lett. B **208**, 351 (1988).
[6] D. Stauffer and A. Aharony, Introduction to Percolation Theory, second edition (Taylor and Francis London, 1992).

Multifragmentation: the Success of Statistical Models

M. Begemann-Blaich,[1] J.C. Adloff,[3] P. Bouissou,[4] T. Hofmann,[2] J. Hubele,[2] G. Imme,[5] I. Iori,[6] P. Kreutz,[1] G.J. Kunde,[2] S. Leray,[4] V. Lindenstruth,[2] Z. Liu,[2] U. Lynen,[2] R.J. Meijer,[2] U. Milkau,[2] A. Moroni,[6] W.F.J. Müller,[2] C. Ngô,[4] C.A. Ogilvie,[2] J. Pochodzalla,[2] G. Raciti,[5] G. Rudolf,[3] H. Sann,[2] A. Schüttauf,[1] W. Seidel,[7] L. Stuttge,[3] W. Trautmann,[2] A. Tucholski,[2] A. Wörner[2]

[1] *Institut für Kernphysik, Universität Frankfurt, D-60486 Frankfurt, Germany*

[2] *Gesellschaft für Schwerionenforschung, D-64220 Darmstadt, Germany*

[3] *Centre de Recherches Nucléaires, F-67037 Strasbourg, France*

[4] *Laboratoire National Saturne, CEN Saclay, F-91191 Gif-sur-Yvette, France*

[5] *Dipartimento di Fisica dell' Universitá and I.N.F.N., I-95129 Catania, Italy*

[6] *Istituto di Scienze Fisiche, Universitá di Milano and I.N.F.N., I-20133 Milano, Italy*

[7] *Forschungszentrum Rossendorf, Postfach 510119, D-01314 Dresden, Germany*

Introduction

The determination of fundamental properties of nuclear matter far from the ground state is one of the principal motivations for the study of collisions between two complex nuclei. At densities slightly above the normal nuclear density transverse flow phenomena are regarded as fingerprints of the nuclear equation of state [1], [2]. At subsaturation densities, on the other hand, the fragmentation pattern of the nuclear system is expected to be influenced by the bulk properties of nuclear matter.The special interest in this low energy region arouse from the idea that a nuclear many-body system might undergo a phase-transition during the disassembly leading to multifragmentation – the simultaneous formation of several complex fragments – of the system [3], [4].

For a nucleus at low excitation energies (below 1 MeV/nucleon) the dominant decay channels are the evaporation of light particles and fission. Due to the small excitation energy the required surface energy necessary for the formation of several complex fragments is not available, only light particles are evaporated and a large heavy residue remains. If the nucleus is excited far beyond its total binding energy, a complete vaporization into individual nucleons is observed, because the system needs all available degrees of freedom to accomodate the energy. Between these two limits, the production of several intermediate mass fragments

is the dominant exit channel. It is obvious that events with multiple fragment production are the favorite candidates for a true multifragmentation.

Multifragment emission is observed in central symmetric heavy ion collisions as well as in peripheral collisions [5], [6]. During the central collision of a symmetric system the whole system forms a hot and dense fireball. Due to the thermal pressure, this excited and highly compressed nuclear matter will expand. If the thermal energy of the system is big enough, the system may reach the region of mechanical instability, i.e. $\partial p/\partial \rho \leq 0$. In this region, density fluctuations are not damped by the mean nuclear field. They will grow exponentially - which leads to the simultaneous formation of several fragments. It is known from the data of the 4 π collaboration [7] that the flow energy in these processes is large, leading to an expansion time in the order of 20 to 40 fm/c to reach a density of $1/3^{th}$ to $1/5^{th}$ of normal nuclear density.

In peripheral collisions or central collisions of nuclei of very different sizes, on the other hand, again a fireball - which contains the participants in the overlap zone of the two nuclei - is formed, but also one or two spectators. Three clearly separated sources can be distinguished: the participant zone, which moves with approximately half of the beam rapidity, the target spectator, which is almost at rest in the lab frame, and the projectile spectator, which moves with approximately beam velocity. Two processes contribute to the excitation of the spectator, the deformation due to the shearing off of the interaction zone and elastic nucleon-nucleon collisions between nucleons of the interaction zone, which are scattered into the spectator mass and which deposit their energy there. Both processes do not lead to a significant compression of the system. On the contrary, its density may even decrease during this excitation phase if spectator nucleons are knocked out. Therefore the flow energy is low and consequently the expansion time may be very long (in the order of 200 fm/c).

It is obvious that we can expect more fragments from a central collision of two heavy nuclei because the system size is much larger. On the other hand, it is more difficult to detect all those complex particles. The investigation of the projectile spectator is experimentally much easier - especially if one uses inverse kinematics - because due to the strong kinematic focussing a much smaller fraction of 4π has to be covered.

Experimental Setup

The ALADIN forward spectrometer at the GSI is designed for the study of the projectile decay in inverse kinematics (for details see [5]). A gold beam of 600 MeV/nucleon hit C, Al, Cu, and Pb-targets with 1 to 3 % interaction probability. The multiplicity of light charged particles – predominantly those from the participant zone of the interaction – were

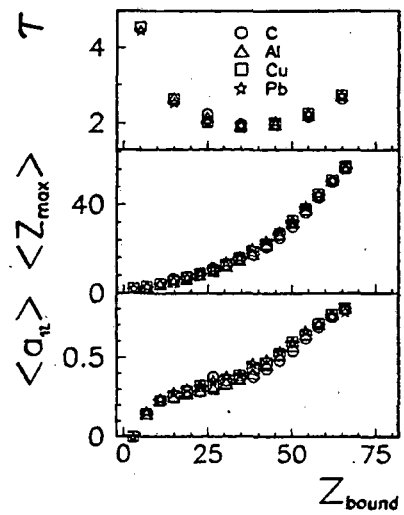

Figure 1:
τ parameter of the Z distributions for Z=3, 5, 6... 15, the mean maximum charge Z_{max} within an event, and the asymmetry $a_{12} = (Z_{max} - Z_2)/(Z_{max} + Z_2)$ between the largest and the second largest fragment versus Z_{bound} for 600 MeV/nucleon Au on C, Al, Cu, and Pb. The distributions are independent of the target [8].

determined by the 64 elements of a Si-CsI forward hodoscope which were placed at angles between 7 and 40 degrees. The acceptance of the spectrometer for fragments with beam velocity is $\pm$ 4.7° in the horizontal and $\pm$ 4.5° in the vertical direction. Due to the inverse kinematics this is sufficient to detect almost all fragments originating from the decay of the gold projectile spectator, because these particles are strongly focussed in the forward direction. With a TOF-wall, the charge and the multiplicity of these fragments were determined. Fragments with a charge of 8 and above were additionally identified and tracked in a TP-MUSIC detector. For these particles the full kinematic information is available, therefore their momenta and their masses can be calculated.

Event Characterization and Experimental Results

In order to characterize the events, a quantity called Z_{bound} – the sum of the atomic numbers of all particles with $Z \geq 2$ detected in the TOF wall – has been introduced. Z_{bound} is the atomic number of the excited projectile spectator reduced by the number of hydrogen nuclei emitted from it. It thus depends on the primary abrasion and the secondary deexcitation stages and reflects the violence of the collision in a two-fold way. It is important to keep

in mind that both - the excitation energy and the mass of the decaying system - vary with Z_{bound}.

The most striking result of the first analysis was the observation that the mean multiplicity of IMFs ($3 \leq Z \leq 30$) was independent of the target, if the reactions were ordered according to Z_{bound} [5]. This feature was found to be a rather general phenomenon [8]. To mention only a few examples (see fig. 1): the τ parameter of the Z distributions for Z=3, 5, 6... 15, the mean maximum charge within an event , the asymmetry a_{12} between the largest and the second largest fragment (see below) as well as other correlations describing the partition into fragments are target independent if plotted as a function of Z_{bound}.

The well established geometric cross section method in a sharp cutoff picture was used to calculate from the observed reaction cross section the maximum impact parameter accepted by our trigger condition. Bins in Z_{bound} or in the number of light charge particles were then successively associated with impact parameter bins that represented the same cross section. For the carbon target the mean IMF multiplicity increases with decreasing impact parameter and reaches a maximum for the most central collisions, whereas for the copper the maximum is reached for relatively large impact parameters. A given value of Z_{bound}, therefore, corresponds to different impact parameters, i.e. to different reaction geometries and the memory of the reaction geometry is lost. In the participant-spectator model the maximum is always reached for a projectile spectator of approximately 150 nucleons. This is a strong indication that a chemical equilibrium may be established prior to the fragmentation process.

A conclusion which goes even beyond this can be drawn from the analysis of the dynamical variables: The transversal and longitudinal velocity distributions are target independent, but in addition the RMS values of the two quantities for all charges and all reaction classes are identical within the statistical and systematic errors. Therefore no deviation from an isotropic emission in the rest frame of the excited nuclear system is found which is a necessary requirement for the existence of a thermal equilibrium.

Comparison with Statistical Decay Models

Due to the indications for both a chemical and a thermal equilibrium, a detailed comparison between the observed distributions and the predictions of statistical models seemed promising. The statistical multifragmentation codes by Gross and coworkers [9] (BERLIN) and Bondorf and coworkers [10] (COPENHAGEN) as well as the statistical multifragmentation code of Botvina [11] (MOSCOW) will be discussed. All three models describe the decay of a nuclear system in thermal and chemical equilibrium which is expanded and hot. At a given

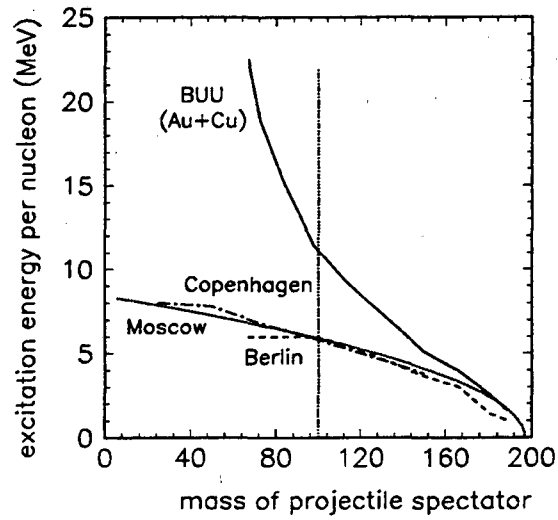

Figure 2:
Excitation energy for a given size of the projectile spectator for the three statistical models described. Also shown is the result of BUU calculations which were previously used to extract the excitation energy [15]. If the mass of the projectile spectator is smaller than approx. 100, the quantity Z_{bound} is zero.

density – the freeze-out density – the system decays simultaneously into several fragments. The weights of possible fragmentation channels are completely determined by the total entropy of the system. As input, all models need the size and the excitation energy of the decaying system. For the comparison with experimental data, these statistical models have therefore to be coupled to a model which describes the initial dynamic stage of the reaction.

To describe the process of multifragment emission as completely as possible, not only the multiplicity of IMFs is studied but also quantities which describe the partition of the system into fragments. To do so, the maximum charge Z_{max} within an event , the charge asymmetries $a_{12} = (Z_{max} - Z_2)/(Z_{max} + Z_2)$ between the largest and the second largest fragment, $a_{23} = (Z_2 - Z_3)/(Z_2 + Z_3)$ between the second largest and the third largest fragment, and the three-body asymmetry $a_{123} = \sqrt{\sum (Z_i - \overline{Z})^2}/(\sqrt{6} \cdot \overline{Z})$ with $\overline{Z} = \frac{1}{3} \cdot \sum Z_i$ between the three largest fragments are evaluated.

All these quantities can only be reproduced – irrespective of the model – if the relation between M_{IMF} and Z_{bound} is used to determine the excitation energy and the system size for a given impact parameter (BERLIN, COPENHAGEN) or the excitation energy for a

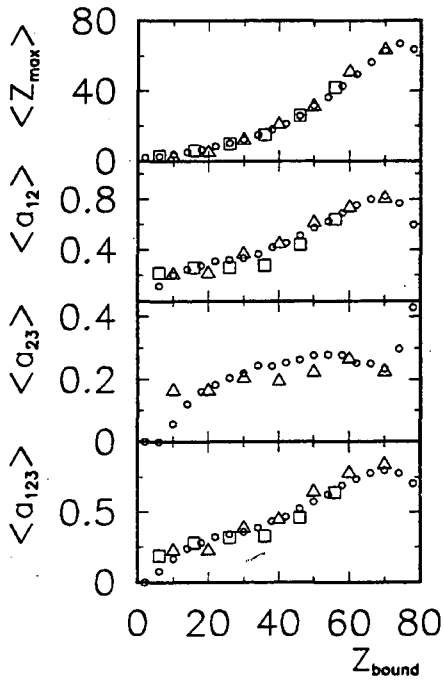

Figure 3:
Z_{max} and the asymmetries a_{12}, a_{23} and a_{123} for Au on Cu at 600 MeV/nucleon. Circles: data, squares: COPENHAGEN, triangles: BERLIN.

given system size (MOSCOW) [12], [13], [14]. The results of this adjustment are shown in fig. 2: The differences between the three models are small and the excitation energy for a given system size is significantly smaller than those obtained for BUU calculations which were previously used to extract the excitation energy [16], [15]. The necessity for an adjustment of the excitation energy shows that Z_{bound} in fact reflects the excitation energy of the projectile spectator. As this excitation energy determines the phase space accessible for the system, the whole decay must be described correctly if the specific statistical model is a valid description for these reactions. Therefore, the agreement of all three models with the data – which is shown in fig. 3 – is interesting: Although the different models start from the assumption of an ensemble of excited fragments at thermal and chemical equilibrium at the freeze out configuration, the details like the volume of this source or the secondary decay of the produced fragments are treated quite differently.

The isotopic composition of the complex fragments depends both on the neutron-to-proton ratio of the decaying system and on the sequential decay process after freeze out. As

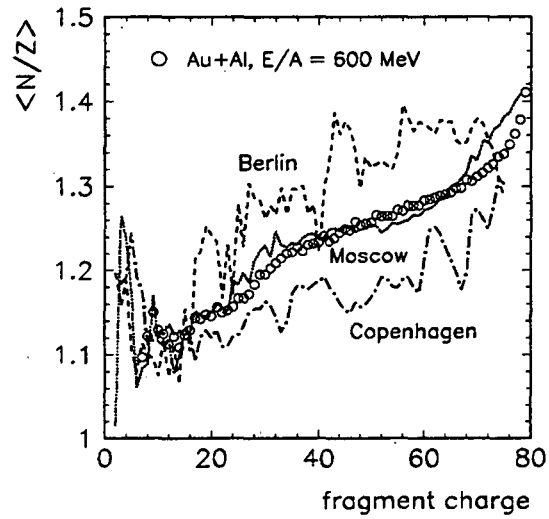

Figure 4:
N/Z ratio as a function of the charge of the detected fragments. The MOSCOW model agrees quite well with the experimental observations, the COPENHAGEN and the BERLIN codes underestimate resp. overestimate the average N/Z-ratios significantly. For Z$\geq$ 65, the data may be distorted by the experimental trigger condition.

the charge distributions are not sensitive to distinguish between the different statistical decay models, the N/Z ratio as a function of the charge of the detected fragments was studied (see fig. 4). The mean neutron-to-proton ratio is independent of the target, and the fragments are generally on the neutron deficient side of the valley of stability. Although the three statistical multifragmentation models give very similar charge distributions, they show clear differences in the isotopic distributions. The MOSCOW model agrees quite well with the experimental observations, the COPENHAGEN and the BERLIN codes underestimate resp. overestimate the average N/Z-ratios significantly [17]. (The large saw tooth-like fluctuations for the COPENHAGEN and BERLIN models should not be taken seriously, they are an artefact of the relatively large bin size used for the relation between excitation energy and the system size.) These derivations from the experimental distributions can neither be compensated by any reasonable variation of the N/Z-ratio of the decaying system nor by fluctuations of the excitation energy. So it is assumed that the different N/Z-ratios reflect the different treatment of the final sequential decay stage after the freeze-out.

An attempt was made to describe also dynamical variables with the statistical models. More characteristic information about the disintegration pattern is expected from the dy-

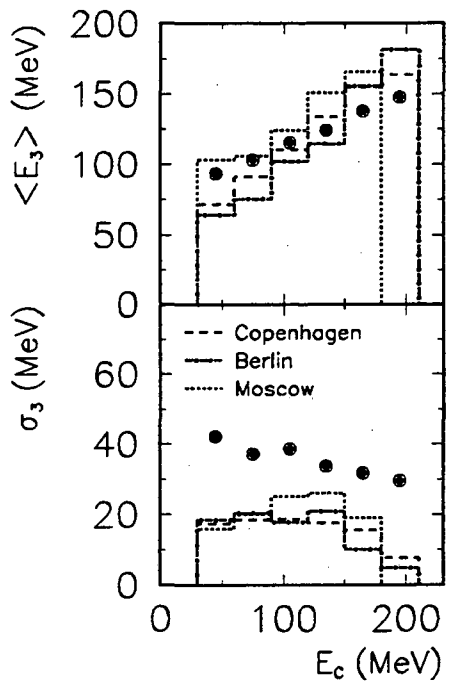

Figure 5:
Kinetic energy E_3 in the joint cm system of the three particles (top) and the width σ_3 of this distribution versus the nominal Coulomb repulsion E_C.

namic of the system, because the kinematic correlations are driven by the Coulomb force. This is presented in more detail in the contribution by V.Lindenstruth to this conference. Here only one result is shown: For events where three fragments were detected in the MUSIC the kinetic energy E_3 in their joint cm system was calculated. In Fig. 5 this kinetic energy is plotted versus the nominal Coulomb repulsion E_C of the three particles which is defined as the sum of the pairwise Coulomb repulsion. The three statistical models reproduce the relation between the mean E_3 and E_C distributions, the width σ_3 however is significantly underestimated. This width is determined by thermal fluctuations and position fluctuations. It therefore seems that the thermal motion and the Coulomb repulsion alone are not able to describe the dynamics in the final disassembly stage. It may be necessary to include the nuclear interaction between the fragments in the successful statistical decay models.

Summary and Conclusion

All quantities studied, like charge correlations, dynamical variables like momentum distributions, isotopic distributions etc., are consistent with the assumption of a chemical and

thermal equilibrium of the excited system prior to its decay. All statistical models, which include an expansion of the excited nuclear system, can reproduce the observed charge distributions and asymmetries if the relation between system size and excitation energy is adapted to reproduce the M_{IMF} versus Z_{bound} distribution. The observed discrepancies in the description of the isotopic distributions call for a more detailed treatment of the secondary decay stage of the fragments.

References

[1] For a recent reviews see, e.g., *The Nuclear Equation of State*, NATO ASI Series B: Physics Vol. 216A, ed. W. Greiner and H. Stöcker (Plenum Press, New York 1989); K.-H. Kampert, J. Phys. **G15**, 691 (1989); H.H. Gutbrod *et al.*, Rep. Prog. Phys. **52**, 1267 (1989).

[2] W. Schmidt *et al.*, Phys. Rev. C **47**, 2782 (1993).

[3] P.J. Siemens, Nature (London) **305**, 410 (1983).

[4] G.F. Bertsch and P.J. Siemens, Phys. Lett. B **126B**, 9 (1983).

[5] J. Hubele *et al.*, Z. Phys. A **340**, 263 (1991).

[6] M.B. Tsang *et al.*, Phys. Rev. Lett. **71**, 1502 (1993).

[7] N. Hermann, Nucl. Phys. **A553**, 739c (1993).

[8] P. Kreutz *et al.*, Nucl. Phys. **A556**, 672 (1993).

[9] for a recent review see D.H.E. Gross, Rep. Prog. Phys. **53**, 605 (1990).

[10] J. Bondorf *et al.*, Nucl. Phys. **A443**, 321 (1985);

[11] A.S. Botvina *et al.*, Yad. Fiz. **42**, 1127 (1985); A.S. Botvina *et al.*, Phys. Lett. B **294**, 23 (1992) and private communication.

[12] B.A.Li *et al.*, Phys. Lett. B **303**, 225 (1993)

[13] H.W.Barz *et al.*, Nucl. Phys. **A561**, 466 (1993).

[14] A.S. Botvina *et al.*, to be published.

[15] C.A. Ogilvie *et al.*, Phys. Rev. Lett. **67**, 1214 (1991).

[16] J. Hubele *et al.*, Phys. Rev. C **46**, R1577 (1992).

[17] V. Lindenstruth *et al.*, to be published.

Dynamical Aspects of Multifragmentation

V. Lindenstruth, J. Pochodzalla, J.C.Adloff, M. Begemann-Blaich, P. Bouissou, J. Hubele, G. Imme, I. Iori, P. Kreutz, G.J. Kunde, S. Leray, Z. Liu, U. Lynen, R.J. Meijer, U. Milkau, A. Moroni, W.F.J. Müller, C. Ngô, C.A. Ogilvie, G. Raciti, G. Rudolf, H. Sann, A. Schüttauf, W. Seidel, L. Stuttge, W. Trautmann, A. Tucholski

The decay channel of excited nuclear matter into multiple complex fragments is still not thoroughly understood. Different scenarios are discussed, for example, the role of sequential decay of multiple binary breakups [1]. Condensation processes in an expanded nucleus are reviewed. The latter is especially interesting due to its link to a nuclear liquid-gas phase transition [2,3,4,5]. More recently it was proposed that the fragmentation process could be introduced by shape instabilities arising from surface fluctuations [6,7].

To understand the decay mechanism it is very important to get an estimate of the size of the decaying source and the relative emission time of the heavy fragments. The different breakup scenarios are expected to leave characteristic signatures in kinematic fragment- fragment correlations. Since the multifragment decay produces heavy fragments, the repulsive long-range Coulomb force is expected to play a dominant role. In the following we present kinematic correlations between three heavy projectile fragments that were produced in Au induced relativistic heavy-ion collisions and compare them with three-body Coulomb trajectory calculations.

The experimental results presented here emerge from an experiment that was performed at the *ALADIN* spectrometer at SIS in 1990 [8,9]. C, Al, Cu and Pb targets with an interaction probability of 3% were bombarded with a 600 MeV per nucleon Au beam. Light fragments emerging from the participant zone of the interaction were detected in a 64 element Si-CsI array with a geometrical acceptance of about 35%. Projectile fragments with a charge of ≥ 2 were detected in a plastic scintillator time-of-flight wall (*ToF*) with an acceptance of almost 100%. Fragments with a charge above the threshold $Z \geq 8$ were also tracked and identified according to their atomic number in a multi sampling ionization chamber (*TP-MUSIC*) [10]. A charge resolution of $\Delta Z=0.5$ (FWHM) and a momentum resolution of $\Delta P/P=2.5\%$ (FWHM) was achieved. The charge of the lighter fragments with $2 \leq Z < 8$ was determined with the time-of-flight wall. Together with the time-of-flight information, the mass of the fragments with $Z \geq 8$ was determined with a resolution of $\Delta A/A \approx 3\%$ (FWHM).

In the following we consider only a class of events where exactly three fragments were tracked and identified in the *TP-MUSIC*. For this subset the sum of all charges $Z \geq 2$ (called Z_{bound}) as detected in the ToF wall varies between 45 and 70. The distribution peaks at $Z_{bound} \approx 55$. The charge sum of these three heavy fragments is typically 80% of Z_{bound}. It was shown in an earlier paper that Z_{bound} can be related to the impact parameter and thus to the size of the prefragment [8]. The average charge and mass of the three fragments sorted according to their size is $\langle Z_i \rangle = 22,13,10$ and $\langle A_i \rangle = 48,29,20$. To ensure the results are not biased due to this event selection we have compared the light particle multiplicity M_{lp} detected in the Si-CsI hodoscope with the appropriate inclusive and binary breakup distributions. The comparison shows that M_{lp} depends only on Z_{bound}.

The momenta of the three fragments in their center of moment system (*cm*) were analyzed. The collective center of moment velocity of the three fragments is smaller than 0.02c both parallel and perpendicular to the beam direction. We found no significant difference in the collective center of moment velocity between the ternary and binary decay mode. This suggests that these different decay channels are competitive exit channels of the same state of the prefragment.

Since the heavy fragments that emerge from the prefragment in a multi fragment decay are themselves excited and evaporate light particles this determination of the *cm* velocity is not exact. However since three fragments carry a large fraction of Z_{bound}, the error introduced was considered small. Therefore the *cm* velocity distribution of the three fragment system is linked to the velocity distribution of the prefragment.

Consequently the velocity distribution of the three fragments in their *cm* system should be related to the velocity distribution of the fragments at decay time.

The long-range repulsive Coulomb interaction is expected to play a dominant role. Therefore the total Coulomb potential energy of the three fragments was calculated for each individual event assuming touching hard spheres

$$E_c = e^2 \sum Z_i Z_j / (r_0 (A_i^{1/3} + A_j^{1/3})) \quad i<j \qquad (1)$$

where r_0 is the radius parameter and is assumed to have a value of 1.4 fm. The total kinetic energy of the three fragments in the *cm* system was calculated correspondingly as

$$E_3 = \sum p_i^2 / (2 m_0 A_i) \qquad (2)$$

where m_0 is the atomic mass unit. Figure 1 shows the experimental dependence of the average kinetic energy $\langle E_3 \rangle$ (top part) and the standard deviation σ_3 of E_3 (lower part). There is no significant target dependence apparent and σ_3 and E_3 depend linearly on E_c. This observation was therefore parametrized with two straight lines. The fit results are: m_E=0.37±0.04, b_E=76±5 for E_3 and m_σ=-0.07±0.01, b_σ=44±4 for σ_3.

To test the sensitivity of our experimental observables to the breakup scenario we performed three body Coulomb trajectory calculations. We tested two breakup configurations: a sequential and, a simultaneous breakup scenario. In both cases a Monte Carlo procedure was adopted which sampled the charges and masses of the observed fragments. In this way we avoided any uncertainties and model presumptions in the event generation. To compensate for light particle evaporation that was performed in a later stage of the simulation the mass and charge of the fragments was adjusted accordingly before the Coulomb explosion was performed. For each individual event the temperature T of the initial prefragment was chosen according to Z_{bound} by the relation $T=f_T \cdot (2 \cdot (79-Z_{bound}))^{1/2}$, where f_T is a free scaling parameter. This formula was found to be consistent with predictions of microscopic transport calculations [11] for f_T=1. The fragments were propagated in their mutual Coulomb- and two fragment proximity potentials [12]. However because simulations were rejected when two fragments overlapped during their propagation, the effect of this proximity force turned out to be fairly small. The produced fragments were assigned an excitation energy equivalent to the temperature T, which was dissipated into light particle evaporation. The recoil was added randomly to the fragment velocity. The fragments were synthesized with isotropic thermal motion. This assumption is supported by the experimental observation that the plane defined by the three momentum vectors of the three fragments in the *cm* system is oriented uniformly relative to the scat-

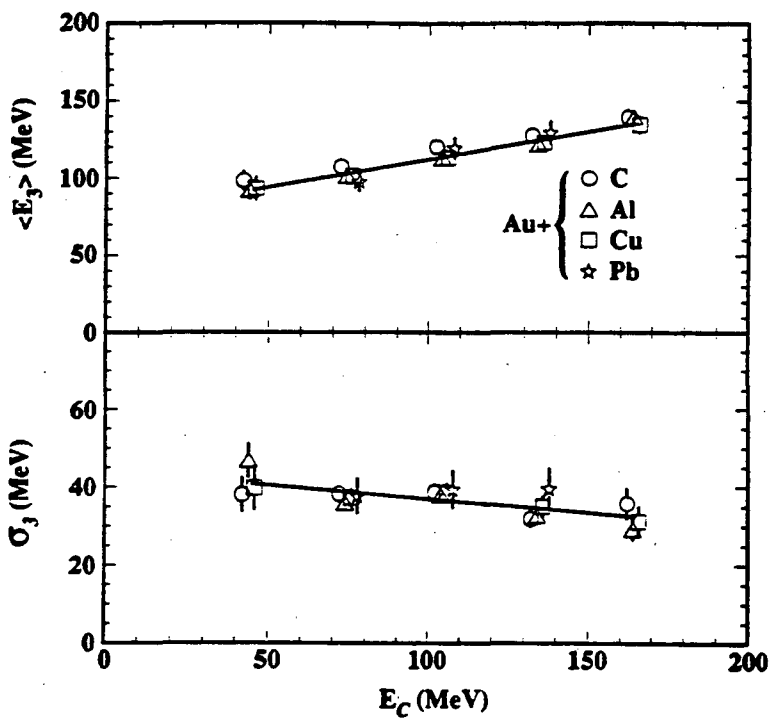

Figure 1: mean total kinetic energy $\langle E_3 \rangle$ of the three largest projectile fragments in their center of moment system (top) and the standard deviation σ_3 of E_3 (bottom) as a function of the nominal Coulomb potential E_c assuming touching hard spheres. The data points were obtained by sorting the data in 30MeV bins.

tering plane. This suggests either a small momentum transfer or a large angular momentum misalignment.

In the first breakup scenario two sequential binary breakups of the initial nucleus are simulated. The relative time between the two breakups was selected according to $P(t) \propto \exp(-\ln 2 \cdot t/\tau)$ while the relative energy of the fragments was chosen as

$$P(E) \propto E^{\alpha} \cdot \exp(-E/T) \qquad (3)$$

where the exponent α was set equal to 1. The binary breakup always occurred at a critical distance, 2D, where D is an adjustable parameter.

The second breakup scenario assumes a simultaneous breakup. The centers of the three fragments were placed randomly into a sphere with radius R. They had a thermal velocity distribution plus a radial flow velocity given as $v_f=(2\epsilon_f/m_0)^{1/2} \cdot d_i/R$ where ϵ_f denotes the flow energy per nucleon and d_i the distance of the fragment i from the center of the volume. The initialization was done with momentum conservation taken into account.

For both models a quantitative measure of the agreement between the experiment and the simulations χ^2 was defined as

$$\chi^2 = 1/5 \cdot \sum (x_i - y_i)^2 / \delta_i^2 \qquad (4)$$

where $x_{1...4}$ represent the four coefficients m_E, b_E, m_σ, b_σ of the fits in figure 1. x_5 is the reduced velocity [14] between the two lightest fragments $\beta_{23}/(Z_2+Z_3)^{1/2}$= 0.026±0.0005, which corresponds to the relative angular distribution. δ_i and y_i are the experimental resolutions and the model predictions, respectively.

Figure 2 highlights the predictions from the sequential model. Part (a) shows χ^2 as a function of the initial fragment distance 2•D and the temperature parameter f_T. In this figure, a life time constant of τ=100fm/c was used. A distinct minimum appears at D=2fm and f_T=1.25. The same minima were found within the quoted uncertainties for all life times below $\tau=10^4$fm/c. However the agreement between the data and the model predictions deteriorate quickly for lifetimes above 2000fm/c (Figure 2b). As a first result the size D and temperature f_T of

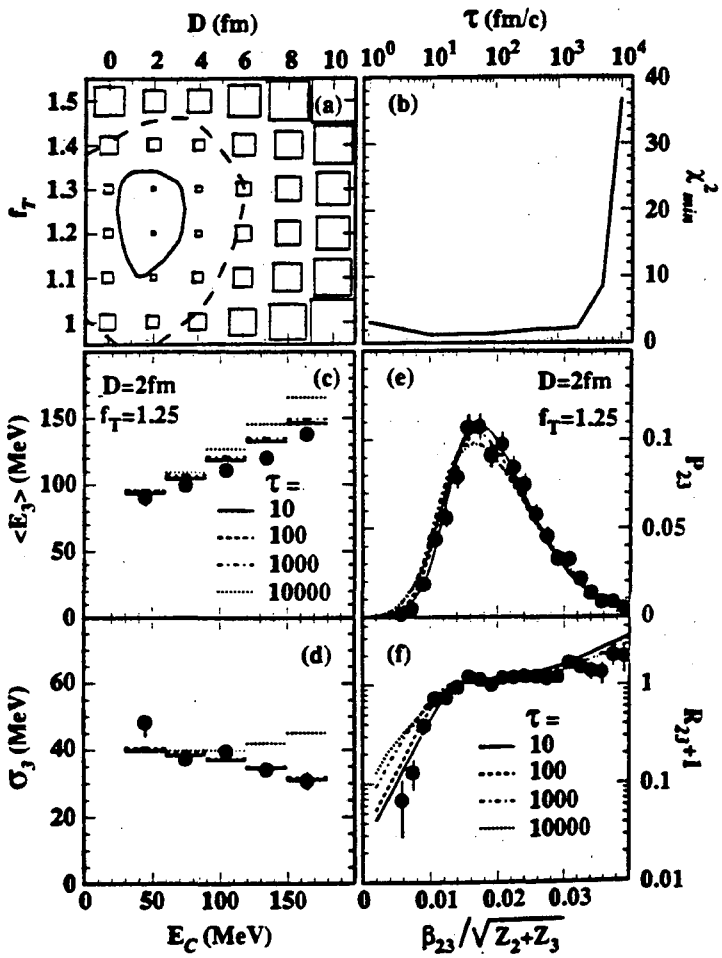

Figure 2: summary of the results of the sequential model calculations.

(a) dependance of χ^2 (eqation 4) for a lifetime τ=100fm/c as a function of the initial fragment distance D and the temperature scaling factor f_T. The areas with the largest blocks correspond to χ^2=50.

(b) dependance of χ^2 on the lifetime τ.

(c, d) comparison of the experimental results and model predictions for optimal D and f_T parameters as a function of the lifetime τ.

(e, f) coincidence yield and two particle correlation function of the two lightest fragments (number 2, 3) of each event as a function of the reduced relative velocity for optimal D and f_T parameters.

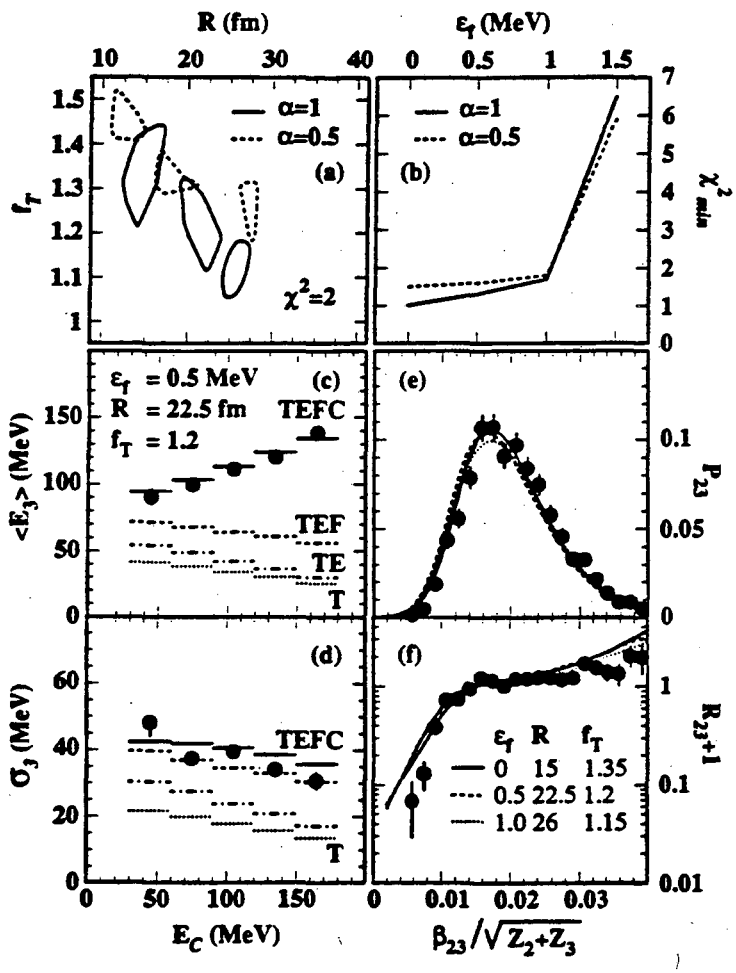

Figure 3: summary results of the simulations assuming simultaneous volume emission.

(a) dependance of χ^2 (eqation 4) on the size of the source volume R and the temperature scaling factor f_T for flow energy parameters ϵ_f=0, 0.5, 1 MeV (increasing from left to right).

(b) minimal χ^2 as a function of ϵ_f

Note: In part (c) ... (f) α was set to 1.

(c, d) comparison of the model prediction with the experimental result for the indicated parameters.

(e, f) coincidence yield and two particle correlation function of the two lightest fragments (number 2, 3) of each event for the indicated parameter sets.

the decaying system are defined independently within the framework of this sequential model. The good agreement between the model predictions and the experimental data for small life times τ is illustrated in figure 2c,d. The black data points represent the total available data covering all the reactions. To further constrain the life time we compare model predictions in figure 2e,f with the experimental, two particle coincidence yield and correlation function of the two lightest fragments as a function of the reduced velocity. The coincidence yields are described fairly well by all life times. However the correlation function is reproduced best by the shortest life time. Note that to minimize the uncertainty due to the collective velocity of the decaying system, the momenta in the *cm* system were used to construct the mixed background events for the correlation function.

The results from the simultaneous emission model are summarized in figure 3. Part (a) shows regions of χ^2<2 for two values of α. A value of α=1 (refer back to eq. 3) would correspond to a surface emission and a value of α=0.5 to a volume emission [13]. There are clear χ^2 minima for every combination of α and ϵ_f. Part (b) of figure 3 shows the corresponding χ^2 minima as a function of the flow energy ϵ_f. The steep rise of χ^2 for ϵ_f >1MeV per nucleon sets an upper limit for the flow energy to about 1 MeV per nucleon. In this scenario the temperature scale f_T, source size R and the flow energy ϵ_f are no longer independent. However for each α there appear obvious trends between ϵ_f, R and f_T. For instance large source sizes require increasingly greater flow energy to describe the data.

The interplay between the various velocity distributions that were taken into account in the calculations is exemplified in part (c) and (d) of figure 3 for the captioned parameter set. Four calculations are presented starting with only the thermal energy contribution (T). Then evaporation (E), flow (F) and finally Coulomb (C) were successively added. When going from ϵ_f=0 (f_T=1.35) to ϵ_f=0.5MeV (f_T=1.35) the thermal con-

tribution to $<E_3>$ drops by about 5MeV. This is small compared to the additional contribution of about 20MeV due to flow (fig. 3c). Therefore Coulomb repulsion and flow are apparently the main competitors. The radial motion in this scenario may be produced by the mutual Coulomb repulsion of the fragments at an earlier stage of the reaction.

The dotted histogram in fig. 3a shows that the slope parameter m_E is also affected by the temperature of the system. This is explained by the smaller average fragment size and the correspondingly smaller E_c of fragments coming from hotter sources. Therefore E_c and T are not independent. Finally we also show in figure 3e,f that the coincidence yield and two particle correlation function are reasonably well reproduced for all flow energies $\epsilon_f \leq 1$MeV.

As a quantitative comparison between the presented models we calculated the average initial distance of the two lighter fragments $<d_{23}>$ for both scenarios, which is a measure of the breakup density. We obtain $<d_{23}> \approx 18$fm for the simultaneous scenario assuming R=15fm and $<d_{23}> \approx 16$fm for the sequential scenario assuming τ=10fm/c.

In conclusion, we have presented experimental results and the analysis in terms of dynamic observables describing the ternary breakup of Au spectators at E/A=600MeV. The observables did not show any dependence on the reaction geometry of the collision. The collective behavior of these reactions, like their center of moment velocity distribution, does not differ from those observed with binary reactions. We argue that the various multiple breakup modes are competitive reaction channels. A comparison of the observed correlations with Coulomb three body trajectory calculations indicates a strong sensitivity to the breakup configuration. Although the present available data does not allow an unequivocally determination of the breakup scenario, it significantly limits the possible parameter space. The simulations consistently suggest a fast disintegration process of a dilute system. The size of the decaying system may however be smaller if other proximity potentials are taken into account.

I wish to thank all members of the collaboration for their excellent contributions to this experiment.

[1] W.A. Friedman, Phys. Rev. C **42**, 667 (1990)
[2] P.J. Siemens, Nature (London) **305**, 410 (1983)
[3] G.F. Bertsch, P.J. Siemens, Phys. Lett. B **126B**, 9 (1983)
[4] J. Bondorf *et al.*, Nucl. Phys. **A443**, 321 (1985)
[5] D.H.E. Gross *et al.*, Phys. Rev. Lett. **56**, 1544 (1986)
[6] L.G. Moretto *et al.*, Phys. Rev. Lett. **69**, 1884 (1992)
[7] W. Bauer, G.F. Bertsch, H. Schulz, Phys. Rev. Lett. **69**, 1888, (1992)
[8] J. Hubele *et al.*, Z. Phys. A **340**, 263 (1991)
[9] P. Kreutz *et al.*, Nucl. Phys. **A556**, 672 (1993)
[10] W.B. Christie *et al.*, Nucl. Inst. and Meth. in Phys. Res. **A255**, 466 (1987)
[11] J. Hubele *et al.*, Phys. Rev. C **46**, R1577 (1992)
[12] J. Lopez, J. Randrup, Nucl. Phys. **A503**, 183 (1989)
[13] A.S. Goldhaber, Phys. Rev. C **17**, 2243 (1978)
[14] Y.D. Kim, *et al.*, Phys. Rev. Lett. **67**, 14 (1991)

PRODUCTION OF NEUTRON DEFICIENT NUCLEI BY FRAGMENTATION OF XE ISOTOPES

J.FRIESE, H.J. KÖRNER, J. REINHOLD, R. SCHNEIDER, and K. ZEITELHACK
Physikdepartment E12, TU München, D-85747 Garching, FRG

H. GEISSEL, A. MAGEL, G. MÜNZENBERG, and K. SÜMMERER
GSI Darmstadt, Plankstr.1, D-64291 Darmstadt, FRG

ABSTRACT

Production cross sections and momentum distributions for neutron deficient projectile fragments were studied in the reaction ^{129}Xe + ^{27}Al at E_{kin}=790A·MeV. The experimental results are compared to an intra nuclear cascade calculation. Obtained cross sections for neutron rich fragments are compared to an earlier experiment with a ^{136}Xe beam.

1 Introduction

Beams of radioactive projectiles have become increasingly important during the last few years for nuclear spectroscopy and reaction studies. In view of future perspectives exotic heavy projectiles are of interest. Projectile fragmentation is a promising production mechanism for these nuclei. Although this has been studied experimentally since the mid seventies [1, 2], only very few data on isotopic yields of heavy ($A \geq 100$) fragments are available. Such data are important to test the existing model descriptions and empirical parameterisations, which allow to estimate secondary radioactive beam intensities for future experiments. Present models [3, 4, 5, for example] describe the underlying reaction mechanism as a twostep process, a fast abrasion followed by a slower de-excitation of the excited prefragments by evaporation of nucleons. To disentangle the different contributions of both reaction steps to the observed mass losses it is necessary not only to measure the production cross sections but also the corresponding momentum transfers. Whereas the isotropic evaporation of nucleons should only lead to a broadening of the momentum distributions, the first reaction step should slow down the fragments with respect to the projectile velocity. This velocity change could be a measure of the excitation energy of the temporary formed prefragments.

Of further interest is the dependence of the fragment yield on the neutron excess of the projectile with respect to the general trend of the line of beta stability ('memory effect'). This effect helps to reach the borderline of nuclear stability by means of projectile fragmentation.

2 Experimental technique

The experiment was performed with a 790 A·MeV ^{129}Xe beam provided by the heavy ion synchrotron SIS18 of the GSI facility in Darmstadt (Germany). The primary beam intensity of up to 10^8 ions per cycle (every 5 seconds) was measured with a secondary electron monitor [6] to an accuracy of 5-10%. The fragments were produced in an 803 mg/cm^2 aluminum target at the entrance of the fragment separator FRS [7]. The detector setup used for fragment identification is described in detail elsewhere [8, 9, 10] and will only be summarized.

Due to the large velocity 99% of the fragments were fully stripped. The first two dipoles of the FRS were used to select the produced fragments according to their magnetic rigidity with an acceptance of ±1%. At the central dispersive image plane a detector array with four layers of commercially available silicon PIN diodes measured the energy loss and the position of the

fragments. Due to the small velocity spread for all fragments the energy loss gives direct access to their nuclear charge number Z. The obtained resolution was ΔZ=0.43(fwhm) and allowed for unambiguous element identification. According to the 2.5mm position resolution of the silicon detector array a momentum resolution $\Delta p/p=3.5\cdot10^{-4}$ was achieved. The second stage of the separator was tuned in an achromatic mode thus focusing all selected fragments to a small area at the final image plane. At this position a ring imaging Čerenkov detector (RICH [8, 9]) measured the velocity of the particles to an accuracy of $\Delta\beta/\beta = 1.8 \cdot 10^{-3}$. The overall mass resolution was ΔM=0.7amu(fwhm). The FRS was operated with 10 different field settings to cover the neutron deficient side of the nuclear chart up to the vicinity of the proton drip line. On the neutron rich side one setting was choosen for comparison with the results of an earlier experiment using a ^{136}Xe beam [9, 10].

3 Results and discussion

3.1 Cross sections

Production cross sections from 30 mbarn down to 1 nbarn were determined for nuclei in the mass region $80 < A < 129$ with nuclear charge numbers from Z=40 up to Z=56. Due to the large amount of data only a subset will be presented here. The whole set will be published in a forthcoming paper. The measured data are compared to a monte carlo simulation (ISAPACE [3, 4]) which consists of an intra nuclear cascade model [11] followed by a statistical evaporation code [12]. The cascade model treats the first reaction step as a sequence of independent nucleon–nucleon collisions in a pure classical but relativistic calculation. The momentum distributions of the participating nucleons is taken from a fermi gas description of the colliding nuclei, which is either a 'Uniform Fermi Gas' (UFG; constant fermi energy) or a 'Local Fermi Gas' (LFG; density dependent fermi energy). The only quantum mechanical concept used is the pauli principle, which forbids collisions where the energy of the colliding nucleons in the exit channel lies beyond the fermi energy. Pion production is allowed for by the formation of the Δ(3,3) resonance.

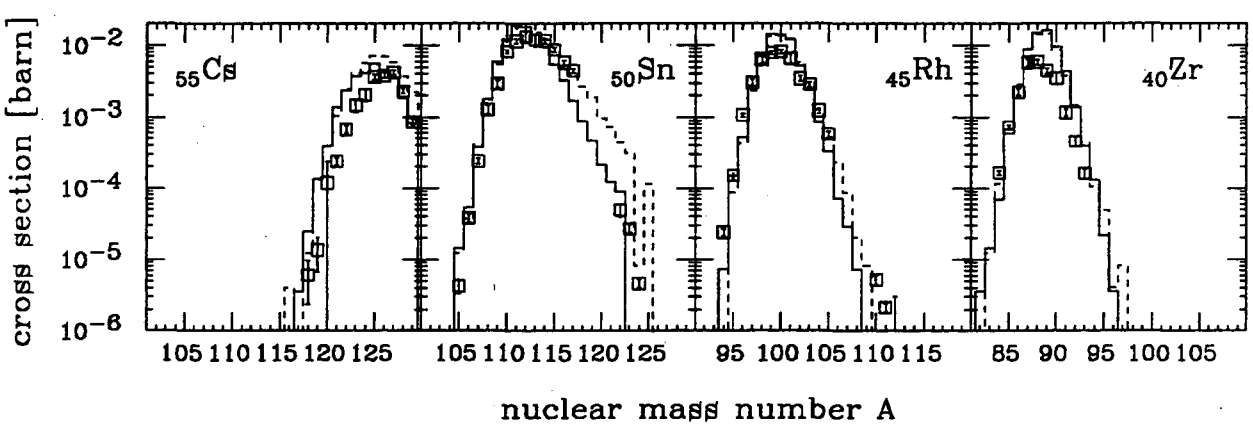

Figure 1: Total production cross sections of four isotopic chains. Squares: ^{129}Xe+Al data. Full line: ISAPACE[3, 4] model with UFG description. Dashed line: ISAPACE model with LFG description.

Four isotopic distributions compared to this model are shown in detail in fig. 1. The calculations reproduce the position and the general shape of the measured distributions. The maximum of the

lighter distributions (Rh and Zr in fig. 1) are overestimated by a factor of about two. There is no evident difference between the two fermi gas descriptions except for the neutron rich isotopes near the projectile mass (Sn–isotopes in fig. 1). In this particular case the LFG description overestimates the production cross section by nearly one order of magnitude. In the model the excitation energy is calculated from the holes generated in the fermi sphere. Hence, the lower fermi energy in the LFG description at the surface of the colliding nuclei leads to lower excitation energies of the prefragments. Therefore less neutrons are lost by evaporation in the second reaction step and more neutron rich fragments are observed in the exit channel of the simulation.

In contrast to a pure abrasion like prescription used in some other models [5], the cascade type simulation used here is also able to produce the charge changing products $\Delta Z = +1$ (Cs fragments). But there are significant deviations at the neutron deficient side of the distribution, which have to be studied. A preliminary analysis of the calculation shows that about 50% of the Cs–isotopes are formed by the excitation of the Δ–resonance and subsequent π^- emission.

3.2 Momentum Distributions

The mean momentum of each fragment species was determined from the position distributions at the central dispersive image plane and a measurement of the magnetic field with hall probes. The momentum shift caused by the different energy loss of projectile and fragment in the target was corrected for. According to ref. [13] we use the same quantity $\langle P_{||} \rangle \equiv M_{proj} \cdot \langle \beta_{proj.fr.} \rangle \cdot c \cdot k$, where M_{proj} denotes the projectile mass , $\langle \beta_{proj.fr.} \rangle$ the mean velocity of the fragment in the projectile rest frame and $k = (\gamma - 1)/(\beta \cdot \gamma)$ a kinematic factor which approaches 1 for large kinetic energies of the projectile. If one neglects the mass loss in the first reaction step, $M_{proj} \cdot c \cdot \langle \beta_{proj.fr.} \rangle$ is the momentum transfer to the prefragment in the projectile rest frame. As pointed out in ref. [13] this quantity could be a measure of the prefragment excitation energy ($\langle P_{||} \rangle \approx c \cdot E^*_{pr.frg.}$).

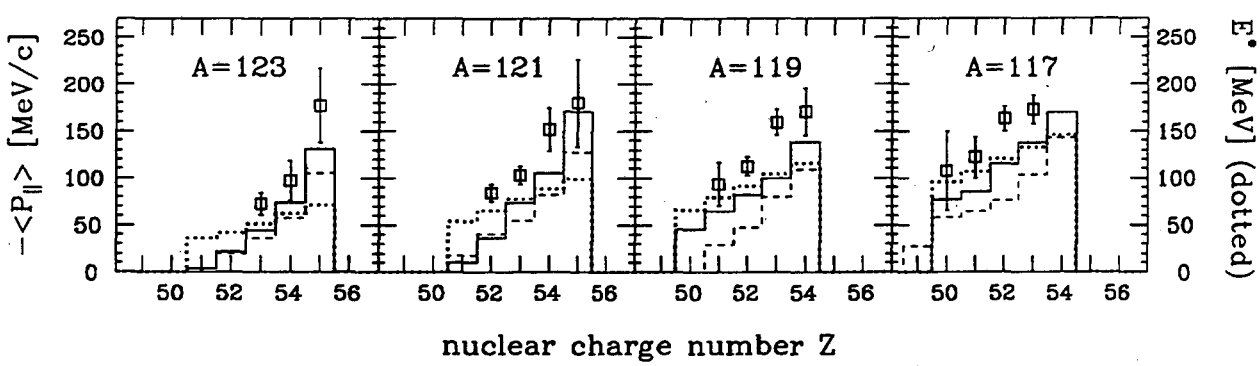

Figure 2: Mean longitudinal momentum transfer compared to ISAPACE calculations. Squares: data ^{129}Xe + Al. Full line: UFG model. Dashed line: LFG model. Dotted line: mean **excitation energy** of the corresponding prefragments simulated with UFG model (same scale, but in units [MeV]).

For fragments with a constant mass to charge ratio the data show on the average the expected trend [13] of roughly $\langle P_{||} \rangle = -\Delta A \cdot 8 MeV/c$. However, an isospin dependence with higher momentum transfer for the neutron deficient isobars was observed, which is not expected from this simple formula. This is shown in fig. 2, again in comparison with the ISAPACE calculation. Both, the UFG (full line) and the LFG (dashed line) description reproduce the slope of the distributions, whereas

the UFG model is in better agreement with the data. This reasonable quantitative agreement could only be achieved by adding a centrifugal barrier for escaping nucleons in the cascade calculation. In the model each barrier leads to a higher excitation energy of the prefragment due to the capture of nucleons above the fermi energy. The mean excitation energy of the corresponding prefragments calculated with the UFG model is shown with the dotted line of fig. 2. The isobaric distributions reveal nearly the same dependence on the increasing charge number as do the momentum transfers. This trend strongly reflects the increasing neutron binding energies for these nuclei. Therefore, the very neutron deficient fragments are produced at very high excitation energies, in contrast to the cold proton removal process observed for neutron rich fragments in this region [14].

3.3 Memory Effect

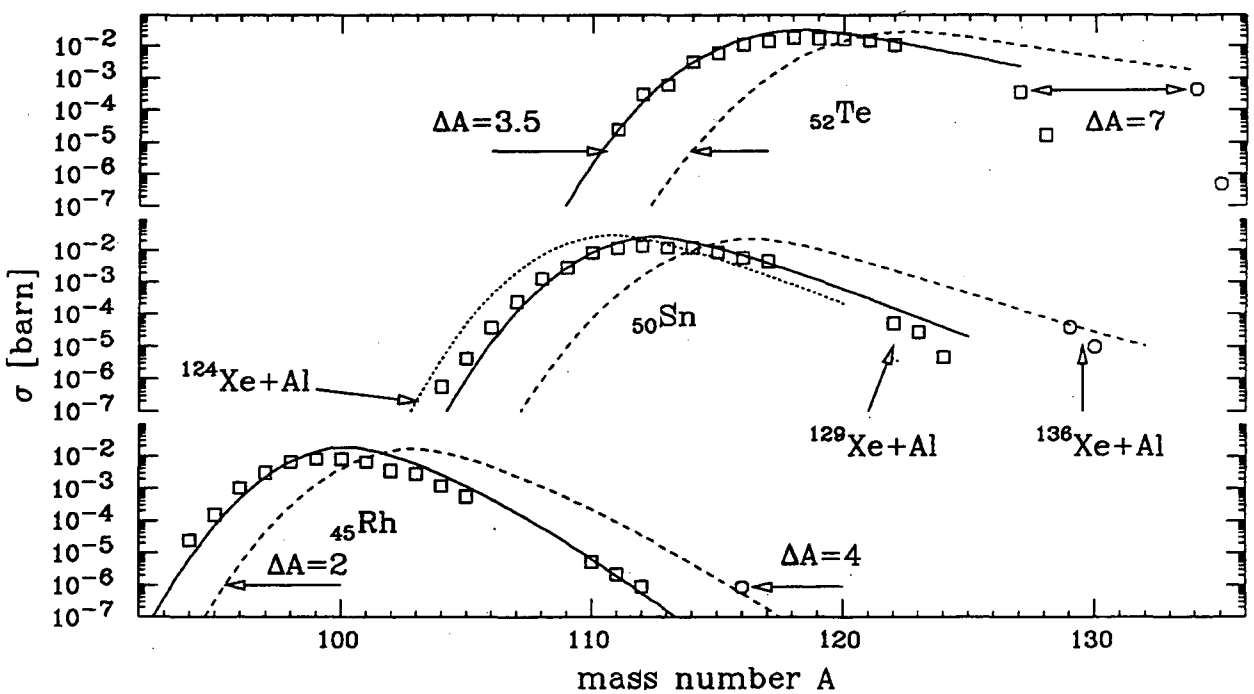

Figure 3: Isotopic distributions for different projectiles. Data: □ ^{129}Xe + Al 790A·MeV, ○ ^{136}Xe + Al 760A·MeV. EPAX parameterisation: full ^{129}Xe + Al, dashed ^{136}Xe + Al, dotted ^{124}Xe + Al.

In an earlier experiment [10] we have measured the fragmentation of ^{136}Xe at 760A·MeV in order to study the influence of the projectile neutron excess on the production cross section for neutron rich isotopes. In fig. 3 we compare three isotopic distributions to the prediction of a cross section parameterisation (EPAX [15]) which is based on data extracted from target fragmentation (spallation) with high energetic protons. Very close to the projectile mass (neutron rich $_{52}$Te–isotopes) the EPAX formula overestimates the measured cross sections by several orders of magnitude, whereas good agreement is found for fragments with higher mass losses. For the neutron rich $_{52}$Te–isotopes the excess of 7 neutrons is fully preserved. Even for mass losses of about 20 nucleons (neutron rich $_{45}$Rh–isotopes) a remaining shift of 4 mass units is obvious. Up to now this 'memory effect' has only been observed for lighter nuclei in the fragmentation of ^{40}Ca and ^{48}Ca [16]. Therefore our data strongly strengthen the prediction power of EPAX even for very heavy projectiles.

If one uses the most neutron deficient isotope ^{124}Xe as a projectile, the EPAX formula predicts a shift of about 1.5 mass units for the neutron deficient Sn–isotopes (see fig. 3). This is of particular interest for the production of the doubly magic nucleus ^{100}Sn. For ^{124}Xe + Al EPAX prédicts a production cross section $\sigma = 1.9 \cdot 10^{-12}$barn. As EPAX underestimates the measured cross sections for the neutron deficient isotopes in the ^{129}Xe case, the cross section for ^{100}Sn might even be higher. With present beam intensities at GSI a production rate of 10 ^{100}Sn/hour is predicted.

4 Summary

We have measured production cross sections for neutron deficient and neutron rich nuclei produced by projectile fragmentation of ^{129}Xe ions. Isotopic chains in the mass region 80<A<130 have been investigated up to very neutron deficient nuclei near the proton drip line. The extracted cross sections are in good agreement with the predictions of an empirical parameterization (EPAX [15]) and a monte carlo simulation (ISAPACE [3, 4]). In contrast to the more sophisticated models like 'BUU' and 'QMD' calculations, the ISAPACE model allows to calculate even cross sections as low as 1 μbarn within reasonable computing time. The measured momentum distributions are sensitive to the first reaction step of the fragmentation process. The comparison with the simulation shows, that higher excitation energies are needed to produce very neutron deficient fragments. For the first time the memory effect has been verified in the A>100 mass region. Therefore the use of heavy projectiles with adapted A/Z ratio is justified when very neutron rich or neutron deficient secondary beams are requested. Nevertheless, considerable disagreements in particular at the outer wings of the isotopic distributions remain. They indicate that the production cross sections for nuclei at the proton drip line are several orders in magnitude higher than expected.

References

[1] T. J. M. Symons et al., Phys.Rev.Lett 42(1979)40.

[2] G. D. Westfall, Phys.Rev.Lett 43(1979)1859.

[3] T. Blaich et al., Phys. Rev. C45(1992)689

[4] M .Fauerbach, Diploma Thesis, Institut für Kernphysik, TH Darmstadt, 1992.

[5] J.–J. Gaimard and K.–H. Schmidt, Nucl. Phys. A531(1991)709.

[6] C. Ziegler et al., GSI Darmstadt, Scientific Report 1990, GSI-91-1(1991)291.

[7] H. Geissel et al., Nucl. Instr. Meth. B70(1992)286.

[8] K. Zeitelhack, GSI-92-25 Report ISSN 0171-4546 (1992).

[9] K. Zeitelhack et al., Nucl. Instr. Meth. A333(1993)458.

[10] J. Friese et al., Nuclear Physics A553(1993)753c.

[11] Y. Yariv and Z. Fraenkel, Phys. Rev. C20(1979)2227.

[12] A. Gavron, Phys. Rev. C21(1980)230.

[13] D.J. Morrissey Phys. Rev. C39(1989)460.

[14] K.–H. Schmidt et al., Nucl. Phys. A542(1992)699.

[15] K. Sümmerer et al., Phys. Rev. C42(1990)2546.

[16] G.D. Westfall et al., Phys.Rev.Lett. 43(1979)1859.

Collective Effects and Flow

Collective Phenomena at the EOS TPC

D. Keane[2] for the EOS Collaboration:
S. Albergo[6], F. Bieser[1], F. P. Brady[4], Z. Caccia[6]*, D. A. Cebra[4], A. D. Chacon[5], J. L. Chance[4], Y. Choi[3]†, S. Costa[6], J. Elliott[3], M. Gilkes[3], J. A. Hauger[3], A. Hirsch[3], E. L. Hjort[3], A. Insolia[6], M. Justice[2], V. Lindenstruth[7], H. S. Matis[1], M. McMahan[1], C. McParland[1], W. F. J. Mueller[7], D. L. Olson[1], M. Partlan[4], N. Porile[3], R. Potenza[6], G. Rai[1], J. Rasmussen[1], H. G. Ritter[1], J. Romanski[6], J. L. Romero[4], G. V. Russo[6], H. Sann[7], R. Scharenberg[3], A. Scott[2], Y. Shao[2], B. Srivastava[3], T. J. M. Symons[1], M. Tincknell[3], C. Tuvè[6], S. Wang[2]‡, P. Warren[3], D. Weerasundara[2], H. H. Wieman[1], and K. L. Wolf[5]

[1] *Lawrence Berkeley Laboratory, Berkeley, California 94720*
[2] *Kent State University, Kent, Ohio 44242*
[3] *Purdue University, West Lafayette, Indiana 47907*
[4] *University of California, Davis, California 95616*
[5] *Texas A&M University, College Station, Texas 77843*
[6] *Università di Catania and INFN-Sezione di Catania, 95129 Catania, Italy*
[7] *Gesellschaft für Schwerionenforschung, D-64220 Darmstadt 11, Germany*

Abstract

Based on a preliminary subsample of Au + Au collisions in the EOS time projection chamber at the Bevalac, we study sideward flow as a function of bombarding energy between 0.25A GeV and 1.2A GeV. We focus on the increase in in-plane transverse momentum per nucleon with fragment mass, and address the possibility of interpreting this as a coalescence effect. We also find event shapes to be close to spherical in the most central collisions, independent of bombarding energy and fragment mass up to ^{4}He.

1. Introduction

A central goal in the study of heavy-ion collisions is to uncover and understand phenomena that cannot be explained in terms of a superposition of proton – nucleus collisions. As far back as the 1950s, hydrodynamic models have been used to predict various kinds of collective behavior that qualify as examples of such phenomena [1]-[4]. For non-zero impact parameters, the predominant fluid dynamic effect is a sideward deflection of the participant matter, termed sidesplash. The principal characteristic of sidesplash is

*Current address: Centro Siciliano di Fisica Nucleare e Struttura della Materia, 95129 Catania, Italy.
†Current address: Sung Kwun Kwan University, Suwon 440-746, Republic of Korea.
‡Current address: Harbin Institute of Technology, Harbin 150001, P. R. China.

a preferential emission of nucleons in the plane defined by the incident nuclei (the reaction plane), towards the projectile side if emitted forward in the center of mass, and towards the target side if emitted backward. Such collective correlations can be understood in terms of the release of compressional energy, and as such, provide a relative measure of the peak nuclear pressure generated in the collision. Models indicate that collective correlations (unlike many other final state observables) are established during the early, high density stage of the collision, and are minimally distorted during the subsequent processes of expansion, decay of excited states, and formation of the final configuration of free nucleons and composite fragments. Thus, fluid-like correlations are regarded as being among the most appropriate observables for studying the equation of state of the compressed nuclear matter produced during the initial stages of a heavy-ion collision.

Experiments at detectors with 4π or near-4π solid angle acceptance have confirmed the existence of collective fluid-like correlations, and have provided measurements of many aspects of the phenomenon; meanwhile, our theoretical understanding has progressed with the help of increasingly sophisticated fluid dynamic and nuclear transport models [5]. The EOS Time Projection Chamber is a new 4π detector which was designed to continue the progress made during the earlier phases of the Bevalac program. It offers a simple and seamless acceptance, good particle identification, and adequate statistics for a comprehensive characterization of the relevant physics. In these proceedings, we summarize some previously-reported [6, 7] sideward flow results based on preliminary EOS data, we present a new analysis of the dependence of sideward flow on fragment mass, and we report preliminary data on event shapes in very central collisions of Au + Au.

2. The EOS Detector

The EOS Time Projection Chamber has a rectangular geometry, and operates in a 1.3 T dipole field provided by a superconducting magnet at the Bevalac's Heavy Ion Spectrometer System (HISS) facility. Unlike previous TPCs, EOS relies solely on pads for readout. The pad plane covers an area of 1.54×0.96 m^2, with 128 pad rows along the longer dimension, and 120 pads per row. Details about the chamber, the electronics and the data acquisition have been reported previously [8]. The standard EOS detector configuration includes the TPC, a multiple sampling ionization chamber (MUSIC II) positioned to intercept projectile spectator fragments, an array of scintillator slats to provide time-of-flight information at small polar angles, and a high efficiency neutron detector (MUFFINS) centered on zero degrees with respect to neutrons emitted from the target. Additional details about the EOS detector configuration and experimental running conditions can be found elsewhere [6, 7]. Only data from the TPC have been used in the current analysis.

In these proceedings, we report preliminary results for collisions of Au + Au at beam energies of 250, 400, 600, 800, 1000 and 1150A MeV; typically 10^4 events have been analyzed for each beam energy, except for the case of 1150A MeV, where the sample size is about 3×10^4 events. These samples correspond to about one-tenth of the total statistics accumulated.

3. In-plane Transverse Momentum

Our initial investigation of collective effects in Au + Au collisions includes the same in-plane transverse momentum analysis with essentially the same data selection criteria as used by the Plastic Ball group [9, 5]. In particular, all nuclear fragment species up to ^{4}He are included, and we select an interval of multiplicity centered about the value where the flow has its maximum. This multiplicity interval corresponds to baryonic fragment multiplicities $0.6M^{max} < M < 0.9M^{max}$, where M^{max} is a value near the upper limit of the M spectrum where the height of the distribution has fallen to half its plateau value. The in-plane transverse momentum method[10] involves estimating the orientation of the reaction plane for each event using the vector $\mathbf{Q} = \sum_{\nu=1}^{M} w(y_\nu)\mathbf{p}_\nu^\perp$, where $\mathbf{p}_\nu^\perp$ is the transverse momentum for the νth baryon track, and $w(y_\nu)$ is a rapidity-dependent weighting factor. To optimize the correlation of $\mathbf{Q}$ with the reaction plane, $w(y_\nu)$ should vary according to the relative magnitude and sign of the sideward deflection of fragments at y_ν; we follow the prescription $w(y'_\nu) = y'_\nu$, where $y'_\nu = (y_\nu/y_{beam})_{cm}$ is defined as the rapidity of the νth fragment divided by the beam rapidity, both evaluated in the center of mass frame. The quantity $\langle p^{x'}(y')/A\rangle$ is the mean component of transverse momentum per nucleon in this estimated reaction plane, where

$$p_\nu^{x'} = \mathbf{p}_\nu \cdot \hat{\mathbf{Q}}_\nu\,, \qquad \mathbf{Q}_\nu = \sum_{\mu\neq\nu} w_\mu \mathbf{p}_\mu^\perp\,, \tag{1}$$

and $\hat{\mathbf{Q}}$ denotes a unit vector. The flow component in the true reaction plane, p^x, is systematically larger than the component in the estimated plane, $p^{x'}$, and for consistency with the Plastic Ball analysis, we use the subevent method [10, 9] to correct for this dispersion effect. Because of the high baryon multiplicity in Au + Au collisions, dispersion correction factors are small, ranging from 1.12 at $0.25A$ GeV to 1.07 at $1.15A$ GeV.

Fig. 1 presents $\langle p^x(y')/A\rangle$ at each of the six bombarding energies under investigation. We observe the classic "S"-shaped curve which changes sign at $y' = 0$. Although projectile-target symmetry dictates $p^x(y') = -p^x(-y')$, even an ideal 4π detector cannot satisfy this condition because absorption and energy loss in the target introduces distortion for y' approaching -1. In the EOS detector, the target was located about 14 cm upstream from the active volume of the TPC, leading to optimized performance near mid-rapidity and above, at the expense of a progressive loss of acceptance approaching target rapidity. At each beam energy, we fit the $\langle p^x(y')/A\rangle$ curves over the region indicated by the solid lines in Fig. 1 with a function of the form $my' - m_3y'^3$; the fitted values of m characterize the overall magnitude of the sideward flow effect among participant fragments, and these slopes are known simply as "flow" in the literature.

All fragment species up to ^{4}He were included when computing the results shown in Fig. 1. In this work, we focus on the dependence of collective effects on fragment mass, and Fig. 2 presents preliminary flow excitation functions ($\langle p^x(y')/A\rangle$ slopes as defined above) separately for protons, deuterons and alphas. The measurements in Fig. 2 are the first of this kind for light composite fragments over a range of intermediate bombarding energies, and show a consistent pattern of increase in sideward flow per nucleon with increasing fragment mass number A. Such an increase was previously reported by the Plastic Ball group for collisions of Au + Au at a single beam energy, namely, $200A$ MeV [11].

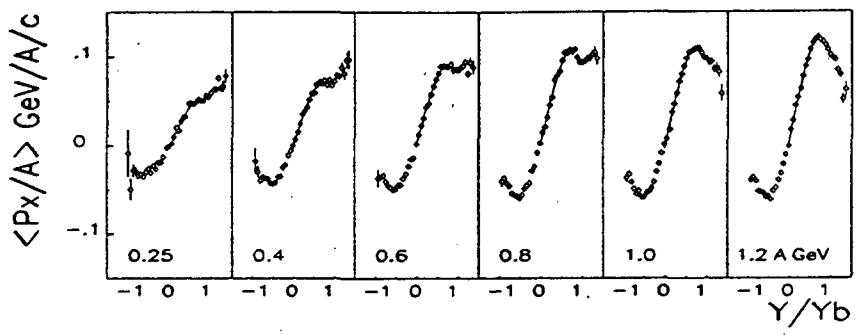

Figure 1: Transverse momentum per nucleon projected on the event reaction plane, as a function of fragment rapidity divided by beam rapidity, for Au + Au collisions at six beam energies between $0.25A$ GeV and $1.2A$ GeV.

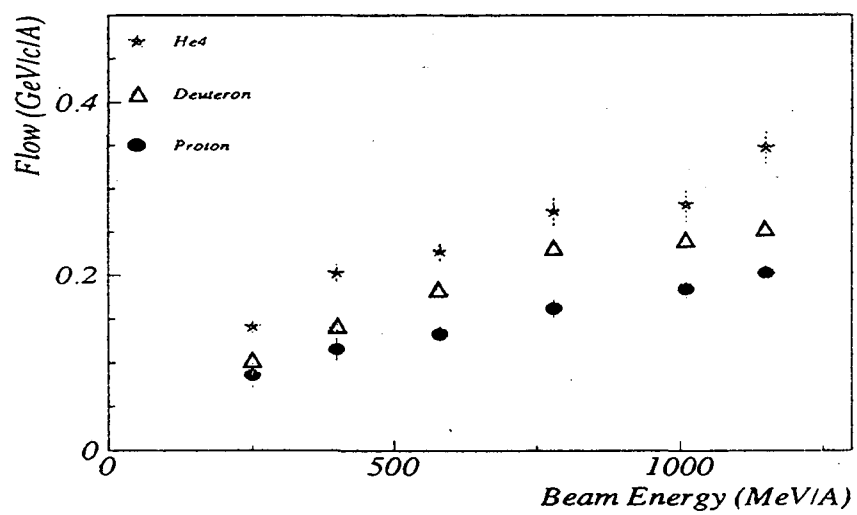

Figure 2: Flow excitation function for protons, deuterons and alphas from Au + Au collisions.

Berenguer *et al.*[12] have argued that the flow for composite fragments provides the most unambiguous measure of the pressure during the early stage of the collision — *i.e.*, the heavier fragments offer advantages over free nucleons for probing the nuclear equation of state. Fragments preferentially come from a cooler, less compressed zone where thermal smearing effects are smaller; nevertheless, they *are* subject to a sideward deflection from the strong potential gradient that surrounds the central high-density zone. Indeed, in a transport model description, particles located at the very center of the collision region at the time of maximum density are likely to experience a *smaller* integrated potential gradient and a smaller sideward deflection. However, coalescence alone produces an increase in $\langle p^x(y')/A\rangle$ with fragment mass number A, and so offers an alternative possible explanation. Coalescence effects are characterized by constant ratios $\rho_A/\rho_{A=1}^A$, where ρ_A is density (in

the appropriate parameter space) of fragments with mass number A. In this instance, an appropriate density is $\rho_A(\varphi)$, which we define as the variation with φ, the fragment's azimuth relative to the collision reaction plane, of the number of fragments having mass A in a given interval of y' and $|\mathbf{p}^\perp|/A$. Sideward flow causes $\rho_A(\varphi)$ to deviate from a flat distribution, and neglecting isospin effects, the coalescence picture predicts

$$\frac{\rho_A(\varphi)}{\langle\rho_A\rangle} = \frac{\rho_{A=1}^A(\varphi)}{\langle\rho_{A=1}\rangle^A}, \tag{2}$$

where the averaging is taken over all φ. However, the results presented in Fig. 2 are not in a form that allows the coalescence picture to be tested, and this is one of the factors motivating an alternative analysis in terms of orthogonal components of sideward flow.

4. Orthogonal Components of Sideward Flow

A comprehensive description of collective flow phenomenon would allow us to write the observed transverse momentum $\mathbf{p}^\perp$ for a fragment in the form

$$\mathbf{p}^\perp = \mathbf{p}^\perp_{uncor} + F\hat{\mathbf{x}} + G\hat{\mathbf{y}}\,, \tag{3}$$

where the unit vector $\hat{\mathbf{x}}$ is aligned with the reaction plane, $\hat{\mathbf{y}}$ is perpendicular to $\hat{\mathbf{x}}$, and $\mathbf{p}^\perp_{uncor}$ represents the transverse momentum distribution for events which do not incorporate the collective effects in question. We can approximate $\mathbf{p}^\perp_{uncor}$ using mixed events, *i.e.*, events generated by randomly selecting M tracks, each from a different observed event with multiplicity M. Existing measurements are inadequate for fully constraining the functions F and G. For example, data on $\langle p^x(y')\rangle$ cannot provide information about the dependence of F on φ. The alternative analysis presented here involves simultaneous measurements of two orthogonal components of the collective sideward motion: the azimuthal component, associated with rotations of $\mathbf{p}^\perp$ relative to an uncorrelated distribution, and the radial component of sideward flow, associated with changes in the magnitude of $\mathbf{p}^\perp$ relative to an uncorrelated distribution. Measurements of these two components complement each other, and together, they place more complete and stringent constraints on dynamical models.

The azimuthal pair correlation function [13] makes use of the variable ψ, the smaller angle between the transverse momenta of two fragments, and is defined as

$$C(\psi) = \frac{P_{cor}(\psi)}{P_{uncor}(\psi)}, \tag{4}$$

where $P_{cor}(\psi)$ is the ψ distribution for observed pairs, *i.e.*, pairs in which both fragments belong to the same event, and $P_{uncor}(\psi)$ is the ψ distribution for pairs from mixed events. Sideward flow leads to an enhanced probability for fragments to be emitted with azimuths close to each other, near the reaction plane orientation; thus, if $C(\psi)$ is plotted for a rapidity interval that is not centered on mid-rapidity, we observe $C(\psi) > 1$ at small ψ and $C(\psi) < 1$ at large ψ. If fragments within a given rapidity interval are distributed in φ according to $P(\varphi) \propto 1+\lambda\cos\varphi$, [13] then $C(\psi) = 1+0.5\lambda^2\cos\psi$. Fitted λ values provide a dimensionless measure of the azimuthal flow component. The azimuthal pair correlation function offers

several advantages over previous flow analyses: it circumvents the need for event-by-event estimates of the reaction plane and the need to correct for dispersion in these estimates, it allows flow measurements in different rapidity intervals to be completely independent of each other, and the denominator in $C(\psi)$ automatically corrects for any azimuthal asymmetry introduced by the detector. Detector-related asymmetry in the transverse plane becomes apparent at $y' < 0$; however, only forward rapidities are studied in the current analysis.

To characterize the radial component of sideward flow, we introduce a new quantity which we call the radial pair variance function:

$$\sigma^2(\psi) = \langle p_{sum}^2(\psi)\rangle - \langle p_{sum}(\psi)\rangle^2 , \tag{5}$$

where $p_{sum} = p_i^\perp/A_i + p_j^\perp/A_j$ is the sum of the $\mathbf{p}^\perp$ magnitudes per nucleon for the pair. This function offers the same advantages as the azimuthal pair correlation function; in this instance, there is no reason to compute a ratio like P_{cor}/P_{uncor}, because $\sigma^2(\psi)$ is flat for mixed events, even at backward rapidities where detector-related asymmetry in the transverse plane is apparent. The fact that $\mathbf{p}^\perp$ magnitudes tend to be larger when a fragment's azimuth is parallel to the flow direction, and tend to be smaller when antiparallel, leads to an inequality $\sigma^2(\psi \sim 0°) > \sigma^2(\psi \sim 180°)$. If F is independent of φ and is large compared with G, σ^2 decreases linearly with increasing ψ; this linearity can be demonstrated analytically for an idealized example where there are no thermal fluctuation in $\mathbf{p}^\perp$, and simulations with realistic momenta also indicate linear $\sigma^2(\psi)$. To characterize the magnitude of the radial component of sideward flow in momentum units, we define $S = \sqrt{(d\sigma^2/d\psi)}$.

Fig. 3 shows azimuthal pair correlation functions $C(\psi)$ and radial pair variance functions $\sigma^2(\psi)$ in five rapidity intervals spanning mid-rapidity to projectile rapidity, for Au + Au at 1.2A GeV. The solid curves in the $C(\psi)$ panels represent least-squares fits using the function $1 + 0.5\lambda^2 \cos\psi$, and the $\sigma^2(\psi)$ data in the lower panels are fitted using a straight line. In this analysis of azimuthal and radial components of sideward flow, only protons and deuterons from events with $M > 0.4M^{max}$ have been included. These fragments make up 73% of all reconstructed tracks within the selected rapidity range at 1.2A GeV. The dependence of the flow components on beam energy is addressed elsewhere [7].

5. Dependence of Components of Sideward Flow on Fragment Mass

In order to investigate fragment mass dependence, we have sorted protons and deuterons into separate samples and computed the same quantities as plotted in Fig. 3. Proton-deuteron pairs are not included in either sample; this approach facilitates interpretation of the data but results in a substantial loss of statistics. The system Au + Au at 1.2A GeV provides the best data on fragment flow among the current preliminary samples, but still does not yield useful same-fragment pair correlation statistics for $A \geq 3$. Fig. 4 shows the fitted sideward flow components λ and S for our standard rapidity intervals spanning mid-rapidity to near projectile rapidity, for Au + Au at 1.2A GeV. At all of the rapidities studied, the observed pattern is consistent with Eq.(2) and the simplest coalescence picture: [14] the radial component of sideward flow S is the same for p and d, while $\lambda_d = 2\lambda_p$ within experimental uncertainties.

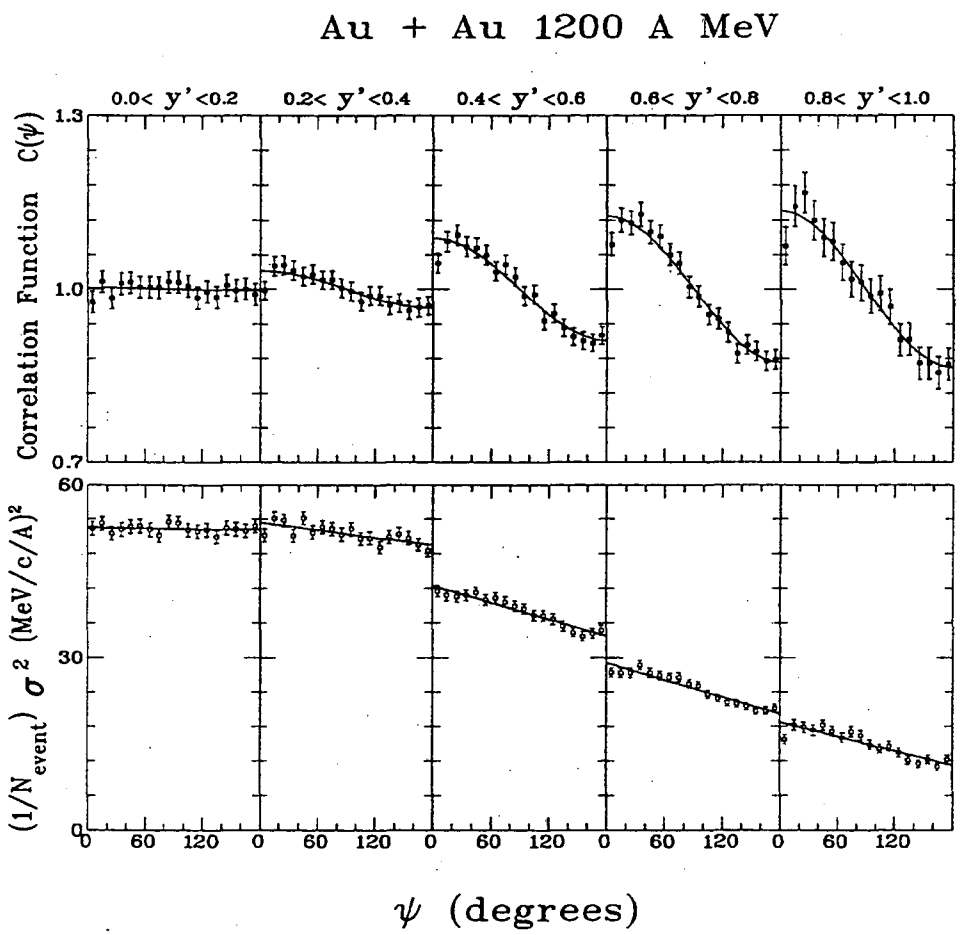

Figure 3: Azimuthal pair correlation functions and radial pair variance functions in five rapidity intervals spanning mid-rapidity to projectile rapidity, for Au + Au at $1.2A$ GeV.

An important advantage of the EOS TPC is its seamless acceptance, which is simple enough to be simulated with good accuracy. To estimate the effect of detector distortion on the observables under investigation, we use events from a version of the *FREESCO*[15] statistical event generator to which a phenomenological flow correlation[16] has been added; GEANT is used to follow all particles from the interaction point in the target through the active volume of the TPC, with trajectories of charged particles determined from the mapped field of the HISS magnet; a fast simulator generates amplitudes and positions for pad-row hits along the tracks, allowing for smearing and merging of hits according to the resolution of the TPC; from this stage onwards, the simulated data are processed through the experimental data reduction codes for track finding, momentum reconstruction and particle identification. These simulations indicate that any detector-related distortion of the measured sideward flow components is no larger than the statistical uncertainty in samples of several thousand events.

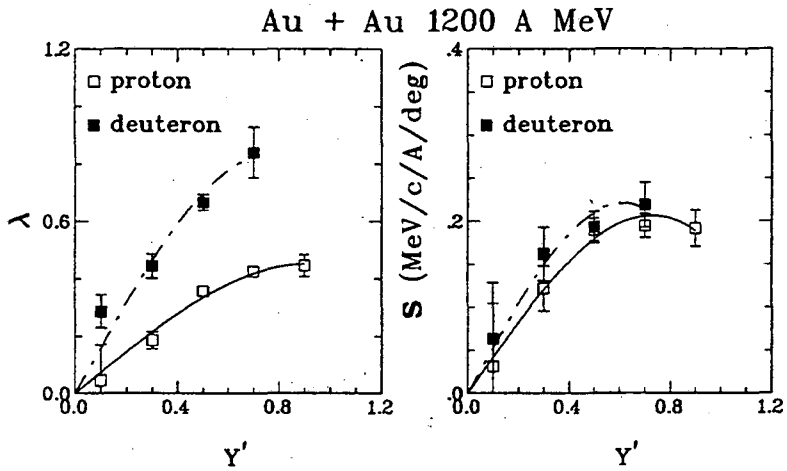

Figure 4: Azimuthal flow component $\lambda(y')$ and radial component of sideward flow $S(y')$ separately evaluated for protons and deuterons from collisions of $1.2A$ GeV Au + Au

6. Event Shapes in Central Collisions

The thermalization ratio $R = 2\sum|\mathbf{p}^{\perp}| \;/\; \pi\sum|p^{z}_{cm}|$, where the sums extend over all fragments in an event, has been widely used since the time when the first 4π measurements became available. An isotropic source implies $R = 1$, and while the converse is not true, measurements of R can provide information about event shapes. For example, it can readily distinguish between shapes that vary along a continuum ranging from a "cigar" aligned with the beam direction, through a sphere, and extending to a "pancake" in the plane perpendicular to the beam. However, in the presence of collective flow effects like sidesplash and squeeze-out, and allowing for kinematic cuts and detector distortion, the interpretation of R becomes complicated. It is only in the limit of very central collisions, where sideward flow effects and other correlations with respect to the reaction plane must drop to zero, that a relatively straightforward interpretation becomes possible.

The sideward flow observed at intermediate impact parameters can be understood as resulting from the release of compressional potential energy. This compressional potential energy increases monotonically with decreasing impact parameter, while sideward flow peaks at intermediate impact parameters and then drops to zero at zero impact parameter. There are several possible scenarios for describing the deexcitation of compressional energy in the most central events. These possibilities include a range of different azimuthally-symmetric patterns of sideward flow, or a simpler isotropic expansion [17]-[20]. The EOS data for $y' > 0$ are well-suited for testing event shapes and elucidating these issues.

Of course, collisions at exactly zero impact parameter have zero probability, and all events in our sample of central collisions, selected for high multiplicity and low sideward flow, must have a small but non-zero impact parameter. Associated with this non-zero impact parameter is the presence of a small amount of spectator matter, which can bias the thermalization ratio R towards lower values. In order to avoid the possibility of such bias,

we include only fragments which satisfy $p_b/A > 0.27$ GeV/c, where p_b denotes fragment momentum transformed into the rest frame of the projectile. This cut biases R in the opposite direction, but it is relatively easy to correct this bias; for this purpose, we use the isotropic participant source from the *FREESCO* [15] event generator with the same cut (see below).

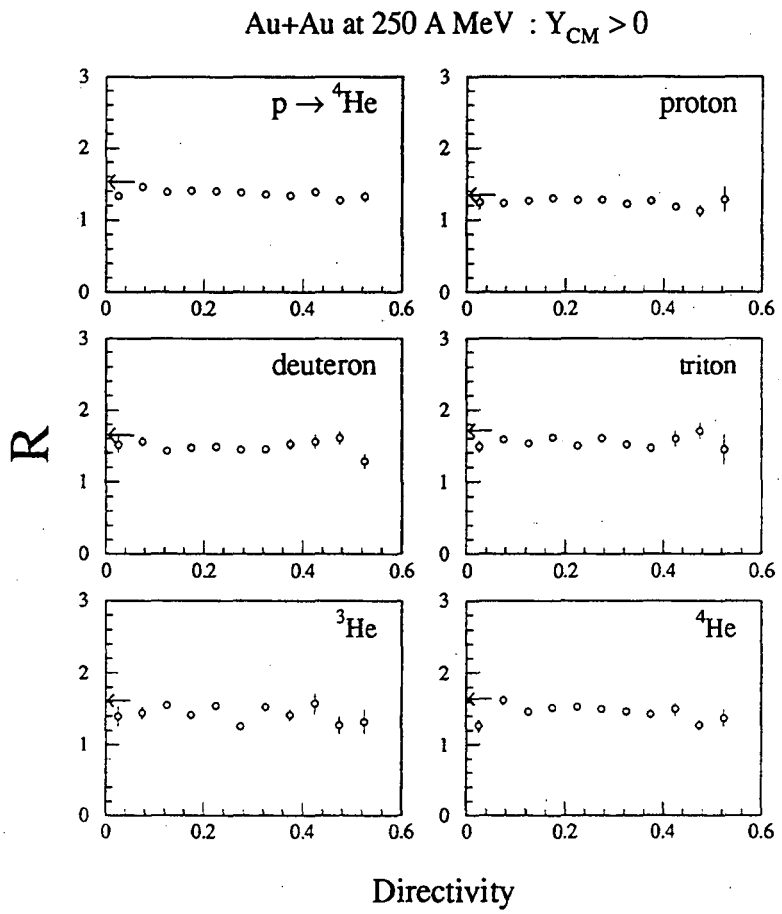

Figure 5: Average thermalization ratio R versus directivity D for different light fragment species from $0.25A$ GeV Au + Au events with more than 30 detected baryonic fragments at forward rapidities ($y' > 0$). Note that R values in the vicinity of the horizontal arrow are consistent with a spherical event shape.

Our conclusions about event shapes are essentially independent of our choice of variable to characterize the magnitude of the sideward flow signal; in these proceedings, we use the directivity variable [20] $\mathbf{D} = \sum \mathbf{p}^{\perp} \; / \; \sum |\mathbf{p}^{\perp}|$. Fig. 5 presents average thermalization ratios R in bins of directivity magnitude D, for different light fragment species from $0.25A$ GeV Au + Au events with more than 30 detected baryonic fragments at $y' > 0$. Fig. 6 presents corresponding results for $1.15A$ GeV Au + Au events with more than 60 detected baryonic fragments at $y' > 0$; results for the other beam energies are as expected by interpolation. The arrows on the vertical scales mark the R values for an isotropic source with the same spectator cut ($p_b/A > 0.27$ GeV/c) as applied to the EOS data. The main conclusion based on these preliminary data is that the most central collisions

(lowest D) are consistent with being close to spherical in shape for all light fragment species at all beam energies studied. As explained above, the interpretation of R for larger D values is more complicated, but the observed data at the higher beam energies are consistent with the sphericity ellipsoid [21] being oriented at a relatively small flow angle (10° to 20°), predominantly elongating event shapes in the beam direction, while at $0.25A$ GeV, the data are consistent with the elongation due to sideward flow affecting the numerator and denominator in R by a comparable amount.

This work is supported in part by the US Department of Energy and the US National Science Foundation.

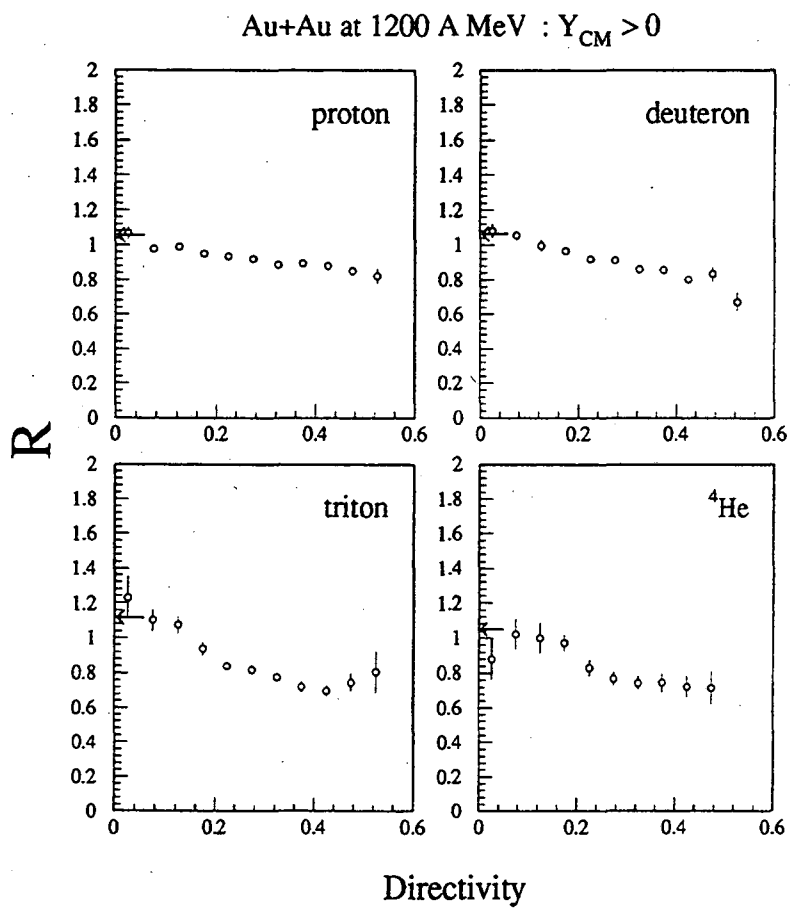

Figure 6: Average thermalization ratio R versus directivity D for different light fragment species from $1.15A$ GeV Au + Au events with more than 60 detected baryonic fragments at forward rapidities ($y' > 0$).

References

[1] S.Z. Belen'kji and L.D. Landau, Nouvo Cimento, **1**, 15 (1956).

[2] G.F. Chapline, M.H. Johnson, E. Teller, and M.C. Weiss, Phys. Rev. D **8**, 4302 (1973).

[3] W. Scheid, H. Müller, and W. Greiner, Phys. Rev. Lett. **32**, 741 (1974).

[4] C.Y. Wong and T.A. Welton, Phys. Lett. **49B**, 243 (1974).

[5] For reviews, see H. Stöcker and W. Greiner, Phys. Rep. **137**, 277 (1986); G. F. Bertsch and S. Das Gupta, Phys. Rep. **160**, 189 (1988); *NATO Advanced Study Institute: The Nuclear Equation of State*, **216B**, ed. W. Greiner and H. Stöcker, (Plenum, NY, 1989), Part A; K.-H. Kampert, Nucl. Part. Phys. **15**, 691 (1989); H.H. Gutbrod, A.M. Poskanzer, and H.G. Ritter, Rep. Prog. Phys. **52**, 1267 (1989); J. Jiang, D. Keane, and Y.M. Liu, Int. J. Mod. Phys. E (in press).

[6] G. Rai, S. Albergo, F. Bieser, F.P. Brady, Z. Caccia, D. Cebra, A.D. Chacon, J. Chance, Y. Choi, S. Costa, J. Elliott, M. Gilkes, A. Hauger, A. Hirsch, E. Hjort, A. Insolia, M. Justice, D. Keane, V. Lindenstruth, H.S. Matis, M. McMahan, C. McParland, W.F.J. Müller, D.L. Olson, M.D. Partlan, N. Porile, R. Potenza, J. Rasmussen, H.G. Ritter, J. Romanski, J.L. Romero, G.V. Russo, H. Sann, R. Scharenberg, A. Scott, Y. Shao, B. Srivastava, T.J.M. Symons, M. Tincknell, C. Tuvè, S. Wang, P. Warren, H. Wieman, and K. Wolf, to appear in Proc. of *International Workshop on Dynamical Features of Nuclei and Finite Fermi Systems*, (World Scientific, Singapore, in press).

[7] D. Keane *et al.* (EOS collaboration as cited above), to appear in *NATO Advanced Study Institute: Hot and Dense Nuclear Matter,* ed. W. Greiner and H. Stöcker, (Plenum, NY, in press).

[8] G. Rai, A. Arthur, F. Bieser, C.W. Harnden, R. Jones, S. Kleinfelder, K. Lee, H.S. Matis, M. Nakamura, C. McParland, D. Nesbitt, G. Odyniec, D. Olson, H.G. Pugh, H.G. Ritter, T.J.M. Symons, H. Wieman, M. Wright, R. Wright, and A. Rudge, IEEE Trans. Nucl. Sci. **37**, 56 (1990).

[9] K.G.R. Doss, H.-Å. Gustafsson, H.H. Gutbrod, K.H. Kampert, B. Kolb, H. Löhner, B. Ludewigt, A.M. Poskanzer, H.G. Ritter, H.R. Schmidt, and H. Wieman, Phys. Rev. Lett. **57**, 302 (1986).

[10] P. Danielewicz and G. Odyniec, Phys. Lett. **157B**, 146 (1985).

[11] K.G.R. Doss, H.-Å. Gustafsson, H.H. Gutbrod, J.W. Harris, B.V. Jacak, K.-H. Kampert, B. Kolb, A.M. Poskanzer, H.-G. Ritter, H.R. Schmidt, L. Teitelbaum, M. Tincknell, S. Weiss, and H. Wieman, Phys. Rev. Lett. **59**, 2720 (1987).

[12] M. Berenguer, C. Hartnack, G. Peilert, A. Rosenhauer, W. Schmidt, J. Aichelin, J. A. Maruhn, W. Greiner, and H. Stöcker, in *NATO Advanced Study Institute: Nuclear Matter and Heavy Ion Collisions*, **B205**, ed. M. Soyeur, H. Flocard, B. Tamain, and M. Porneuf, (Plenum, NY, 1989), p. 343.

[13] S. Wang, Y.Z. Jiang, Y.M. Liu, D. Keane, D. Beavis, S.Y. Chu, S.Y. Fung, M. Vient, C. Hartnack, and H. Stöcker, Phys. Rev. C **44**, 1091 (1991).

[14] Y. Shao, Ph.D. thesis, Kent State U. (1994).

[15] G. Fai and J. Randrup, Nucl. Phys. **A404**, 551 (1983); Comp. Phys. Comm. **42**, 385 (1986).

[16] A.F. Barghouty, G. Fai, and D. Keane, Nucl. Phys. **A535**, 715 (1991).

[17] H.W. Barz, J.P. Bondorf, R. Donangelo, R. Elmér, F.S. Hansen, B. Jakobsson, L. Karlsson, H. Nifenecker, H. Schulz, F. Schussler, K. Sneppen, and K. Söderström, Nucl. Phys. **A531**, 453 (1991).

[18] P. Danielewicz and Q. Pan, Phys. Rev. C **46**, 2002 (1993).

[19] J. Randrup, Comp. Phys. Comm. **77**, 153 (1993).

[20] N. Herrmann, Nucl. Phys. **A553**, 739c (1993); S.C. Jeong *et al.*, to be published.

[21] M. Gyulassy, K. A. Frankel, and H. Stöcker, Phys. Lett. **110B**, 185 (1982); P. Danielewicz and M. Gyulassy, Phys. Lett. **129B**, 283 (1983); G. Fai and J. Randrup, Nucl. Phys. **A404**, 551 (1983).

FRAGMENT–FRAGMENT CORRELATIONS

G. Peilert, T.C. Sangster, M.N. Namboodiri, and H.C. Britt

Lawrence Livermore National Laboratory,
Livermore, CA 94550
USA

A topic of great interest in nuclear physics is the multifragmentation of heavy nuclei at moderate excitation energies. In the experiments from the Purdue group [1, 2] first attempts have been made to relate the results in these reactions to the critical exponents of a phase transition, analogous to the liquid gas transition in condensed matter physics. Within the last years it became possible to study such reactions in highly exclusive experiments and to vary the order parameter of the proposed phase transition in order to extract the critical properties. This can be achieved by investigating the moments of the mass distributions as it was proposed by Campi [3]. Investigations utilizing the percolation model [4] show indeed that this infinite matter phase transition is observable even in small finite systems of the size of nuclei [5].

Such a procedure, however will not provide the physical quantities that drive the transition from a nuclear liquid to the vapor phase. If one wants to extract quantities like a critical temperature and density one has to rely on models that describe the whole dynamical process of a heavy ion collision. Unfortunately there is presently no complete model available that describes the process of the thermally driven multifragmentation in heavy ion collisions in a single, consistent approach. Current modeling involves a pre equilibrium stage described in

the earliest approaches by an Intranuclear Cascade Model, INC, [6, 7] and more recently by molecular dynamics pictures such as the Quantum Molecular Dynamics Model, QMD, [8, 9] or by using single particle models from the VUU/BUU type [10]. Following this stage there remains a distribution of nucleons and complex fragments which can themselves be highly excited. These excited fragments then undergo further statistical decay. This statistical decay process has been modeled in various codes as a sequential evaporation [11, 12, 13] or as an explosive simultaneous multifragmentation [14, 15, 16, 17, 18]. The simultaneous multifragmentation models assume a statistical break–up of a hot source into many intermediate mass fragments and then calculate the most probable fragment distribution by exploiting the available phase space. On the other side the sequential models assume that the source decays by the successive, binary emission of nucleons and heavy fragments. None of these models, however, includes the dynamics of the fragmentation.

Recent investigations with the QMD model have shown, that for central collisions of heavy nuclei at high energies a rapid compression–decompression mechanism emerges in the initial stage of the reaction and leads to an direct multifragmentation process, where a highly excited heavy residue is no longer formed with a high probability [9, 19]. These investigations suggest that the region to search for the thermally driven multifragmentation in heavy ion reactions is in central collisions at low bombarding energies (E/A $\approx$ 100 A MeV) or in peripheral (or highly asymmetric) reactions at high energies (E/A $\approx$ 1 A GeV) . In this type of reaction the direct reaction leads to a highly excited source that then breaks up into many IMFs.

Many experiments [19, 20, 21] have unambiguously proven that nuclear multifragmentation is indeed a new decay mechanism for highly excited nuclei, but up to now there is still little understanding of the physical process that drives this multifragmentation. One of the basic questions that still is not answered is whether the fragmentation takes place by sequential emission of fragments or by a simultaneous "explosion". Since for both scenarios most of the final state observables like multiplicities, fragment yields, energy spectra etc. are identical, one has to find new observables that are sensitive to the details of break–up mechanism, e.g., the emission time scale and the Freeze–Out volume.

Recently attempts have been made to extract the emission time scale out of different experimental data sets [21, 22, 23]. Complimentary to these investigations we will show in this

letter, that the same data can be explained by assuming a simultaneous multifragmentation and we will extract the corresponding Freeze–Out volume.

For the following comparison to experimental data we will use the QMD+SMM approach to model the dynamical reaction with the following statistical decay of the excited pre fragments. The QMD model provides a microscopic dynamical calculation of a heavy ion reaction. The basic version of the QMD model uses a local two and three–body Skyrme interaction and a Coulomb and Yukawa interaction. The parameters of the interactions are adjusted to reproduce the properties of infinite nuclear matter, as well as the binding energy and radii of nuclei in the mass regime from A=2 - 200. The numerical simulation of the collision takes place in three steps. First the projectile and target are initialized in their rest frames. Successfully initialized nuclei are then boosted towards each other with the proper center of mass velocities using relativistic kinematics. Each nucleon is then propagated corresponding to the Hamilton equations with a second order Runge-Kutta integration algorithm. After each integration step the hard N–N collisions are treated via a stochastic scattering term. Two nucleons can scatter if the spatial distance of the centroids of their Gaussians is smaller than $\sqrt{\sigma/\pi}$. For the present calculation we used an isotropic, isospin independent scattering cross section of 41 mb. Whenever a collision occurs, the resultant phase-space distribution around the final states of the scattering partners is checked whether the resultant configuration violates the Pauli principle. Whenever a collision is blocked, the momenta of the scattering partners are replaced by the values they had prior to the scattering.

In order to simulate the Fermi motion we employ a so called Pauli potential [25]. The implementation of the Pauli potential into the dynamical QMD model yields two major improvements. First the ground states are now well defined and the Monte Carlo procedure can be used to initialize projectile and target in their real ground state. Secondly the excitation energy of the resulting fragments can then be determined with respect to their true ground state.

Previous investigations with the QMD model have shown that there are two different mechanisms leading to the multifragmentation process. One is related to the mechanical rupture of the system, whenever compression effects are important. The other mechanism produces fragments thermally from an equilibrated source. This thermal multifragmentation has so far not been described in a microscopic model like QMD [9]. In the first comparison

to inclusive IMF data it was shown that a two step model was necessary to reproduce the experimental angular distributions [24]. This two step model involved the calculation of initial kinematics and excitation energy of all pre fragments with QMD model and a subsequent de excitation calculation utilizing the Statistical Multifragmentation Model (SMM) of Botvina et al. [16]. The input for the SMM stage of the reaction is the mass and the excitation energy of the fragments produced in QMD. These values are consistently determined within the QMD approach.

This model describes the multifragmentation of highly excited nuclei based on the statistical approach and a liquid–drop description of hot fragments. It is assumed that the excited primordial fragments, characterized by their excitation energy, mass and charge, break up into an assembly of nucleons and fragments. All these decay products are described as Boltzmann particles in a Freeze–Out volume $V = V_0(1 + \kappa)$, where κ is a model parameter and V_0 is the volume of the system corresponding to normal nuclear matter density. Since all the produced fragments are excited (only particles with A $\leq$ 4 are considered as elementary particles) the final de excitation of those fragments is treated as a Fermi break up for light fragments (A < 16) and via an evaporation of nucleons and clusters up to ^{18}O for heavier fragments (for details see Ref. [16]).

In the following we will vary the volume parameter κ of the SMM model in order to extract the Freeze–Out volume out of the two fragment correlation data.

Figure 1 shows a comparison between the experimental data [24] and the QMD+SMM calculations using $\kappa = 2, 5$ and 10 for two different projections of the double differential cross section $d^2\sigma/(dZd\Omega)$. Both the data and the calculations are for central collisions only (for details see Ref. [24]). The upper part of figure 1 shows the charge yield distribution at a laboratory angle of 72° (±13°), while the lower part shows the angular distribution of fragments with Z=10. In both cases it can be seen that the variation of the volume parameter κ does not influence those semi exclusive observables and all calculations agree reasonably well with the data. The calculated angular distributions, however, are still slightly too steep and under predict the data at backward angles.

Recently it has been shown from Kim et al., [21] that the technique of intensity interferometry can be applied to light fragments, in order to extract the time scale of the reaction. For this purpose they used a final state Coulomb interaction model based on the

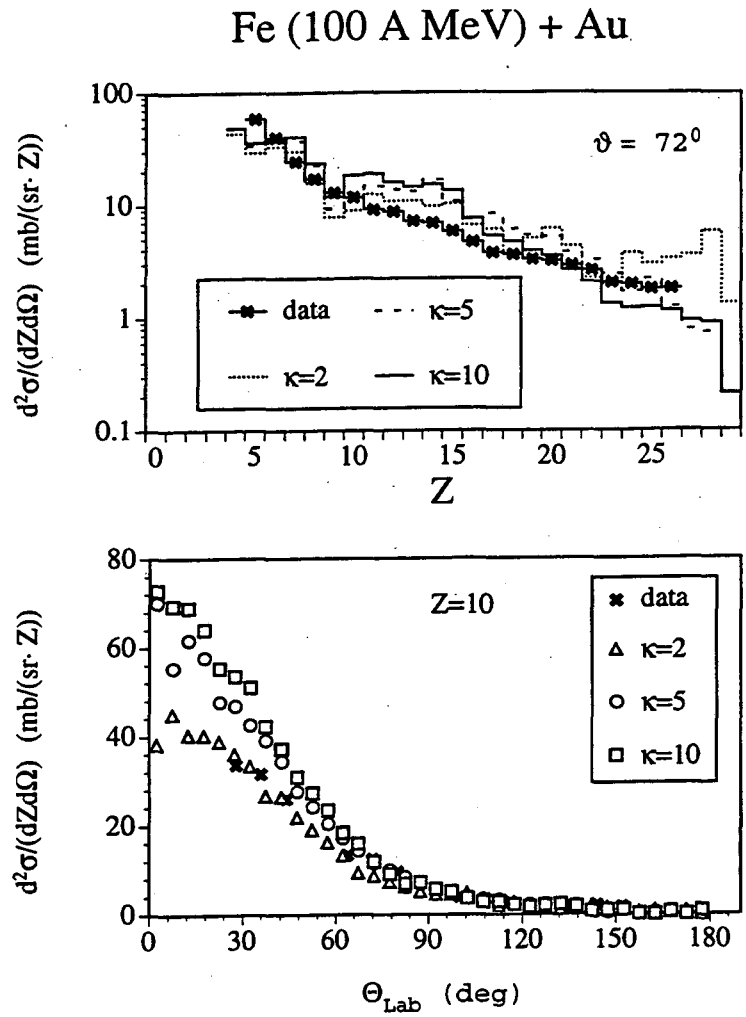

Figure 1:

Projections of the semi exclusive triple differential cross section $d^2\sigma/(dZd\Omega)$ for the reaction Fe (100 A MeV, b = 0 - 6 fm) + Au. The symbols show the data [24], for the charge distributions for fragments at $\vartheta_{Lab} = 72°$ (upper panel) and the angular distributions for fragments with $Z = 10$ (lower panel). The histograms show the calculations with the QMD+SMM model for different volume parameters κ as indicated.

Koonin–Pratt formalism [26]. This formalism is, however, restricted to the case, where the fragment-fragment correlation function is governed by the final state Coulomb interaction of the fragment pair under consideration only. Whether this assumption can hold in the case

where one has many (up to 10) fragments which may have been produced in a small volume at the same time, is at least questionable.

A different approach to extract the emission time scales has been used by Sangster et al. [22] and Lacey et al. [23]. They used a the classical three-body trajectory code *MENEKA* [27] that simulates an isotropic surface emission of IMFs from a spherical source characterized by a unique radius parameter with angular momenta chosen randomly from a triangular distribution. The emission energies are selected to reproduce the experimentally measured distributions and the distribution of time delays between fragment emission is given by a Gaussian. Those studies showed that the correlation data are consistent with a emission time between 50 and 500 fm/c [22] and that this time scale saturates with decreasing bombarding energy [23].

All the limitations that restrict the studies using the Koonin Pratt formalism or trajectory calculation do not apply to the QMD calculations. In this case the Hamilton equations of all nucleons are integrated, which implies, that correlations between all the existing nucleons and fragments are treated in all orders. This is especially important in the case when one deals not only with two IMF's, but with many. In the following we present the fragment-fragment correlation function for the reaction Fe (100 A MeV) + Au for central collisions (b = 0 - 6 fm) in comparison to the data of Ref. [24]. After the break-up of the hot target remnant within the SMM model (this takes place after 300 fm/c reaction time) we neglect the nuclear forces and follow the Coulomb trajectories of the charged particles. This propagation is stopped when the total Coulomb interaction is sufficiently small.

The reduced velocity correlation functions shown in figure 2 have been obtained by taking ratios between correlated IMFs in a single event divided by the same quantities where the quantity of interest was obtained from two IMFs taken from different physical events, thereby eliminating the final state correlations. In all cases the true ($Y_{true}(v_{red})$) and background distributions ($Y_{back}(v_{red})$) were developed separately for two classes of events: 1) two IMFs detected on opposite sides of the beam and 2) two IMFs detected on the same side of the beam. In the areas where these two correlations overlap in relative velocity it was found that the correlations obtained from the two acceptance ranges were effectively identical and so in this paper the results have in all cases been combined into single distributions. The

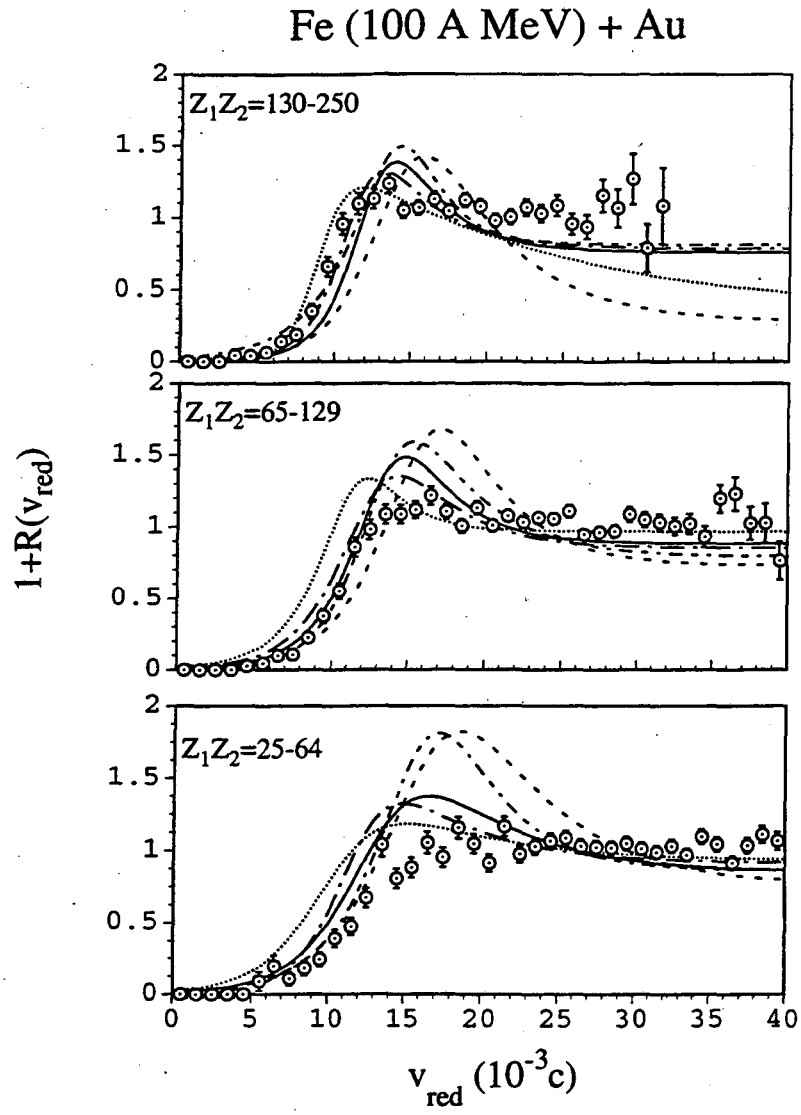

Figure 2:

Mixed fragment reduced velocity correlation functions for three different constraints on the Coulomb product $Z_1 \cdot Z_2$. The symbols show the data of ref. [22], while the curves are fits to equation 2 obtained with the QMD+SMM model. The different lines show calculations done with the volume parameter $\kappa = 1$ (dashed line), $\kappa = 2$ (variable length dashed line), $\kappa = 5$ (solid line), $\kappa = 10$ (dash–dotted line) and $\kappa = 15$ (dotted line),

two fragment correlation function is then calculated according to

$$1 + R(v_{red}) = \frac{Y_{true}(v_{red})}{Y_{back}(v_{red})}. \tag{1}$$

Note that there is no additional normalization factor in equation (1). If both the true yields and the background are normalized and there are no additional correlations (and only then) the correlation function approaches unity for large values of v_{red}.

Fig. 2 shows the experimental correlation function (symbols) for the three different charge product bins $Z_1 \cdot Z_2 = 25 - 64$, $65 - 129$ and $130 - 250$ (the smallest detected charge is Z=5 in all cases) compared to the calculated results (lines) for different volume parameters κ in the SMM model (note that $V = V_0(1 + \kappa)$). The theoretical curves show fits to the actual correlation functions using the fitting function

$$1 + R(v_{red}) = a\frac{1 + e^{\frac{d - v_{red}}{c}}}{1 + e^{\frac{b - v_{red}}{c}}}. \tag{2}$$

It can be seen that the size of the Coulomb hole can be explained within the QMD+SMM approach if a volume parameter between $\kappa = 2$ and 10 is used; both $\kappa = 1$ and $\kappa = 15$ clearly disagree with the data for the heavier fragments ($Z_1 \cdot Z_2 = 65-129$ and $130-250$). For the lightest fragments under consideration the smallest volume parameter seems to describe the data best, but here the sensitivity to the Freeze-Out volume is less pronounced. This may indicate that the fragments do not come from one Freeze-Out volume, but the smaller fragments are emitted earlier from a smaller volume.

This results are in good agreement with previous investigations of the same data using the sequential MENEKA model [22]. In this case a emission time in the order between 50 and 500 fm/c was found. These time scales are comparable to the typical time a fragment needs to traverse a Freeze-Out volume of roughly 5 times the nuclear volume.

Another feature that can be observed in the calculated correlation functions in figure 2 is the strongly pronounced peak at $v_{red} \approx 15 - 20$. This kind of additional correlation is absent in the present data and it is also not seen in the data of the MSU group [21], except for very peripheral collisions [28]. Our calculations show indeed that this effect is more pronounced for the more peripheral collisions and it also increases (see figure 2) with decreasing volume parameter in the SMM model (a similar behavior has recently been found in the Berlin model [29] when the excitation energy is decreased). This effect is due to an additional correlation in the fragment–fragment correlation function because of the Coulomb repulsion due to a heavy third body.

Acknowledgement:

This work was supported by the US Department of Energy by LLNL under Contract W-7405-ENG-48. One of us (G.P.) gratefully acknowledges support from the Wissenschaftsausschuss of the NATO via the DAAD and the Alexander von Humboldt Foundation.

References

[1] J.E. Finn et al., Phys. Rev. Lett. **49**, 1321 (1982).

[2] R.W. Minich et al., Phys. Lett. B**118**, 458 (1982).

[3] X. Campi, Phys. Lett. B**124**, 8 (1984) and J. Phys. A **19**, L917 (1986).

[4] D. Stauffer, Introduction to percolation theory, Taylor and Francis, London, 1985 and Phys. Rep. **54**, 1 (1979).

[5] X. Campi, Phys. Lett. B **208**, 351 (1988).

[6] Y. Yariv and Z. Fraenkel, Phys. Rev. C **20**, 2227 (1979) and Phys. Rev. C **24**, 488 (1981).

[7] K.K. Gudima and V.D. Tonnev, Yad. Fiz. **27**, 67 (1978) [Sov. J. Nucl. Phys. **27**, 67 (1978)].

[8] G. Peilert et al., Phys. Rev. C **39**, 1402 (1989); J. Aichelin et al., Phys. Rev. C **37**, 2451 (1988).

[9] G. Peilert et al., Phys. Rev. C **46**, 1457 (1992).

[10] J.J. Molitoris, H. Stöcker, and B.L. Winer, Phys. Rev. C **36**, 220 (1987); G. Bertsch and P.J. Siemens, Phys. Lett. B **126**, 9 (1983); C. Gregoire et al., Nucl. Phys. A **465**, 317 (1987).

[11] M. Blann, Phys. Rev. Lett. **54**, 2215 (1985) and Phys. Rev. C **32**, 1231 (1985); M. Blann, T. Komoto, and I. Tservaya, Phys. Rev. C **40**, 2498 (1989); M. Blann et al, Phys. Rev. C **44**, 431 (1991).

[12] R.J. Charity et al., Nucl. Phys. A **453**, 371 (1988); D.R. Bowman et al., ibid. A **523**, 386 (1991).

[13] W.A. Friedman, Phys. Rev. Lett. **60**, 2125 (1988).

[14] G. Fai and J. Randrup, Nucl. Phys. A **381**, 557 (1982) and Nucl. Phys. A **404**, 551 (1983).

[15] J.P. Bondorf et al., Nucl. Phys. A **443**, 321 (1985); J.P. Bondorf et al., Nucl. Phys. A **444**, 460 (1985).

[16] A.S. Botvina et al., Nucl. Phys. A **475**, 663 (1987); A.S. Botvina, A.S. Iljinov, and I.N. Mishustin, Nucl. Phys. A **507**, 649 (1990).

[17] D.H.E. Gross and X.Z Zhang, Phys. Lett. B**161**, 47 (1985); D.H.E. Gross, X.Z. Zhang, and S.Y. Xu, Phys. Rev. Lett. **56**, 1544 (1986); D.H.E. Gross, Rep. Prog. Phys. **53**, 605 (1990).

[18] D. Hahn and H. Stöcker, Nucl. Phys. A **476**, 718 (1988).

[19] B. Tsang et al., Phys. Rev. Lett. **71**, 1502 (1993).

[20] J. Hubele et al., Z. Phys. A **340**, 263 (1991); C.A. Ogilvie et al., Phys. Rev. Lett. **67**, 1214 (1991).

[21] Y.D. Kim et al., Phys. Rev. C **45**, 338 (1992); Y.D. Kim et al., Phys. Rev. C **45**, 387 (1992).

[22] T.C. Sangster et al., Prog. Part. Nucl. Phys. Vol. 30, 189 (1993) and Phys. Rev. C **47**, R2457 (1993) .

[23] R. Lacey et al., Phys. Rev. Lett. **24**, 3705 (1993).

[24] T.C. Sangster et al., Phys. Rev. C**46**, 1404 (1992).

[25] G. Peilert et al., Phys. Lett. B **260**, 271 (1991).

[26] S.E. Koonin, Phys. Lett. B**70**, 43 (1977); W.G. Gong et al., Phys. Rev. C43, 781 (1991).

[27] A. Elmaani et al., Nucl. Instrum. Methods A**313**, 401 (1992).

[28] D.R. Bowman et al., Phys. Rev. Lett. **23**, 3534 (1993).

[29] O. Schapiro, A.R. DeAngelis, and D. Gross, Preprint HMI 1993/P1-Schap 1.

Neutron squeeze-out observed in ^{197}Au + ^{197}Au collisions †

Y. Leifels, Th. Blaich, J. Keller and D. Lambrecht
for the **LAND**- and **FOPI**-collaborations
Univ. Bochum, IPNE Bucharest, CRIP Budapest, LPC Clermont-Ferrand, GSI Darmstadt, INFN Firenze, Univ. Frankfurt, Univ. Heidelberg, Univ. Cracow, Univ. Mainz, KIAE and ITEP Moscow, FZ Rossendorf, CRN Strasbourg, Univ. Warsaw, RBI Zagreb

Introduction

Collective flow of nuclear matter in relativistic heavy-ion collisions is one of the aspects presently under investigation at SIS. This phenomenon was predicted by hydrodynamical models [1] and was first observed in symmetric heavy-ion collisions of Au+Au and Nb+Nb in experiments at the Bevalac [2]. The predictions of the magnitude and behaviour of collective flow effects by microscopic model calculations depend on the parameterization of the nucleon-nucleon interaction. It is hoped that the comparison of the experimental data to the model calculations does restrict the parameter ranges, and thus yields information on the nucleon-nucleon interaction in hot and compressed nuclear matter. Until now most of the investigations on collective flow (e.g. sideward flow and squeeze-out of nuclear matter) have been performed with charged particles. The experimental information remains, however, incomplete as long as the flow of neutral matter is not detected. Hence, it is important to look at neutrons which contribute to a least half of the baryonic flow and do not feel the long-range Coulomb force.

One of our objectives is the study of collective flow properties of neutrons in comparison to light charged particles, protons in particular, to investigate the implications of the final state Coulomb interaction. The construction of a 4π-neutron detector for collective flow investigations with sufficient momentum and spatial resolution is not feasible. However, if the global observables (e.g. impact parameter and azimuthal angle of the reaction plane) are obtained from charged particles detected in 4π-geometry, the simultaneous measurement of neutrons by a dedicated detector with a limited solid angle yields the complete information on collective flow. The set-up realized at the GSI consists of the FOPI-spectrometer [3] and the Large Area Neutron Detector LAND [4]. The FOPI-spectrometer (Phase I) covers most of the forward hemisphere of the CM-system in symmetric collisions at energies above $\approx$ 150 MeV. LAND determines the momenta of neutrons and light charged particles in the mid- and target-rapidity region.

Data on the collective properties of neutrons has been reported earlier [5, 6]. However, charged particles were not investigated, and comparisons to other experiments are not straightforward. The attractive advantage of the set-up described above is the measurement of neutrons *and* light charged particles in the same detector and the same region of phase space: Spectra may be compared without further intra- or extrapolations or acceptance corrections.

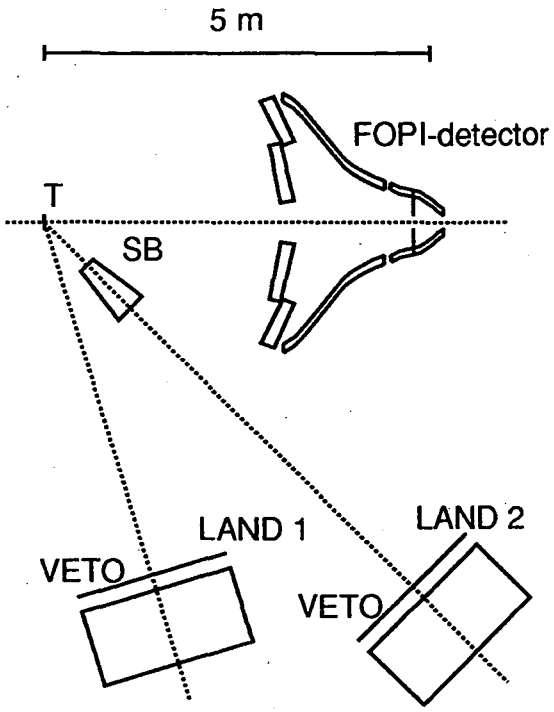

Figure 1: Experimental setup of the joint experiment of LAND and FOPI-spectrometer (Phase I). LAND was split into two halves, one positioned at 45°±8°, the other at 73°±12°. The FOPI- spectrometer allowed for charged particle measurements with full azimuthal angle coverage at $1° \leq \Theta_{lab} \leq 30°$. The shadow bar (SB) positioned in front of LAND 2 is an example for the setup during a shadow bar run.

Experimental setup and results

The experimental setup is depicted in fig. 1. Detailed descriptions of the two detector systems can be found in [3, 4]. Data were taken for the system ^{197}Au + ^{197}Au at 400, 600 and 800 MeV/u. Results of the data at 400 MeV/u have been published in [7]. The analysis at the other bombarding energies was performed likewise. Estimates for impact parameter and azimuth of the reaction plane of each event were determined from the charged particles measured in the FOPI-detector. (i) As a measure of the impact parameter the ratio of transverse to longitudinal energy in the cm-system is taken, $E_{rat} = E_{\perp}/E_{||}$, $E_{\perp}$ and $E_{||}$ are calculated by summing over all charged particles detected in each event, $E_{\perp,||} = \sum \frac{p^2_{\perp,||}}{2m}$ The data of E_{rat} are grouped into five equally spaced bins of 'energy ratio' denoted E1 through E5. E5 is indicating the highest ratio of transversal to longitudinal energy, i.e. the most central collisions. The identification of the E_{rat}-bins with impact parameter ranges is done via QMD-model calculations [8]. Representative results for E_{rat}-bins considered here are: E2 $\approx$ 7±3 fm, E3 $\approx$ 4±2 fm, E4 $\approx$ 2±1 fm, E5 $\approx$ 1.5±0.5 fm. (ii) The azimuth of the reaction plane φ_R is determined from the total transverse momentum of all charged particles detected in the forward hemisphere of the reaction. Neutrons and charged particles detected in LAND are not considered. Thus there is no problem of autocorrelation.

While performing neutron studies it is necessary to investigate the background originating from scattering of neutrons off all massive parts within the experimental area and

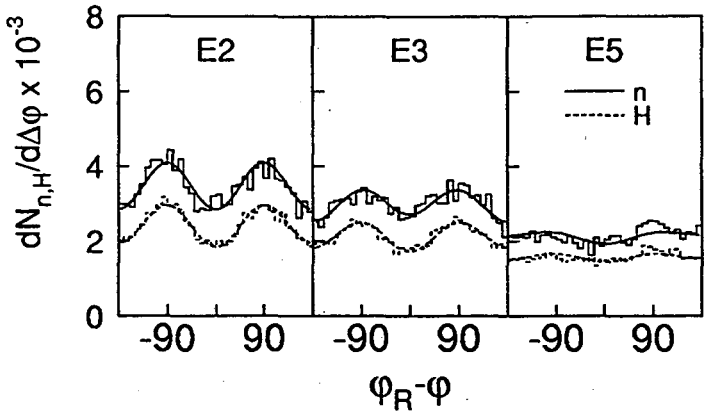

Figure 2: Azimuthal distributions of mid-rapidity neutrons (solid histogram) and hydrogen (dashed histogram) at 400 MeV/u for three different E_{rat}-bins. Lines are fits to the histograms with a sum of Legendre-polynomials up to second order.

off the concrete walls. For this purpose iron shadow bars were inserted between the target and each LAND separately, in such a way that the neutron detectors were shielded from particles coming directly from the target. During the analysis all spectra are accumulated three times, once for all runs without shadow bars and twice for runs with the shadow bars in place. To eliminate the background the latter spectra are subtracted. The integral background is found to be as large as 30-33 % for LAND 2 and 10-14 % for LAND 1 rising with beam energy. Also it is important to note that the background is event-correlated and not isotropic with respect to the reaction plane.

Squeeze-out of neutrons and hydrogen

The collective properties of neutrons and hydrogen nuclei are investigated by means of azimuthal distributions with respect to the reaction plane about the beam axis. Here we will concentrate on the squeeze-out of mid-rapidity particles perpendicular to the reaction plane ($0.4 \leq Y/Y_p \leq 0.6$, Y particle rapidity, Y_p projectile rapidity). The squeeze-out effect is depicted in fig. 2 for three different impact parameter ranges. The maxima of the count rate N at $\Delta\varphi = \varphi - \varphi_R = \pm 90°$ are due to the preferential emission perpendicular to the reaction plane. The anisotropy is very large at intermediate impact parameters, and diminishes with increasing centrality of the collision. At most central collisions the reaction zone expandd azimuthally symmetrically and no squeeze-out signal is observed.

The magnitude of the squeeze-out signal is expressed in terms of the ratio $R_{sqz} = (N(+90°) + N(-90°)) / (N(0°) + N(180°))$. Its value depends strongly on the transverse momentum $p_\perp$ of the particles as can be seen in fig. 3. At the highest transverse momenta the largest anisotropies are reached, larger than ever observed for baryons before. The LAND-acceptance is missing particles with small $p_\perp$. But hydrogen nuclei detected in the FOPI-spectrometer complete the picture of the $p_\perp$-dependence of the squeeze-out signal to lower values of transverse momenta. We do see a non-linear rise of the squeeze-out ratio with $p_\perp$. Neutrons show a similar behaviour as hydrogen, but — in general — with somewhat smaller magnitude of R_{sqz}. Due to the isotopic composition of the hydrogen nuclei their effective mass is significantly larger than one. Heavier fragments exhibit stronger

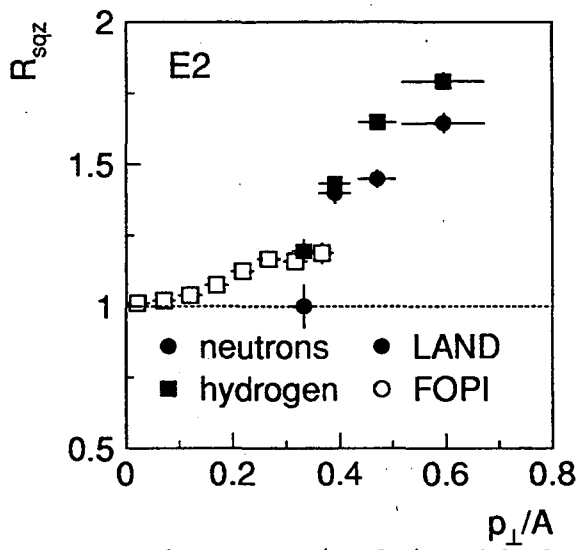

Figure 3: Squeeze-out ratio of neutrons (circles) and hydrogen nuclei(filled squares) detected in LAND as a function of transverse momentum $p_\perp$ at 400 MeV/u. For comparison and completeness data for hydrogen nuclei measured with FOPI (open squares) are also shown.

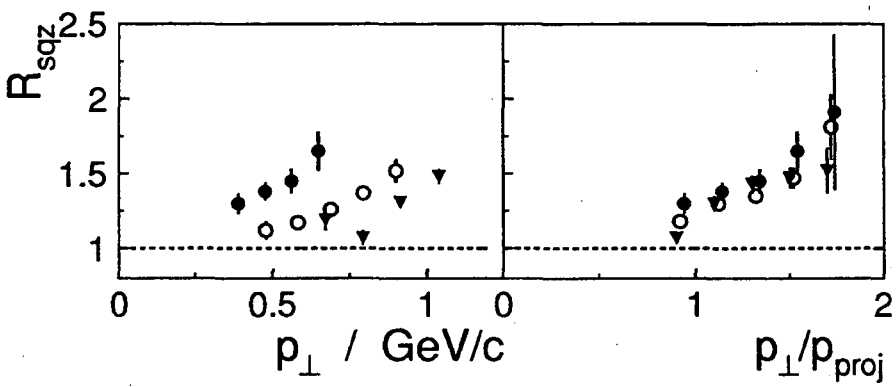

Figure 4: Squeeze-out ratio of neutrons as a function of $p_\perp$ (left panel) and $p_\perp/p_{proj}$ (right panel) for three different bombarding energies, 400 MeV/u (dots), 600 MeV/u (circles) and 800 MeV/u (triangles). The E2-cut was applied to select events of intermediate impact parameters.

flow effects [9], wherewith the discrepencies between neutron and hydrogen are explained qualitatively. By employing the calorimetric information of LAND it is possible to enrich protons in the data sample. There are no differences left between neutrons and protons selected in this manner.

With this evidence of neutrons and protons showing the same behaviour, we will restrict the following discussion to neutrons. The results for the bombarding energy dependence of the squeeze-out effect are summarized in fig. 4: In the left panel of fig. 4 one observes that the maximum values of the squeeze-out ratio R_{sqz} are the same at all beam energies. However, the maxima are reached at different transverse momenta. With increasing beam energy the squeeze-out signal shifts to higher values of $p_\perp$ and does not diminish as earlier investigations might imply [10]. By measuring the transverse momentum not in absolute

numbers but in fractions of the projectile momentum in the center-of-mass system p_{proj}, the data points for the different bombarding energies fall on top of each other as can be seen in the right panel of fig. 4. The observed scaling behaviour is most striking at intermediate impact parameters where the squeeze-out signal is largest. At more central collisions the signature gets less obvious.

Summary

We have presented detailed investigations on azimuthal distributions of mid-rapidity neutrons and hydrogen nuclei in the bombarding energy range of 400 MeV/u$\leq$ E_{proj} $\leq$800 MeV/u. It is observed that neutrons and protons — selected by employing the calorimetric characteristics of LAND — do show the same behaviour. This finding indicates that the final state Coulomb interaction — despite its long range — is of minor importance for the observables considered here. The squeeze-out effect depends strongly on the transverse momentum of the particles. With increasing bombarding energy the strength of the signal is shifted to higher values of $p_\perp$. Scaling of the transverse momenta with the projectile momentum in the cm-System leads to an universal curve. Such a behaviour is predicted by non-viscous hydrodynamical models [11]. The scaling observed here for particle squeeze-out *perpendicular* to the reaction plane is found also for directed sideward-flow of particles *in* the reaction plane [12].

† supported by German Federal Secretary for Research and Technology and by GSI

References

[1] W.Scheid et al., Phys. Rev. Lett. **32**, 741 (1974)

[2] H.Gustafsson et al., Phys. Rev. Lett **52**, 1590 (1984)

[3] A.Gobbi et al., Nucl. Instr. and Meth. **A324**, 156 (1993)

[4] Th.Blaich et al., Nucl. Instr. and Meth.

[5] J.Schambach et al., in: The Nuclear Equation of State, Proceedings of a NATO Advanced Study Institute, Peniscola 1989, Vol. 216B, edited by W.Greiner and H.Stöcker, part A, p. 115

[6] R.Madey et al., Proceedings of the International Nuclear Physics Conference, Wiesbaden 1992, Nucl. Phys. **A553**, 779c (1993)

[7] Y.Leifels et al., Phys. Rev. Lett. **71**, 963 (1993)

[8] J.Aichelin and H.Stöcker, Phys. Lett **B176**, 14 (1986)

[9] K.Doss et al., Phys. Rev. Lett. **57**, 302 (1986)

[10] H.Gutbrod et al., Phys. Rev. **C42**, 640 (1990) **A314**, 126 (1992)

[11] A.Bonasera et al., Nucl. Phys. **A476**, 159 (1988)

[12] D. Keane (1993), contribution to this proceedings

Members of LAND-collaboration

Th.Blaich[5], Th.W.Elze[4], H.Emling[3], H.Freiesleben[1,8], K.Grimm[4], W.Henning[3,7], R.Holzmann[3], J.G.Keller[1], H.Klingler[4], J.V.Kratz[5], R.Kulessa[2], D.Lambrecht[5], S.Lange[1], Y.Leifels[1], E.Lubkiewicz[2], E.F.Moore[3,6], W.Prokopowicz[2], R.Schmidt[3], C.Schütter[4], H.Spies[4], K.Stelzer[4], J.Stroth[3], E.Wajda[2], W.Waluś[2], M.Zinser[3], E.Zude[3]

(1) Institut für Experimentalphysik, Ruhr-Universität Bochum, 44801 Bochum, Germany
(2) Institute of Physics, Jagellonian University, PL-30-059 Cracow, Poland
(3) Gesellschaft für Schwerionenforschung, 64291 Darmstadt, Germany
(4) Institut für Kernphysik, Johann-Wolfgang-Goethe-Universität, 60325 Frankfurt, Germany
(5) Institut für Kernchemie, Johannes-Gutenberg-Universität, 55099 Mainz, Germany
(6) present address: Dept. of Physics, North Carolina State University, P.O.Box 8202, Raleigh, NC 27695-8202
(7) present address: Physics Division, Argonne National Laboratory, Argonne, IL 60439
(8) present address: Institut für Kern- und Teilchenphysik, Technische Universität Dresden, 01069 Dresden

Members of the FOPI-Collaboration

J.P.Alard[3], Z.Basrak[13], N.Bastid[3], I.M.Belayev[8], D.Best[7], M.Bini[5], Th.Blaich[7], R.Bock[4], A.Buta[1], R.Čaplar[13], C.Cerruti[11], N.Cindro[13], J.P.Coffin[11], M.Crouau[3], P.Dupieux[3], J.Erö[2], Z.G.Fan[4], P.Fintz[11], Z.Fodor[2], R.Freifelder[4], L.Fraysse[3], S.Frolov[8], M.Gnirs[6], A.Gobbi[4], G.Goebels[6], Y.Grigorian[9], G.Guillaume[11], E.Häfele[6], N.Herrmann[6], K.D.Hildenbrand[4], S.Hölbling[13], O.Houari[11], S.C.Jeong[4], M.Jorio[3], F.Jundt[11], J.Kecskemeti[2], P.Koncz[2], Y.Korchagin[8], R.Kotte[10], M.Krämer[4], C.Kuhn[11], I.Legrand[1], A.Lebedev[8], C.Maguire[11], V.Manko[9], T.Matulewicz[12], G.Mgebrishvili[9], J.Mösner[10], D.Moisa[1], G.Montarou[3], P.Morel[3], W.Neubert[10], A.Olmi[5], G.Pasquali[5], D.Pelte[6], M.Petrovici[1], C.Pinkenburg[4], G.Poggi[5], F.Rami[11], W.Reisdorf[4], A.Sadchikov[9], D.Schüll[4], Z.Seres[2], B.Sikora[12], V.Simion[1], S.Smolyankin[8], U.Sodan[4], N.Taccetti[5], K.Teh[4], R.Tezkratt[11], M.Trzaska[6], M.A.Vasiliev[9], P.Wagner[11], J.P.Wessels[4], T.Wienold[6], Z.Wilhelmi[12], D.Wohlfarth[10], A.V.Zhilin[8]

(1) Institute for Physics and Nuclear Engineering, Bucharest
(2) Central Research Institute for Physics, Budapest
(3) Laboratoire de Physique Corpusculaire, Clermont-Ferrand
(4) Gesellschaft für Schwerionenforschung, Darmstadt
(5) Università and INFN, Florence
(6) Physikalisches Institut der Universität Heidelberg, Heidelberg
(7) Universität Mainz, Mainz
(8) Institute for Experimental and Theoretical Physics, Moscow
(9) Kurchatov Institute for Atomic Energy, Moscow
(10) Zentralinstitut für Kernforschung, Rossendorf
(11) Centre de Recherches Nucléaires and Université Louis Pasteur, Strasbourg
(12) Institute of Experimental Physics, Warsaw University, Warsaw
(13) Rudjer Boskovic Institute, Zagreb

Azimuthal Asymmetry of Neutral Pion Emission in Au+Au Reactions at 1 GeV/u

H. Löhner, A.E. Raschke, R.H. Siemssen, M. Sumbera,
L.B. Venema and H.W. Wilschut
Kernfysisch Versneller Instituut (KVI), Groningen, The Netherlands
for the TAPS collaboration
GANIL - Gießen - GSI - KVI - Münster

Abstract

The azimuthal angle distributions of neutral pions at midrapidity from Au+Au reactions at 1 GeV/u incident energy have been measured. An enhanced emission of π^0 perpendicular to the reaction plane is observed. The azimuthal asymmetry is dependent on the π^0 momentum. The integrated yield of π^0 emission in-the-reaction-plane is suppressed by 10% with respect to the out-of-plane yield. This fact suggests that the main reason for the observed azimuthal asymmetry is the enhanced absorption of fast pions in the reaction plane by the spectator matter.

The production probability of mesons in the course of a relativistic heavy ion collision and their observed momentum distribution allow to derive the degree of thermal excitation in the collision zone [1]. The collective motion of nucleons from the collision zone is influenced by repulsive forces among the interacting nucleons or, in a hydrodynamic model description, by the compressional energy [2]. Recently a new component of the collective flow, the out-of-reaction-plane *"squeeze-out"* of charged baryons, was discovered experimentally [3]. QMD calculations [4] reproduce these observations and show a dependence of the collective emission pattern on the equation of state of nuclear matter.

We present here the observation of enhanced π^0 emission perpendicular to the reaction plane in the Au+Au reaction at 1 GeV/u [5]. A Au-target (0.188 g/cm^2) of 0.1 mm thickness was bombarded with a Au-beam extracted from the SIS accelerator of GSI with a kinetic energy of 1 GeV/u. The intensity was kept near 10^6 particles per spill, with a spill duration of 4 s, and a repetition rate of 9 s. Photons from the π^0 decay (branching ratio 98.8% for two photon decay) were detected in the Two Arm Photon Spectrometer (TAPS) [6]. Charged particles emitted in the forward direction were detected in the Forward Wall of the FoPi-collaboration [7] and used for the event characterization.

In this experiment the TAPS detector system consisted of 256 BaF_2 detectors arranged in 4 blocks with individual Charged Particle Veto detectors (CPV) in front of each module. The Forward Wall is a plastic scintillator wall covering the polar angular range from 1° to 30°. It consists of two parts, the Outer Plastic Wall (OPW) and a zero-degree detector. Only the OPW was used in the present analysis covering the angular range from 7° to 30°. The 512 bars are grouped into 8 sectors, each sector spanning 45° in azimuthal angle.

The π^0-mesons are identified through the invariant mass analysis of all photon pairs detected by TAPS, using the relation $m_{\gamma\gamma} = \sqrt{2E_1E_2(1-\cos\Theta_{12})}$ where E_1 and E_2 are the photon energies and Θ_{12} is the opening angle of the photon pair. The resolution (FWHM / peak position) of the π^0 mass-peak is 17%.

The transverse momentum spectrum of π^0-mesons emitted in the rapidity interval $-0.15 \leq y_{cm} \leq 0.15$ in the reaction Au+Au at 1 GeV/nucleon is measured up to 1.2 GeV/c in transverse momen-

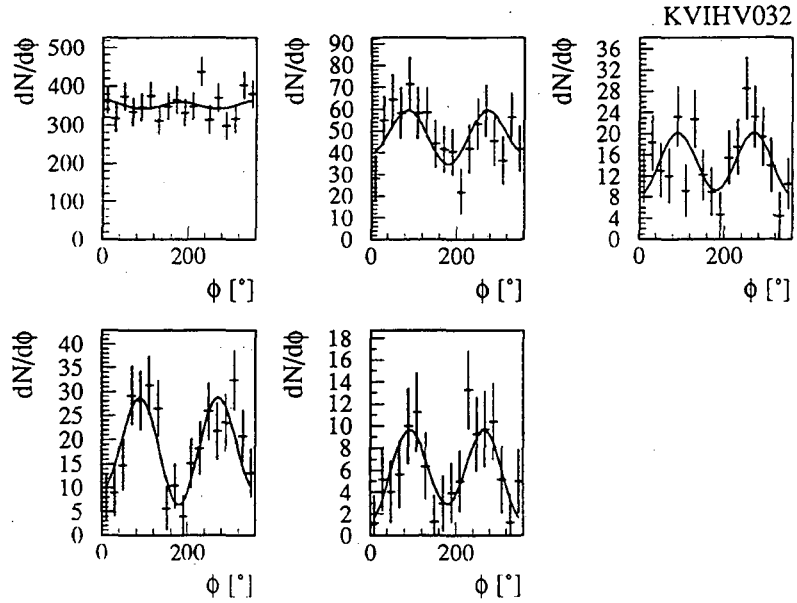

Figure 1: Azimuthal angle (ϕ) distributions of π^0 from Au+Au collisions at 1 GeV/u for increasing transverse momentum (from top left to bottom right) in equal bins of 200 MeV/c from 0 to 1000 MeV/c. The solid curves represent fits according to eq. (3).

tum. A fit with a single-slope thermal distribution at midrapidity according to

$$\frac{dN}{dp_T} \sim p_T m_T \exp\left(-\frac{m_T}{\mathcal{T}}\right), \tag{1}$$

with $m_T = \sqrt{m_{\pi^0}^2 + p_T^2}$ results in a slope parameter $\mathcal{T} = 64 \pm .7$ MeV. The fit quality demonstrates the inconsistency of the experimental data with a thermal distribution. Our data confirm earlier observations [8, 9] of a concave spectrum shape. A more satisfactory 2-slope parametrization results in $\mathcal{T}$ parameters $\mathcal{T}_1 = 50 \pm 4$ MeV and $\mathcal{T}_2 = 86 \pm 7$ MeV.

The orientation of the reaction plane was determined by performing a modified transverse momentum analysis [10]. Each of the 8 sectors of the OPW was represented by its unit-vector $\hat{\mathbf{u}}_i$ pointing to the center of a sector. The vectors $\hat{\mathbf{u}}_i$ were taken orthogonal to the beam axis. Since the coverage of the forward wall excludes the majority of particles with $y < y_{c.m.}$, the *plane vector* $\vec{Q}$ can be approximated by

$$\vec{Q} \approx \sum_{sectors} \hat{\mathbf{u}}_i \mathcal{M}_i. \tag{2}$$

$\mathcal{M}_i$ is the multiplicity measured in sector i of the OPW and $\sum_{sectors} \mathcal{M}_i \geq 30$ (25% of max. OPW multiplicity) was demanded in order to remove peripheral reactions. $\vec{Q}$ can only define the reaction plane if the flow is sufficiently pronounced. Therefore, a gate with $||\vec{Q}|| \geq 4$ was applied. In order to determine particle emission patterns, the reaction plane of each event was rotated so that the x-axis coincided with $\vec{Q}$. Auto-correlations [10, 11] are absent because the OPW determines the reaction plane independently of the measurement in TAPS. The angular coverages of the OPW and TAPS were mutually exclusive.

Table 1: Strength parameters of eq. (3) for the distribution of emission angles of π^0 with respect to the reaction plane for two gates on $\|\vec{Q}\|$. Results are presented for different π^0 transverse momenta near midrapidity ($|y_{c.m.} - y| \leq 0.15$).

p_T	$\|\vec{Q}\| \geq 4$			$\|\vec{Q}\| \geq 0$		
(MeV/c)	S_1	S_2	R	S_1	S_2	R
0– 200	0.01±0.04	0.03±0.03	0.9±0.1	0.02±0.03	0.03±0.03	0.9±0.1
200– 400	0.05±0.08	-0.23±0.08	1.6±0.3	0.07±0.07	-0.19±0.10	1.5±0.3
400– 600	-0.03±0.13	-0.39±0.13	2.3±0.7	0.02±0.11	-0.41±0.11	2.4±0.6
600– 800	0.09±0.09	-0.56±0.11	3.5±1.1	0.08±0.09	-0.49±0.08	3.5±1.1
800–1000	-0.13±0.15	-0.64±0.16	4.6±2.5	-0.12±0.15	-0.54±0.15	3.3±1.4

The accuracy of the reaction plane determination was estimated in the following way. Each event was divided into two parts by randomly assigning each particle hit in the OPW to one of two subsets. From the difference between the reaction plane azimuths for these two subsets we deduce a resolution (σ) of 27°.

The acceptance of TAPS for neutral pions covers a narrow window around midrapidity $|y_{c.m.} - y| \leq 0.15$ and is independent of the energy of the π^0. Figure 1 shows the azimuthal distribution of π^0 relative to the reaction plane for different cuts in transverse momentum. A parametrization according to

$$f(\phi) = N(1 + S_1 \cos(\phi) + S_2 \cos(2\phi)). \tag{3}$$

is shown with parameter values listed in table 1.

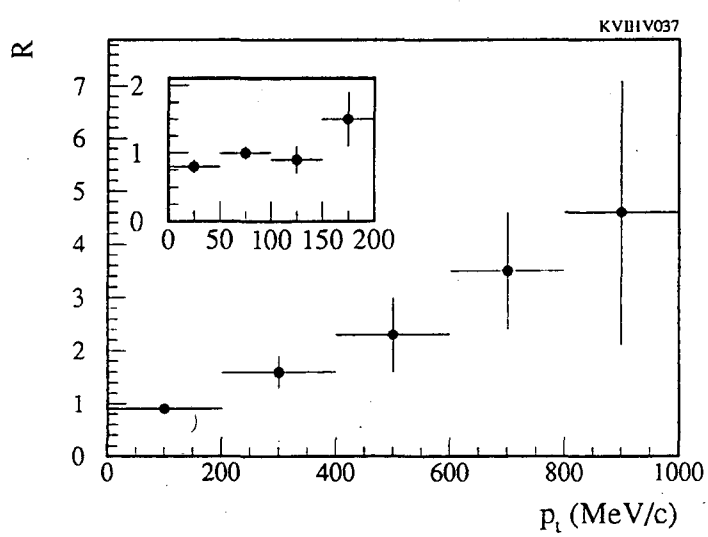

Figure 2: The "squeeze-out" ratio R versus transverse momentum p_t for neutral pions. The inset shows the region below 200 MeV/c in more detail.

The $\cos(\phi)$ term is sensitive to the yield *within* the reaction plane. The parameter S_1 is a measure of the strength of the collective particle flow. The parameter S_2 reflects the out-of-the-reaction-plane emission and is a measure of the strength of the so-called "squeeze-out" effect

observed earlier for baryons. From studies of the azimuthal symmetry of the forward wall response we conclude a residual systematic uncertainty in S_2 of 0.03. In the following, the azimuthally asymmetric emission of pions will be called squeeze-out irrespective of its physical origin.

The squeeze-out ratio R is defined as

$$R = \frac{\frac{dN}{d\phi}(90°) + \frac{dN}{d\phi}(270°)}{\frac{dN}{d\phi}(0°) + \frac{dN}{d\phi}(180°)} = \frac{1 - S_2}{1 + S_2}. \tag{4}$$

We observe a gradual increase in the squeeze-out ratio R with increasing transverse momentum as shown in figure 2. The yield of high energy pions as compared to low energy pions is strongly reduced when emitted in the reaction plane. R decreases when we relax the condition $||\vec{Q}|| \geq 4$ to $||\vec{Q}|| \geq 0$ (see table 1). This effect is expected due to isotropic emission which is associated with small $||\vec{Q}||$. Recently the KaoS collaboration reported [12] squeeze-out for π^+ in the same reaction as studied here. They observe a dependence on transverse momentum which is not as strongly pronounced. This may indicate the importance of the rapidity window which is $y \approx y_{c.m.}$ in our case versus $y \approx y_{c.m.} + 0.2$ in [12].

Figure 3 shows the transverse momentum spectra of the π^0-mesons gated on two regions in azimuth: the first (I, in the reaction plane, open circles) given by $\phi = 0° \pm 45°$ and $\phi = 180° \pm 45°$ and the other (II, out of the reaction plane, closed circles) by $\phi = 90° \pm 45°$ and $\phi = 270° \pm 45°$.

The spectrum of the π^0-mesons emitted perpendicular to the reaction plane is much harder than the in-plane π^0 spectrum, as is indicated by the average transverse momentum: $< p_T >_I = 168 \pm 5$ MeV/c, and $< p_T >_{II} = 188 \pm 5$ MeV/c. These spectra have been compared to a thermal distribution at midrapidity according to equation 1. Resulting $\mathcal{T}$ parameters show significant differences: $\mathcal{T}_I = 58 \pm 1$ MeV and $\mathcal{T}_{II} = 67 \pm 1$ MeV. Equation 1 can only provide a rough description of the momentum distributions since in general a concave shape of the spectra is observed.

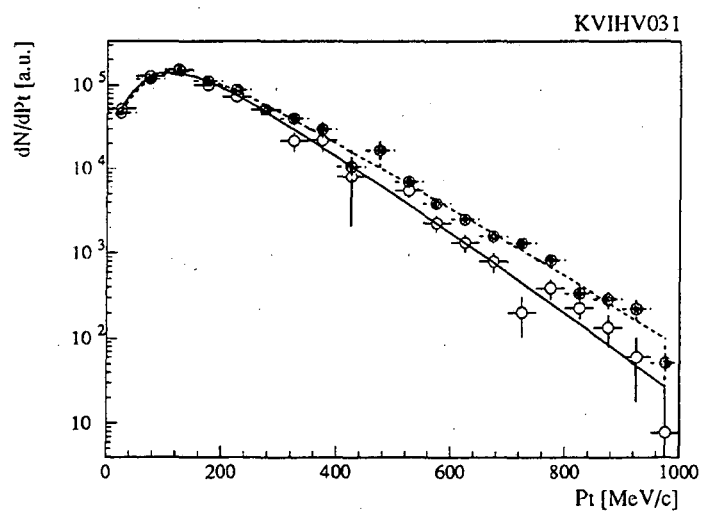

Figure 3: Transverse momentum spectra of π^0-mesons emitted parallel to the reaction plane (I, open circles) and perpendicular to the reaction plane (II, closed circles), respectively. The curves represent a fit according to eq. (1).

The integrated yield of π^0 emission in-the-reaction-plane is suppressed by $(9\pm5)\%$ with respect to the out-of-plane yield. This fact suggests that the main reason for the observed azimuthal asymmetry is the enhanced absorption of fast pions in the reaction plane by the spectator matter.

Recent results from IQMD calculations [13] and from a hadronic transport model based on the BUU equation [14] show an enhanced out-of-plane emission of π^0 with $R \approx 1.2 - 1.4$ for minimum bias data and $p_T > 400$ MeV/c. In those calculations explicit tests are made to identify the cause of the azimuthal asymmetry in pion emission. The absorption ($\pi NN \rightarrow \Delta N \rightarrow NN$) channel and scattering channel ($\pi N \rightarrow \Delta \rightarrow \pi N$) were disabled independently of each other. The authors conclude that the shadowing effect of the spectator through both pion reabsorption and rescattering is responsible for the observed anisotropy.

We conclude that a squeeze-out effect for neutral pions has been observed in Au + Au collisions at 1 GeV/u. A determination of the reaction plane was achieved with a resolution of 27°. The π^0 momentum spectrum observed perpendicular to the reaction plane appears to be harder than the spectrum in the reaction plane. The selection of meson spectra with respect to the orientation of the reaction plane allows to study the Δ interaction in nuclear matter and provides a test case for the correct treatment of the π and Δ dynamics in dynamical microscopic models.

This work was supported in part by GSI, BMFT, IN2P3 and FOM.

References

[1] R. Stock, Phys. Rep. **135**, 259 (1986).

[2] W. Scheid, H. Müller, and W. Greiner, Phys. Rev. Lett. **32**, 741 (1974).

[3] H.H. Gutbrod *et al.*, Phys. Lett. **216B**, 267 (1989).

[4] Ch. Hartnack *et al.*, Nucl. Phys. **A538**, 53c (1992).

[5] L.B. Venema *et al.*, TAPS collaboration, Phys. Rev. Lett. **71**, 835 (1993).

[6] R. Novotny *et al.*, IEEE Trans. on Nucl. Sc. **38**, 379 (1991).

[7] A. Gobbi *et al.*, Nucl. Instr. Meth. **A324**, 156 (1993).

[8] R. Brockmann *et al.*, Phys. Rev. Lett. **53**, 2012 (1984).

[9] G. Odyniec *et al.*, LBL report 24580 (1988).

[10] P. Danielewicz and G. Odyniec, Phys. Lett. **157B**, 146 (1985).

[11] K.G.R. Doss *et al.*, Phys. Rev. Lett. **57**, 302 (1986).

[12] P. Senger *et al.*, KaoS collaboration, Prog. Part. Nucl. Phys. **30**, 115 (1993);
D. Brill et al., Phys. Rev. Lett. **71**, 336 (1993).

[13] S.A. Bass, C. Hartnack, H. Stöcker, and W. Greiner, Phys. Rev. Lett. **71**, 1144 (1993).

[14] Bao-An Li, Phys. Lett. **319B**, 412 (1993).

PION PRODUCTION AND ABSORPTION IN RELATIVISTIC NUCLEUS-NUCLEUS COLLISIONS

P.Senger[1] and the KaoS Collaboration

[1]GSI Planckstr.1, 64291 Darmstadt, Germany

Probing nuclear reaction dynamics with pions

In a relativistic nucleus-nucleus collision the projectile kinetic energy is not only converted into thermal and compressional energy of the nucleonic system, but also into internal excitation energy of the nucleons. At bombarding energies around 1 GeV/nucleon a substantial amount of baryonic resonances is produced which decay predominantly into pions. Thus the pion multiplicity, momentum and angular distributions provide information on the space time dynamics of the nuclear reaction system [1].

Pioneering experiments on pion production in nuclear collisions have been performed at the Bevalac at LBL. Inclusive pion production cross sections have been measured with a magnetic spectrometer at different bombarding energies and projectile/target combinations [2]. A scaling behaviour of the inclusive pion cross section $\sigma^{incl} \propto A^{5/3}$ has been found for A+A collisions with $A \leq 40$. Exclusive experiments with a streamer chamber have found the pion multiplicity to increase linearly with the number of participant nucleons [3]. Attempts have been made to determine the nuclear matter equation-of-state using the pion multiplicity as a measure of the thermal energy of the hot and dense nucleonic system [4].

The sensitivity of the measured pion multiplicity on nuclear matter properties might be reduced considerably by final state interactions of pions or delta resonances. According to the isobar model pions are produced, scattered inelastically and absorbed via an intermediate delta resonance:

$$NN \rightleftharpoons \Delta N \rightleftharpoons NN\pi$$

In the dense reaction zone, where the mean free path of the baryons is small and the time between two collisions is short compared to the delta life time, the produced delta will be scattered and might be reabsorbed. When the nuclear system starts to expand and the density decreases, the delta will decay into a nucleon and a pion. Pion absorption, which is a two step process, will

be reduced from now on and further pion-nucleon interactions will modify the pion momentum and emission angle only. However, in contrast to the expanding participant zone the spectators still have saturation density and hence are less transparent for pions. The crucial question is, whether the pion yield is a measure of the 'primordial' delta abundancy. In particular, it would be interesting to know how the existence of cold spectator matter affects the pion multiplicity and distributions in configuration and momentum space.

There is experimental evidence for pion absorption effects in relativistic nuclear collisions. The $A^{5/3}$ scaling found for light symmetric collision systems at 800 MeV/nucleon overpredicts the pion yield measured in ^{139}La+^{139}La collisions at the same energy by a factor of about 2 [5]. This effect was discussed as possibly due to pion absorption by the heavy spectator fragments in peripheral and semicentral collisions. A more direct absorption effect due to spectator matter was found in pion angular distributions measured in asymmetric ^{20}Ne+^{208}Pb collisions at 800 MeV/nucleon [6]. The preferential emission of charged pions away from the interaction zone towards the projectile side was attributed to shadowing by the heavy target spectator.

In this paper we report on experiments which try to measure the 'primordial' delta or pion abundancy. The idea is to compare the pion yields measured in a heavy and a light system: in the first case pion final-state interactions should happen much more frequently than in the second case. Both inclusive pion cross sections and pion multiplicities per participant nucleon are measured. In addition we study the pion emission pattern with respect to the reaction plane to sort out pions which are less affected by absorption and rescattering even in a heavy collision system.

The experiment

The experiments were performed with the magnetic Kaon Spectrometer (KaoS) at the heavy ion synchrotron SIS at GSI [7]. KaoS is a compact Quadrupole-Dipole combination to minimize meson decay in flight with a large acceptance in solid angle ($\Omega \approx$30 msr) and momentum ($p_{max}/p_{min} \approx$2 up to p_{max}=1.8 GeV/c). The time-of-flight stop detector is positioned along the focal plane of the spectrograph. This arrangement allows for a very fast mass selective trigger. A row of water and lucite Cherenkov detectors behind the focal plane improves the proton suppression. Two large-area multi-wire chambers are used for trajectory reconstruction. The spectrometer and its detector system are optimized for the detection of rare reaction products (i.e. K-mesons) in a large background

of other charged particles. It can be used therefore to measure very selectively high energy pions which have very low cross sections. In this case the relatively small angular acceptance as compared to a 4π detector is overcompensated by a high beam luminosity. Information on collision centrality, number of participants and on the reaction plane are extracted from the particles detected by two plastic scintillator arrays positioned downstream the target [7].

We investigated the collision systems ^{197}Au+^{197}Au and ^{20}Ne+NaF at a beam energy of 1.0 GeV/nucleon and ^{209}Bi+^{208}Pb at 0.8 GeV/nucleon. Double differential cross sections $d^2\sigma/dpd\Omega$ for protons and pions have been measured within a polar angular range of $40° < \Theta_{lab} < 48°$. Inclusive cross sections are determined by integrating the measured double differential cross sections $d^2\sigma/dpd\Omega$ over momentum and solid angle assuming an isotropic emission in the N-N center-of-mass system.

Results and discussion

The effect of pion absorption in symmetric collision systems is demonstrated in Fig.1 showing the total pion multiplicity per nucleon M_π/A as a function or the nuclear mass A. The pion multiplicity is given by $M_\pi = \sigma_\pi^{incl}/\sigma_{geo}$. The total inclusive pion cross section σ_π^{incl} is calculated from the measured π^+ cross section by the isobar model whereas the reaction cross section is assumed to be the geometrical cross section $\sigma_{geo} = 4\pi r_o^2 A^{2/3}$ with r_o=1.2 fm for a symmetric collision system. In Fig.1 our pion data (squares: 1 GeV/nucleon, triangle: 0.8 GeV/nucleon) are compared with the results of Hayashi et al. (circles: 0.8 GeV/nucleon) [5]. The latter data are derived from π^- cross sections via the isobar model and take into account the measured angular distribution.

A constant value of M_π/A for all A corresponds to the $A^{5/3}$ dependence of the inclusive pion cross section mentioned above. The decrease of M_π/A with increasing number of nucleons for the same bombarding energy is a clear signature of pion absorption in systems with large A. The pion multiplicity per nucleon is reduced by a factor of 2 when going from light to heavy collision systems. This factor is not affected significantly by assumptions on the pion emission pattern as it cancels out in first order. Considering a measured forward-backward peaked pion angular distribution [1] all our data in Fig.1 have to be multiplied by a factor of 1.3. For the heavy systems the anisotropic contribution might be smaller due to the increased pion final state interaction. This would even enhance the factor of 2 quoted above.

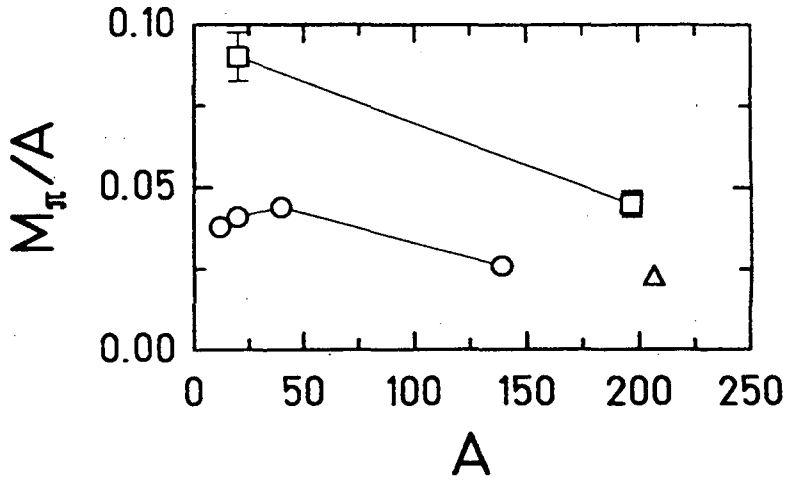

Fig.1: *Pion multiplicity per nucleon M_π/A as a function of mass A for A + A collisions. Squares: 1 GeV/nucleon (KaoS); triangle: 0.8 GeV/nucleon (KaoS); circles: 0.8 GeV/nucleon (ref. [5]).*

A more exclusive way to study pion production and absorption is to look at pion multiplicities as a function of 'participating' nucleons A_{part} rather than A. Fig.2 shows M_π/A_{part} versus A_{part} for Ne+NaF (left) and Au+Au collisions (right) at 1.0 GeV/nucleon. The pion multiplicity per participant nucleon is determined in the following way: we divide the inclusive cross sections into three groups according to M_c, which is the charged particle multiplicity at midrapidity and thus a measure of the collision centrality. The π multiplicity per participant nucleon is given by

$$\frac{M_\pi(M_c)}{A_{part}(M_c)} = \frac{d\sigma_\pi^{incl}(M_c)}{d\sigma_p^{incl}(M_c) \times A/Z \times f_{coal}} \tag{1}$$

with A/Z the nuclei mass to charge ratio. The coalescence factor f_{coal} is the ratio of the total nuclear charge bound in participants to the total participant proton charge which is approximately 1.7 for Au+Au and 1.3 for Ne+NaF [8,2]. The accuracy of f_{coal} is about 15 %. The participating proton cross section $\sigma_p^{incl}(M_c)$ is determined from the high energy protons measured at midrapidity with the spectrometer by integration over momentum and angle. The extrapolations assume a Maxwell-Boltzmann distribution fit to the high energy tail and isotropic emission in the center-of-mass frame. The number of participating nucleons shown in the abscissa of Fig.2 is calculated by

$$A_{part}(M_c) \;=\; 2 \times A/Z \times (Z - Z_{sum}(M_c)) \tag{2}$$

with $Z_{sum}(M_c)$ the summed 'spectator' charge determined from the measured projectile fragments

[7]. Fig.2 demonstrates, that the pion multiplicity for Au+Au and for Ne+NaF collisions at 1 GeV/nucleon depends linearly on the number of participating nucleons. However, the pion multiplicity per participant in the heavy system is about a factor of 2 smaller than in the light system. A very peripheral Au+Au collision and a central Ne+NaF collision involve about the same number of participants, but differ largely in spectator nucleons. Therefore, the observed reduction in pion yield in the heavy system must be due to absorption in spectator matter. About 50% of the produced pions are reabsorbed in the Au+Au system, when assuming the 'primordial' abundancy per participant determined by the Ne+NaF data. This result is in agreement with microscopic transport calculations, which find the ratio of the pion yield with and without absorption in Au+Au collisions at 1 GeV/nucleon to be 0.42 - 0.61 depending on the low momentum cutoff of the pions [9].

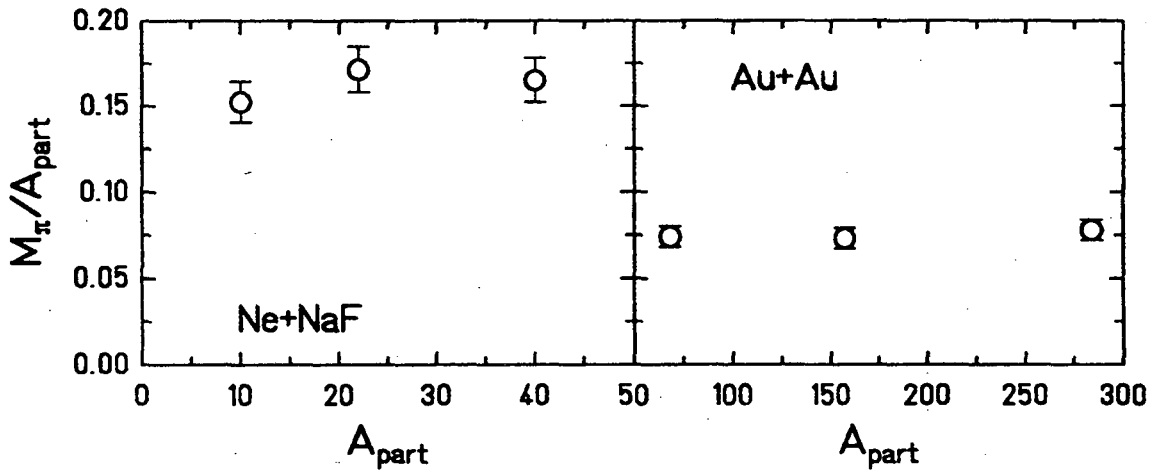

Fig.2: *Pion multiplicity per participating nucleon as a function of participating nucleons for Ne+NaF (left) and Au+Au (right) collisions at 1.0 GeV/nucleon.*

On the other hand it is interesting to note that the change in spectator size when going from a peripheral to a central Au+Au collision obviously does not influence the pion multiplicity per participant. This effect might be due to the fact that the pion yield is dominated by low energy pions ($\approx$ 150 MeV kinetic energy) strongly interacting with the surrounding nucleons via the Δ resonance [10]. The mean free path of these pions ($\approx$ 1 fm) is small compared to the size of the reaction volume. This volume, which is responsible for the absorption of low energy pions, includes not only 'participant' nucleons as defined above, but also many 'spectator' nucleons close to the reaction zone.

When investigating the collision geometry in more detail and looking at the azimuthal pion emission pattern, we found a preferential pion emission out of the reaction plane [11]. This effect is more pronounced for high energy pions which have much longer mean free path ($\approx$ 5 fm). These pions escape more likely from the reaction zone and then may interact with the the bulk of spectator nucleons depending on their azimuthal emission angle [9,12]. However, the high energy pions emitted perpendicular to the event plane are little affected by absorption and hence may provide a window to look into the hot and dense collision zone.

The KaoS Collaboration:

W. Ahner[1], P. Baltes[2], R. Barth[1], D. Brill[2], M. Cieślak[1], M. Debowski[1], E. Grosse[1], P. Koczoń[1], B. Kohlmeyer[4], D. Miśkowiec[1], Ch. Müntz[2], H. Oeschler[2], H. Pöppl[4], F. Pühlhofer[4], R. Schicker[1], E. Schwab[1], P. Senger[1], Y. Shin[3], J. Speer[4], R. Stock[3], H. Ströbele[3], Ch. Sturm[2], K. Völkel[4], A. Wagner[2], W. Waluś[5]

[1]GSI Darmstadt, [2]TH Darmstadt, [3]Universität Frankfurt, [4]Universität Marburg (Germany), [5]University Kraków (Poland).

References

[1] R.Stock, Phys.Rep. 135, 259 (1986)

[2] S.Nagamiya et al., Phys.Rev.C 24 971 (1981)

[3] J.W.Harris et al., Phys.Rev.Lett. 58 (1987) 463

[4] J.W.Harris et al., Phys.Lett. B153, 377 (1985)

[5] S.Hayashi et al., Phys.Rev.C 38, 1229 (1988)

[6] J.Gosset et al., Phys.Rev.Lett. 62, 1251 (1989)

[7] P.Senger et al. Nucl. Instr. Meth. A 327 (1993) 393

[8] H.Pöppl, PhD Thesis, Univ. Marburg 1993

[9] Bao-an Li, see these proceedings and Phys.Lett. B (1993) to appear

[10] Ch.Müntz et al., see these proceedings

[11] D.Brill et al., Phys.Rev.Lett. 71, 336 (1993)

[12] S.A.Bass et al., Phys.Rev.Lett. 71, 1144 (1993) and these proceedings.

MULTIFRAGMENTATION OF GOLD BY 1-AND 3.6 GEV/A HELIUM

E. NORBECK[a], W. BAUER[b], V. LIPS[c], R. BARTH[c], H. OESCHLER[c], S.P. AVDEYEV[d], V.A. KARNAUKHOV[d], W.D. KUZNETSOV[d], L.A. PETROV[d], O.V. BOCHKAREV[e], L.V. CHULKOV[e], E.A. KUZMIN[e], W. KARCZ[f], W. NEUBERT[g]

[a] *University of Iowa, Iowa City, IA 52242, USA*
[b] *Michigan State University, E. Lansing, MI 48824, USA*
[c] *Institut für Kernphysik, Technische Hochschule Darmstadt, 64289 Darmstadt, Germany*
[d] *Joint Inst. for Nucl. Research, Dubna, Head Post Office, P.O.Box 79, Moscow, Russia*
[e] *Kurchatov Institute, P.O.Box 123182, Moscow, Russia*
[f] *Henryk Niewodniczanski Institute of Nuclear Physics, 31-342 Cracow, Poland*
[g] *Inst. für Kern- und Hadronenph. Forschungsz. Rossendorf, 01314 Dresden, Germany*

Multifragmentation of the system α + ^{197}Au has been studied at incident energies of 1 and 3.6 GeV/nucleon with the new 4π array, "FASA". Mass, energy and velocity of a few fragments are measured with high precision using time-of-flight telescopes, while for the other fragments, global multiplicity information is obtained from 55 thin CsI(Tl) detectors. Very high mean IMF (intermediate mass fragment) multiplicities of $\langle M \rangle_{IMF} = 5.1 \pm 0.8$ are observed at the higher incident energy, 40% more than at the lower energy. BUU calculations indicate that the higher incident energy is close to the optimum for high energy deposition. The calculations show that, for central collisions, the projectile goes about 2/3 of the way through the gold. The nucleus stays intact as a bubble forms in the center where the maximum energy is deposited. The experiments were performed at the synchrophasotron (an accelerator similar to the Bevatron) at the JINR in Dubna, Russia.

Hot nuclear systems formed by the interaction of two heavy nuclei break up into fragments from three different sources. There are fragments from the beam, fragments from the target, and fragments from the interaction zone. There is no such mixture of different sources for the reaction α + ^{197}Au. All of the detected fragments are emitted from the target. There are additional advantages to heating the nuclear system by α particles. The low center-of mass velocity allows high-precision measurement of the relative velocities and the relative angular correlations from which the geometry and the time scale of the decay process can be deduced [1]. Because dynamical effects are small and the compression of the target nucleus is negligible for this type of reaction, our information is complementary to that from heavy-ion collisions where such effects are important.

The experiments were performed at the synchrophasotron of the JINR, in Dubna, using the new 4π array, "FASA" [2]. The synchrophasotron is similar to the Bevatron, but larger. Its first beam was on April 17, 1957. For the last 20 years it has been used mostly for accelerating heavy ions. The FASA array was designed to determine with high precision the energy, velocity and mass of some fragments from the collision and the rest of the fragments with less precision. The main parts of FASA are: (i) A fragment multiplicity detector (FMD), consisting of 55 thin CsI(Tl) detectors covering most of the available solid angle. The thin scintillators give, via their ΔE information, the number of light charged particles (LCP's) and intermediate mass fragments (IMF's). (ii) Five time-of flight telescopes (TOF's) that measure the energy, velocity and mass of fragments at laboratory

angles of 50°, 68°, 94°, 103°, and 117°, and serve as a trigger for the readout of the system. (iii) A position-sensitive parallel-plate avalanche counter (PPAC) that measures angular and velocity distributions of fragments detected in coincidence with the time-of flight telescopes. Details of the detectors and their calibration are given in Ref. [2]. The self- supporting ^{197}Au targets had a thickness of 1.0 mg/cm^2. The α beams had energies of 1 and 3.6 GeV/nucleon at intensities of 5×10^8 particles/spill (spill length 300 ms, spill period 10 s).

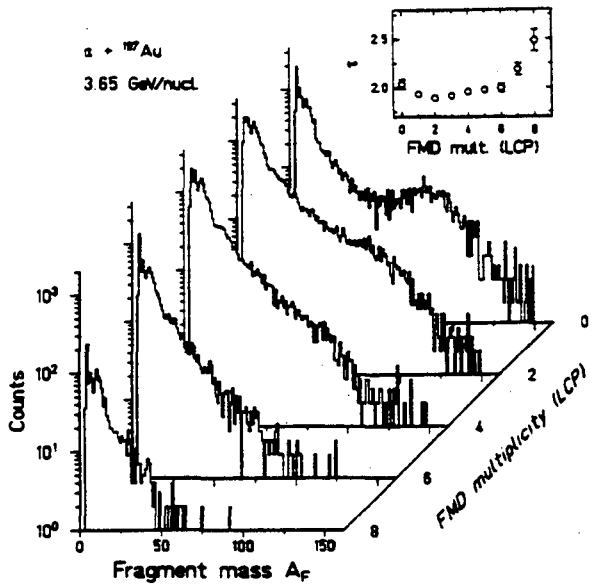

Figure 1: Mass spectra measured in the TOF telescopes as a function of the multiplicity of LCP's, measured in the fragment multiplicity detector. The insert gives the τ parameters deduced from the mass spectra in the region $10 \leq A \leq 40$.

The multiplicity of IMF's and LCP's was used to to examine various observables as a function of excitation energy. In Fig. 1, the mass distributions measured in the five TOF telescopes (added since they are similar) are given as a function of the measured LCP multiplicity ($Z \leq 2$), detected in the FMD array (but not corrected for efficiency). For low LCP multiplicities the mass distributions show both heavy and light fragments. The heavy fragments, with mass number around 80, are most likely fission fragments. This contribution disappears rapidly with increasing LCP multiplicity, reflecting an increasing excitation energy. Lighter-mass fragments are seen for all LCP multiplicities. The mass yield in this region is well described with a $A^{-\tau}$ dependence for masses between 10 and 40. The exponent τ is shown in the insert of Fig. 1 as a function of the LCP multiplicity. A minimum is observed at measured multiplicities of 2-4 light charged particles. A similar minimum of the τ parameter has also been reported by the ALADIN collaboration [3].

Further information about the excitation energy regime reached can be deduced from the IMF multiplicities measured for the various event classes. The fission event class was easily separated by plotting the fragment mass deduced in the TOF telescopes versus the relative velocity between both fragments. The fragment detected in the PPAC is identified by its velocity and ΔE information. For the TOF telescopes IMF's are defined as fragments with $6 \leq A_{IMF} \leq 30$, and in the CsI scintillators as fragments with $3 \leq Z_{IMF} \leq 15$. To deduce the primary multiplicities, corrections

must be made for the solid angle and efficiencies of the detectors and for double hits. An additional correction takes into account the fact that the trigger probability is higher for the high-multiplicity events because the readout is triggered by the TOF telescopes which cover only a small solid angle. These corrections are combined into a response matrix that represents the experimental filter. Reasonable assumptions were made for the shapes of the primary distributions. Their mean values were calculated by fitting the primary distributions, folded by the experimental filter, to the experimental ones. The primary IMF multiplicity distribution class was assumed to be shaped like a Fermi function. This choice was motivated by calculations using the model of Botvina et al. [4]. For the binary fission event class the primary IMF distribution was assumed to have an exponential shape. Different shapes of the primary distributions, e.g., a Poisson distribution for the fragmentation class, also described the experimental distributions reasonably well. The different shapes give nearly identical values for the mean IMF multiplicity as long as the fit to the experimental distribution is reasonable.

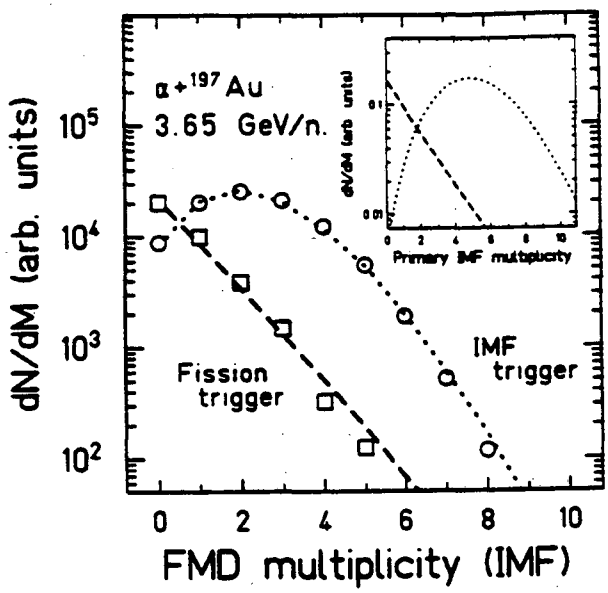

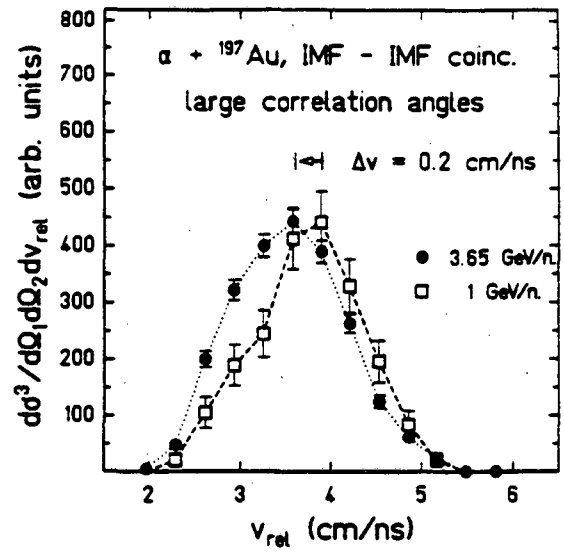

Figure 2: (left) Multiplicity distributions measured in the FMD when selecting fission fragment coincidences (open boxes) and when requiring one IMF in a TOF (open circles). They are fitted with exponential (dashed line) and Fermi (dotted line) distributions, folded with the experimental filter. The insert gives the corresponding primary distributions.

Figure 3: (right) The distribution of relative velocities between two IMF's at large correlation angles shifts to lower values with increasing incident energy.

Fig. 2 shows the experimental distributions deduced for: (i) events with an IMF ($6 \leq A \leq 30$) in at least one TOF telescope (open circles), (ii) events with fission fragment coincidences in the TOF and the PPAC (open boxes). The experimental distributions are fitted with a folded Fermi distribution (dotted line) and a folded exponential distribution (dashed line), the primary distributions are given in the insert. Even the tails are well described. The mean values for the primary distributions are given in Table 1 for the two event classes at both incident energies. For the IMF trigger the primary multiplicity is much higher and it increases by 40% going from 1 to 3.6 GeV/nucleon incident energy indicating a still increasing energy deposition. Our value of 5.1

may be compared with the maximum value of 13 (6.5 for each gold nucleus) found for ^{197}Au + ^{197}Au at 100 MeV/nucleon [5]. This indicates that α particles can be used to excite heavy nuclei to the excitation energy regime that produces the highest IMF multiplicity.

Event class	1 GeV/nucl	3.6 GeV/nucl
Fission	1.1±0.2	1.1±0.2
IMF	3.8±0.6	5.1±0.8

Table 1: Primary IMF multiplicities observed in coincidence with fission events or with events that have one IMF in one of the TOF telescopes.

The density of the nuclear system at the instant of breakup is a question of great interest. It has been shown that the relative velocities of IMF's detected at large relative angles are governed by the geometry of the nuclear system at the instant of their emission due to Coulomb repulsion [6]. The relative velocities in our experiment were determined for coincidences of the two TOF telescopes at 103° and 117° and the position sensitive PPAC on the opposite side, covering a correlation angle range of 130° - 180°. Going from 1.0 to 3.6 GeV/nucleon incident energy decreased their mean value by 0.2 cm/ns, as shown in Fig. 3. The statistical fragmentation model of Gross et al. [7] was used to calculate the density and excitation energy of the system at the instant of breakup. The freeze-out density and excitation energy were determined simultaneously from the dependence of the average relative velocity between IMF's at large correlation angle on the multiplicity of IMF's [8]. In the framework of these calculations the relative velocities are consistent with an excitation energy that increases with beam energy and with a constant and low breakup density of only 1/7 that of the usual nuclear density.

BUU calculations [9,10] were made for central collisions of 14.6 GeV ^{4}He on ^{197}Au. Fig. 4 shows the α particle penetrating deeply into the gold nucleus depositing its energy. This calculation indicates that the excitation energy of 70 MeV/nucleon is not distributed uniformly throughout the nucleus. The outer edge is cooled by evaporation while the central part is turned into a gas. The BUU calculations also suggest that a beam energy much larger than 3.6 GeV/nucleon would allow the α particle to knock out energetic nucleons in the forward direction. These energetic particles would carry away much of the original beam energy so that the total excitation of the gold nucleus would be less. Our preliminary results indicate that the formation of bubbles in our system has a somewhat different origin than proposed for this phenomenon at lower energies and for symmetric systems, where it is driven by mean field compression and subsequent radial expansion [10]. In our case, the bubble formation seems to be rather due to kinetic pressure and 'shock waves' with delta resonance formation.

[1] R. Trockel et al., Phys. Rev. Lett. **59**, 2844 (1987); G. Klotz-Engmann et al., Phys. Lett. **B187**, 245 (1987); G. Klotz-Engmann et al., Nucl. Phys. **A499**, 392 (1989).

[2] S.P. Avdeyev, Nucl. Inst. Meth. A **332**, 149 (1993).

[3] J. Hubele, Z. Phys. **A340**, 263 (1991).

[4] A.S. Botvina, Nucl. Phys. **A507** 649 (1990).

[5] W.G. Lynch, private communication; B.V. Jacak, Nucl. Phys. **A488**, 325c (1988); T. Wienold,

Dissertation Universität Heidelberg, GSI Report 93-28 (1993).

[6] D.H.E. Gross et al., Phys. Lett. **B224**, 29 (1989).

[7] D.H.E. Gross, Nucl. Phys. **A428**, 313c (1984); Sa Ban-Hao, D.H.E. Gross, Nucl. Phys. **A437**, 643 (1985); D.H.E. Gross, Rep. Progr. Phys. **53**, 605 (1990).

[8] Bao-An Li, D.H.E. Gross, V. Lips, and H. Oeschler (to be published).

[9] W. Bauer, Phys. Rev. Lett. **61**, 2534 (1988).

[10] W. Bauer et al., Phys. Rev. Lett. **69**, 1888 (1992).

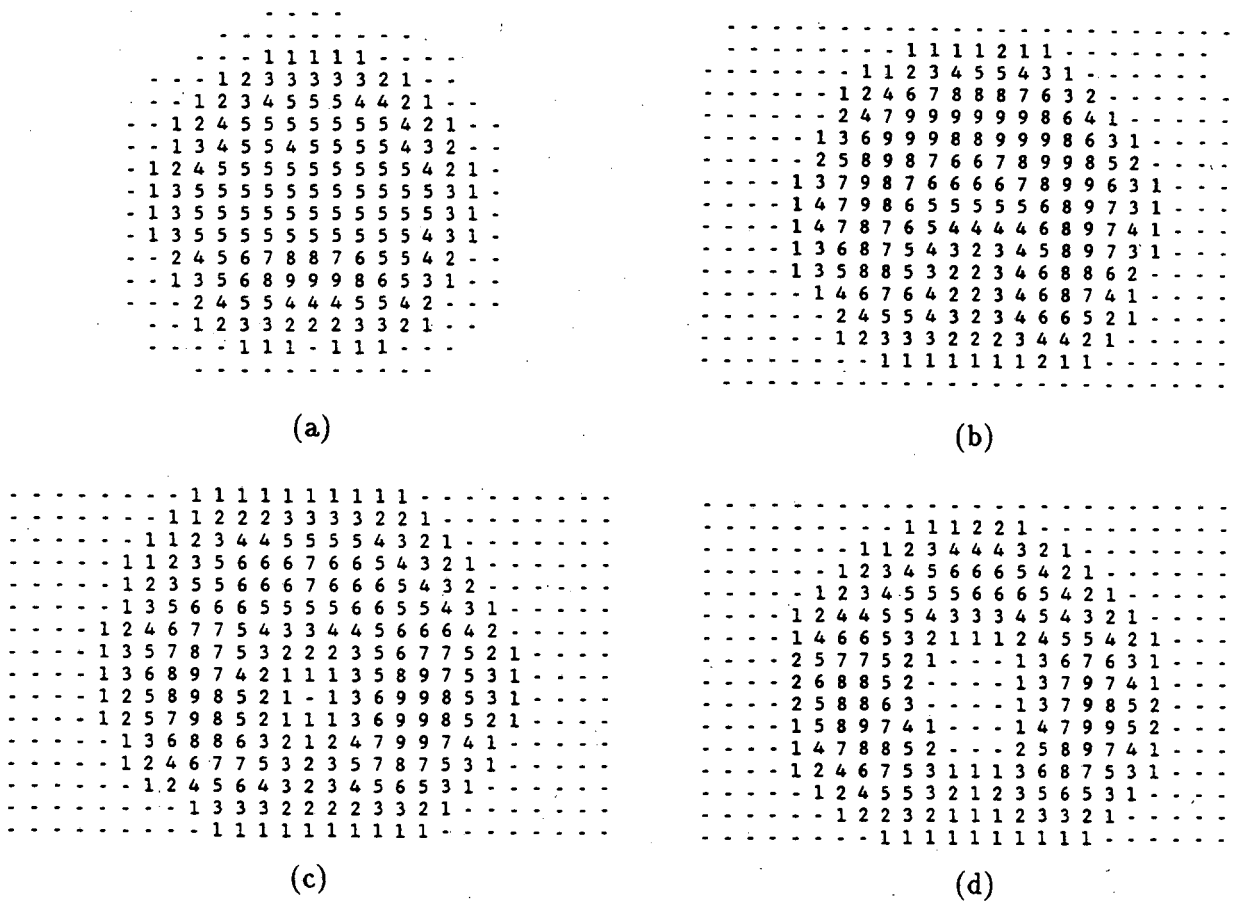

Figure 4: Contour plots showing the results of BUU calculations for central collisions of 14.6 GeV ^{4}He on gold. The α particle enters from the bottom. The nucleon density ranges from - to 9 in these sections through the center of the gold nucleus. The density contours are lowered as time increases to compensate for evaporation.
(a) t = 10 fm/c The α particle has just passed the center of the gold nucleus.
(b) t = 25 fm/c The α particle has stopped.
(c) t = 50 fm/c Deposited energy has caused the gold nucleus to expand. A bubble of hot nuclear gas is forming.
(d) t = 70 fm/c The outer part of the nucleus has evaporated and the central bubble has enlarged.

Fragmentation of Hot Nuclear Systems Formed in Xe-Induced Reactions at E_{beam}=60 MeV/nucleon#

W. Skulski, K. Tso, N. Colonna, G. J. Wozniak, L. G. Moretto, D. R. Bowman, M. Chartier+, C. K. Gelbke+, W. C. Hsi+, M. A. Lisa+$, W. G. Lynch+, G. F. Peaslee+@, L. Phair+, C. Schwarz+, and M. B. Tsang+*

Introduction

Multifragment disintegration of highly excited nuclear systems is the subject of much current interest, both experimentally and theoretically (see (1) and references therein). In theoretical calculations, one can specify the range of impact parameters of the reaction or its "centrality". In experimental studies however, the impact parameter is not measured directly. Therefore, one typically uses the light charged particle multiplicity as a measure of the centrality of the collision.[2,3] Recently, a study of the Xe+Bi reaction at 28 MeV/nucleon indicated that a binary reaction mechanism persists even for high particle multiplicity and/or large intermediate mass fragment (IMF) multiplicity.[4] Thus, it is not clear if central collisions are well characterized by the sole requirement of high particle multiplicity. The aim of the present paper was to investigate reactions of Xe with a range of targets to see, to what extent a binary reaction pattern persists at 60 MeV/nucleon.

Experimental procedure

The experiment was performed at the K1200 Cyclotron of the National Superconducting Cyclotron Laboratory at Michigan State University. A 60 MeV/nucleon ^{129}Xe beam bombarded targets of ^{27}Al, ^{nat}Cu, ^{89}Y, ^{165}Ho and ^{197}Au of thickness 2.07, 2.0, 1.0, 2.0 and 1.3 mg/cm^2, respectively. The detection system subtended angles from 2° to 160° with respect to the beam axis and had a geometric acceptance of ~88% of 4π. At forward angles (2° - 16°), fragments (Z = 1 - 54) were detected in a 16-telescope Si(300 μm)-Si(5 mm)-Plastic(7.6 cm) array[5] with good energy and position resolution. The geometrical efficiency of the forward array was about 64%. Individual elements were resolved for Z=1 to 54, when counting statistics allowed. Representative detection thresholds in the forward array were 13, 21 and 27 MeV/u for fragments of Z = 8, 20 and 54, respectively. Energy and position calibrations were performed by utilizing analog beams of q/A=1/6 [D^4He^+, $^6Li^+$, $^{12}C^{2+}$, $^{18}O^{3+}$] at 22 MeV/nucleon, and two "cocktail" beams[6] at 60 MeV/nucleon: [^{30}Si, ^{60}Ni, ^{90}Zr] and [^{43}Ca, ^{86}Rb, ^{129}Xe]. (A "cocktail" beam consists of 3 different ion beams with nearly identical charge to mass ratios.) These low intensity beams were swept directly across each of the array telescopes. These data were used to measure the nonuniformity in the 300 μm ΔE detector thickness and corrections were made off-line. The pulse-height defect was measured and corrected for according to ref. (7). The overall energy calibration was accurate to about 1% and the position calibration to within 1.5 mm.

At larger angles (16° - 160°), light charged particles and fragments (Z = 1 - 35) were detected in the MSU Miniball[8] consisting of 171 fast plastic (40 μm) - CsI(2 cm) phoswhich detectors. The most forward-angle ring and four detectors of the second ring of the Miniball were removed to accommodate the forward-angle Si array. Representative detection thresholds were 2, 3, and 4 MeV/u for Z = 3, 10, and 18 fragments. For H and He, individual isotopes could be resolved. For heavier elements, only elemental resolution was achieved. The energy calibration was obtained by scaling the previous calibration[9] to hydrogen punch-through points in every detector. This procedure was checked for a subset of 8 Miniball

detectors that were extensively calibrated by sweeping the q/A=1/6 beams across the face of the detectors. For this limited subset of detectors, a satisfactory agreement with the existing calibration was found.

Results

I. Global reaction patterns

As the excitation energy of the heavy reaction products is increased, one expects the number of evaporated neutrons and light charged particles to increase. Thus, many groups have used 4π neutron or charged particle detectors to determine the extent to which the kinetic energy available in the entrance channel is thermalized. In fact, recent measurements[4)] that combine both detection techniques have shown a strong correlation between the measured neutron and charged particle multiplicities. In our measurements, we utilize the total charged particle multiplicity M which consists of the measured number of light charged particles (LCPs) and intermediate mass fragments (IMFs). Low M values are characteristic of low-dissipation, peripheral events, while high M is associated with more violent, central collisions. One should note, that for light targets (Al, Cu) the present experiment does not detect the most peripheral events with good efficiency due to the grazing angle falling below the minimum detection angle of the forward array. In this case a PLF can be detected in the forward array only if it is deflected to $\theta > 2^{o}$ due to a sequential decay. This introduces a certain bias against large impact parameter events. For heavier targets (Y, Ho, Au) events from a large range of impact parameters can be observed.

For the ideal 4π detection system with 100% efficiency, one would expect to see constant value of the total detected kinetic energy, independent of the degree of dissipation, except for small variations due to different Q-values of the different reaction channels. For the actual detection system, the total detected energy is smaller than the idealized limit. First, neutrons are not measured by the present experimental setup. Second, some charged particles may not be observed due to thresholds and dead regions between the detectors. Figure 1 shows a comparison of the total detected charge, kinetic energy and linear momentum versus the total number of detected particles M for five targets. For the lightest target ^{27}Al, the total charge distribution has two peaks. For the upper peak, 90% of the total charge of the system is detected (Z_{total} = ~50), whereas for the lower peak, only a small percentage is detected (Z_{total} = ~10). The lower peak corresponds to the situation when the heavy projectile-like fragment (PLF) is not detected due either to it being emitted into an angle smaller than 2° or the dead region between telescopes. When the heavy forward-going PLF is not detected, one sees only light particles emitted from the target and projectile-like residues. For heavier targets, one observes two branches (e.g., see the Au target). For small values of M, the upper branch starts at the projectile Z-value. As M increases, this branch rises slowly, and then joins the rapidly rising lower branch. For the most central collisions, the total detected charge is greater than the projectile charge. For heavy targets, the two-branch region can be associated with peripheral collisions: the lower branch arises when the forward-going PLF is missed and only LCPs have been detected; whereas the upper branch results when both are detected. For peripheral collisions, one does not detect the total charge of the system because the slow moving target-like fragment (TLF) is below the detector thresholds. As the impact parameter decreases, the TLF becomes more excited and emits increasing numbers of light charged particles causing the lower branch to increase until the two branches merge. For the most central collisions, the system presumably breaks into many small fragments and no large projectile-like or target-like fragment remain. A very similar pattern is observed in plots

of the total kinetic energy and the total linear momentum detected versus the total multiplicity (see Figure 1).

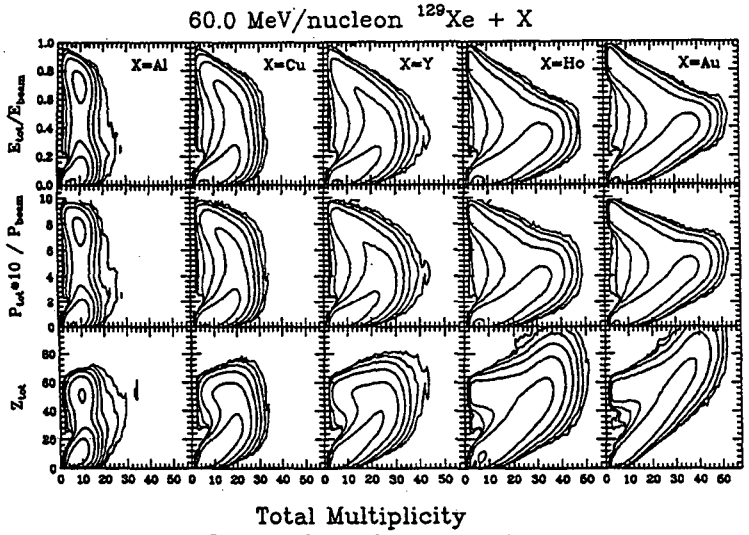

Fig. 1. For each event, the detected total energy (upper row), total detected parallel momentum (second row) and total detected charge (third row) are plotted vs. total charged particle multiplicity, for the 60 MeV/u ^{129}Xe + ^{27}Al, ^{nat}Cu, ^{89}Y, ^{165}Ho and ^{197}Au reactions.

The two branches in Fig. 1 should have roughly the same slope as a function of M, unless the size of the largest fragment decreases with M, in which case the branches should merge for high values of M. This is indeed the case, as shown in Figure 2, in which the mass of the largest fragment detected in every event is plotted as a function of M. (The mass was inferred from the measured charge according to ref. (10).) Two branches can be clearly seen in case of heavier targets like Ho and Au, while for Al the distribution resembles the previous figure. A clear anti-correlation of the size of the largest detected fragment with M is observed for all targets except Al. The parallel to the beam velocity component of the largest detected fragment is roughly constant as a function of multiplicity, as shown in Figure 3. For low and intermediate multiplicity, the largest fragments are the dominant, "leading" ones, and they carry memory about the projectile. The leading fragments contribute roughly constant energy per nucleon and constant momentum per nucleon to the measured total energy and total momentum in Fig. 1. At the same time, there is a big difference in mass between the biggest and the next biggest detected fragment, see Figure 2.

Projectile-like fragments can be produced following substantial energy dissipation, as indicated by the high charged-particle multiplicity values. The dissipated energy is being transferred to the collision products at the expense of the initial kinetic energy present in the entrance channel. This is shown in Figure 3, in which the parallel velocity of the largest fragment is plotted as a function of M. For low dissipation (low multiplicity values) the PLFs have almost the beam velocity, while for large dissipation (large M-values) the decrease in the PLF velocity is substantial. This decrease corresponds to a large energy missing from the entrance channel. For example, if a fragment of Z=35, A=80 is slowed to about 90% of the beam velocity, it loses about 870 MeV. It is also interesting to note, that for targets heavier than Al for high values of M, a low-velocity target-like component gradually builds up in the velocity spectra in Figure 3.

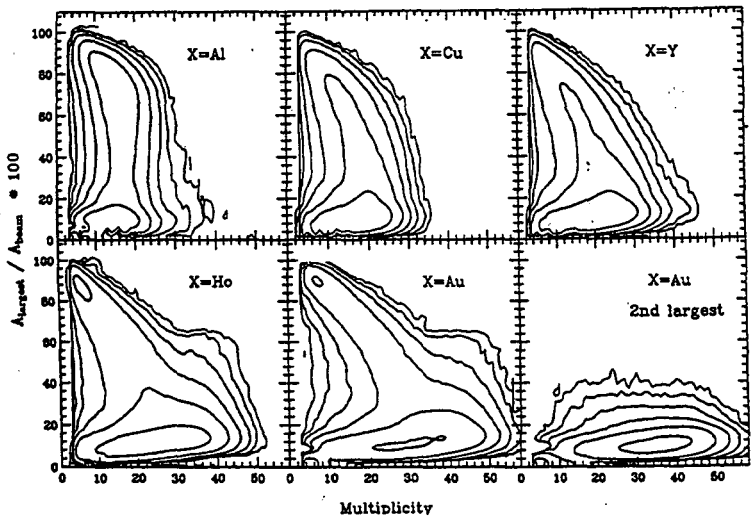

Fig. 2. For each event, the mass of the largest detected fragment is plotted vs. total charged particle multiplicity, for the 60 MeV/u $^{129}Xe + ^{27}Al$, ^{nat}Cu, ^{89}Y, ^{165}Ho and ^{197}Au reactions.

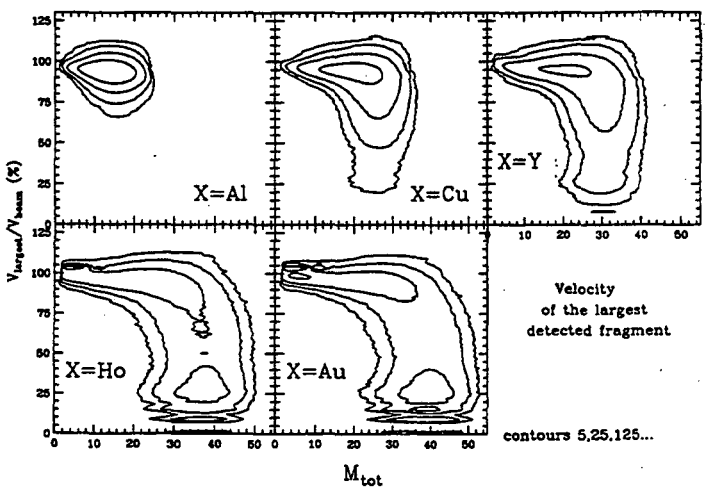

Fig. 3. For each event, the velocity of the largest detected fragment is plotted against the total charged particle multiplicity M for the 60 MeV/u $^{129}Xe + ^{27}Al$, ^{nat}Cu, ^{89}Y, ^{165}Ho and ^{197}Au reactions. Velocity is relative to beam velocity.

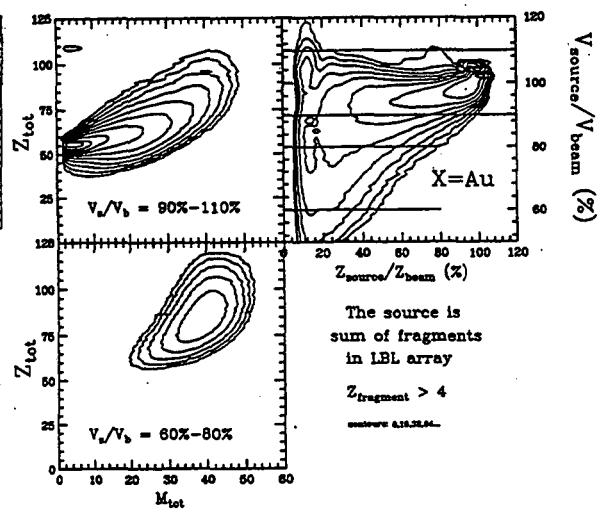

Fig. 4. For 60 MeV/nucleon $^{129}Xe + ^{197}Au$ reaction. *Upper right panel:* Contour plot of the mean parallel velocity of the PLF source versus the size of the source (see text). *The left-hand panels:* The distributions of the total detected charge Z_{total} versus multiplicity, gated on two ranges of the PLF source velocity: 90%-110% and 60%-80% of V_{beam}. More dissipative events correspond to slower PLF sources, as shown by the increased multiplicity and Z_{total}.

II. Primary PLF fragments

As the energy dissipation in the reaction increases, as reflected by the increasing multiplicity, the excitation of the forward-going primary PLF also increases. At large

excitation energies, the primary PLF can decay into a several secondary fragments. With our forward array we can detect most of them. During the off-line analysis, we reconstructed the primary PLF "source". We defined a "primary source" as being the sum of all fragments detected in the forward array, $Z_{fragment}>4$.[1] When discussing "PLF sources", only "completely" measured events will be considered, defined as those with total detected energy of at least 50% of the beam energy (see the first row in Figure 1). This 50% cutoff serves as a convenient discrimination against incompletely measured events, in which the PLF was not detected due to less than 100% detection efficiency.

In Figure 4 the parallel velocity of the reconstructed PLF source is plotted versus its reconstructed charge (upper-right panel). The triangular pattern of the charge-velocity contour plots is similar to those previously reported in the La-induced reactions between 35 and 55 MeV/nucleon.[1] This pattern was previously interpreted as a result of the incomplete fusion followed by extensive particle evaporation, see (1) for details. One of the conclusions of the previous study was that slower PLF sources correspond to increased energy dissipation. One can test this by looking at the total detected charge and/or multiplicity in coincidence with PLF "sources" moving with different velocities. Both the total detected charge and total multiplicity are increased on the average, when the gate is set on the slower-moving PLF source, see the left-hand side of Figure 4. The increase is due to higher degree of dissipation, what corroborates the conclusions of ref. (1). One should note a conspicuous absence of peripheral collisions in the lower left panel of Figure 4.

III. Determination of the reaction plane

One of the key features of a binary PLF-TLF reaction is a strong kinematical correlation between the primary projectile-like and target-like fragments. Even though the present experiment did not detect target-like fragments with good efficiency due to detection thresholds in the Miniball, the PLF-TLF correlation can be explored indirectly through the LCP and light fragment emission patterns. Namely, the primary PLF source (for which the detection efficiency is almost complete) can be utilized to determine the reaction plane. The emission pattern in the Miniball can then be examined to determine the correlation with the primary PLF, when viewed relative to the reaction plane. Figure 5 shows the distribution of the relative azimuthal angle between the PLF and TLF sources. The azimuthal angle in the array ϕ_{PLF} is defined as that of the primary PLF source, while ϕ_{TLF} is the azimuthal angle of the average momentum of all particles detected in the Miniball (excluding punch-through Z=1 particles). The relative azimuthal angle is the difference $\phi_{relative}=\phi_{PLF}-\phi_{TLF}$. It shows a very distinct peak at $\phi_{relative}=180^{o}$, indicating a strong directional anticorrelation between the two sources. This anticorrelation is evidence for a binary reaction mechanism. The width of the peak is of the order of 60° in case of Al target, and close to 100° in case of Au target. For the Au target the width increases as a function of multiplicity. In Al case the width changes very little as a function of multiplicity, since mainly central collisions are detected in case of Al target, as discussed earlier.

Summary and conclusions

We have established that in 60 MeV/nucleon $^{129}Xe + ^{27}Al$, ^{nat}Cu, ^{89}Y, ^{165}Ho and ^{197}Au reactions a projectile-like fragment is formed, especially at low values of multiplicity. The velocity of the PLF s close to the beam velocity even though its mass changes with multiplicity from close to the projectile mass (at low value of multiplicity) to a small fraction at high multiplicity values. The distributions of total detected energy, total momentum and total charge versus multiplicity show a characteristic two-branch pattern. At a given

multiplicity, the upper branch is due to completely measured events, where the leading projectile-like fragment has been detected. The lower branch results, when the leading fragment is not detected, either due to the small grazing angle or to the incomplete efficiency of the forward array.

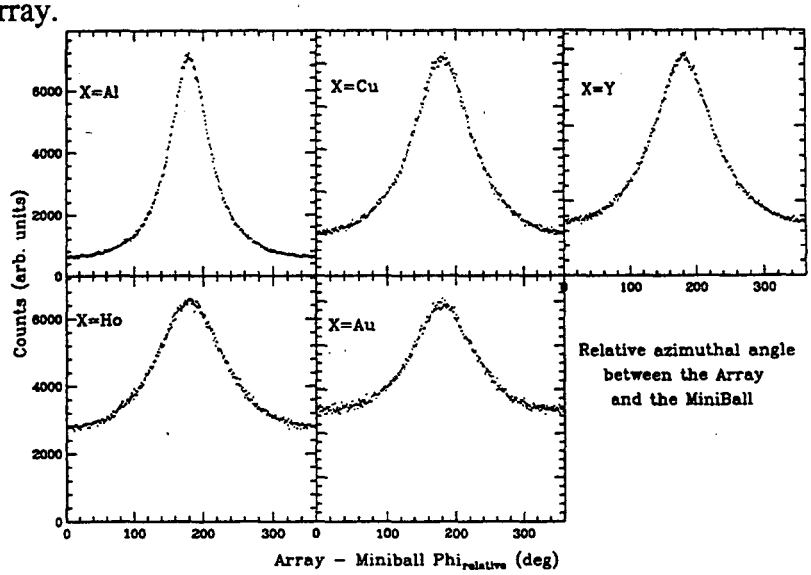

Fig. 5. The distribution of the relative azimuthal angle $\phi_{relative}$ between the PLF source in the forward array and the mean momentum vector in the Miniball.

For heavier targets (Au, Ho) there is also a region above roughly M=35, where the two branches merge together and there seems to be no clearly defined leading fragment. Events above M=35 therefore seem to be promising candidates for "central collisions", characterized by complete overlap of the projectile with the target. Even there, substantial fragments with parallel velocity component close to beam velocity were detected. Thus, a substantial fraction of highly dissipative events seems to be of a binary-like type.

The parallel velocity of the reconstructed PLF source was used to select events with varying degree of dissipation. More dissipative events were selected on the average in coincidence with slow sources, than the ones observed in coincidence with fast moving sources. A PLF source - TLF source directional anticorrelation was demonstrated.

Footnotes and References

#This work was supported by the Dir., Office of Energy Research, Div. of Nuclear Physics, Office of High Energy and Nuclear Physics of U.S. DOE.

*On leave of absence from Heavy Ion Laboratory, Warsaw University, Poland

+NSCL, Michigan State University

$Present address: Lawrence Berkeley Laboratory, Berkeley, CA 94720

@Present address: Hope College, Chemistry Dept., Holland, MI 49423

1) L.G.Moretto and G.J.Wozniak, Annual Review of Nucl. and Part. Physics **43** (1993) 379.
2) D. R. Bowman, et al., *Phys. Rev. Lett.* **67** (1991) 1527.
3) D. R. Bowman, et al., *Phys. Rev.* **C46** (1992) 1834.
4) B. Lott, et al., *Phys. Rev. Lett.* **68** (1992) 3141.
5) W. L. Kehoe, et al., *Nucl. Instr. Meth.* **A311** (1992) 258.
6) M. A. McMahan, et al., *Nucl. Instr. Meth.* **A253** (1986) 1.
7) J. B. Moulton, et al., *Nucl. Instr. Meth.* **157** (1978) 325.
8) R. T. d. Souza, et al., *Nucl. Instr. and Meth.* **A295** (1990) 109.
9) Y. D. Kim, et al., *Phys. Rev.* **C45** (1992) 338.
10) R. J. Charity, et al., *Nucl. Phys.* **A483** (1988) 371.

Beam and Radioactive Beam Studies

MEASUREMENT OF ELECTRON CAPTURE FROM ELECTRON - POSITRON PAIR PRODUCTION

Harvey Gould[a], A. Belkacem[b], B. Feinberg[c], and R. Bossingham[d]
Lawrence Berkeley Laboratory, Berkeley, CA 94720 USA
W. E. Meyerhof[e]
Stanford University, Stanford, CA 94305 USA

During the collision of two relativistic heavy ions, large transient electromagnetic fields result in a high probability of electron- positron pair production. Capture from pair production is the process in which the electron from this pair emerges from the collision bound to an ion[**1,2**]. The cross section for electron capture from pair production is expected to increase with increasing collision energy: this distinguishes it from all other electron-capture mechanisms whose cross sections are known to decrease at increasing relativistic energies. Capture from pair production is also unique in that it requires no electron be present in the initial state.

As a result of these properties, electron capture from pair production is expected to be the dominant recombination mechanism at highly relativistic energies. It may be the major source of beam loss for the heaviest ions at relativistic heavy ion colliders[**3**] such as RHIC and LHC. Achieving the highest luminosity thus requires an understanding of this capture process.

Since a relativistic heavy ion collider was not available, we performed the measurement at the LBL Bevalac, using fixed (neutral atom) targets and much lower energies. The large number of electrons in the target results in difficulties due to competing electron-capture processes, and a large background of knock-on electrons. These and other effects are discussed in Ref. 2. Our measurements were performed using bare U^{92+} projectiles at 0.956 GeV/u and bare La^{57+} at 0.405, 0.956 and 1.3 GeV/u.

After passage through the target foil (typically 1 - 4 mg/cm^2 thick) 0.1 to 1 percent of the incident bare ions change their charge state, mostly through the transfer of an electron from the target to the projectile. The beam charge is analyzed with large dipole magnets and each charge state is detected by a plastic scintillator-photomultiplier detector. A signature of the capture from the pair-production process is the detection of a positron, that is emitted at the target, in coincidence with a one-electron ion (La^{56+} or U^{91+}). To validate the event we require the detection of one of the two 511-keV photons emitted when the positron annihilates at rest in the plastic

scintillator. We used the Advanced Positron Spectrometer (APS) to detect the positrons. A description of the APS and a brief discussion of its performance can be found in Ref. 2.

Figure 1 shows the energy distribution of positrons emitted in coincidence with a charge-changed U^{91+}, for a 0.956 GeV/u U^{92+} beam incident on a 1 mg/cm^2 Au target. The data for the forward and backward directions are taken simultaneously, and thus are normalized to the same number of incident uranium ions. Both spectra show a relative suppression of low-energy positrons due to repulsion by the positively charged gold nucleus, at rest in the laboratory frame.

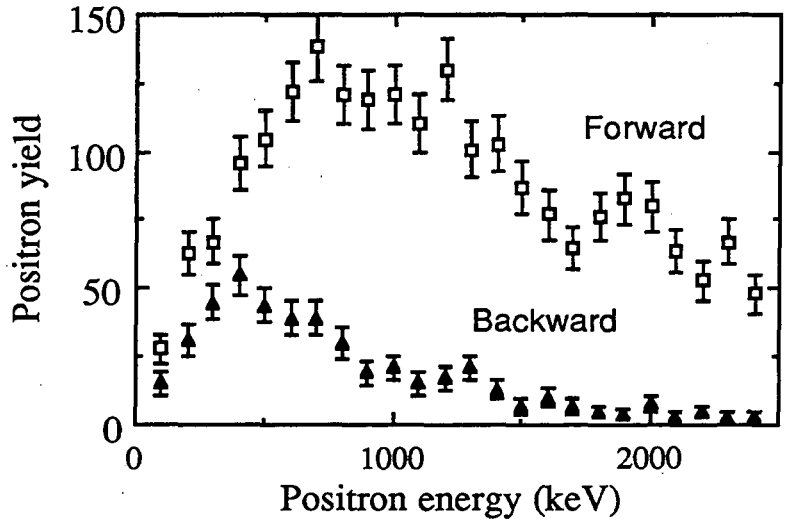

Figure 1- Relative positron yield versus positron kinetic energy measured for electron capture from pair production by 0.956 GeV/u U^{92+} on a Au target.

We measure the total cross section for capture from pair production by a 0.956 GeV/u U^{92+} on a gold target to be 2.19 (0.25) barns. The major contributions to the uncertainty are statistics (0.1), target thickness measurement (0.1) and possible systematic effects (0.2).

If we assume that the fraction of positrons that are detected is the same regardless of whether or not the electron emerges from the collision bound to the projectile, then we obtain a cross section of 3.3 (0.65) barns for the free-pair process (electron - positron pair production *without* capture of the electron). We find it striking that, at 1 GeV/u, the electron of the electron-positron pair is almost as likely to emerge from the collision bound to the uranium ion as it is to emerge free.

A calculation based on perturbation theory[**4**], yields a value of 1.01 barns for capture from pair production by U^{92+} in Au, which underestimates the measured total cross section by about a factor of 2.2. Recently, a non-perturbative, coupled-channels calculation of capture from pair production has been published[**5**] for Pb on Pb at 1.2 GeV/u . Using scaling from perturbation theory to extrapolate the results in Ref. 5 to U on Au gives a value that overestimates our measured cross section by about a factor of 2.

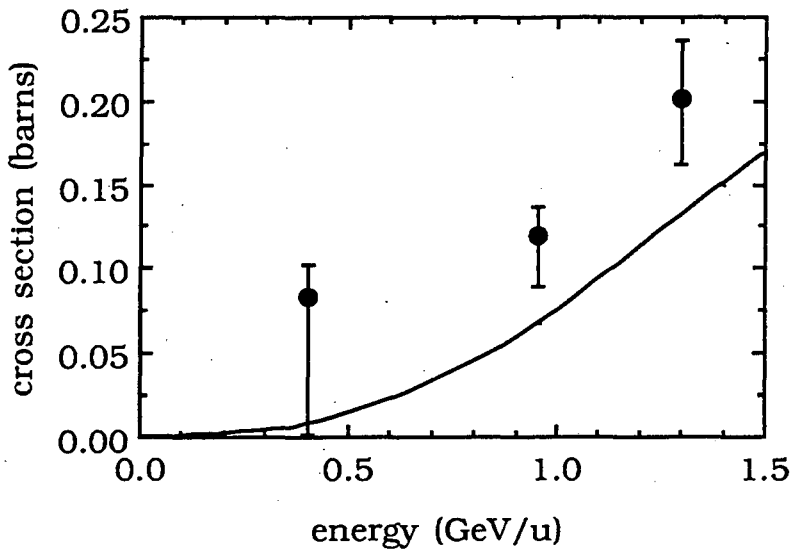

Figure 2 - Dependence of the cross section for electron capture for pair production of La^{57+} on Au as a function of energy

Figure 2 shows the preliminary total cross section of capture from pair production for La^{57+} on Au measured for three different projectile energies (0.405, 0.956, and 1.300 GeV/u). The cross section is found to increase with increasing projectile energy, in agreement with theoretical predictions. This increase reaches almost a factor of two between 0.405 GeV/u and 1.3 GeV/u. Figure 2 also shows the results of a calculation based on the first-order perturbation theory[**4**]. We find that, in the energy range studied here, first order perturbation theory again underestimates the measured cross sections.

ACKNOWLEDGMENTS

We thank Steven Abbott for the engineering design of the APS, Richard Leres for the data acquisition software development and Harvey Oakley and the Bevalac technical support staff for helping put together the experiment in a record time in order to meet the deadline set by the shutdown of the Bevalac. We thank Donald Jourdain and Cory Lee for helping us to design and build very efficient scintillating detectors. We thank Charles Munger and Lynette Levy for their assistance during the data taking, and we thank Klaus

Momberger for fruitful discussions about the theory of capture from pair production. This work was supported by the Director, Office of Energy Research, Office of Basic Energy Sciences, Division of Chemical Sciences, of the U.S. Department of Energy (DOE) under contract No. DE-AC-03-76SF00098. One of us (BF) was supported by The Office of High Energy and Nuclear Physics, Division of Nuclear Physics, of the U.S. DOE. One of us (WM) was partially supported by NSF grant No. PHY8614650.

REFERENCES

(a) internet address: GOULD@LBL.GOV
(b) internet address: BELKACEM@LBL.GOV
(c) internet address: FEINBERG@LBL.GOV
(d) internet address: RRBOSSINGHAM@LBL.GOV
(e) bitnet address: FE.WEM@STANFORD.BITNET

[1] H. Gould, *Atomic Physics Aspects of a Relativistic Nuclear Collider*, Lawrence Berkeley Laboratory Report, LBL-18593 (1984).

[2] A. Belkacem, Harvey Gould, B. Feinberg, R. Bossingham, and W. E. Meyerhof, Phys. Rev. Lett. **71**, 1514 (1993).

[3] *Conceptual Design of the Relativistic Heavy Ion Collider-RHIC*, BNL Report BNL-52195, pp 117-121. See especially Table IV. 3-10.

[4] U.Becker, J. Phys. **B20**, 6563 (1987); values used here were computed by K. Momberger.

[5] K. Rumrich, K. Momberger, G. Soff, W. Greiner, N. Grün and W. Scheid, Phys. Rev. Lett. **66**, 2613 (1991), and K. Momberger, private communication.

RADIOACTIVE BEAM STUDIES AT SIS

K. Sümmerer

Gesellschaft für Schwerionenforschung, D-64220 Darmstadt, Germany

ABSTRACT

During the first three years of operation of the GSI projectile fragment separator, FRS, radioactive beams have been produced for studies directly at the FRS, for injection into the storage ring, ESR, and for experiments with complex detector systems in the SIS target hall. Examples for all three types of experiments are presented. As a novel production mechanism at these energies, fission of ^{238}U is used to produce a large number of new neutron-rich isotopes. Up to now, the storage and cooling of radioactive beams in the ESR has only been performed in a pilot study showing the feasibility of such techniques. Future secondary beam experiments at GSI will profit greatly from a new direct beam line between the FRS and the SIS target hall presently under construction.

1. Introduction

The studies of projectile-like fragments from relativistic heavy-ion beams performed at the LBL BEVALAC where groundbreaking in two respects: firstly, they drew attention to the potential of projectile fragmentation as a means to produce new and exotic isotopes, and secondly, they established the basic physics of this reaction mechanism where all further developments in this field were based upon. Most of the results were obtained for rather light nuclei, such as ^{12}C, ^{16,18}O, ^{40}Ar, and ^{48}Ca (Refs.1, 2, 3, 4). The projectile fragmentation data for these light systems were complemented by target fragmentation data for heavier systems obtained with radiochemical techniques (see e.g. Refs. 5, 6, 7, 8).

Since the beginning of the operation of the GSI projectile fragment separator, FRS, in late 1990, we have extended projectile fragmentation studies towards heavier nuclei up to uranium. These studies served to (i) add to our knowledge of the physics of projectile fragmentation, (ii) provide radioactive beams for first experiments with secondary fragments. These secondary beam experiments can be performed directly at the exit of the FRS, by injecting a radioactive beam into the ESR storage ring, or by transmitting it to the SIS target hall to make use of the big detector arrays installed there.

The present contribution tries to give a survey of representative results obtained with FRS beams during the last three years, with respect to both, the physics of projectile fragmentation, and the radioactive beams experiments. Important aspects of this work are dealt with in two separate contributions to this conference: Reinhold et al.[9] report on a detailed study of ^{129}Xe projectile fragmentation, whereas Schwab et al.[10] summarize radioactive beam studies of the neutron halo nuclei ^{11}Be and ^{11}Li performed at GSI.

2. Production of radioactive beams at FRS

A schematic drawing of the FRS and its associated detectors to separate and identify individual projectile fragments is shown in Fig.1. A detailed description of the FRS and its

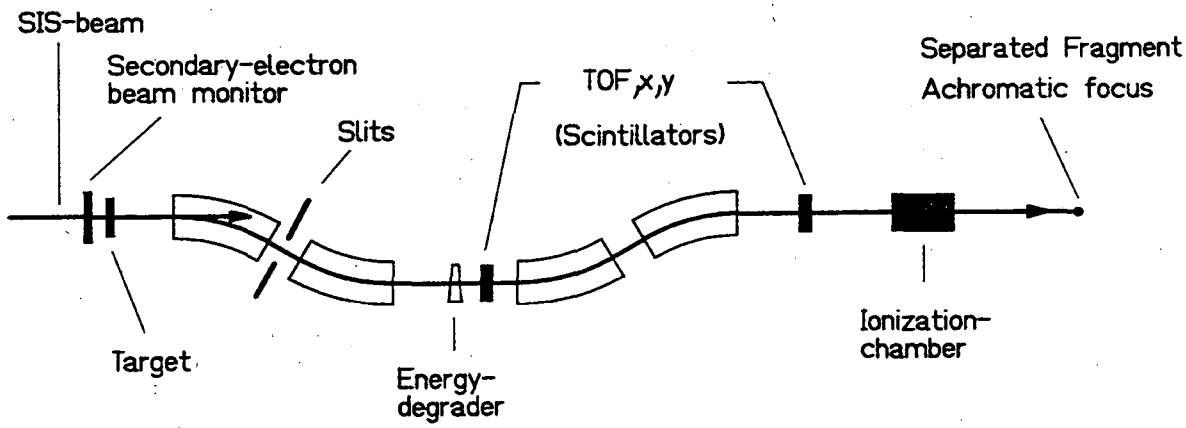

Fig. 1: Schematic layout of the GSI projectile fragment separator, FRS, with the detectors installed to identify the separated fragments. The FRS is described in full detail in Ref.11.

ion-optical and isotope-separation properties is given by Geissel et al.[11]. The observables that are straightforward to measure at the FRS are inclusive formation cross sections of individual isotopes and their longitudinal momentum distributions. The former make use of a secondary-electron beam-intensity monitor in front of the production target. The latter are derived from transverse position distributions measured in the dispersive midplane of the FRS.

2.1. Formation cross sections

Extensive sets of formation cross sections have now been measured for ^{58}Ni (Ref.12), ^{86}Kr (Ref.13), and ^{129}Xe (Ref.9) at energies between 500 and 700 A MeV. The most remarkable result of these measurements is the observation that, contrary to our expectation based on the EPAX parametrization[14], the yields of very neutron-deficient isotopes are enhanced by large factors[9,12]. Close to the p-drip line this amounts to more than two orders of magnitude. This has enabled us to find evidence that e.g. ^{50}Ni is particle-stable, whereas ^{49}Co and ^{53,54}Cu are unbound [12]. Results for ^{129}Xe are discussed in a separate contribution to this meeting[9].

A novel mechanism has been employed at the FRS to produce secondary beams of very neutron-rich isotopes: we have bombarded a lead target with an uranium beam at 950 A MeV to produce projectile-fission fragments. The *electromagnetic-fission* component (with a cross section of the order of 1 barn[15]) produces a mass-asymmetric fragment spectrum very similar to that of thermal-neutron-induced fission. At the same time, *nuclear-fission* events produce fragments at mass symmetry where we have found a large number of previously unknown, very neutron-rich isotopes[16]. Fig.2 shows an energy-loss vs. velocity plot taken at 1.08 times the magnetic rigidity of the primary uranium beam, selecting fission fragments that are emitted forward in beam direction in the projectile rest frame. The doubly-magic isotope ^{132}Sn is the most abundant fragment in this setting, it is produced at a rate of approximately 1 s^{-1}. The full line in Fig.2 indicates the limit of presently known isotopes[18]. At the left-hand side of this line, towards heavier masses, a large number of new isotopes can be identified, in particular in the region of symmetric mass splits around palladium (Z=46). By projecting the two-dimensional spectrum of Fig.2 onto the velocity axis for each nuclear charge, a total of 48 new isotopes could be identified[16]. Formation cross sections for these

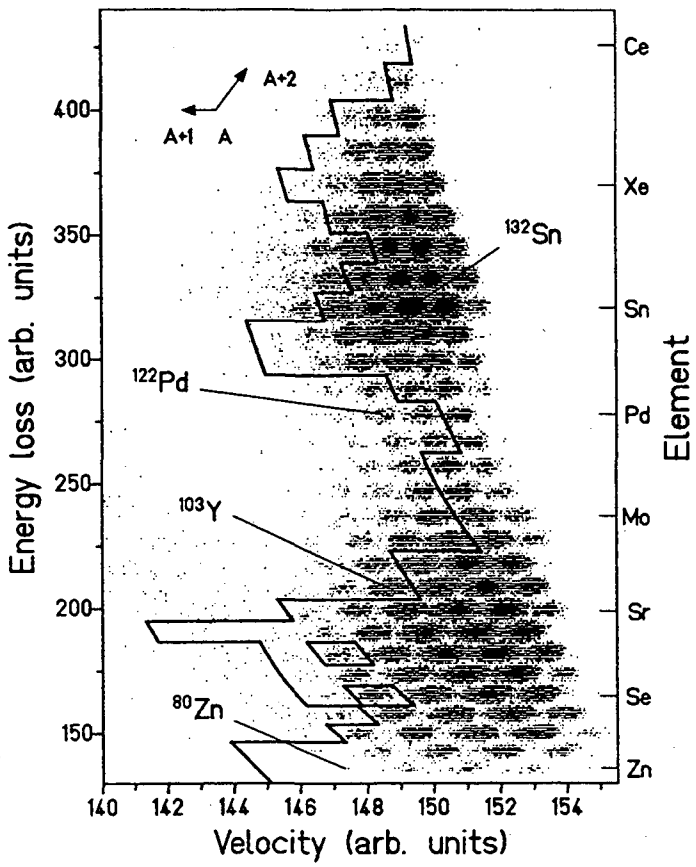

Fig. 2: Two-dimensional spectrum of energy loss versus velocity for ^{238}U fission fragments measured at the FRS at a $B\rho$ - setting of 1.08 times the magnetic rigidity of the primary uranium beam. The full line denotes the limit of the presently known isotopes according to the Strasbourg 1992 Chart of the Nuclides. Some of the new isotopes observed in this experiment are indicated on the left-hand side of this line (from Ref.16).

new isotopes range between 1 μb and 500 μb.

2.2. Kinematics of fragmentation reactions

The kinematics of fragmentation reactions are of crucial importance for a precise modelling of the separation properties of the FRS and for the calculation of accurate transmission values. We have measured longitudinal momentum distributions from ^{86}Kr (Ref.13), ^{136}Xe, and ^{197}Au (Ref.19). These distributions are found to be Gaussians with sigma width parameters close to those given by the empirical formula of Morrissey[20]. Fig.3 visualizes this observation for the case of ^{136}Xe fragments.

Distinct deviations from this systematics are observed, however, for nuclei very close to the projectile: Nuclei that are formed by proton-removal (^{135}I,^{134}Te) show wider parallel momentum distributions, whereas neutron-removal products have narrower widths. We interpret this as being due to the different roles that evaporation plays in forming these products[19,21]: for the neutron-rich projectiles studied, proton-removal products are remainders of the first, fast part of the heavy-ion reaction without significant contribution from

evaporation. Their longitudinal momenta seem to be well described by Goldhaber's simple Fermi-gas model[22], indicated by the dotted curve in Fig.3. The neutron-removal products, on the other hand, can also be formed by purely evaporative processes, with correspondingly narrower momentum widths.

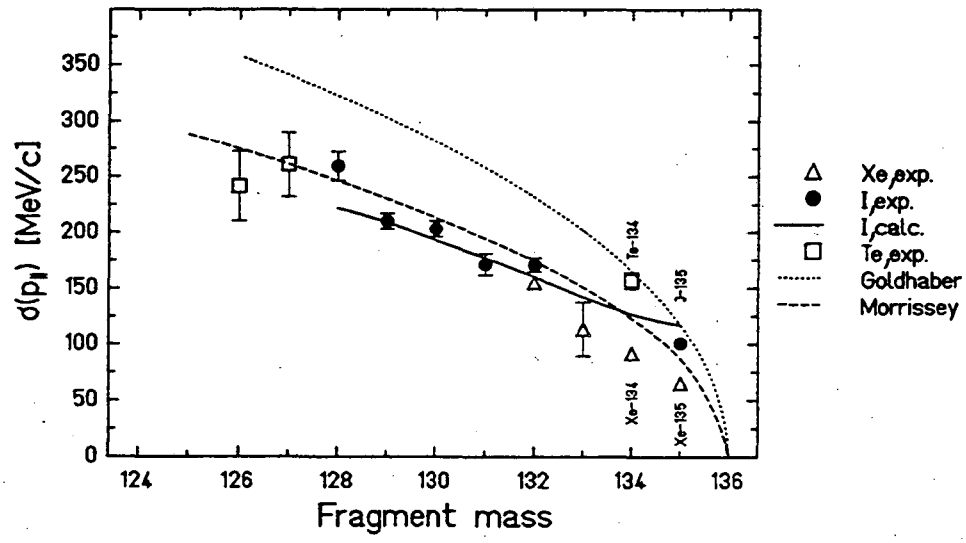

Fig. 3: Sigma widths of longitudinal momentum distributions for fragments from ^{136}Xe. The data are compared to the sudden-breakup model of Goldhaber[22] (dotted curve) and to an abrasion-ablation calculation for the iodine isotopes[19] (full line). The dashed curve represents Morrissey's empirical systematics [20].

The empirical systematics of Morrissey is in general also in good agreement with the measured centroids of the Gaussian momentum distributions. Again, however, a closer look reveals deviations from this general trend. This is elaborated in more detail in the contribution of Friese et al. to this meeting[9].

3. Experiments with radioactive beams at SIS

Fig.4 shows a general layout of the present GSI facility. As can be seen from this figure, radioactive beams from the FRS can be used directly at the FRS (marked "A" in Fig.4). Other options include injection into the ESR (marked "B") or transfer to the SIS target hall (marked "C") via the ESR. The direct beam line from the FRS to the SIS target hall bypassing the ESR (dashed line in Fig.4) is presently under construction. In the following subsections, illustrative examples of first experiments performed at the three locations mentioned above are presented.

3.1. Experiments directly at the FRS

For a typical fragment with 1 mb formation cross section, about 2×10^{-4} of the primary beam intensity (which presently ranges between about 10^{10} Ne ions and about 5×10^{7} U ions per spill) can be converted to a secondary beam. It is obvious that the highest intensities of secondary beams produced in the FRS production target can be obtained at the final focus directly behind the FRS. The drawback of this experimental area is the limitation

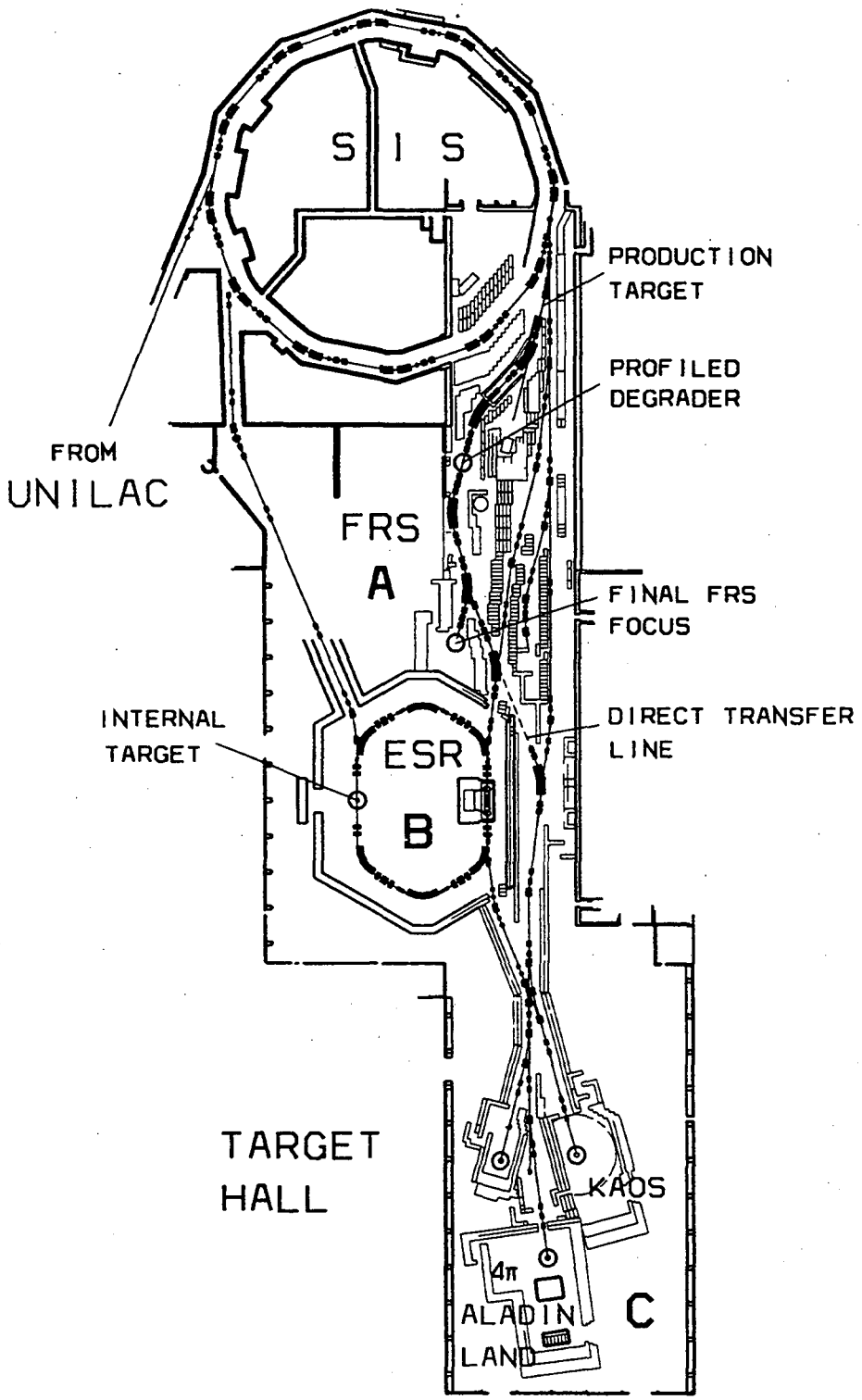

Fig. 4: Schematic layout of the GSI high-energy facility consisting of the SIS18 heavy-ion synchrotron, the fragment separator, FRS, the experimental storage ring, ESR, and the three caves in the target hall housing, among others, the LAND neutron detector and the ALADIN spectrometer.

in space restricting us to rather small experimental setups. Nevertheless, interesting first results could be obtained for both light and heavy secondary beams. Measurements of ^{11}Be and ^{11}Li longitudinal momentum distributions are presented in a separate contribution of Schwab et al. to this conference[10].

In another experiment at the FRS, the nuclear structure of the doubly-magic nucleus ^{56}Ni has been investigated by Kraus et al.[23] studying inelastic proton scattering in inverse kinematics at 100 A MeV. Fig.5 shows the experimental setup at the final focus of the FRS. A radioactive beam of about 3×10^4 ^{56}Ni ions per spill impinged on a CH_2 target surrounded by a ring of Si detectors detecting recoil protons approximately at 90 degrees to the beam direction. Fig.6 shows the measured energy spectrum of recoil protons in comparison to a Monte-Carlo simulation. The excitation of the ground state and the first 2^+ level can

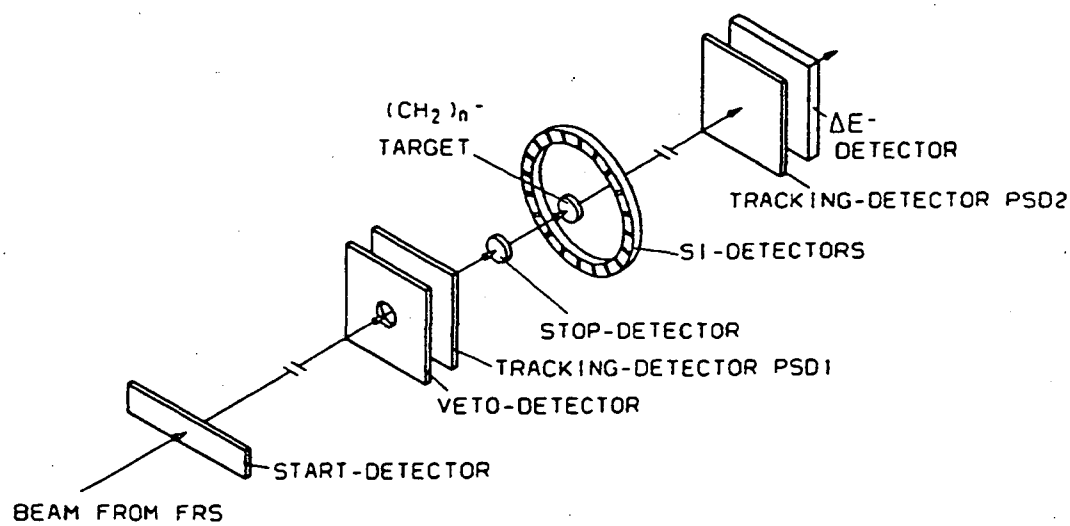

Fig. 5: Experimental setup to track the secondary ^{56}Ni beam and to observe recoil protons from the $p(^{56}Ni,^{56}Ni^*)p'$ reaction performed by Kraus et al.[23] at the FRS.

clearly be separated. For the 2^+ level, a B(E2) value of $600 \pm 120\ e^2 fm^4$ has been extracted. This value is very close to B(E2) values of neighbouring non-doubly-magic nuclei and about a factor of six larger than e.g. the value for the doubly-magic nucleus ^{48}Ca. This finding reflects the much weaker shell closure of Z=N=28 nuclei compared to Z=N=20 (Ref.23).

Another example of secondary beam studies performed at the FRS makes use of the unique potential of the SIS-FRS facility to provide radioactive beams of sub-uranium nuclei for fission studies[24]. Fig.7 shows the experimental setup mounted behind the final focus of the FRS: the isotopically-resolved secondary beam of ^{238}U fragments hits a reaction target of Pb foils. This target is subdivided into seven layers and immersed in argon-methane counting gas to localize the layer where a secondary fission occurs. Pb as a target material was chosen to enhance the proportion of electromagnetic excitation of the secondary beams, leading to a correspondingly large proportion of low-energy fission in addition to the unavoidable nuclear fission part. Nuclear-charge distributions of the fission products are measured in an ionization chamber (MUSIC) and a pair of scintillator detectors that allow to separate the signals of

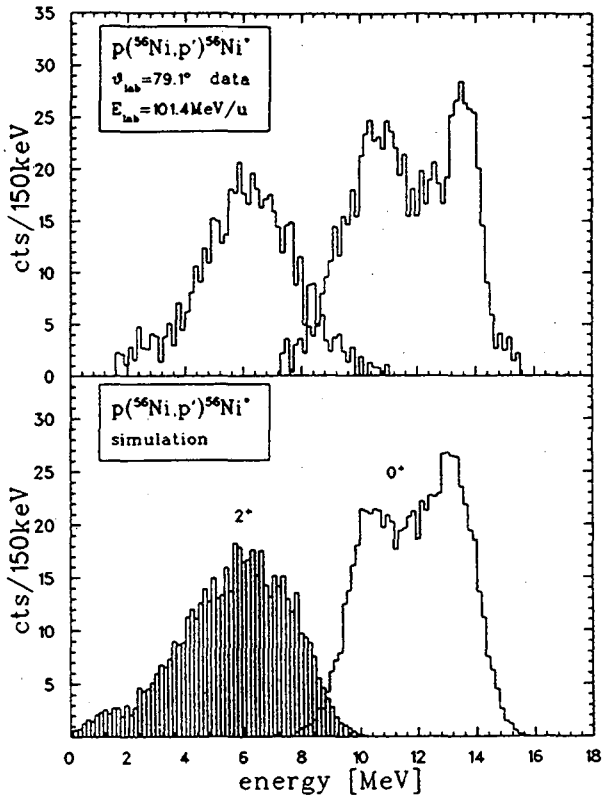

Fig. 6: Energy spectrum of recoil protons measured with the setup shown in Fig.5 (top part) im comparison with simulated spectra (bottom part). The left-hand peak corresponds to an excitation of the first 2^+ state in ^{56}Ni (from Ref.23).

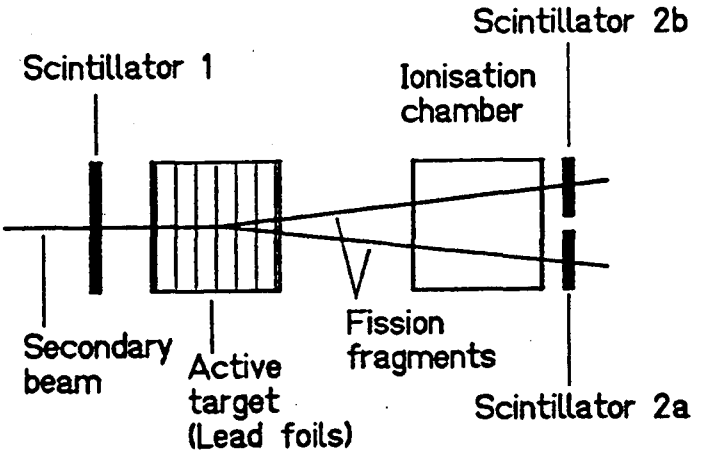

Fig. 7: Experimental setup at the FRS to study the nuclear charge distribution of fission of secondary beams produced by projectile fragmentation of ^{238}U.

the two fission fragments. Fig.8 shows examples of Z distributions for several secondary beams arranged according to the N and Z of the secondary beam. Though the counting statistics is rather poor for most of the examples shown, a transition from asymmetric fission close to ^{238}U towards symmetric fission for neutron numbers below N=138 is clearly visible, in agreement with fission studies performed with transfer reactions on stable or long-lived targets (see references in Ref.24). Future experiments with improved Z resolution and better statistics should allow to map a large area of fissile nuclei and help to delineate the regions of symmetric and asymmetric fission.

3.2. Experiments with radioactive beams in the ESR

Clearly, the unique potential of the GSI high-energy facility lies in the combination of SIS, FRS, and ESR. For future direct reactions like (p,p') or (d,p) in inverse kinematics with unstable nuclei, a cooled beam is indispensable, therefore the next generation of this type of experiments will be performed in the ESR using a hydrogen or deuterium gas target. Another interesting field accessible with the ESR are mass measurements of unstable nuclei. The methods envisaged are either a frequence analysis of the coasting beam with the so-called Schottky diagnostics or a time-of-flight measurement over several turns in the ESR ring when it is tuned in the isochroneous mode. The former method, which is rather straightforward to apply if the nuclei to be measured are sufficiently long-lived, has been tested in a pilot study with ^{20}Ne fragments by Geissel et al.[25]. This experiment also demonstrated for the first time that projectile fragments with their large spread in angle and momentum can be stored and cooled in a storage ring. Fig.9 shows a Schottky spectrum of a cooled ^{20}Ne beam and its fragments with $A/Z = 2$ (among them 110 min ^{18}F). The accuracy of the mass determination for ^{18}F was about 5×10^{-6}. We are presently improving the diagnostic tools and the phase-space matching to obtain a larger injection efficiency. At the same time, the sensitivity of the Schottky diagnostics now allows to detect as few as about $10^5/Z^2$ charges stored in the ring, i.e. as few as about 10 uranium ions!

3.3. Experiments with radioactive beams in the SIS target hall

Up to now, the use of radioactive beams from the FRS in the SIS target hall was hampered by the fact that these beams had to be transmitted via the ESR, imposing severe restrictions in terms of maximum $B\rho$ and transmission. Nevertheless, radioactive beams of ^{8}He, ^{11}Be, and ^{11}Li have been delivered to the ALADIN large acceptance spectrometer and the LAND neutron detector to measure longitudinal and transverse momentum distributions of the 1n and 2n decay channels, respectively. Results from this study are reported in the contribution of Schwab et al. to this meeting[10].

In the future, the combination of ALADIN and LAND with the Crystal Ball γ-ray detector will be used to study the nuclear structure of radioactive beams in more detail. [26,27]. To facilitate such experiments, a direct beam line connecting the FRS with the SIS target hall is being constructed, which can accommodate the 18 Tm beams delivered by SIS and FRS. This will improve e.g. the ^{11}Li transmission by at least one order of magnitude.

This presentation was made possible by the continuous efforts of many FRS collaborators. Since it would take too much space to list them individually, the reader is referred to the publications cited in the bibliography. In addition, we acknowledge the excellent technical

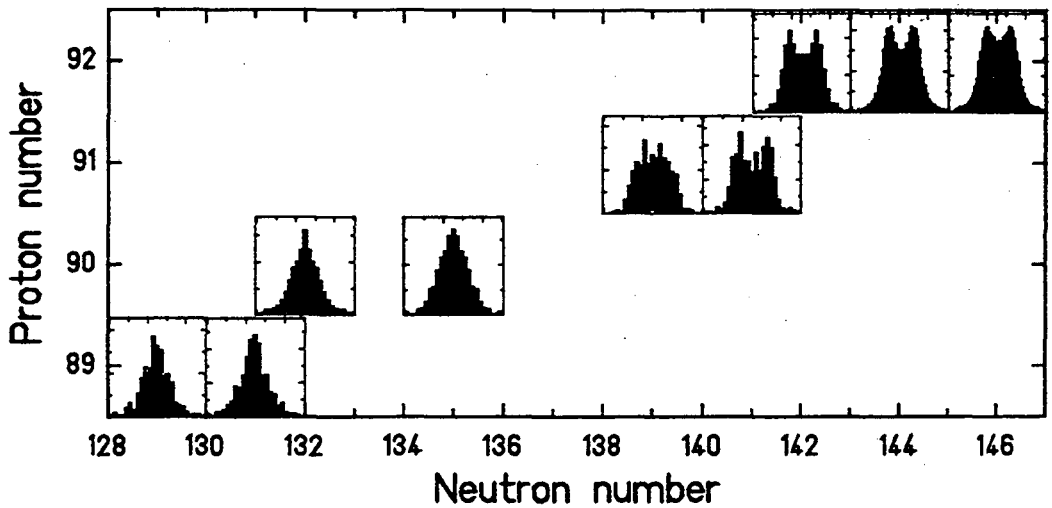

Fig. 8: Nuclear-charge distributions of fission fragments from secondary beams as measured with the setup shown in Fig.7. The individual distributions are centered at the N and Z of the secondary beam that underwent fission (from Ref.24).

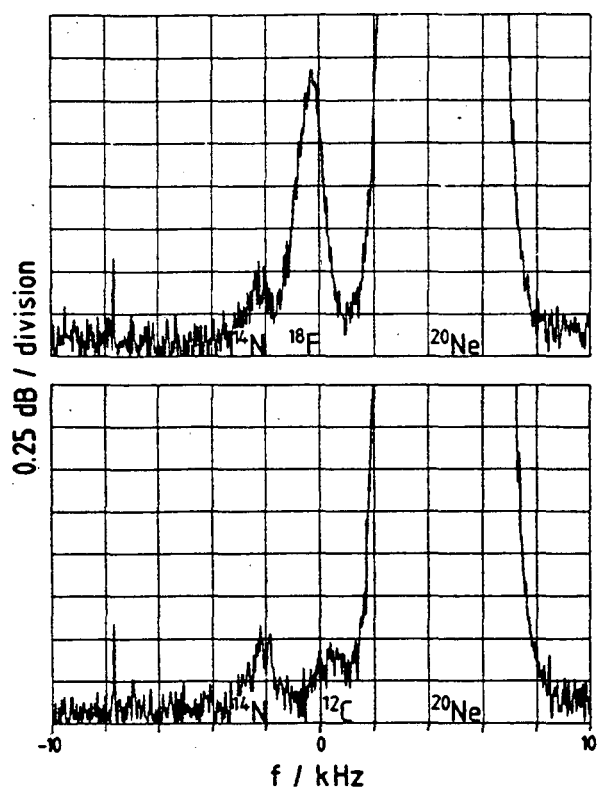

Fig. 9: Schottky spectrum of a cooled fragment beam produced from 310 A MeV ^{20}Ne (from Ref.25). The top part shows the spectrum directly after injection and cooling, the bottom part 12 h later demonstrating that 110 min ^{18}F has decayed.

work contributed by K.-H. Behr, K.-H. Burkard, A. Brünle, E. Pfeng, and the GSI target laboratory.

4. References

[1] D.L. Olson et al., Phys. Rev. C **24**, 1529 (1981); Phys. Rev. C **28**, 1602 (1983).
[2] T.J.M. Symons et al., Phys. Rev. Lett. **42**, 40 (1979).
[3] Y.P. Viyogi et al., Phys. Rev. Lett. **42**, 33 (1979).
[4] G.D. Westfall et al., Phys. Rev. Lett. **43**, 1859 (1979).
[5] J.B. Cumming et al., Phys. Rev. C **17**, 1632 (1978), and references cited therein.
[6] N.T. Porile et al., Phys. Rev. C **19**, 2288 (1979).
[7] D.J. Morrissey et al., Phys. Rev. C **21**, 1783 (1980).
[8] P.L. McGaughey et al., Phys. Rev. C **31**, 896 (1985).
[9] J. Reinhold, Ph.D Thesis and Proc. Third. Int. Conf. on Radioactive Nuclear Beams, East Lansing, Michigan (1993), to be published; J. Friese et al., Contribution to this Conference.
[10] W. Schwab et al., Contribution to this Conference.
[11] H. Geissel et al. Nucl. Instr. Meth. in Phys. Res. **B70**, 286 (1992).
[12] B. Blank et al., Proc. Third. Int. Conf. on Radioactive Nuclear Beams, East Lansing, Michigan (1993), to be published.
[13] M. Weber et al., Z. Phys. A **343**, 67 (1992); M. Weber et al., GSI Preprint 93-74 (1993).
[14] K. Sümmerer et al., Phys. Rev. C **42**, 2546 (1990).
[15] D.E. Greiner et al., Phys. Rev. C **31**, 416 (1985).
[16] M. Bernas et al., to be published in Phys. Lett. B.
[17] K.-H. Schmidt et al., Nucl. Phys. **A542**, 699 (1992).
[18] M.S. Antony, Chart of the Nuclides - Strasbourg 1992.
[19] E. Hanelt et al., Z. Phys. A **346**, 43 (1993).
[20] D.J. Morrissey, Phys. Rev. C **39**, 460 (1989).
[21] K.-H. Schmidt et al., Nucl. Phys. A **542**, 699 (1992).
[22] A. S. Goldhaber, Phys. Lett. B **53**, 306 (1974).
[23] G. Kraus et al., Proc. Third. Int. Conf. on Radioactive Nuclear Beams, East Lansing, Michigan (1993), to be published.
[24] K.-H. Schmidt et al., Phys. Lett. B, in print.
[25] H. Geissel et al., Phys. Rev. Lett. **68**, 3412 (1992).
[26] J. Gerl et al., Proposal "Nuclear structure experiments with the Crystal Ball spectrometer", unpublished (1993).
[27] H. Emling et al., Proposal "Nuclear structure experiments with relativistic and radioactive beams", unpublished (1993).

NEUTRON HALO NUCLEI STUDIED AT GSI

W. Schwab

Gesellschaft für Schwerionenforschung, D-64220 Darmstadt, Germany

ABSTRACT

In the energy range between 300 and 700 MeV/u longitudinal momentum distributions of the break-up products in the reaction (^{11}Li,^{9}Li) were measured for the first time. These data were obtained with the Fragment Separator FRS in a high-resolution energy-loss mode. At 300 MeV/u also the transverse momentum distributions for both the outgoing fragments and the neutrons were measured in coincidence in a kinematically complete experiment with ray-tracing detectors at the facilities ALADIN and LAND. The longitudinal and transverse momentum distributions of ^{9}Li at the lowest energy give comparable widths demostrating that the break-up reaction occurs at large impact parameters.

1. Introduction

Experiments with radioactive beams produced via projectile fragmentation have demonstrated new possibilities for nuclear structure studies [1,2]. Interaction cross sections of exotic nuclei and momentum distributions of their fragmentation products reveal the halo structure of light isotopes near the neutron dripline. From cross section measurements of ^{11}Li a dramatic increase in radius of about 30%, compared with ^{9}Li was obtained. Knowing the small binding energy for the last two neutrons of about 320 keV and the fact that ^{10}Li is unbound, ^{11}Li was viewed as a ^{9}Li core surrounded by two orbiting neutrons which extend far from the core via quantum-mechanical tunneling [3].

Among other techniques used to establish the existence of a halo in a nucleus, the momentum measurements have provided striking results using the direct link between momentum and spatial distribution via Heisenberg's uncertainty principle. In first experiments at the BEVALAC [4] a narrow transverse momentum distribution of ^{9}Li after break-up reaction of ^{11}Li was observed. Much narrower distributions were found from the fast neutrons of the reaction in a low energy experiment [5]. Since the transverse momentum distribution could be influenced both by Coulomb and nuclear contributions the longitudinal momentum distribution is a more direct measure for the spatial distributions of the halo neutrons [6]. However, its investigation requires experimentally high-resolution which must be independent of the relatively large momentum spread (a few percent) of the incident halo nuclei produced in projectile fragmentation. First measurements of the longitudinal momentum were made at MSU with the A1200 [7] at 66 MeV/u [8].

2. Momentum measurements

The experiment at GSI combined different facilities to investigate the properties of light neutron halo nuclei at relativistic energies. The ^{11}Li beam was produced via fragmentation of a ^{18}O beam at 340, 519 and 702 MeV/u respectively in a production target at the entrance

of the FRS [11]. The obtained intensities were up to $4 \bullet 10^9$ projectiles per second. The rates for ^{11}Li detected at the exit of FRS were up to $1 \bullet 10^4$/s using a 8 g/cm^2 Be target.

In the first part of the experiment the longitudinal momentum distributions of the break-up fragments were measured in aluminum and lead targets of 5.4 g/cm^2 and 8 g/cm^2, respectively [9]. The FRS was operated in the energy-loss mode allowing that the momentum width caused by the ^{11}Li production process did not contribute, in first-order ion-optical imaging, to the width measured in the secondary break-up reaction. An ion-optical scheme of the FRS used as energy-loss spectrometer is presented in figure 1. The position spectra

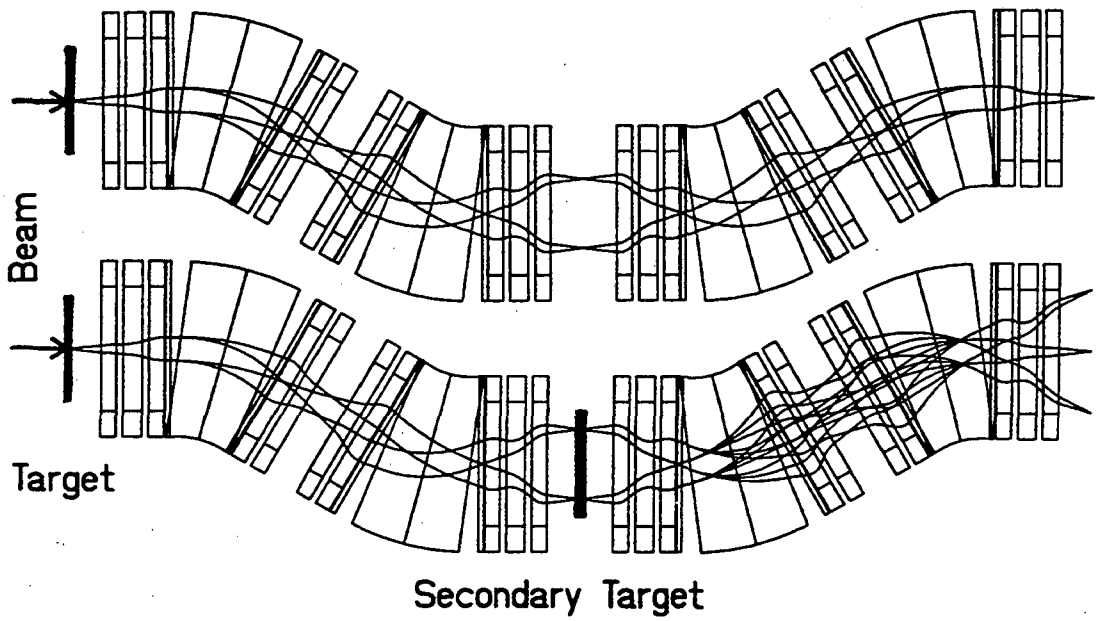

Fig. 1: Scheme of the FRS in the energy-loss mode with envelopes in the direction of the dispersion. The upper part shows the priciple of the achromatic imaging without the influence of the secondary target. Shown are two envelopes with different momenta which are refocused at the final focal plane. In the lower part additional momentum spread originating from the secondary target is simulated.

obtained at the final focal plane were transformed into momentum spectra in the projectile frame using the measured mean magnetic rigidity and the corresponding momentum dispersion. The use of secondary targets with a constant thickness along the direction of the dispersion deteriorated the required achromatism of the FRS resulting in a weak dependence of the position at the final focal plane on the momentum in front of the secondary target. After correction the measured widths reduced by several percent. With the magnetic field determination of better than 10^{-4} and position resolutions of the ray-tracing detectors of about 2 mm the resulting momentum widths were measured within about 5 % uncertainty. Multiple scattering, energy-loss straggling in the secondary target, and the ion-optical image aberrations were taken into account by using the non-reacting ^{11}Li particles measured under the same conditions as a reference. The width of the ^{11}Li distribution was deconvoluted from the ^{9}Li distribution. Furthermore we investigated the energy-loss straggling which results from the different locations of the break-up reaction of ^{11}Li in the thick secondary target by

computer simulations [10]. This was a minor contribution of about 10^{-3} and can therefore be neglected.
A representative result for the lowest energy (265 MeV/u) is shown in figure 2. The distribution is fitted by a Gaussian characterized by a FWHM of about 47 MeV/c. This result is roughly by a factor 5 smaller than the Goldhaber prediction. In the rigth hand side of the picture the corresponding widths of the ^{9}Li momentum distributions are shown for different energies up to 700 MeV/u. Since mainly the spatial distribution of the halo structure is reflected in the momentum distribution only a weak energy dependence is expected as confirmed by our data.

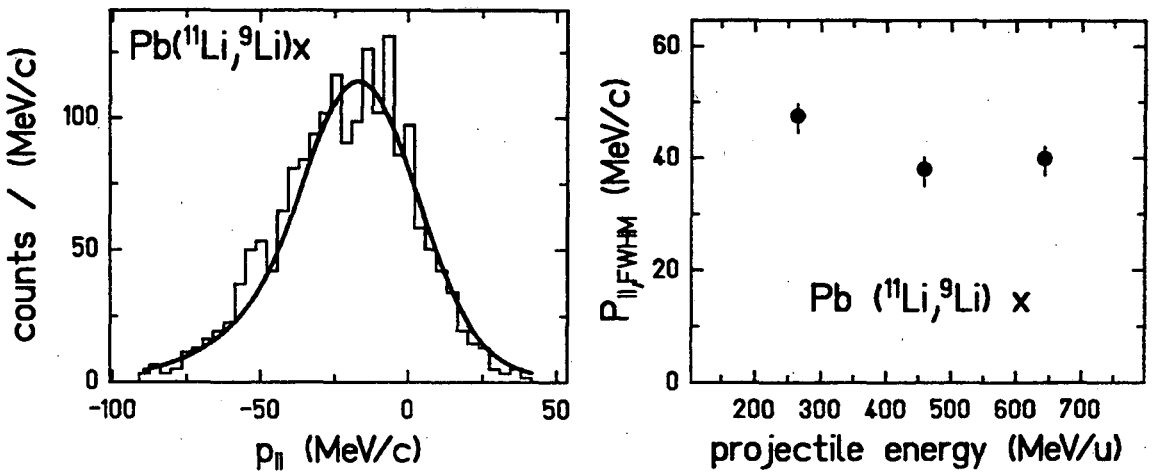

Fig. 2: Left hand side: Measured longitudinal momentum distribution of ^{9}Li. The absolute mean value of the distribution has an uncertainty of about 30 MeV/c, while the width could be determined with an accuracy of about 5 %.
Right hand side: The corresponding widths (FWHM) at different energies after break-up in Pb secondary targets.

The second part of the experiment required the transport of the secondary beam to the experimental facilities ALADIN and LAND via the ESR [12,13]. This condition limited both the maximum magnetic rigidity of the beam to 9.5 Tm and the intensity by transmission losses. The secondary beam was traced in front of the break-up target as well as behind ALADIN (see figure 3). This arrangement allowed to measure the angular distribution for the break-up reaction fragments corresponding to a range of ±200 MeV/c. The angular measurements were done in the nondispersive plane to avoid the coupling of the momentum spread. The neutrons were detected in the position sensitive Large Area Neutron Detector LAND with an acceptance of ±80 MeV/c.
Figure 4 shows the result of the transverse momentum distributions of the break-up fragment ^{9}Li (left side) and the neutrons (middle part) giving widths of 55 MeV/c and 30 MeV/c FWHM respectively.

3. Discussion

In our experiments we have obtained results on the transverse as well as on the longitudinal momentum distribution for the ^{9}Li fragments. At the lowest energy (280 MeV/u) both

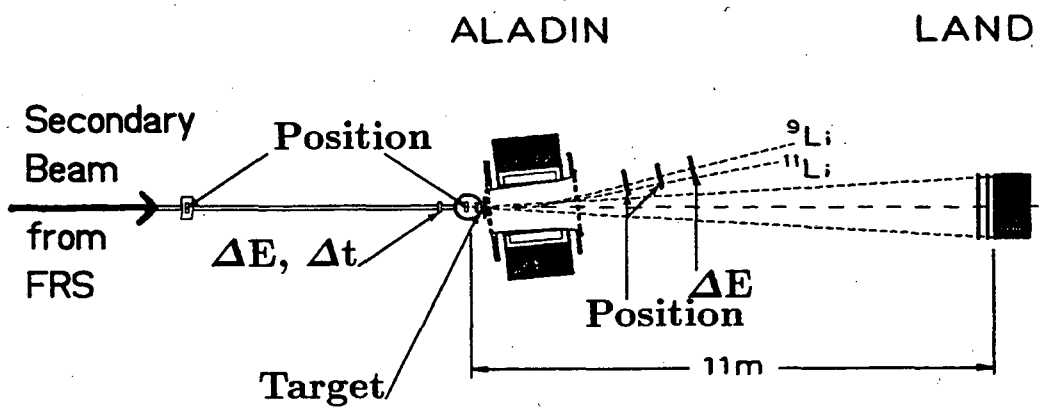

Fig. 3: The secondary beam provided from the FRS is fragmented in a target in front of ALADIN which is used for magnetic rigidity analysis. Position measurements allowed to reconstruct the angular deflection induced in the break-up reaction. The momentum distribution of the neutrons were measured with the 2-dimensional position sensitive neutron detector LAND [15].

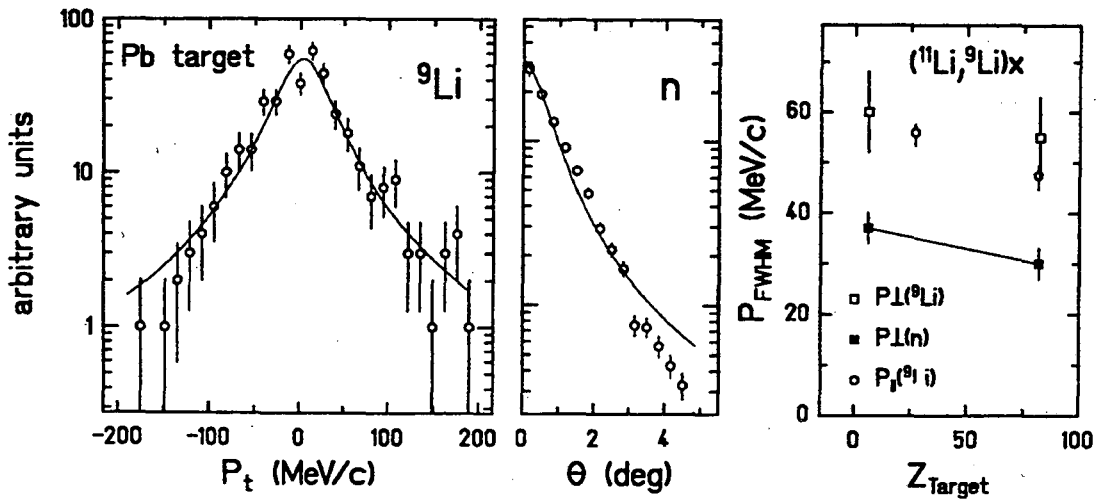

Fig. 4: Left : The transverse momentum distribution of the ^{9}Li and the neutrons deduced from measured angular distributions. The transverse momentum distribution of the neutrons was recorded in coincidence with the ^{9}Li nuclei.
Right : The comparison between $p_{||}$ and p_t shows a fair agreement, which may indicate that the break-up occurs at large impact parameters. There is a slight dependence of the measured width of the target Z.

distributions were measured. The results show that the measured widths of the momentum components are quite similar. The width of the transverse distribution is about 10 % larger which might be attributed to the Coulomb deflection at smaller impact parameters.
The observed transverse momentum distribution of ^{9}Li fragments is well reproduced by a Lorentzian shape. This characteristic can be interpreted in terms of the Fourier transformed Yukawa wave function for the outermost neutrons of ^{11}Li reflecting the spatial extension of the halo. Although the magnitudes of the FWHM are similar the longitudinal momentum

distribution is better reproduced by a Gaussian function. A possible explanation of this observation might be ion-optical transmission losses from the dispersive to the final focal plane of the FRS.
A comparison of our measured longitudinal widths at 700 MeV/u with the results obtained for transverse momenta at LBL at 800 MeV/u [4,14] reveal that ours are much narrower. This might be due to Coulomb deflection and multiple scattering components since it cannot be attributed to the different energies used in both experiments. Indeed we have clearly demonstrated with our results that the energy dependence between 300 and 700 MeV/u is very weak which shows that the nuclear reaction mechanism has no significant influence in this energy range.
The target dependence at fixed velocity for both the fragment and the corresponding neutrons is very weak in agreement with previous experiments at much lower energy [5,8].
The observed width for the neutrons is approximately a factor of $\sqrt{2}$ smaller than that of the ^{9}Li fragments. This is an indication [3] that the two neutrons in the halo are not strongly correlated. The measured momentum widths of the neutrons can be used to deduce the size of the spatial distribution of the two neutrons. Using the Fourier transform of the momentum distribution (Lorentzian) the spatial distribution can be represented by a Yukawa nuclear potential. The input of a $\Gamma \approx 30$ MeV/c results in a rms radius of the halo neutrons of about 10 fm. Since the analysis is still in progress the final results will be published [16].

In future experiments we will extend our investigations of halo nuclei to larger atomic numbers and use the new direct beam line from FRS [17] to the ALADIN and LAND facilities which is characterized by a much higher transmission.

I am grateful to all collaborators in the experiment and especially to the technicians of the FRS and target laboratory.

4. References

[1] I. Tanihata et al., Nucl. Phys. A**553**(1993)361.
[2] P.G. Hansen et al., Nucl. Phys. A**553**(1993)89c.
[3] P.G. Hansen and B. Jonson, Europhys. Lett. 4(1987)409.
[4] I. Tanihata et al., Phys. Rev. Lett. **55**(1985)2676.
[5] R. Anne et al., Phys. Lett. B **250**(1990)19.
[6] C. Bertulani et al., Phys. Rep. 226, No. 6 (1993).
[7] B.M. Sherrill et al., NIM B **56/57**(1991)1106.
[8] N.A. Orr et al., Phys. Rev. Lett. **69**(1992)2050.
[9] W. Schwab et al., Scientific Report 1992 GSI-93-1,p.22.
[10] H. Irnich, PhD in preparation.
[11] H. Geissel et al., NIM B**70**(1992)286.
[12] K. Sümmerer et al., Contribution to this Conference.
[13] F. Humbert et al., Scientific Report 1992 GSI-93-1,p.21.
[14] T. Kobayashi et al., Phys. Lett. B**232**(1989)51.
[15] Th. Blaich et al., NIM A**314**(1992)136.
[16] F. Humbert et al., to be published.
[17] H. Irnich et al., Scientific Report 1992 GSI-93-1,p.363.

Scattering and Particle Production

THE DISAPPEARANCE OF FLOW, CRITICAL BEHAVIOR, AND THE ONSET OF MULTIFRAGMENTATION

Gary D. Westfall
National Superconducting Cyclotron Laboratory and
Department of Physics and Astronomy
Michigan State University
East Lansing, Michigan 48824-1321 USA
for the 4π Collaboration

I. INTRODUCTION

The nuclear equation of state (EOS) is very basic information concerning the response of nuclear matter to compression and excitation.[1] One way of representing the EOS is shown in Figure 1. In this figure, the energy per nucleon of nuclear matter is plotted versus the density for a schematic description of the EOS corresponding to a stiff EOS (K=380 MeV) and a soft EOS (K=200 MeV) where K is the nuclear incompressibility. In the region of compression accessible using beams from the NSCL K1200 Superconducting Cyclotron, compressions of up to 1.5 normal nuclear matter densities are predicted in transport theories such as BUU corresponding to energy differences of several MeV per nucleon. Another way of representing the EOS is shown in Figure 2 in which the pressure is plotted as a function of the density for several isotherms.[2] In this representation, the critical point of nuclear matter can be located and a critical temperature defined. The critical temperature in this plot is 16.5 MeV.

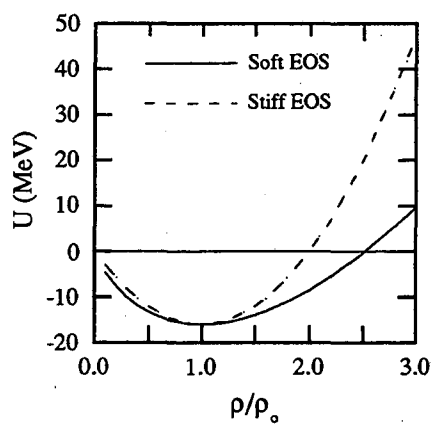

Figure 1. Equation of state of infinite nuclear matter for soft and stiff equations of state.

In order to study the EOS, we must prepare the system with a known excitation and known number of participant nucleons. In the present talk, we will carry out this task by selecting central collisions of nearly symmetric systems. This method allows us to specify the number of participant nucleons and to vary the excitation energy of the system by varying the incident energy. The type of collisions being studied here are illustrated in Figure 3 by an event recorded using the MSU CCD camera system at the LBL Streamer Chamber at the Bevalac.[3] In this picture, a 70 MeV/nucleon La nucleus collides with a target La nucleus. Visible in the event are many light particles and several highly ionizing tracks which are intermediate mass fragments (IMFs).

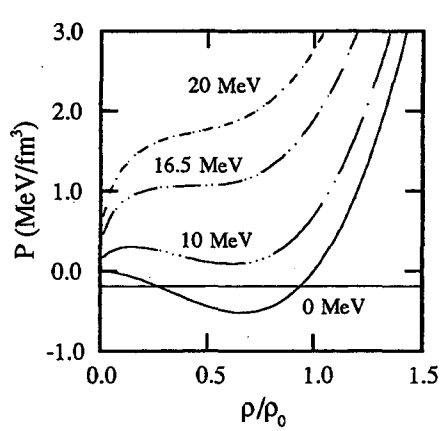

Figure 2. Representation of the EOS depicting pressure versus nuclear density for various isotherms.

Pioneering work concerning the EOS was done by the Plastic Ball group using the observable of collective flow.[4] Comparing these results with transport models such as BUU enabled researchers to extract information about the compressibility of nuclear matter. At high incident energies, the reaction between two nuclei

was found to be dominantly repulsive. A low incident energies, the interaction between two nuclei is dominantly attractive. At an incident energy termed the balance energy, E_{bal}, the repulsive interaction balances the attractive interaction and collective flow disappears. systematic study of E_{bal} can yield information about the EOS by comparing the measured values with predictions of the BUU model which incorporates the attractive interaction through the nuclear mean field and the repulsive interaction through nucleon-nucleon scattering.[5-7] An advantage of using E_{bal} to carry out studies of the EOS is that a detailed treatment of the effects of detector acceptance on the predictions of BUU is not necessary.

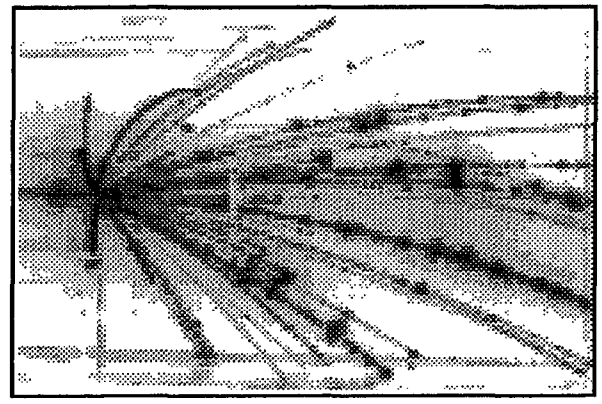

Figure 3. Streamer chamber picture using the MSU CCD camera system of a reaction of La+La at 70 MeV/nucleon.

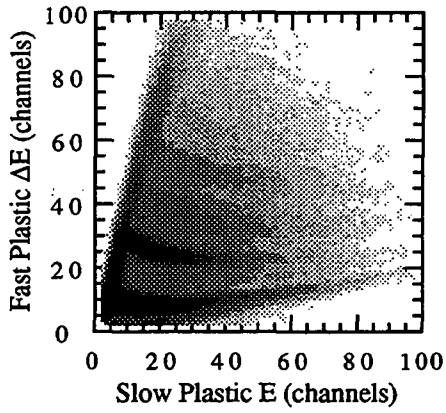

Figure 4. Fast plastic ΔE versus slow plastic E for typical phoswich counter in the MSU 4π Array.

Another observable that can be related to the EOS is Z distributions. This observable carries information concerning the breakup of the system after it is heated and compressed. These data may also carry signals of the liquid-gas phase transition in nuclear matter. A related phenomenon is multifragmentation which is defined as the prompt breakup of the interaction region in to many intermediate mass fragments (IMFs). Specifically, a systematic study of the onset of nuclear multifragmentation is crucial to the understanding of nuclear matter.

To study these concepts, we have carried out a systematic set of measurements using the MSU 4π Array and beams from the NSCL K1200 Superconducting Cyclotron. The MSU 4π Array consists of 215 fast/slow plastic phoswich counters and 55 Bragg curve counters. Figure 3 shows a two dimensional histogram of ΔE vs. E for a typical phoswich counter. In Figure 4, a typical two-dimensional spectrum from a Bragg curve counter versus the fast plastic counter demonstrates the resolution obtained for Z=2 fragments and heavier.

The systems studied include C+C, Ne+Al, Ar+Sc, Kr+Nb, and Xe+La at beam energies ranging from 15 to 155 MeV/nucleon.[5-7] In all cases, data were taken with a trigger condition requiring two particles in any of the 215 phoswich counters producing minimum bias data sets. For the flow data presented below, central collisions were chosen by taking the 10% most central events using transverse momentum. The reaction plane was determined using the method of azimuthal correlations.

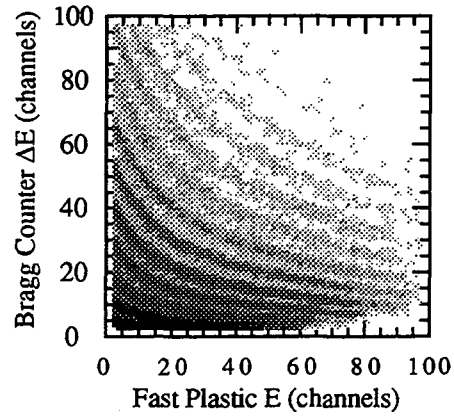

Figure 5. Typical Bragg curve counter ΔE versus fast plastic E showing resolution of IMFs from Z=2 to 13.

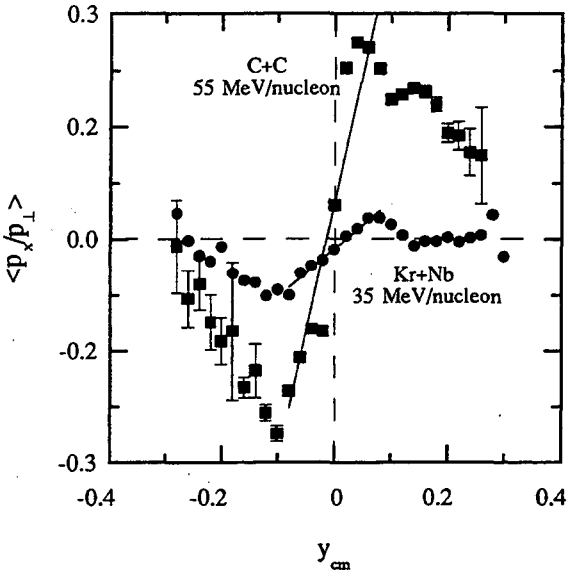

Figure 6. Average transverse momentum in the reaction plane as a function of rapidity in the center of mass for 55 MeV/nucleon C+C and 35 MeV/nucleon Kr+Nb.[7]

For the Z distribution from Ar+Sc presented below, the 10% most central events were selected using midrapidity charge, Z_{mr}, transverse momentum, p_t, and charged particle multiplicity, N_{chg}, combined into one scaled variable $\sqrt[3]{\left(Z_{mr}/Z\right)\left(p_t/p_{proj}\right)\left(N_{chg}/Z\right)}$ where Z is the charge of the combined projectile/target system and p_{proj} is the projectile momentum.[8,9]

2. The Disappearance of Flow

In Figure 6, the average transverse momentum in the reaction plane divided by the total transverse momentum, $\langle p_x/p_\perp \rangle$, is plotted versus the rapidity in the center of mass frame, y_{cm}. for alpha particles from the reactions of C+C, and Kr+Nb.[7] One can see the S-shaped curve characteristic of collective flow measured at higher energies. The reduced flow is defined as the slope of this curve from $0.8 * y_{tar} \le y_{cm} \le 0.8 * y_{pro}$ where y_{tar}, y_{pro} are the target, projectile rapidities in the center of mass, respectively.

In Figure 7, the reduced flow is plotted for protons from Ar+Sc at incident energies ranging from 35 to 115 MeV/nucleon. The reduced flow decreases with increasing incident energy up to about 85 MeV/nucleon after which the reduced flow begins to increase again. The incident energy at which the reduced flow disappears, E_{bal}, is readily apparent in this figure.

We associate the reduced flow values at incident energies below E_{bal} with attractive scattering and flow values above E_{bal} with repulsive scattering according to expectations from BUU calculations. To extract a quantitative value for E_{bal}, we employ the method of inverting the flow values at low energies. A straight line is then fit to the resulting points as shown in Figure 7. This method depends on the choice of which points to flip. The systematic error caused by the ambiguity in flipping the reduced flow values is included in the systematic error for the extracted E_{bal}.

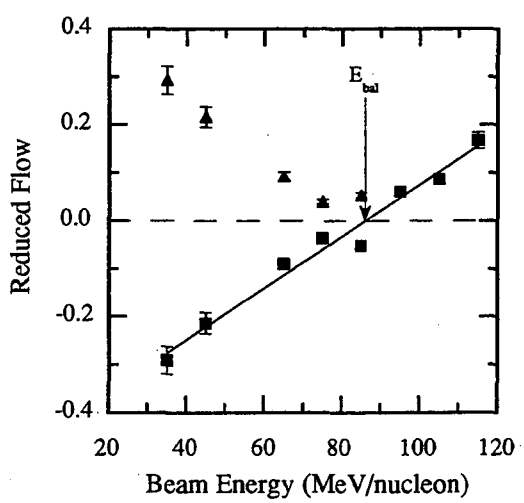

Figure 7. Reduced flow values for protons from Ar+Sc. The squares represent reduced flow values that were inverted below the balance energy as described in the text.[7]

In Figure 8, the independence of the balance energy on particle type is demonstrated for reduced flow values for p,d,t, and He fragments from Ar+Sc. The method described above was employed and one can see that the

resulting values of E_{bal} are nearly independent of the particle type.

The extracted balance energies as a function of the combined system mass, A, for C+C, Ne+Al, Ar+Sc, and Kr+Nb[7] are shown in Figure 9 along with a previously measured point for Ar+V[6]. Error bars shown in this figure include both statistical and systematic errors. The solid line in Figure 8 depicts a power law of the form $A^{-1/3}$. This behavior is consistent with the idea that the balance energy represents the competition between the attractive interaction, which should scale as the surface, $A^{-2/3}$. and the repulsive interaction, which should scale as the volume of the nuclei, A.

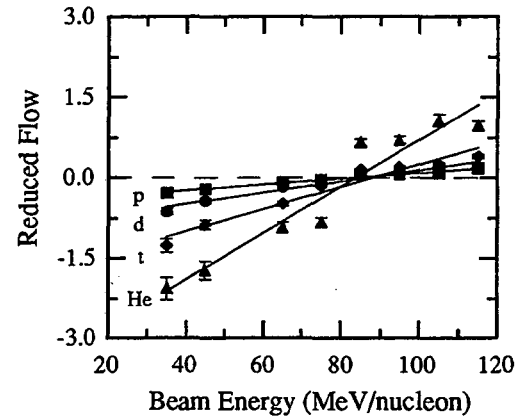

Figure 8. Reduced flow values for p, d, t, and He fragments from Ar+Sc. The lower energy points are inverted as described in the text.[7]

Also shown in Figure 9 are BUU calculations for the balance energy as a function of system mass. Two calculations are shown corresponding to a soft EOS (K=200 MeV) and a stiff EOS (K=380 MeV). Both sets of calculation under predict the measured balance energies and there is no clear differentiation between the predictions for soft and stiff EOS. However, the BUU calculations do reproduce the trend in the measured balance energies with system mass confirming the interpretation of the balance energy as an interplay between attractive and repulsive interactions. The BUU calculations incorporate the attractive interaction through the mean field and the repulsive interaction through nucleon-nucleon scattering.

There is strong theoretical evidence that the nucleon-nucleon scattering cross sections may be lowered in the nuclear medium. This effect will raise the predicted balance energies. The in-medium reduction of the nucleon-nucleon cross sections should depend on the energy of the nucleons and the density at which the interactions occur. As a first approximation, Bauer and Klakov expressed the nucleon-nucleon cross sections in-medium, σ_{nn}, in terms of the free nucleon-nucleon cross sections, σ_{nn}^{free}, $\sigma_{nn} = (1 + \alpha_1 \frac{\rho}{\rho_0})\sigma_{nn}^{free}$ where α_1 is a parameter representing the density dependent reduction of the nucleon-nucleon cross sections.[7] In Figure 10, the extracted balance energies are plotted along with the BUU predictions for a soft EOS, predictions for a soft EOS with α_1 = -0.1, and predictions for a soft EOS with α_1 = -0.2. The reduction in nucleon-nucleon cross section indeed raises the predicted balance energies. For α_1 = -0.2

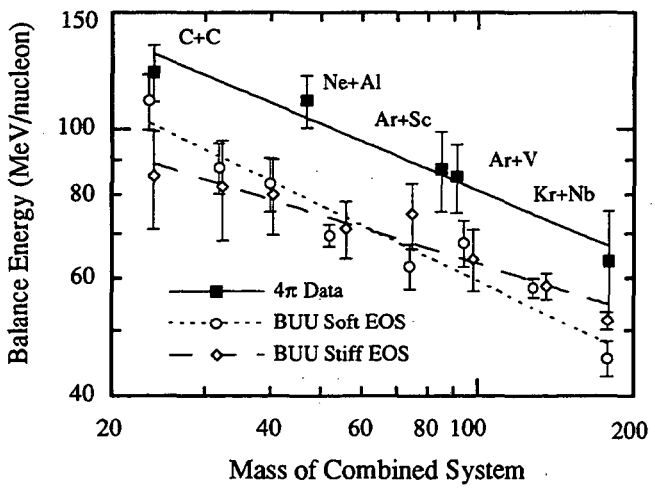

Figure 9. Extracted balance energies for C+C, Ne+Al, Ar+Sc, and Kr+Nb.[7] The value for Ar+V is from previous work.[6] The solid line is a fit of the fit $A^{-1/3}$. BUU calculation are shown for a soft EOS (K=200 MeV) and a stiff EOS (K=380 MeV). The dashed and dotted lines correspond to power law fits.

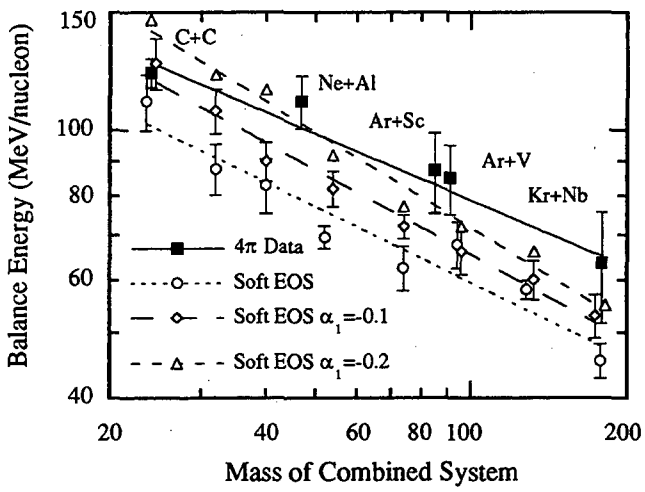

Figure 10. Extracted balance energies for C+C, Ne+Al, Ar+Sc, and Kr+Nb.[7] Value for Ar+V is from previous work.[6] BUU calculations are shown for a soft EOS and for 10 and 20% density dependent reductions of the in-medium nucleon-nucleon cross sections.

initial compression state is followed by a final expansion state. A systematic study of these collisions will provide information about the thermodynamic properties of nuclear matter and thus about the EOS if finite size effects are taken into account. A liquid-gas phase transition has been predicted to occur in nuclear matter. The cluster size at the critical point is given by $A^{-\tau}$ where τ is the critical exponent and A is the cluster size. For small systems in the vicinity of the critical point, the A distribution can be fit by a power law with an apparent exponent λ which has a minimum at the critical point.

To search for this critical point, we carried out a systematic study of central collisions (selected as described above) of Ar+Sc from 15 to 115 MeV/nucleon.[8,9] This incident energy range covers excitation energies available in the center of mass from around 4 MeV/nucleon up to 30 MeV/nucleon. The observable used was Z distributions which can be related to the cluster size distribution assuming $A \approx 2Z$. In Figure 11, the Z distributions from central collisions of Ar+Sc are shown for $1 \leq Z \leq 12$. The cross sections have been corrected for experimental acceptance and each higher energy has been divided by a factor of 5 for clarity of presentation. The Z distributions are steep at 115 MeV/nucleon and get progressively flatter as the beam energy is lowered. At 25 MeV/nucleon, the maximum flatness is reached. The Z distributions can be characterized by power law distributions .

qualitative agreement between the data and the predictions is obtained. However, the predicted balance energies decrease more quickly with mass than the observed values. Thus from Figure 9 and 10 we observe that the study of balance energies cannot distinguish whether the EOS is soft or stiff. However, the BUU predictions are sensitive to the in-medium nucleon-nucleon cross sections and a density dependent reduction of around 20% provides qualitative agreement with experiment.

II. Critical Phenomena in Nuclear Matter

In central collisions, an

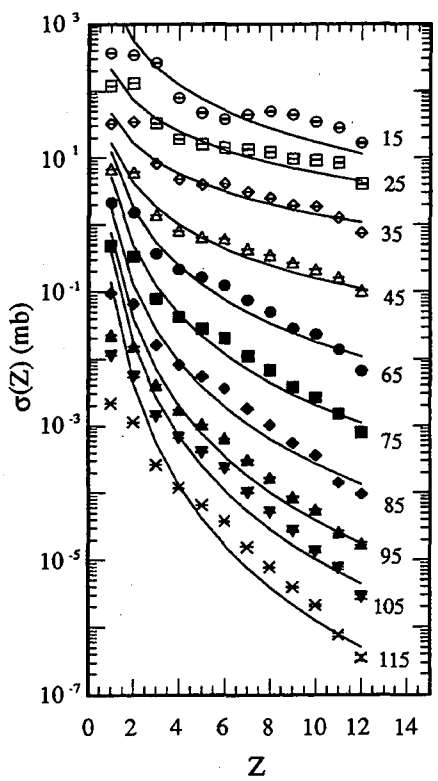

Figure 11. Z distributions from central collisions of Ar+Sc from 15 to 115 MeV/nucleon. Data from each higher energy are divided by a factor of 5. Lines represent power law fits for $3 \leq Z \leq 12$.[9]

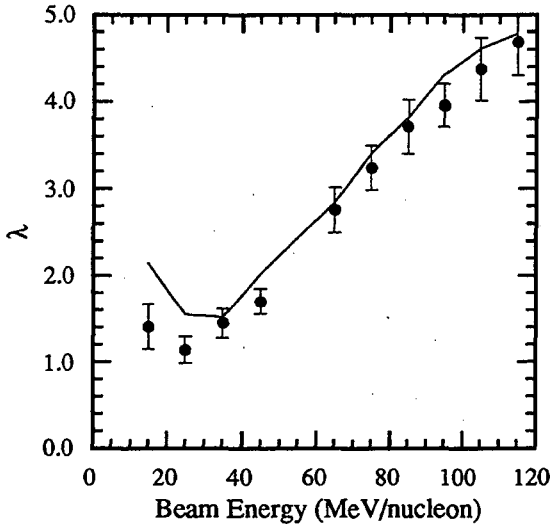

Figure 12. Power law parameters extracted from Z distributions from central collisions of Ar+Sc. Solid line represents percolation calculations.[9]

In Figure 12, the power law exponent, λ, is plotted for $3 \leq Z \leq 12$ for the ten incident energies. A minimum is observed at 25 MeV/nucleon which could be a signal for critical phenomena. One method of interpreting these distributions is the percolation model in which one assumes that each nucleon is linked to it nearest neighbors by potential bonds. Each bond can absorb a maximum amount of energy and has a probability to break of P_b. To relate the incident energy to P_b we assume that the energy distributed into each bond can be described by a Boltzmann distribution. P_b is then calculated as the probability of a nucleon having an energy above the binding energy using the proton energy spectra to determine the apparent temperature of the system.

Using this prescription, one can calculate the Z distributions based on a given binding energy and system size. In Figure 12, the solid lines show the power law parameter fitted to percolation calculations for a binding energy of 7.8 MeV/nucleon and a system size of 68 nucleons. This calculation shows a minimum in λ around 30 MeV/nucleon qualitatively reproducing the experimental results. One can use the percolation model to extrapolate our results for a finite system to nuclear matter by using the same parameters in the calculations except that the size of the system is increased. In Figure 13 the effective power law parameter is shown as a function of system size. One can see this parameter saturates at a value of about 2.3.

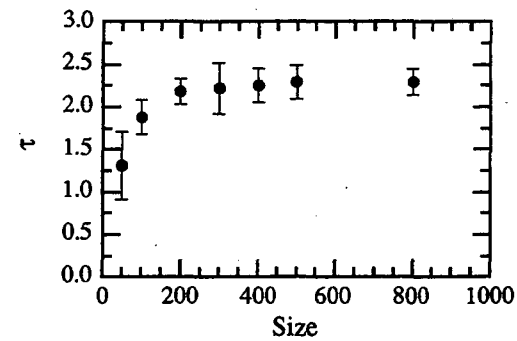

Figure 13. Effective power law parameter from the percolation model as a function of system size.

A corresponding extrapolation can be made for the apparent temperature. The apparent critical temperatures as a function of system mass are shown in Figure 14. Here the temperature saturates at a value around 13.1 MeV. Thus, an extrapolation of the measurement of the maximum flatness of the Z distributions from central collisions of Ar+Sc yields a critical exponent of nuclear matter of 2.3±0.2 and a critical temperature of 13.1±0.6 MeV.

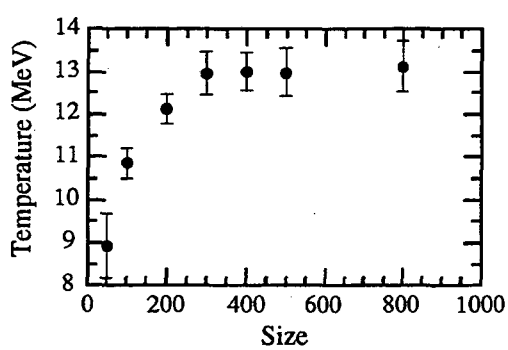

Figure 14. Apparent critical temperature from the percolation model as a function of system mass.

IV. The Onset of Multifragmentation

Multifragmentation is defined as the simultaneous breakup of a hot nuclear system into three or more IMFs. This type of breakup is contrasted with sequential, two body emission. Multifragmentation has been observed by several

groups. However, the onset of this phenomenon is not well understood. In this paper, we will present a systematic set of data concerning multifragmentation using two observables.[10,11] The first is the average number of IMFs, $\langle N_{imf} \rangle$, versus the charged particle multiplicity, N_{ch}. This variable is related to the multifragment character of the breakup of the system. However, a definitive statement concerning the dynamics of the system probably requires additional measurements. A sensitive way to attack this question is to study the shapes of the events in momentum space. Any kinematic correlations resulting from breakup of the system will be reflected in the shape of the event in momentum space. For example, a fission-like event will be greatly elongated in momentum space due to the large, opposite recoiling momentum of the two fission fragments. The systems studied include Ne+Al, Ar+Sc, Kr+Nb, and Xe+La from 15 to 140 MeV/nucleon.

Comparing different systems can give a more clear picture of the onset of multifragmentation. In Figure 15, $\langle N_{imf} \rangle$ versus N_{ch} is shown for central collisions of Ne+Al, Ar+Sc, Kr+Nb, and Xe+La as several representative incident energies. Note the dramatic change in the number of IMFs as the system mass is increased. For Ne+Al, $\langle N_{imf} \rangle$ is always below 1 while for Xe+La values of $\langle N_{imf} \rangle$ approaching 6 are observed.[10] In these data are clear candidates for multifragmentation. However, the understanding of these events in more detail

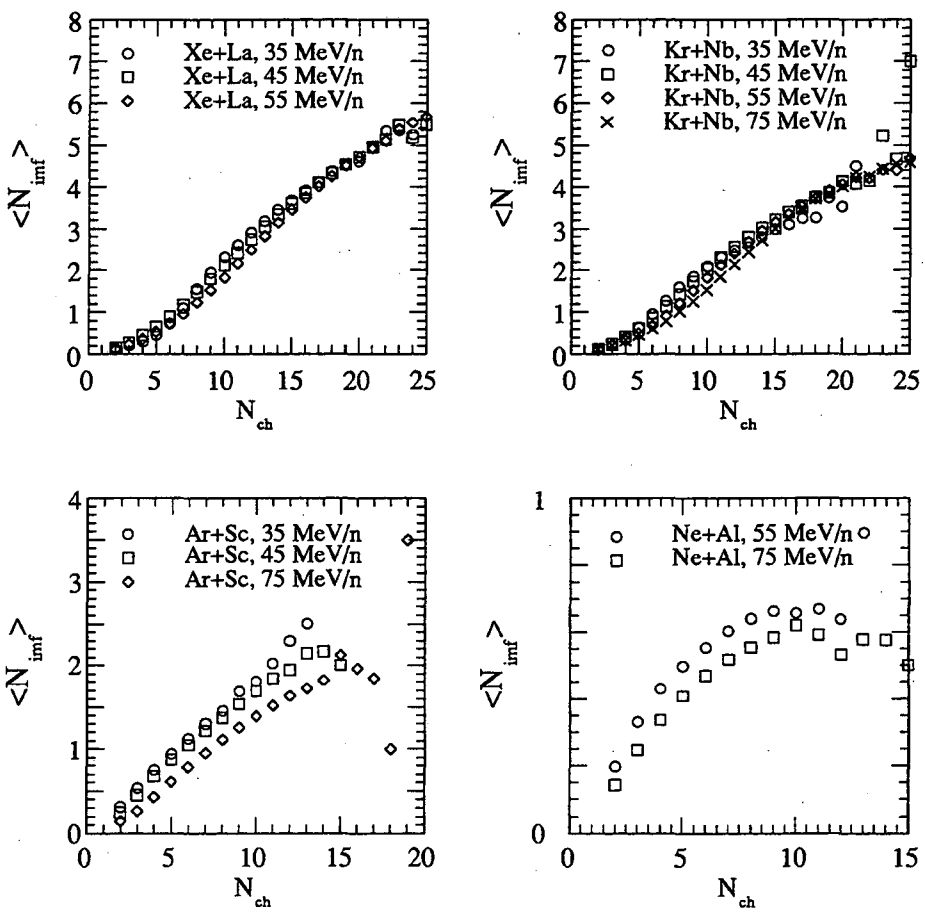

Figure 15. Average number of IMFs versus charged particle multiplicity.

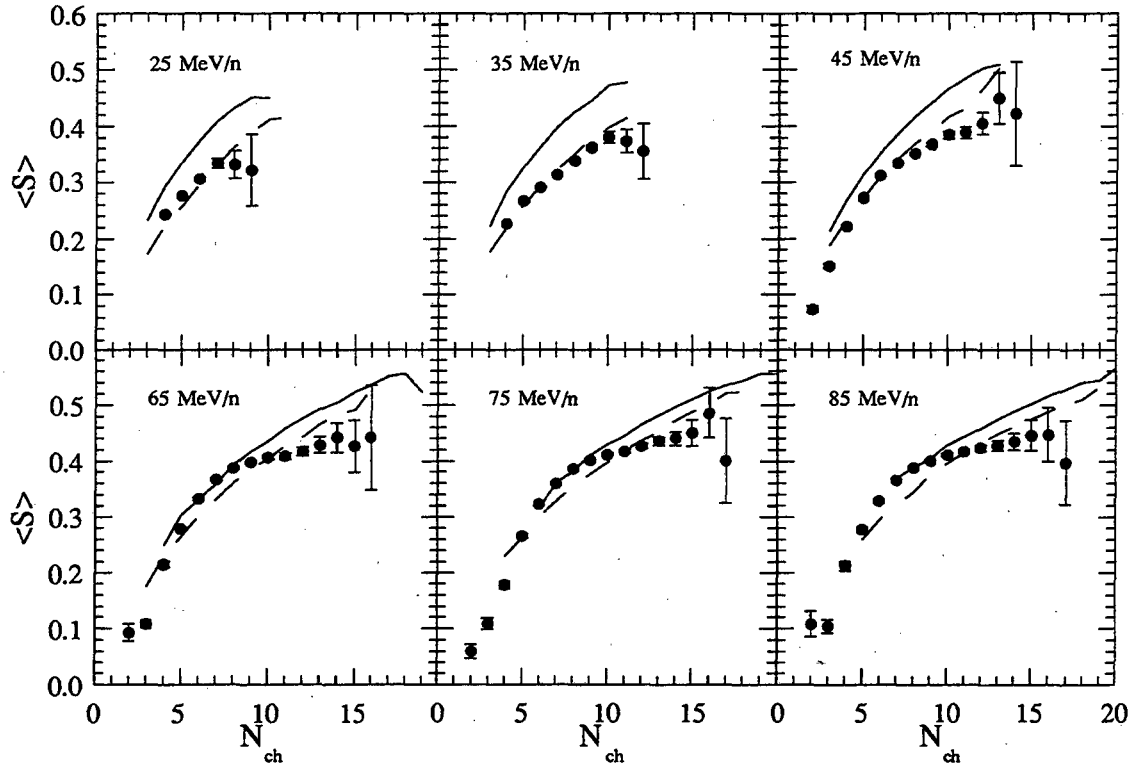

Figure 16. Average sphericity versus charged particle multiplicity for Ar+Sc reactions. Solid lines stand for multifragmentation calculations and dashed lines stand for sequential emission calculations.[11]

concerning the breakup mechanism requires more information.

One method of demonstrating the onset of multifragmentation is to model the collisions with a theory that incorporates sequential emission and with a theory that describes multifragmentation as a function of incident energy. By comparing the two sets of calculations with a systematic set of data, a trend can be demonstrated. The model comparisons shown below use the BUU model to characterize the initial conditions of the reactions including the number of participant nucleons and the excitation of the system.[10,11]

Using these initial conditions, the model GEMINI was used to describe the evolution of the system in terms of sequential two body decay. Two models were used to treat multifragmentation, the Berlin model and the Copenhagen model. The observable chosen for comparison is the average sphericity. Sphericity is a measure of the shape of the event in momentum space and can be defined in terms of an energy/momentum tensor. The ordered eigenvalues can be extracted from this tensor and used to produce reduced quantities which can be related to sphericity . A value of $\langle S \rangle = 1$ corresponds to a completely spherical distribution in momentum space. However, finite multiplicity decreases the observed $\langle S \rangle$. To account for this effect, we simply plot $\langle S \rangle$ versus N_{ch} which explicitly treats the multiplicity dependence.

In Figure 16, $\langle S \rangle$ is shown as a function of N_{ch} for reaction of Ar+Sc from 25 to 85 MeV/nucleon. The solid lines correspond to multifragmentation calculations and the dashed lines represent sequential calculations. At 25 MeV/nucleon, the emission patterns agree with the sequential calculations. As the beam energy is raised, a definite transition is observed above 45 MeV/nucleon from agreement with the sequential calculations to agreement with the multifragmentation results. At the highest energies, the difference between the two model calculations lessens.

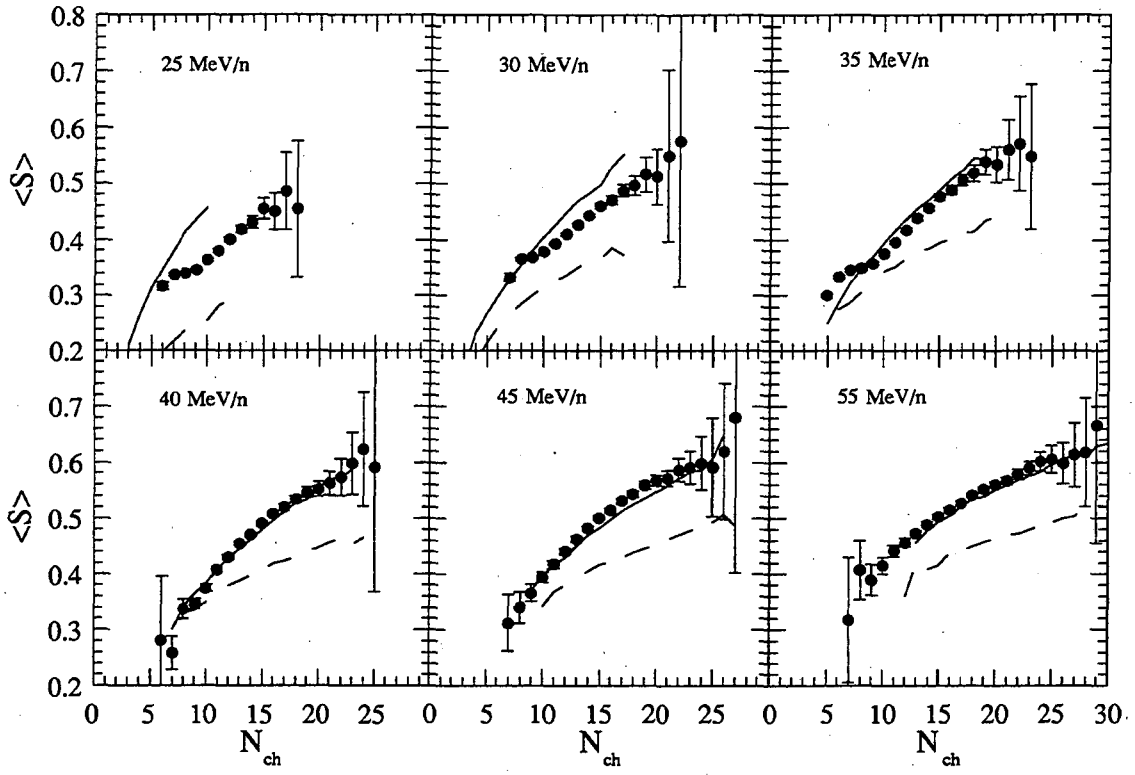

Figure 17. Average sphericity versus charged particle multiplicity for Ar+Sc reactions. Solid lines stand for multifragmentation calculations and dashed lines represent sequential calculations.[11]

To bolster this observation, the <S> is shown as a function of multiplicity for reactions of Xe+La from 25 to 55 MeV/nucleon. At the lowest energy, the model calculations bracket the experimental results. As the beam energy is raised, the comparison between models and data definitely favors the interpretation that multifragmentation is occurring at the highest energies and that a strong transition takes place around 35 MeV/nucleon.[10,11]

V. Conclusions

The mass dependence of the disappearance of flow has been measured and compared with BUU calculations. The BUU prediction for E_{bal} do not depend strongly on K while they are very sensitive to the in-medium cross sections. A 20% density dependent reduction of the in-medium cross section produces qualitative agreement with the measure balance energies. Central collisions of Ar+Sc have the flattest Z distributions at 25 MeV/nucleon which may signal critical phenomena at this energy. Using a percolation calculation, this result can be extended to nuclear matter. The onset of multifragmentation has been observed in Ar+Sc around 45 MeV/nucleon and in Xe+La around 35 MeV/nucleon using a shape analysis technique.

VI. References

1. Subal Das Gupta and Gary D. Westfall, *Physics Today* **46**, No. 5, 34 (1993).

2. Joseph Kapusta, Phys. Rev. **C29**, 1735 (1984).

3. D. Krofcheck, G.M. Crawley, C. Djalali, S. Howden, C.A. Ogilvie, A. Vander Molen, G.D. Westfall, W.K. Wilson, and R.S. Tickle, Nucl. Inst. Meth. **A288** 497 (1990).

4. H.H. Gutbrod, A.M. Poskanzer, and H.G. Ritter, Rep. Prog. Phys. **52**, 1267 (1989), and references therein.

5. C.A. Ogilvie, W. Bauer, D.A. Cebra, J. Clayton, S. Howden, J. Karn, A. Nadasen, A. Vander Molen, G.D. Westfall, W.K. Wilson, and J.S. Winfield, Phys. Rev. **C42**, R10 (1990).

6. D. Krofcheck, D.A. Cebra, M. Cronqvist, R. Lacey, T. Li, C.A. Ogilvie, A. Vander Molen, K. Tyson, G.D. Westfall, W.K. Wilson, J.S. Winfield, A. Nadasen, and E. Norbeck, Phys. Rev. **C43** 350, (1991).

7. G.D. Westfall, W. Bauer, D. Craig, M. Cronqvist, E. Gualtieri, S. Hannuschke, D. Klakow, T. Li, T. Reposeur, A.M. Vander Molen, W.K. Wilson, J.S. Winfield, Y. Yee, S.J. Yennello, R. Lacey, A. Elmaani, J. Lauret, A. Nadasen, and E. Norbeck, Phys. Rev. Lett. **71**, 1986 (1993).

8. T. Li, W. Bauer, D. Craig, M. Cronqvist, E. Gualtieri, S. Hannuschke, R. Lacey, W.J. Llope, T. Reposeur, A.M. Vander Molen, G.D. Westfall, W.K. Wilson, J.S. Winfield, J. Yee, S.J. Yennello, A. Nadasen, R.S. Tickle, and E. Norbeck, Phys. Rev, Lett. **70**, 1924 (1993).

9. T. Li, W. Bauer, D. Craig, E. Gualtieri, S. Hannuschke, W. J. Llope, R. Pak, A. M. Vander Molen, G. D. Westfall, J. S. Winfield, J. Yee, S. J. Yennello,
R. Lacey, A. Nadasen, R. S. Tickle, and E. Norbeck, Phys. Rev. C in press (1993).

10. W.J. Llope, D. Craig, E. Gualtieri, S. Hannuschke, R.A. Lacey, T. Li, A. Nadasen, E. Norbeck, R. Pak, N. Stone, A.M. Vander Molen, G.D. Westfall, J.S. Winfield, J. Yee, and S.J. Yennello, MSUCL-900, submitted to Physical Review C, 1993.

11. W.J. Llope, C.M. Mader, W. Bauer, J. Conrad, D. Craig, E. Gualtieri, S. Hannuschke, R.A. Lacey, T. Li, A. Nadasen, E. Norbeck, R. Pak, N. Stone, A.M. Vander Molen, G.D. Westfall, J. Yee, and S.J. Yennello, MSUCL-907, submitted to Physical Review Letters, 1993.

High-Energy Pions: A Probe for the Hot and Dense Collision Zone?+

C. Müntz (TH Darmstadt)
for the KaoS Collaboration*: GSI Darmstadt, TH Darmstadt, Univ. Frankfurt/Main, Univ. Marburg (Germany), Univ. Kraków (Poland)

Abstract: *The double differential cross sections of positive pions from collisions of Ne+NaF and Au+Au at 1 GeV/nucleon incident energy were studied close to midrapidity with the Kaon Spectrometer at SIS. In this talk I would like to point out the production of high-energy pions produced beyond the free nucleon-nucleon kinematical limit. Their yield increases more than linearly with the number of participating nucleons. High-energy pions are interpreted as originating from decaying Δ_{33} resonances, preferentially populated in the high-density phase of the reaction. They represent a tool to probe the hot and dense reaction zone.*

One well-established tool for studying the properties of hot and compressed nuclear matter is the investigation of subthreshold particle production in heavy-ion collisions [1]. At incident energies around 1 GeV/nucleon the production of kaons is expected to be a sensitive probe of the hot and dense nuclear matter which is formed in energetic heavy-ion collisions [2, 3]. Their production mechanism is strongly linked to the excitation of baryonic resonances [4, 5] dominated by the Δ_{33} resonance in this energy regime. Therefore, the dynamics of resonance formation in heavy ion collisions has to be understood. Since the main decay channels of these resonances contain pions, the detailed study of pion production in relativistic heavy-ion collisions is of high interest. I want to present data on positive pions emitted close to midrapidity for two mass-symmetric systems Au+Au and Ne+NaF at 1 GeV/nucleon incident energy as a function of the centrality of the collision. Emphasis is put to the properties of high-energetic pions, i.e. those with kinetic energies above the free kinematical nucleon-nucleon limit of 447 MeV.

The experiments have been performed with the Kaon Spectrometer [6] installed at SIS/GSI. The spectrometer covers a solid angle of $\Omega = 15 - 35$ msr with a momentum resolution over the full solid angle of $\delta p/p \simeq 1\%$. The SIS accelerator has provided beam intensities of 2×10^5 Au and 6×10^7 Ne projectiles per spill. Targets of 1.93 g/cm^2 and 0.45 g/cm^2 for Au and NaF have been used, respectively. The positive pions are detected in a momentum range of 150–1100 MeV/c and in an angular range of 40–48 degrees. This corresponds to normalized rapidities of $0.50 < y/y_{Beam} < 0.75$. The pions are identified by a time-of-flight measurement together with a tracking analysis. Pions from central and peripheral collisions are separated by means of the hit multiplicity of charged particles in the Large Angle Hodoscope (LAH), a 96-fold segmented detector at angles of 12–48 degrees close to the target. In this angular range participating proptons are the most abundant particles. The impact-parameter selection has been controlled [7] by the correlation of this multiplicity with the summed nuclear charges of spectator-like particles observed in the Small Angle Hodoscope (SAH). This 380-fold segmented detector, located 7 m downstream of the target, covers polar angles between 0.5 and 11 degrees where predominantly spectator fragments are emitted.

Figure 1 (left part) shows the inclusive, acceptance-corrected invariant production cross sections of positive pions observed in the symmetric mass systems Au+Au and Ne+NaF at 1 GeV/nucleon incident energy as a function of the total pion energy in the c.m. system. The

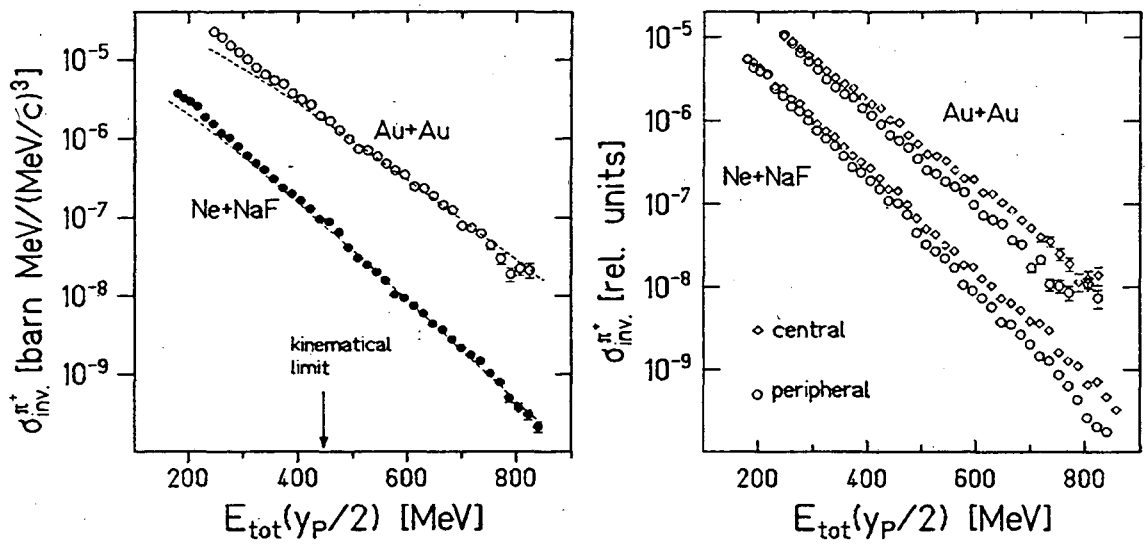

Figure 1: *Left part: Invariant production cross sections of positive pions for Au+Au (open circles) and Ne+NaF (full circles) reactions at 1 GeV/nucleon incident energy as a function of the total pion energy in the midrapidity system. The dashed lines indicate a Maxwell-Boltzmann fit to the high-energy tails of the spectra above the free kinematical limit of 447 MeV total pion energy, marked by an arrow.*
Right part: The spectra of positive pions from central and peripheral collisions. The centrality selection is performed via the charged particle multiplicity in the Large Angle Hodoscope, see text.

pions are assumed to be emitted from a source located at midrapidity in the polar angular range covered by the spectrometer. The measured shapes cannot be described by a single thermalized pion source at midrapidity. This deviation is illustrated, for example, by the dashed lines in Fig. 1 (left part) representing Maxwell-Boltzmann distributions $\sigma_{inv} \propto E \exp(-E/T)$ fitted to the high-energy tails of the spectra. The slope parameter of the high-energy part increases with the mass of the collision system. They are $T = 76 \pm 3$ MeV for Au (top) and $T = 61 \pm 3$ MeV for Ne (bottom).

In order to study the variation with impact parameter the spectra from central and peripheral collisions are compared in Fig. 1 (right part). They are distinguished by the multiplicity of charged particles Z_{LAH} in the Large Angle Hodoscope ($Z^{Au}_{LAH}(central) > 50$, $Z^{Au}_{LAH}(peripheral) < 32$, $Z^{Ne}_{LAH}(central) > 13$, $Z^{Ne}_{LAH}(peripheral) < 5$) and adjusted to match in the low-energy part. For the heavy-mass system the corresponding number of participating nucleons A_{part} is deduced from the simultaneously measured summed projectile charge Z^{sum}_{proj} in the Small Angle Hodoscope by $A_{part} = A/Z \times 2 \times (Z - Z^{sum}_{proj})$ [8] with A and Z the mass and charge of the gold nucleus giving $A^{Au}_{part}(central) > 230$ and $A^{Au}_{part}(peripheral) < 130$. The small sensitivity on the centrality is reflected by a minor variation of the slope parameter T of the asymptotic high-energy slopes by

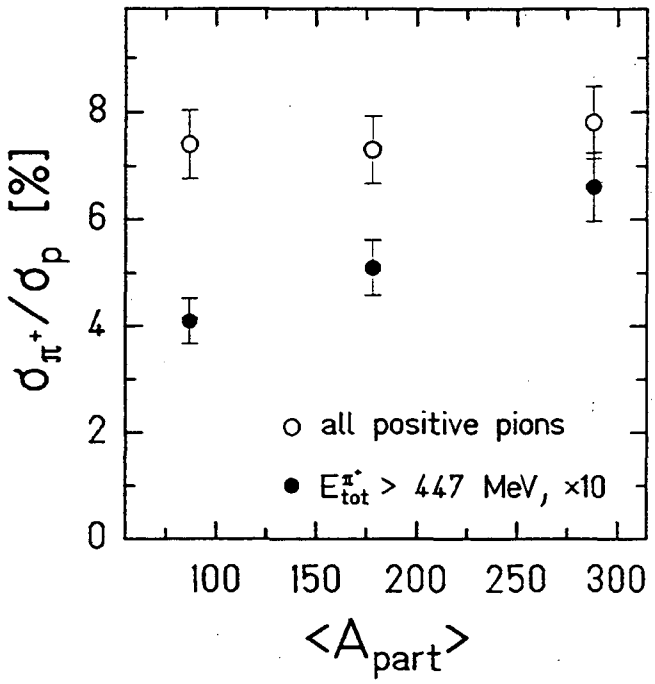

Figure 2: *The ratio of the energy-integrated cross sections for positive pions to protons from Au+Au reactions as a function of the average number of participating nucleons A_{part}. The open symbols represent the integral over all pion energies while for the full symbols only pions with E_{tot} > 447 MeV are taken into account. The error bars are dominated by errors due to normalization, statistical errors can be neglected.*

5 ± 2 MeV (3 ± 1 MeV) for Au+Au (Ne+NaF) reactions. This result is in contrast to the proton spectra which are measured in the same runs; they exhibit a more pronounced variation with the reaction centrality by 30 ± 5 MeV (13 ± 5 MeV) [9]. *The small variation of the slope parameter of the high-energy part of the pion spectra underlines that a thermal interpretation of the pion spectra even for high-energy pions is not justified.*

To obtain further insight into the mechanism of the pion emission Fig. 2 represent the ratio of the energy-integrated production cross sections (open data points) for positive pions to the proton cross sections for the Au+Au reaction as a function of the reaction centrality given by the average number of participating particles A_{part}. The proton cross sections are the integral over a Maxwell-Boltzmann distribution fitted to the high-energy protons with 800 MeV/c $\leq p_{Lab} \leq$ 1440 MeV/c emitted close to midrapidity. They define the size of the reaction volume, i.e. the number of participating nucleons. The pion cross sections are the results of the integral over the sum of two Maxwell-Boltzmann distributions which represents a proper fit of the pion spectra [9]. The open data points exhibit no significant dependence of the energy-integrated pion to proton ratio on the centrality. This result demonstrates that the number of pions which is dominated by the low-energy part of the spectra, exhibits a linear increase with the number of participating nucleons as already reported in [10].

A totally different behaviour is observed if one selects high-energy pions as represented by the

full data points in Fig. 2. Now, the pion spectra are only integrated above the free kinematical limit of 447 MeV total energy in the center-of-mass frame. These high-energy pions are subthreshold particles at 1 GeV/nucleon incident energy. In contrast to the previous result the high-energy pion-to-proton ratio increases for more central collisions. This increase is even stronger if one selects higher and higher kinetic energies of the pions. Trivial absorption in spectator matter [11] does not seem to explain the data since the low-energetic pions do not exhibit such a trend although their absorption cross section is even higher. Such a dependence on the centrality has also been observed for the simultaneously measured positive kaons [8, 12, 13]. It has been interpreted as an experimental signature that subthreshold kaons are produced by preference in central collisions where multiple nucleon-nucleon collisions as well as secondary ΔN and πN collisions happen more frequently. This scenario seems valid also for high-energy pions and is confirmed in Fig. 1 (left part), where the production of high-energy pions in the low-mass system Ne+NaF is strongly reduced.

The interpretation of the results presented above is related to the understanding of the observed spectral shapes. In heavy-ion reactions in the energy regime of 1 GeV/nucleon pions are preferentially produced by the decay of Δ_{33} resonances. These resonances are excited in nucleon-nucleon collisions by $N\,N \rightarrow N\,\Delta$ or, in later stages of the reaction, when pions are more abundant, by the "absorption" of pions via $\pi\,N \rightarrow \Delta$. Hence, the Δ excitation and their decay kinematics play a key role in the interpretation of the pion spectra [14]. As the Q value of the Δ decay is comparable to the pion rest mass, the pion momentum depends strongly on the "effective" Δ mass whereas the momentum of the Δ resonance has a small effect. Therefore, we do not expect thermal spectra but those which are determined from the decay kinematics. This explains why the shapes of the pion spectra vary little with impact parameter in contrast to the behaviour of the proton spectra. However, the measured pion spectra can hardly be explained by assuming decaying thermalized Δ resonances with a Breit-Wigner mass distribution centered at 1232 MeV/c^2: The low- and the high-energy part of the spectrum is underpredicted [9]. Due to the permanent creation and decay of these resonances via $N\,N \rightleftharpoons N\,\Delta$ and $\pi\,N \rightleftharpoons \Delta$, the mass distribution is affected by the Δ-formation cross section and the relative energies available in these elementary nucleon-nucleon and nucleon-pion collisions. At a later stage of the collision these energies are lower and the mass distribution is populated preferentially at lower Δ masses. Hence, the experimental pion spectrum can be interpreted as a superposition of pions from decaying Δ resonances at various stages of the collision [15]. It reflects the decrease of the average available energy in nucleon-nucleon and nucleon-pion collisions due to the continuous cooling of the reaction zone. The high-energy part of the resonance mass distribution is preferentially excited in the early hot stage of the collision whereas the low-energy part is filled by preference in a later stage of the collision. This dynamical reduction of the mean Δ mass with time has already been reported in intra-nuclear-cascade calculations [16] as well as in BUU [17] and Isospin-QMD [18] calculations.

In conclusion, the double differential cross sections of positive pions have been measured in the reactions Au+Au and Ne+NaF at 1 GeV/nucleon incident energy. The shape of the spectra exhibits a significant dependence on the mass system. A small variation is found as a function of the centrality of the reaction. This observation can be understood by the fact that the slopes of the pion spectra do less reflect temperatures but mainly the decay kinematics of the Δ resonance. The total number of pions is proportional to the number of participating nucleons. In strong contrast to that the yield of high-energy pions - those produced beyond the free nucleon-nucleon kinematical limit - rises stronger with the number of participants which can be interpreted as signiture for multistep processes. The high-energy pions are assumed to originate from decaying

heavy-mass Δ_{33} resonances populated in multiple collisions during the early high-density phase of the collision and represent a new and promising probe of the hot and compressed collision zone.

References

[1] R. Stock, Phys. Rep. 135(1986)259.

[2] J. Aichelin et al., Phys. Rev. Lett. 58(1987)1926.

[3] W. Cassing et al., Phys. Rep. 188(1990)363.

[4] J. Aichelin, Phys. Rep. 202(1991)233.

[5] A. Lang, W. Cassing, U. Mosel, K. Weber, Nucl. Phys. A 541(1992)507.

[6] P. Senger et al., Nucl. Instr. Meth. A327(1993)393.

[7] W. Ahner et al., Z. Phys. A 341(1991)123.

[8] D. Miśkowiec et al., submitted to Phys. Rev. Lett.

[9] C. Müntz, PhD Thesis, Technische Hochschule Darmstadt (1993), ISNN 0171-4546, GSI report 93-41.

[10] J.W. Harris et al., Phys. Rev. Lett. 58(1987)463.

[11] P. Senger, these proceedings.

[12] P. Senger et al., Nucl. Phys. A553(1993)757c.

[13] E. Grosse, these proceedings.

[14] R. Brockmann et al., Phys. Rev. Lett. 53(1984)2012.

[15] B.A. Li, W. Bauer, Phys. Rev. C44(1991)450; B.A. Li, Nucl. Phys. A in press.

[16] J. Cugnon et al., Nucl. Phys. A379(1982)553.

[17] W. Ehehalt et al., Phys. Rev. C 47(1993)R2467.

[18] S.A. Bass, C. Hartnack, H. Stöcker and W. Greiner, submitted to Phys. Rev. Lett.; S.A. Bass, these proceedings.

[19] D. Brill et al., Phys. Rev. Lett. 71(1993)336.

+ supported by BMFT and GSI.

* I would like to thank the members of the KaoS-Collaboration:

P. Baltes, H. Oeschler, A. Sartorius, C. Sturm, A. Wagner (*Technische Hochschule Darmstadt, D-64289 Darmstadt, Germany*),
P. Beckerle, C. Bormann, D. Brill, Y. Shin, J. Stein, K. Stiebing, R. Stock, H. Ströbele (*Johann Wolfgang Goethe-Universität, D-60325 Frankfurt/Main, Germany*),
W. Ahner, R. Barth, M. Cieślak, M. Dębowski, E. Grosse, W. Henning (Present address: Argonne National Laboratory, Argonne, IL 60439, USA), P. Koczoń, D. Miśkowiec, R. Schicker, E. Schwab, P. Senger (*Gesellschaft für Schwerionenforschung, D-64220 Darmstadt, Germany*),
B. Kohlmeyer, H. Pöppl, F. Pühlhofer, B. Schlei, J. Speer, K. Völkel (*Philipps-Universität, D-35037 Marburg, Germany*),
W. Waluś (*Jagiellonian University, PL-30-059 Kraków, Poland*).

SUBTHRESHOLD KAON, ANTIKAON, AND ANTIPROTON PRODUCTION AT BEVALAC/SIS ENERGIES

G. Q. Li, C. M. Ko, X. S. Fang and Y. M. Zheng
Cyclotron Institute and Department of Physics
Texas A&M University, College Station, Texas 77843, USA

The study of particle production in heavy-ion reactions at energies that are below the thresholds for their production from the nucleon-nucleon interaction in free space is a topic of great interests in heavy-ion physics. The main purpose of this investigation is to learn about both the properties of dense nuclear matter and the in-medium properties of hadrons. First measurements of kaons, antikaons, and antiprotons from heavy-ion collisions at subthreshold energies were carried at the Bevalac at LBL in 1980s[1]. Recently, more systematic experiments for subthreshold particle production are being carried out at the SIS at GSI [2].

Nucleus-nucleus collisions at intermediate energies can be described by relativistic transport models [3-5] based on the Walecka-type effective Lagrangian [6]. At these energies, the colliding system consists mainly of nucleons, deltas and pions. Both their propagations in the mean-field potential and their mutual collisions are treated explicitly. The production of kaons, antikaons, and antiprotons are, however, treated perturbatively as their production probabilities are small at subthreshold energies. Nevertheless, we include explicitly their propagations in the mean-field potential and their interactions with baryons. In this way, we are able to treat quantitatively the effects due to rescatterings and reabsorptions. This is particularly important for antikaons and antiprotons as their absorption and annihilation cross sections are appreciable.

While the pion mean-field potential is neglected, the propagation of nucleons and deltas in the mean-field potential is treated according to the following equations of motion

$$\frac{d\mathbf{x}}{dt} = \frac{\mathbf{p}^*}{E^*}, \quad \frac{d\mathbf{p}}{dt} = -\nabla_x[E^* + (\frac{g_\omega}{m_\omega})^2\rho_B], \tag{1}$$

with $E^* = (m^{*2} + \mathbf{p}^{*2})^{1/2}$, $m^* = m - g_\sigma\langle\sigma\rangle$, and $p^*_\mu = p_\mu - g_\omega\langle\omega_\mu\rangle$. The expectation values of the scalar field $\langle\sigma\rangle$ and vector field $\langle\omega_\mu\rangle$ in the medium are determined from

$$m_\sigma^2\langle\sigma\rangle + b\langle\sigma\rangle^2 + c\langle\sigma\rangle^3 \approx g_\sigma\rho_s, \ \langle\omega_\mu\rangle = (g_\omega/m_\omega^2)\rho_\mu, \tag{2}$$

where the nuclear scalar density ρ_s and current density ρ_μ are

$$\rho_s = \int \frac{d^3\mathbf{p}^*}{(2\pi)^3} f(\mathbf{x},\mathbf{p}^*)m^*/E^*, \ \rho_\mu = \int \frac{d^3\mathbf{p}^*}{(2\pi)^2} f(\mathbf{x},\mathbf{p}^*)p^*_\mu/E^*. \tag{3}$$

In the above, $f(\mathbf{x},\mathbf{p}^*)$ is the nucleon phase-space distribution function.

As usual, we use m_σ= 550 MeV and m_ω= 783 MeV. The coupling constants and the strength of the sigma-meson self-interaction are determined by fitting the nuclear matter saturation properties, i.e., the saturation density ρ_0= 0.16 fm^{-3} and the energy per nucleon

$(\mathcal{E}/A)_{\rho_0}$= -16.0 MeV. Furthermore, we fix the nuclear matter incompressibility and the nucleon effective mass at ρ_0 to be K=200 MeV and $m^* = 0.83m$, respectively. This corresponds to the so-called soft equation of state. The parameters have been given in Ref. [7].

Furthermore, the following elastic and inelastic reactions among nucleons, deltas and pions are included,

$$NN \to NN,\ N\Delta \to N\Delta,\ \Delta\Delta \to \Delta\Delta, NN \leftrightarrow N\Delta, \Delta \leftrightarrow \pi N.$$

The standard Cugnon parametrizations and detailed-balance prescription are used for these two-body collisions [8,9].

Kaons are mainly produced from $BB \to NYK^+$. The parametrizations by Randrup and Ko [10] are used for kaon production in these elementary processes. For example, for kaon production from nucleon-nucleon interaction, we have

$$\sigma_{K^+}(\sqrt{s}) = 36.0\ \frac{p_{max}}{m_K}\ \mu b. \tag{4}$$

Medium effects are included by evaluating p_{max} using effective masses [11], i.e.,

$$p_{max} = \Big\{\frac{1}{4s^*}[s^* - (m^* + m_Y^* + m_{K^+}^*)^2][s^* - (m^* + m_Y^* - m_{K^+}^*)^2]\Big\}^{1/2},$$

with

$$m_Y^* = m_Y - \frac{2}{3}g_\sigma\langle\sigma\rangle,\ \sqrt{s^*} = (m_1^{*2} + \mathbf{p}_1^{*2})^{1/2} + (m_2^{*2} + \mathbf{p}_2^{*2})^{1/2} + \frac{1}{3}(\frac{g_\omega}{m_\omega})\rho_B.$$

In the mean-field approaximation to the chiral Lagrangian, the kaon effective mass in a medium is given by

$$m_K^* \approx m_K\Big(1 - \frac{\Sigma_{KN}}{m_K^2 f_K^2}\rho_s + \frac{3}{4}\frac{\rho_B}{f_K^2 m_K}\Big)^{1/2}. \tag{5}$$

Antikaons are mainly produced from $BB \to NNK^+K^-$. The antikaon production cross section in these elementary processes is parametrized by [12,13]

$$\sigma_{K^-}(\sqrt{s}) = 12.4\ \frac{p_{max}}{m_K}\ \mu b. \tag{6}$$

Again, p_{max} is calculated with in-medium masses, i.e.,

$$p_{max} = \Big\{\frac{1}{4s^*}[s^* - (2m^* + m_{K^+}^* + m_{K^-}^*)^2][s^* - (2m^* + m_{K^+}^* - m_{K^-}^*)^2]\Big\}^{1/2}.$$

Based on the G-parity transformation, the antikaon effective mass is given by

$$m_{\bar{K}}^* \approx m_K\Big(1 - \frac{\Sigma_{KN}}{m_K^2 f_K^2}\rho_s - \frac{3}{4}\frac{\rho_B}{f_K^2 m_K}\Big)^{1/2}. \tag{7}$$

Using the kaon decay constant $f_K \approx 97$ MeV and the KN sigma term $\Sigma_{KN} \approx 300$ MeV, we find that the kaon mass increases slightly with density while the antikaon mass decreases with density, as shown in Fig. 1.

Antiprotons are mainly produced from $BB \rightarrow NNp\bar{p}$. The antiproton production cross section in these elementary processes is parametrized as [7,14]

$$\sigma_{pp}^{\bar{p}}(\sqrt{s}) = 0.012\ (\sqrt{s} - \sqrt{s_0})^{1.846}\ \text{mb}, \tag{8}$$

with the in-medium threshold $\sqrt{s_0^*} = 4m^*$obtained from the G-parity transformation of the antiproton self-energies.

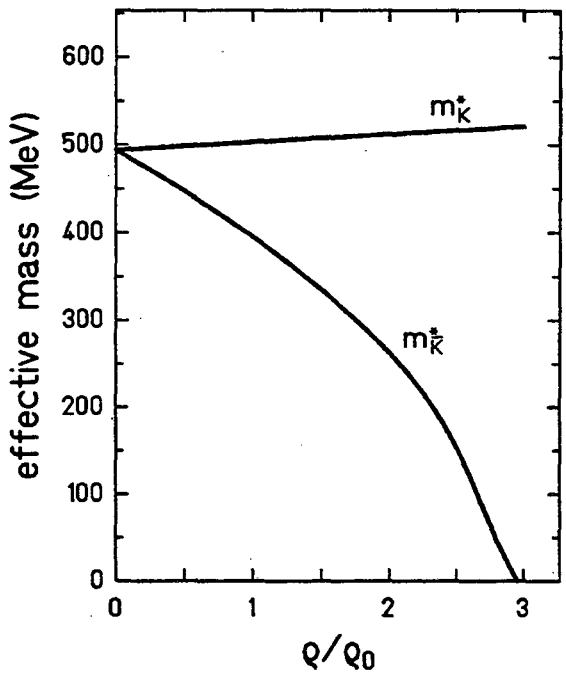

Fig. 1. Density dependence of the kaon and antikaon effective masses. ρ_0 =0.16 fm^{-3}.

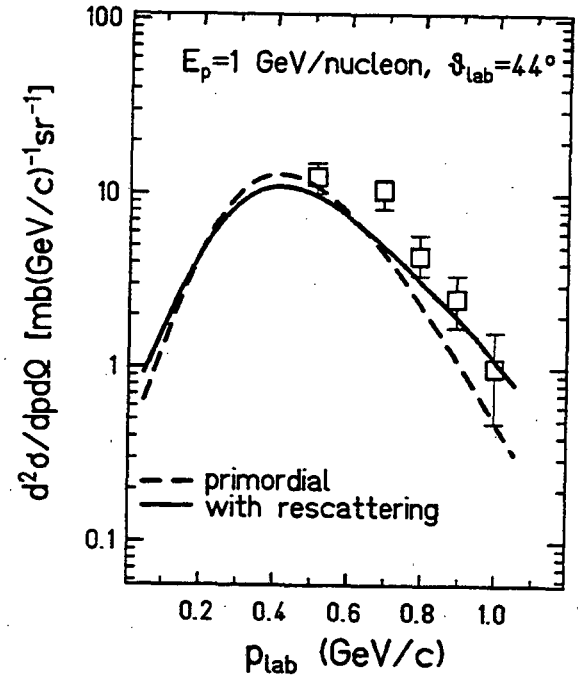

Fig. 2. Kaon spectra in a Au+Au collision at 1 GeV/nucleon.

After their production, kaons, antikaons, and antiprotons are propagated in the mean-field potentials and undergo collisions with baryons. For example, the equations of motion for kaons are

$$\frac{d\mathbf{x}_{K+}}{dt} = \mathbf{p}^*_{K+}/E^*_{K+}, \quad \frac{d\mathbf{p}_{K+}}{dt} = -\nabla_{\mathbf{x}} E^*_{K+}. \tag{9}$$

with $E^*_{K+} = ({m^*_{K+}}^2 + {\mathbf{p}^*_{K+}}^2)^{1/2}$; and similar equations for antikaon and antiprotons. Because of strangeness conservation, a kaon interacts with a baryon only elastically. A constant elastic cross section of 10 mb is used in the treatment of kaon rescatterings [15]. In addition to the elastic scattering, antikaons can be absorbed by baryons through the charge-exchange reaction, $K^-N \rightarrow Y\pi$. The cross sections for antikaon elastic and absorption processes are parametrized in terms of the invariant energy of the K^-N system [13] using the K-matrix method of Ref. [16]. For antiprotons, we need to take into account their annihilations. Again, the parametrized cross section of [17] is used in the numerical simulation.

In Fig. 2, we show the kaon production cross section in a Au+Au collision at 1 GeV/nucleon. The dashed and solid curves give the theoretical results for the primodial and the final kaon spectra, respectively. The rescattering effect enhances the kaon yield at high momenta and bring the theoretical spectrum in better agreement with the experimental data [2]. In Fig. 3, we discuss the role of the attractive kaon scalar potential in subthreshold kaon production. The solid and dashed curves give the theoretical results with and without the kaon scalar potential, respectively. When the attractive scalar potential is neglected, the experimental data is underestimated by about a factor of 3.

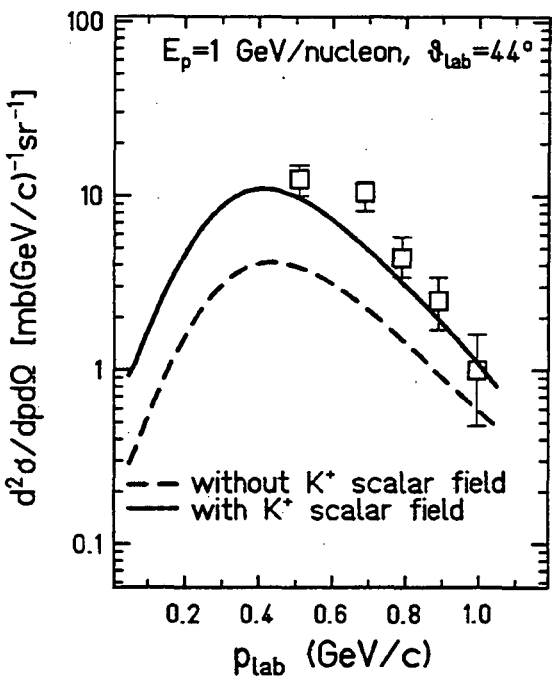

Fig. 3. Kaon spectra in a Au+Au collision at 1 GeV/nucleon.

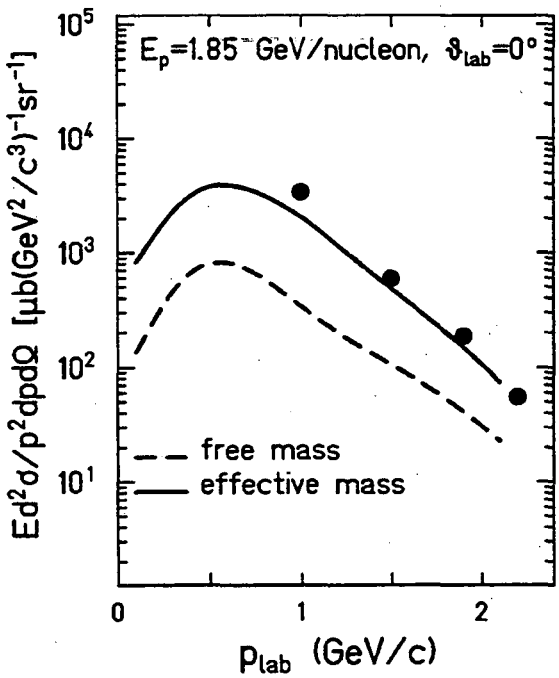

Fig. 4. Antikaon spectra in a Ni+Ni collision at 1.85 GeV/nucleon.

In Fig. 4, we compare our results for antikaon production in a Ni+Ni colliison at 1.85 GeV/nucleon with the experimental data [2]. The solid and dashed curves give the results obtained using the in-medium and free kaon and antikaon masses, respectively. It is clearly seen that if kaon and antikaon self-energies are neglected, i.e., the free masses are used, the experimental data are underestimated by a factor of 5-10.

Finally, we show in Figs. 5 and 6 the results for the antiproton production cross section in a Si+Si at 2.1 GeV/nucleon [1] and a Ni+Ni at 1.85 GeV/nucleon [2]. Dashed curves give the primordial antiproton spectra, while solid curves give the final antiproton spectra that include the effects due to propagation, rescattering and annihilation of antiprotons. The annihilation plays a particularly important role and should be treated quantitatively.

In summary, we have generalized the relativistic transport model to include the kaon, antikaon and antiproton degrees of freedom, and treated consistently their production, propagation, elastic rescattering, and absorption in the hadronic matter. Our investigation indicates that these medium effects, especially the attractive kaon and antikaon scalar potential, are needed for a quantitative explanation of recent data from the SIS experiments.

Experiments on subthreshold particle production thus provide the opporturnity to learn about both the properties of dense nuclear matter and the in-medium properties of hadrons.

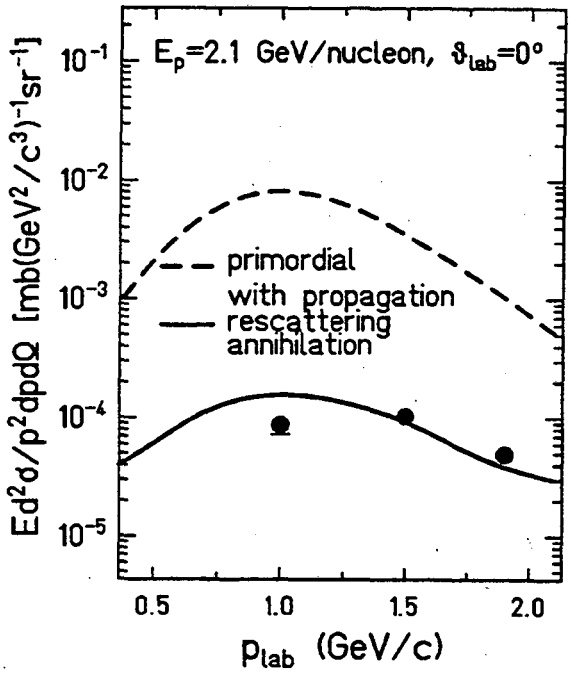

Fig. 5. Antiproton spectra in a Si +Si collision at 2.1 GeV/nucleon.

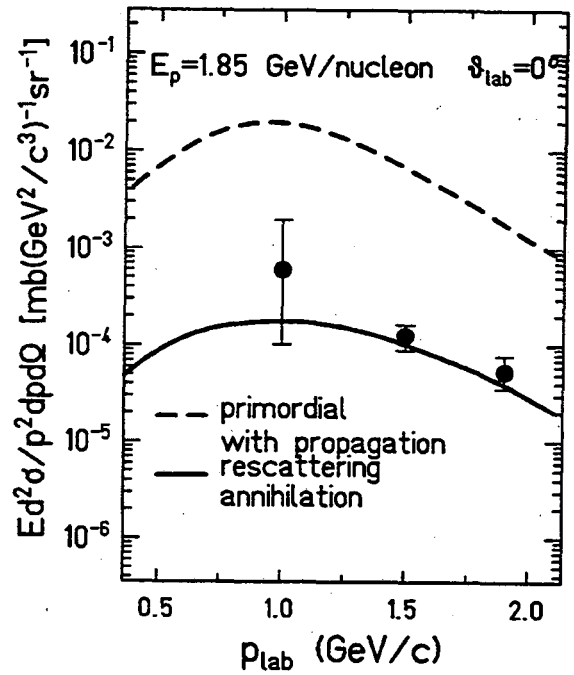

Fig. 6. Antiproton spectra in a Ni +Ni collison at 1.85 Gev/nucleon.

This work was supported in part by the National Science Foundation under Grant No. PHY-9212209 and the Welch Foundation under Grant No. A-1110.

[1] J. Carroll, Nucl. Phys. **A488**, 203c (1988).
[2] E. Grosse, Prog. Part. Nucl. Phys. **30**, 89 (1993); V. Metag, Nucl. Phys. **A553** 283c (1993); A. Schröter, Ph. D. thesis, Universität München, 1993.
[3] C. M. Ko, Q. Li, and R. Wang, Phys. Rev. Lett. **59**, 1084 (1987); C. M. Ko and Q. Li, Phys. Rev. C **37**, 2270 (1988);
[4] W. Cassing, W. Metag, U. Mosel, and K. Niita, Phys. Rep. **188**, 363 (1990)
[5] G. Q. Li, A. Faessler, and S. W. Huang, Prog. Part. Nucl. Phys. **31**, 159 (1993).
[6] B. D. Serot and J. D. Walecka, Adv. Nucl. Phys. **16**, 1 (1986).
[7] G. Q. Li, C. M. Ko, X. S. Fang, and Y. M. Zheng, Phys. Rev. C, in press.
[8] J. Cugnon, D. Kinet, and J. Vandermeullen, Nucl. Phys. **A379**, 553 (1982).
[9] G. F. Bertsch and S. Das Gupta, Phys. Rep. **160**, 189 (1988).
[10] J. Randrup and C. M. Ko, Nucl. Phys. **A343**, 519 (1980); **A441**, 537 (1983).
[11] X. S. Fang, C. M. Ko, G. Q. Li and Y. M. Zheng, Phys. Rev. C, in press.
[12] W. Zwermann and B. Schürmann, Phys. Lett. B **145**, 315 (1984).
[13] G. Q. Li, C. M. Ko, and X. S. Fang, Phys. Lett. B, submitted.
[14] G. Batko, W. Cassing, U. Mosel, K. Niita and Gy. Wolf, Phys. Lett. B **256**, 331 (1991).
[15] X. S. Fang, C. M. Ko, and Y. M. Zheng, Nucl. Phys. **A556**, 499 (1993).
[16] C. B. Dover and G. E. Walker, Phys. Rep. **89**, 1 (1982).
[17] J. Cugnon and J. Vandermeulen, Ann. de Phys. **14**, 49 (1989)

"Collective Effects" of Mesons at SIS-Energies

S. A. Bass[a,b], C. Hartnack[b,c], R. Mattiello[a],
H. Stöcker[a] and W. Greiner[a]

[a]Institut für Theoretische Physik der Universität,
Postfach 11 19 32, 60054 Frankfurt am Main, Germany
[b]GSI Darmstadt, Postfach 11 05 52, 64220 Darmstadt, Germany
[c]Laboratoire de Physique Nucléaire, 44072 Nantes, France

November 1993

1 Introduction

New experimental facilities at Darmstadt (GSI) and Berkeley (LBL) allow for the first time the experimental investigation of correlations of secondary particles - pions and other mesons - with the outgoing baryon resonace matter. This is important to probe the properties of hot and dense baryon rich matter in heavy ion collisions [1, 2, 3]. It has been thought that the pion–multiplicity reflects the thermal energy per nucleon in addition to the compressional energy of high nuclear density. The large cross section for pion nucleon interactions in the middle and late phases of heavy ion collisions has severely hampered the usefulness of pion spectra in the investigation of nuclear properties and reaction dynamics. The new experimental setups KaoS and FOPI (together with TAPS and LAND) at GSI and EOS/TPC at LBL enable us to investigate the emission pattern and properties of secondary particles in a far more detailed manner than ever before.

2 The IQMD-Model

For our investigation we use an extension of the **Q**uantum **M**olecular **D**ynamics model (QMD) [4, 5, 6, 7] which expicitely incorporates isospin and pion production via the delta resonance (IQMD) [8, 9, 10]. In the QMD model the nucleons are represented by Gaussian shaped density distributions. They are initialized in a sphere of a radius $R = 1.14A^{1/3}$ fm, according to the liquid drop model. Each nucleon is supposed to occupy a volume of h^3, so that the phasespace is uniformly filled. The initial momenta are randomly choosen between 0 and the local Thomas-Fermi-momentum. The A_P and A_T nucleons interact via two- and three-body skyrme forces, a Yukawa potential, momentum dependent interactions, a symmetry potential (to achieve a correct distribution of protons and neutrons in the nucleus) and explicit Coulomb forces between the Z_P and Z_T protons. They are propagated according to Hamiltons equations of motion. Hard N-N-collisions are included by employing the collision term of the well known VUU/BUU equation [3, 11, 12, 13, 14, 23]. The collisions are done stochastically, in a similar way as in the cascade models [16, 17]. In addition,

the Pauli blocking (for the final state) is taken into account by regarding the phase space densities in the final states of a two body collision.

Pions are treated in the IQMD model via the delta resonance. The following inelastic reactions are explicitly taken into account:

a)	$N\,N$	$\rightarrow$	$\Delta\,N$	(*hard–delta*–production)
b)	Δ	$\rightarrow$	$N\,\pi$	(Δ–decay)
c)	$\Delta\,N$	$\rightarrow$	$N\,N$	(Δ–absorption)
d)	$N\,\pi$	$\rightarrow$	Δ	(*soft–delta*–production)

Experimental cross sections are used for processes a) and d) [18], for the delta absorption, process c), we use a modified detailed balance formula [19] which takes the finite width of the delta resonance into account. A mass-dependent decay width is used for the Δ-decay. In between these inelastic reactions pions are propagated on curved trajectories with Coulomb forces acting upon them. The different isospin channels are taken into account using the respective Clebsch–Gordan–coefficients:

$$\Delta^{++} \rightarrow 1(p+\pi^+) \qquad \Delta^{+} \rightarrow \tfrac{2}{3}(p+\pi^0)+\tfrac{1}{3}(n+\pi^+)$$
$$\Delta^{0} \rightarrow \tfrac{2}{3}(n+\pi^0)+\tfrac{1}{3}(p+\pi^-) \qquad \Delta^{-} \rightarrow 1(n+\pi^-)$$

After a pion is produced (be it free or **bound** in a delta), its fate is governed by two distinct processes:

1. absorption $\quad \pi\,N\,N \rightarrow \Delta\,N \rightarrow N\,N$
2. scattering (resorption) $\quad \pi\,N \rightarrow \Delta \rightarrow \pi\,N$

By suppressing first the *soft-delta*-production and then the delta-absorption (while allowing the *soft-delta*-production) we are able to distinguish between effects caused by pion absorption and by pion scattering.

3 Angular correlations in the reaction plane

Figure 1 shows the $\langle p_x \rangle(y)$ distribution for π^+ and protons in Au(1AGeV)Au collisions with a minimum bias impact parameter distribution and a ϑ_{lab}-angular cut according to the Phase-II setup of the FOPI-spectrometer at GSI. The protons show the expected collective flow [20, 21, 22]. The $\langle p_x \rangle$ of the pions is anticorrelated to that of the protons. However, the anticorrelation is impact parameter dependent: For $b \leq 5$ fm the transverse velocities of pions and protons are correlated. Only for larger impact parameters the anticorrelation is visible. This hints towards the importance of spectator matter for the observation of the anticorrelation; for central collisions the pions reflect the flow of the Δ-resonances from which they have been emitted.

We have studied the origin of the particular shape of the pion angular distribution and the $\langle p_x \rangle$ spectrum by sequentially suppressing first the *soft-delta*-production and then the delta-absorption (while allowing the *soft-delta*-production). If we deactivate the *soft–delta*–production, $\pi\,N \rightarrow \Delta$, pions are neither scattered nor absorbed after the initial production. No $\langle p_x \rangle$ for pions is observed. In order to decide whether the $\langle p_x \rangle$ spectrum is caused by absorption or by scattering we now deactivate the reaction $\Delta\,N \rightarrow N\,N$. We thus suppress pion absorption but allow scattering – the anticorrelation between pions and protons in the $\langle p_x \rangle$ returns. In contrast to

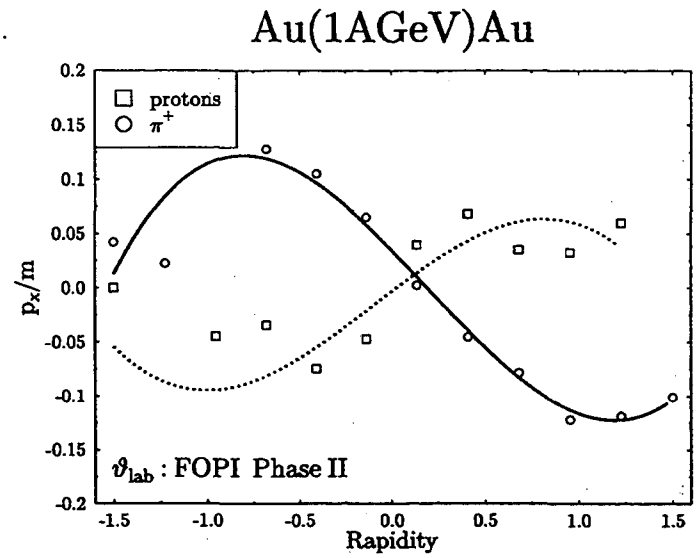

Figure 1: Rapidity y vs. $\langle p_x \rangle / m$ for π^+ and protons in a Au(1AGeV)Au collision with minimum bias impact parameter distribution. The protons show the expected bounce-off. The $\langle p_x \rangle$ of the pions is always directed oppositely to that of the protons.

previous publications, which investigated the asymmetric system Ne(800AMeV)Pb and suggested the anticorrelation of pionic and nucleonic $\langle p_x \rangle$ at target rapidities to be caused by pion absorption [23], our investigation reveals the $\langle p_x \rangle$ spectrum of the pions to be dominated by the pion scattering process.

The following simplified picture can explain the origin of the observed phase space distribution [24]: The Δ decays isotropically in its rest-frame, therefore 50 % of the pions are emitted with a positive p_x and 50 % with a negative p_x. At target rapidity those pions which obtain a positive p_x-value usually do not have the chance to rescatter: Most of the target nucleons are located in the **negative** p_x **area!** Those pions which **do** rescatter at target rapidity are the ones with an initially **negative** p_x: Every time a Δ decays (isotropically) there is a 50% chance that this pion is emitted **upward**, i.e. into an azimuthal angle between $-90° \leq \phi \leq 90°$. These ϕ-values characterize the hemisphere of positive p_x, by definition. This leads for$\approx$ 50% of the pions with - originally - negative p_x to a shift towards a positive p_x. This remains true even after transforming back into the laboratory frame. The same consideration applies vice versa for projectile rapidity: Most projectile nucleons are located in the **positive** p_x **area**. The pions are rescattered in this area which results in a negative $\langle p_x \rangle$ and a maximum in the azimuthal angular distribution in the $90° \leq \phi \leq 270°$ interval.

It is important to note, however, that the $\langle p_x \rangle$ spectrum of the pions is caused by totally different physics than the *flow* of the nucleons.

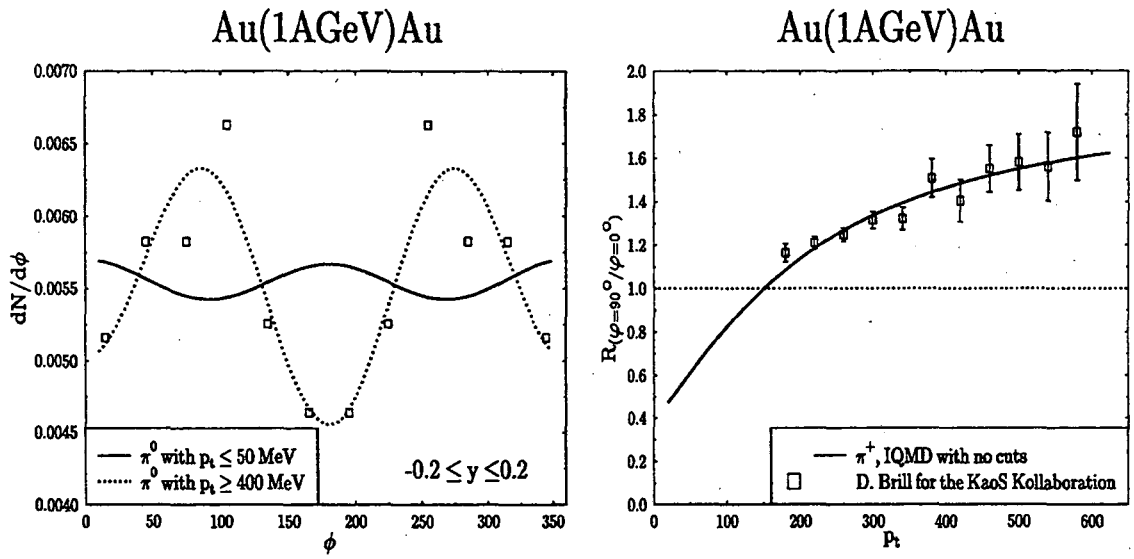

Figure 2: Azimuthal angular distribution (left frame) $dN/d\varphi$ for π^0 with low and high transverse momentum p_t at mid-rapidity in the reaction Au(1AGeV)Au and $R_{out/in}$ versus transverse momentum p_t for π^+ (right frame). The maximum at $\varphi = 90°$ corresponds to a preferential emission of high p_t pions perpendicular to the event-plane which is due to pion absorption by large pieces of spectator matter predominantly located in the reaction plane. Low p_t pions have rescattered more often which is only possible in the reaction plane. The data points (right frame) stem from the KaoS collaboration.

4 Angular correlations perpendicular to the reaction plane

In order to investigate the emission of pions perpendicular to the event-plane we plot the azimuthal (φ) distribution of the pions. φ is the angle between the transverse momentum vector $\vec{p_t}$ and the x-axis (which lies in the reaction plane and is perpendicular to the beam axis). Thus $\varphi = 0$ degrees denotes the projectile hemisphere and $\varphi = 180$ degrees corresponds to the target hemisphere. The left frame of figure 2 shows the respective distributions for neutral pions in the transverse momentum bins $p_t \leq 50$ MeV and $p_t \geq 400$ MeV at a minimum bias impact parameter distribution. The azimuthal angular distribution for π^0 with low p_t shows maxima at $\varphi = 0°$ and $\varphi = 180°$ corresponding to a preferential emission in the reaction plane. The high p_t π^0, however, show a maximum at $\varphi = 90°$ which is associated with preferential emission perpendicular to the reaction plane. The magnitude of the observed anisotropy and its dependence on the transverse momentum is best studied by using the following ratio:

$$R_{out/in} = \left. \frac{\frac{dN}{d\varphi}(\varphi = 90°) + \frac{dN}{d\varphi}(\varphi = 270°)}{\frac{dN}{d\varphi}(\varphi = 0°) + \frac{dN}{d\varphi}(\varphi = 180°)} \right|_{y=y_{CM}}$$

For positive values pions are emitted preferentially perpendicular to the event-plane.

The right frame of Figure 2 shows the transverse momentum dependence of $R_{out/in}$ for Au+Au collisions with an impact parameter of b=6 fm: In contrast to pions with

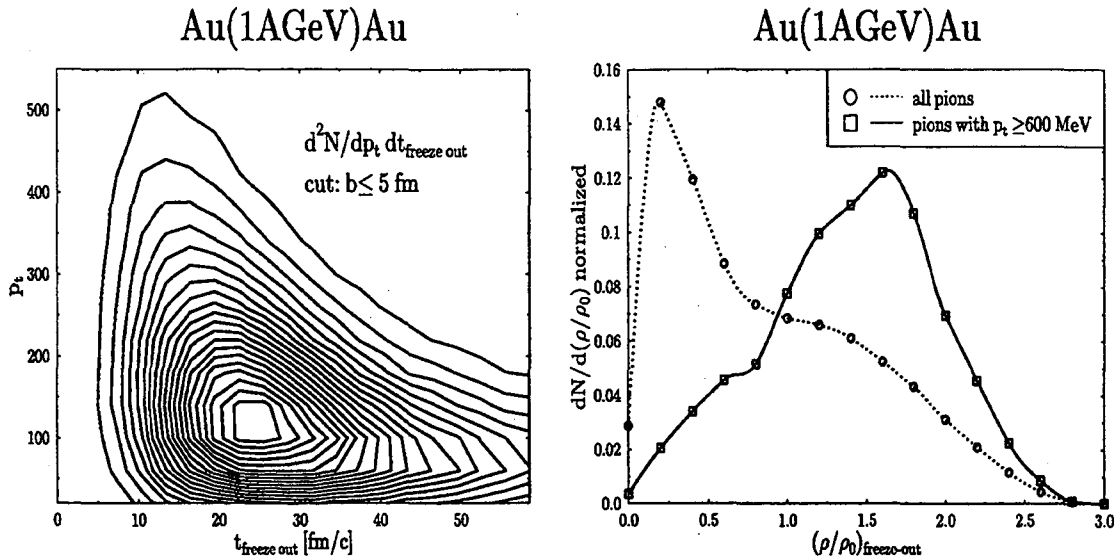

Figure 3: Contour plot of p_t vs. freeze out time t_{f_T} for all pions and normalized freeze out density distribution for all pions and pions with high p_t. Pions with high transverse momentum are mostly emitted in the early reaction stages at times up to 20 fm/c and probe freeze out densities larger than nuclear ground state density.

low transverse momentum, which are emitted preferentially in the reaction plane, high p_t pions are preferentially emitted perpendicular to the reaction plane. The data points stem from the KaoS collaboration [25] but serve only as a qualitative comparison. Due to our lack of statistics we were unable to employ the correct angular cuts of the KaoS spectrometer needed for a full comparison. Nevertheless the mid-rapidity pion-acceptance of the KaoS-spectrometer compares well with the IQMD calculations. Simultaneously with the KaoS collaboration the TAPS collaboration has reported an azimuthal asymmetry for the emission of π^0 [26].

The cause of the preferential emission of high p_t pions perpendicular to the event-plane is studied in the same manner as the in-plane anticorrelation between pions and protons: By deactivating the reaction $\pi N \rightarrow \Delta$, pion absorption as well as scattering are eliminated and no preferential emission perpendicular to the eventplane is observed. In order to decide whether the anisotropy is caused by absorption or by scattering we now deactivate the reaction $\Delta N \rightarrow N N$. We thus suppress pion absorption but allow scattering – no real anisotropy is observed. Therefore we assume the anisotropy to be dominated by the pion absorption process.

We conclude that the preferential emission of pions perpendicular to the reaction-plane stems from pion absorption by large pieces of nucleonic spectator matter which are located in the reaction-plane. Perpendicular to the plane there is no such spectator matter and pions with high p_t can leave the reaction zone without further interaction [27]. In the reaction plane pions are likely to scatter several times. This causes a loss of transverse momentum. Therefore we observe an excess of low p_t pions in the reaction plane.

The correlation between high p_t and early freeze-out time can be seen in the left frame of figure 3. A contour-plot is displayed in order to show the width of the distribution: High p_t pions are only emitted in the early stages of the reaction until approximately 20 fm/c. In order to prove this correlation between high p_t and

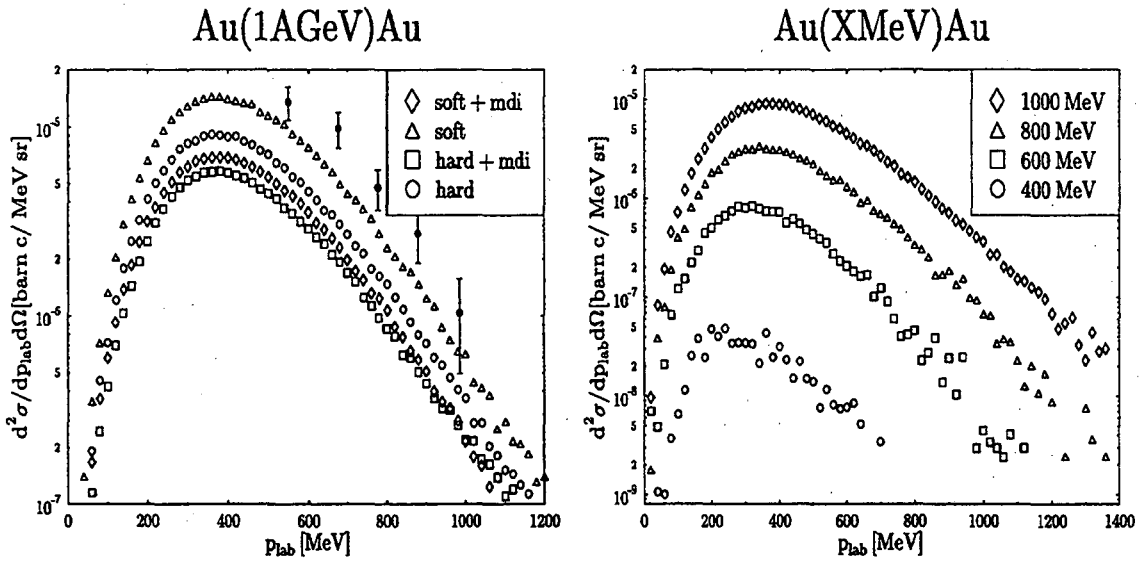

Figure 4: Equation of state dependence of kaon spectra for Au+Au at 1 GeV/nucleon and Kaon spectra for Au+Au collisions at 400, 600, 800 and 1000 MeV per nucleon (calculated with a hard eos) as calculated by the IQMD model. Ratios between spectra at different incident energies might help to dissolve ambiguities concerning the eos-dependence of the spectra with regard to the elementary production cross sections and the in-medium nucleon-nucleon cross section.

the hot and dense reaction phase conclusively, we calculated the freeze out density distribution for all pions and compared it with the respective distribution for high p_t pions in the right frame of figure 3 (the distributions are normalized in order to fit into the same frame): The average freeze out density for all pions lies well below nuclear ground state density; this is well known and has severely diminished the usefulness of pions as probes for the hot and dense reaction phase [8, 14]. High p_t pions, however, freeze out at far higher densities: Their average freeze out density lies between 1.2 and 1.5 ρ/ρ_0 with some of them even freezing out at densities near the maximum density obtained in the collision.

5 Kaon production

Kaon production at SIS energies is a subthreshold process. This means that the $\sqrt{s}$ of a collision of a nucleon at beam energy with a target nucleon at rest is too small to produce the desired kaon. In order to produce the kaon either one of the colliding nucleons must have gained energy in a preceding collision or the intrinsic fermi momenta of the nucleons must add up to increase the available energy above the threshold for kaon production. Therefore kaons may be sensitive to the reaction dynamics and (especially when produced in a multistep process) the nuclear equation of state [28]. In the IQMD model there are three relevant processes for kaon production:

$$\begin{aligned} N + N &\rightarrow N + Y + K^+ \\ N + \Delta &\rightarrow N + Y + K^+ \qquad Y = \{\Lambda, \Sigma\} \\ \Delta + \Delta &\rightarrow N + Y + K^+ \end{aligned}$$

The cross section parametrization which is used has been developed by Randrup and Ko[29].

Apart from their small production cross section kaons have also a very low reabsorption cross section due to strangeness conservation. Their production can therefore be calculated in a perturbative way regarding only the production probabilities in each collision. Figure 4 shows the equation of state dependence of kaon spectra at 1 GeV/nucleon incident energy (left frame) as well as spectra for 400, 600 and 800 MeV beam energy (right frame, calculated with a hard eos) as calculated by the IQMD model. The data points stem from the KaoS collaboration [30]. Apart from the equation of state the kaon yield unfortunately depends strongly on the in medium nucleon nucleon scattering cross section which is also unknown. Furthermore different parametrizations for the elementary production processes can amount to a change in the kaon yield by orders of magnitude. To dissolve these ambiguities it might help to investigate ratios between kaon spectra at different energies.

The differences between the Kaon spectra shown in figure 4 and the respective QMD calculations performed by Hartnack et. al. [31, 32] are caused by the use of the frozen delta approximation in the QMD model and a different treatment of the Pauli-blocking in the collision term.

References

[1] S. Nagamia, M.C. Lemaire, E. Moeller, S. Schnetzer, G. Shapiro, H. Steiner, and I. Tanihata. Phys. Rev. **C24**, 971 (1981).

[2] J. Harris , R. Bock, R. Brockmann, A. Sandoval, R. Stock, H. Stroebele, G. Odyniec, L. Schroeder, R. E. Renfordt, D. Schall, D. Bangert, W. Rauch and K. L. Wolf. Phys. Lett. **B153**, 377 (1985).

[3] H. Stöcker and W. Greiner. Phys. Reports **137**, 277 (1986).

[4] J. Aichelin and H. Stöcker. Phys. Lett. **B176**, 14 (1986).

[5] J. Aichelin, A. Rosenhauer, G. Peilert, H. Stöcker, and W. Greiner. Phys. Rev. Lett. **58**, 1926 (1987).

[6] G. Peilert, A. Rosenhauer, J. Aichelin, , H. Stöcker, and W. Greiner. Phys. Rev. **C39**, 1402 (1989).

[7] J. Aichelin. Phys. Reports **202**, 233 (1991).

[8] Ch. Hartnack, H. Stöcker, and W. Greiner. In H. Feldmeier, editor, *Proc. of the International Workshop on Gross Properties of Nuclei and Nuclear Excitation, XVI, Hirschegg, Kleinwalsertal, Austria* (1988).

[9] C. Hartnack, L. Zhuxia, L. Neise, G. Peilert, A. Rosenhauer, H. Sorge, J. Aichelin, H. Stöcker, and W. Greiner. Nucl. Phys. **A495**, 303 (1989).

[10] Ch. Hartnack. PhD thesis, GSI-Report 93-5 (1993).

[11] H. Kruse, B. V. Jacak, and H. Stöcker. Phys. Rev. Lett. **54**, 289 (1985).

[12] J. J. Molitoris and H. Stöcker. Phys. Rev. **C32**, 346 (1985).

[13] J. Aichelin and G. Bertsch. Phys. Rev. **C31**, 1730 (1985).

[14] G. Wolf, G. Batko, W. Cassing, U. Mosel, K. Niita, and M. Schäfer. Nucl. Phys. **A517**, 615 (1990).

[15] G. Bertsch, S. Das Gupta, and H. Kruse. Phys. Rev. **C29**, 673 (1984).

[16] Y. Yariv and Z. Frankel. Phys. Rev. **C20**, 2227 (1979).

[17] J. Cugnon. Phys. Rev. **C22**, 1885 (1980).

[18] B. J. VerWest and R. A. Arndt. Phys. Rev. **C25**, 1979 (1982).

[19] P. Danielewicz and G. F. Bertsch. Nucl. Phys. **A533**, 712 (1991).

[20] J. J. Molitoris and H. Stöcker. Phys. Lett. **B162**, 47 (1985).

[21] H.-A. Gustafsson, H. H. Gutbrod, B. Kolb, H. Löhner, B. Ludewigt, A. M. Poskanzer, T. Renner, H. Riedesel, H. G. Ritter, A. Warwick, F. Weik, and H. Wieman. Phys. Rev. Lett. **52**, 1590 (1984).

[22] J. J. Molitoris, H. Stöcker, and B. L. Winer. Phys. Rev. **C36**, 220 (1986).

[23] B. A. Li, W. Bauer, and G. F. Bertsch. Phys. Rev. **C44**, 2095 (1991).

[24] S. A. Bass, C. Hartnack, R. Mattiello, H. Stöcker, and W. Greiner. Phys. Lett. **B302**, 381 (1993).

[25] D. Brill and the Kaos Collaboration. Phys. Rev. Lett. **71**, 336 (1993).

[26] L. Venema and the TAPS-Collaboration. Phys. Rev. Lett. **71**, 835 (1993).

[27] S. A. Bass, C. Hartnack, H. Stöcker, and W. Greiner. Phys. Rev. Lett. **71**, 1144 (1993).

[28] A. Shor et. al. Phys. Rev. Lett. **48**, 1597 (1982).

[29] J. Randrup and C. M. Ko. Nucl. Phys. **A343**, 519 (1980) and **A411**, 537 (1983).

[30] P. Senger and the KaoS collaboration. Nucl. Phys. **A553**, 757c (1993).

[31] C. Hartnack, S. A. Bass, J. Aichelin, H. Stöcker and W. Greiner Proceedings of the *International Workshop on Gross Properties of Nuclei and Nuclear Excitations XXI*, Hirschegg, Kleinwalsertal, Austria 1993.

[32] C. Hartnack, J. Jaenicke and J. Aichelin. Rapport Interne LPN 93-11 and submitted Nucl. Phys. **A**

Proton and Pion Production in the Target Rapidity Region

B. Roters[a], C. Blume[b], H.R. Schmidt[a], and H. H. Gutbrod[a*]

[a] Gesellschaft für Schwerionenforschung
64220 Darmstadt, Germany
[b] Univ. of Münster
48149 Münster, Germany

for the WA80 collaboration,
and the GSI/LBL Plastic Ball team

ABSTRACT

The production of protons and pions in the target rapidity region in ultrarelativistic heavy-ion reactions has been studied. The experimental data which were taken by the GSI/LBL collaboration in Berkeley and by the WA80 collaboration at CERN using the Plastic Ball detector [1] are compared to results of the event generators VENUS 3.07 [2] and RQMD 1.07 [3].

The observables investigated are $dN/d\eta$ distributions, azimuthal correlations, proton emission into the backward hemisphere and pp correlations. It is shown that rescattering and π-absorption with realistic cross sections are necessary ingredients for event generators in order to reproduce the experimental data.

* invited speaker

Introduction

In the clean cut participant-spectator picture, no "cross talk" is assumed between the participant and the spectator parts of the collision. Thereby, the participant zone is defined by the geometrical overlap volume of the two colliding nuclei, while all nucleons outside this zone are dubbed spectators.

Excitations in target spectator matter can, for example, be initiated by secondary particles which are formed fast enough ($c \cdot \tau_{lab} < R_{target}$) in the hot zone to start a cascade in target spectator matter, or recoil protons from elastic collisions.

Above beam energies of 5 GeV, the momentum transfer in an elastic collision with a recoil proton remains constant, as well as the cross section for this process. Here the question arises whether pions emitted into negative rapidity also cause cascading in the target region, i. e. contribute to particle production at backward angles.

The formation time (τ_0) accounts for the fact that it takes a certain time until a new particle is formed and on mass shell. During the formation process, its cross section is reduced. Inspired by the uncertainty principle, a first estimation for the formation time is

$$\tau_0 \sim \hbar / m_T.$$

In the laboratory system, formation time is described by

$$\tau_{lab} = \gamma \cdot \tau_0 = \cosh(y) \cdot \tau_0 \sim \exp(y)/m_T.$$

For event generators, it is very important which formation time is chosen: is the pathlength during formation time greater than the target nucleus radius, the particle is only formed outside and thus cannot contribute to cascading. Is the corresponding pathlength smaller than the nucleus radius, that particle is subject to subsequent collisions in the target. Therefore, a comparison of experimental data in the target rapidity region with suitably equipped event generators could give a handle to study both the formation of particles and their subsequent absorption in nuclear matter on a microscopic scale.

Experiment

The reactions studied were p + Au at 4.9 GeV (at the LBL Bevatron), and 60 GeV and 200 GeV (at the CERN SPS), as well as also 200 AGeV O and S induced reactions. The WA80 collaboration used a variety of target nuclei to study A dependence effects. p, d, t and positive pions in the region $-1.7 < \eta < 1.3$ ($\doteq 160° - 30°$) were detected by the Plastic Ball detector [1]. Proton energies were measured between 40 and 300 MeV, while π^+ were identified in the range 20 - 120 MeV with less than 4% misidentification [1]. The momentum resolution is better than 10 MeV/c for π^+ and about 30 MeV for protons. For global event characterization, two calorimeters are employed in WA80: the Midrapidity calorimeter MIRAC [5] for transverse energy E_T in $2.4 \leq \eta \leq 6$, and the Zero-degree calorimeter ZDC [6] for the forward energy in $\eta \geq 6$. Central and peripheral collisions differ by the fraction of total energy deposited in the ZDC as well as by the amount of E_T produced.

Results

Particle yields

In p + Au collisions, it was found experimentally that the number of protons emitted into the region $-1.7 < \eta < 1.3$ is independent of the incident energy over the range 4.5 GeV to 200 GeV [7]. This finding is consistent with earlier experimental results [8] and has been labeled "limiting fragmentation". The results are well reproduced by the event generator VENUS, which includes rescattering. In 200 GeV p + nucleus, VENUS also reproduces the experimental $dN/d\eta$ for various targets in the target rapidity region. In fig. 1, the α from the parametrization of the yield as A^α is shown for baryons and pions as a function of η. The value of $\alpha \simeq 1$ for protons in the target fragmentation region indicates the excitation of the whole target nucleus. Also in fig. 1, the experimental parameters α are compared to VENUS. There is good agreement with VENUS for the baryons; this indicates that cascading of secondaries amongst themselves and with other particles is a major source for target protons. However, the A-dependence of pions in the target rapidity region with a similar parametrization that was found in WA80 data is not reproduced by VENUS.

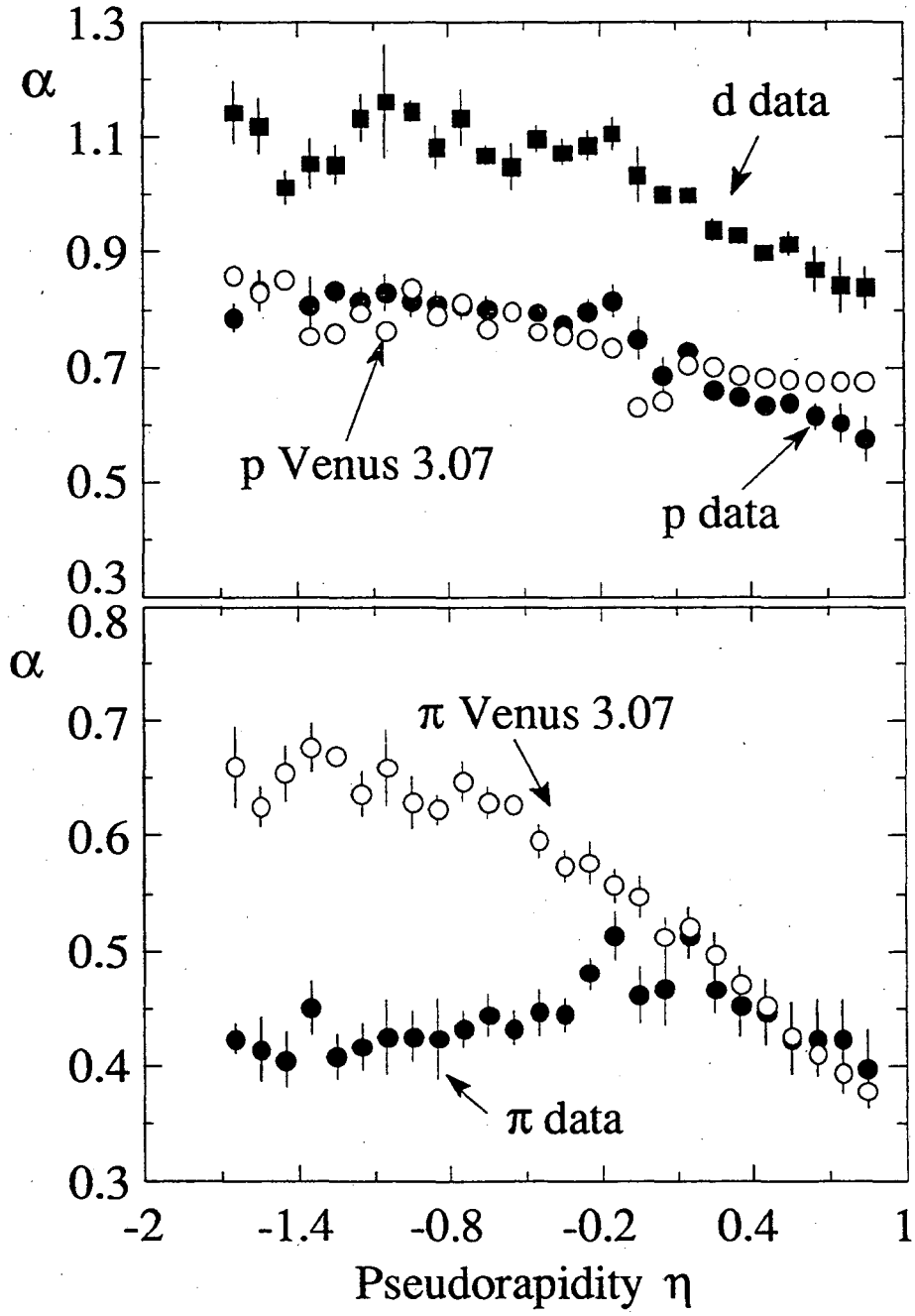

Figure 1: The target mass dependence of the yield of baryons and pions for 200 GeV p induced reactions in target rapidity. The yields are parametrized as A^{α}. The η - dependence of the slope parameter α from experimental data is compared to VENUS results (open circles).

Azimuthal correlations

Azimuthal correlations between the forward and backward hemisphere with respect to the rest frame of of the target system are investigated by constructing

$C(\Delta\varphi) := \frac{dN}{d(\Delta\varphi)}$ with

$$\Delta\varphi = \arccos \frac{\vec{Q}_{back} \cdot \vec{Q}_{forw}}{|\vec{Q}_{back}| \cdot |\vec{Q}_{forw}|}$$

where

$$\vec{Q}_{back} := \sum_{y \leq y_0} \vec{p}_T{}^i \qquad \vec{Q}_{forw} := \sum_{y > y_0} \vec{p}_T{}^i$$

y_0 is chosen as 0.2, the expected rapidity of excited target matter. The results for this variable show a similar behaviour independent of incident energy over the range 4.9 GeV to 200 GeV, see fig. 2. Interestingly, the proton correlation shows an enhancement at $\Delta\varphi = 180°$, which means that protons are emitted preferentially with a large opening angle, i. e. "back-to-back". This can be understood as a consequence of (local) transverse momentum conservation. Pions are mainly scattered "side-by-side", i. e. $\Delta\varphi = 0°$. A possible explanation is based on the geometrical picture that pions in a peripheral collision experience a stronger absorption the longer the way through target spectator matter is, which means that pions are emitted preferentially at the side of the target which is close to the point of impact.

Further understanding evolves by looking at the dn/d($\Delta\varphi$) distributions the event generators give for protons and pions, respectively, see fig. 3. While both event generators reproduce the proton data, VENUS again disagrees on the pion dn/d($\Delta\varphi$), where RQMD has the same description as seen in the WA80 data. This might be due to the fact that RQMD, in contrast to VENUS, employs energy dependent experimentally measured cross sections for πN reactions. These findings suggest that pions are absorbed in excited target matter. The formation of the Δ resonance has a large cross section in the kind of reactions investigated, so the processes involved are mainly the following:

$$\pi + \mathrm{N} \rightarrow \Delta$$

$$\Delta + \mathrm{N} \rightarrow \mathrm{N} + \mathrm{N}$$
$$\Delta + \Delta \rightarrow \mathrm{N} + \Delta$$

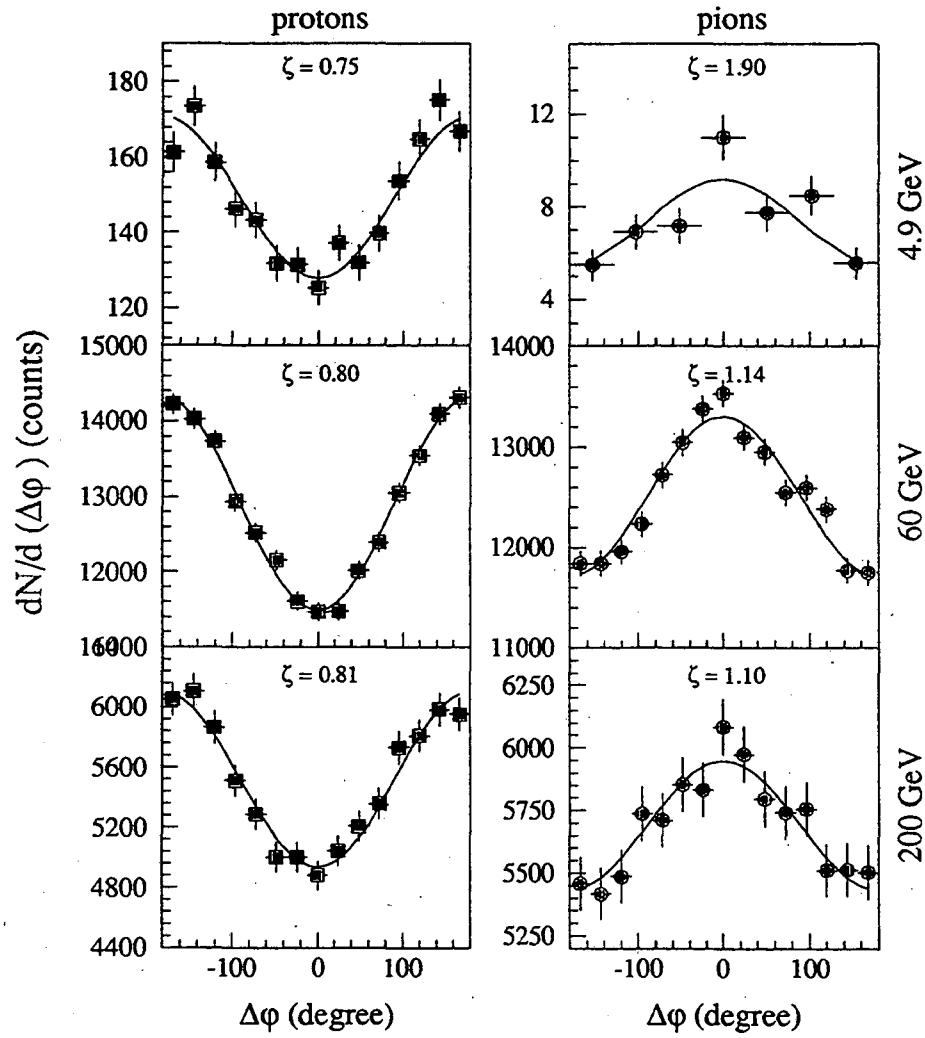

Figure 2: Azimuthal correlations for protons (left panel) and pions (right panel) from p + Au reactions for different incident energies: 4.5 GeV (top), 60 GeV (second row) and 200 GeV (third row).

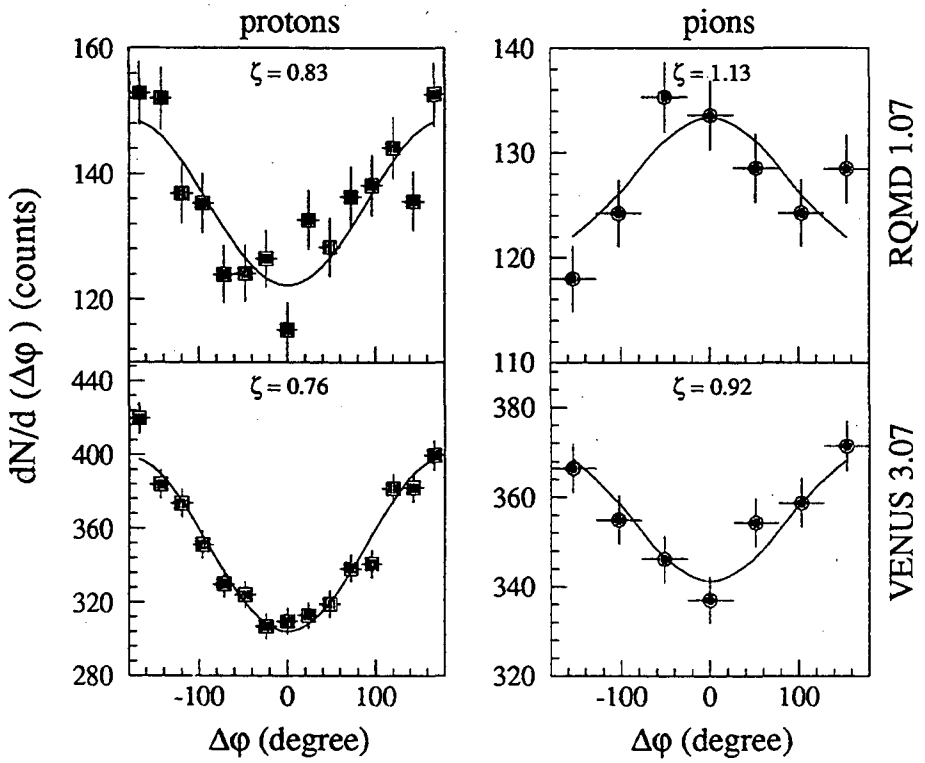

Figure 3: Azimuthal correlation for simulated protons (left panel) and pions (right panel) from p + Au reactions from RQMD (upper part) and VENUS (lower part).

Backward emission of protons

The emission of high energetic protons into the backward hemisphere ($\theta_{lab} > 90°$), which is kinematically forbidden for binary NN collisions, has been found in ultrarelativistic reactions and named cumulative effect [9]. It is a sensitive probe of particle production mechanisms from correlated nucleons, or other rare objects since it maximizes the momentum transfer to the scattered particle. Two mechanisms for cumulative particle production can be thought of: first, rescattering amongst nucleons in spectator matter, and secondly a single collision with a massive object. In order to be sensitive for the second effect, it was chosen to analyze central collisions in almost symmetric systems. This choice minimizes the amount of spectator matter which could contribute to rescattering. For central 200 AGeV S + Al and O + C reactions, an exponential falloff in the proton cross sections as a function of the emission angle was found, which increases with increasing lab angle, see fig. 4. By fitting the cross sections, a mean kinetic energy can be extracted from the slopes.

It shows for the backward hemisphere relatively uniform slopes corresponding to the emission of protons with a mean kinetic energy around 50 MeV. However, this is independent of the centrality of the reaction, i. e. also in peripheral reactions the protons emitted into the backward hemisphere have a similar mean kinetic energy. Since the volume available for rescattering is much larger in peripheral collisions, a similarity of results for both centrality classes may indicate that resonances play an important role for the emission of particles into the backward hemisphere.

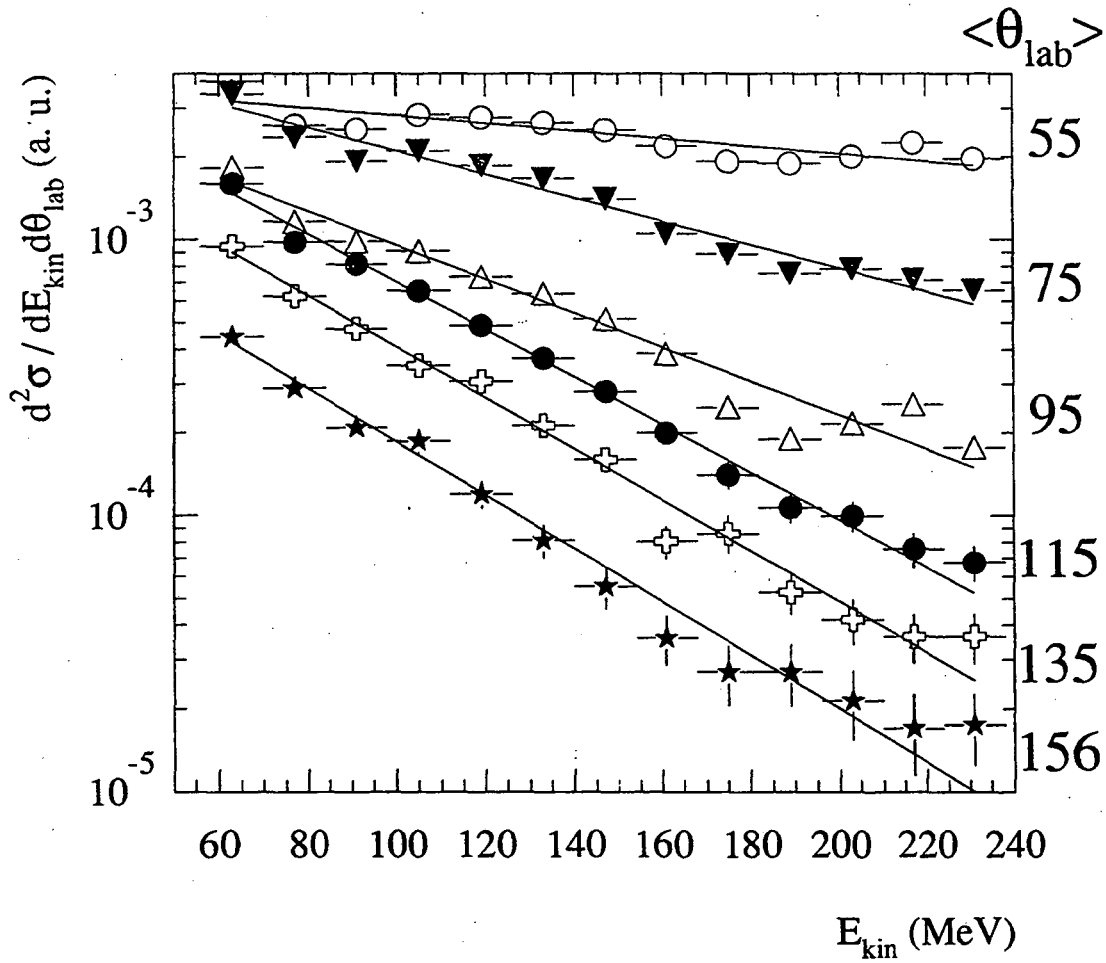

Figure 4: The proton cross sections as a function of kinetic energy in different bins of ϑ_{lab} from central 200 AGeV S + Al collisions. The mean angle refers to Plastic Ball rings.

pp Correlations

By studying the two-particle correlation function of identical particles in different directions of phase space, it is possible to obtain measurements of the transverse and longitudinal size, of the lifetime, and of flow patterns of the hadronic fireball at the moment where it breaks up into separate hadrons [10]. Two proton-correlations in the target rapidity region provide information about the size of the target region participating in the reaction. The experimental two-proton correlation function was obtained by dividing a distribution of correlated proton pairs by uncorrelated pairs from the event-mixing method. Since there is no simple analytical expression for the two-proton correlation function, the radius parameters have to be extracted by comparing a numerical simulation to the data. The radius parameters from WA80 data show a significant proportionality to $A_T^{1/3}$, as is displayed in fig. 5 [11]. For p-induced reactions, the parameters are very close to the geometrical nuclear radii estimated by

$R_{geo} = \frac{1}{\sqrt{2}} \cdot \sqrt{\frac{2}{3}} \cdot 1.29 \cdot A_T^{1/3}$, which is indicated by the hatched band in fig. 5.

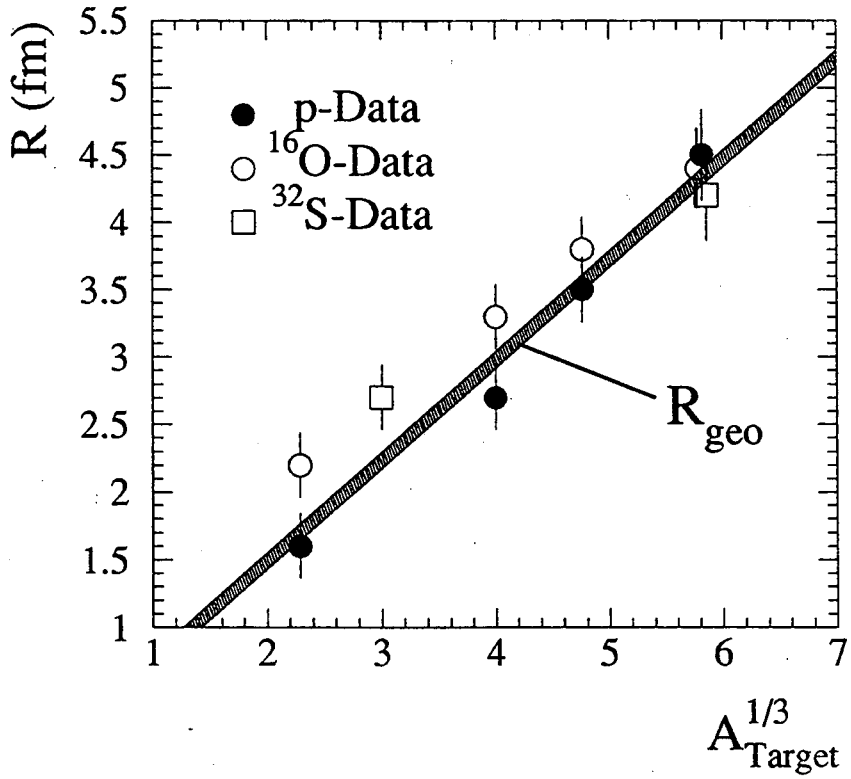

Figure 5: The target dependence of pp-correlation radii for 200 GeV p, 200 AGeV O and S induced reactions from WA80 data. The hatched line corresponds to R_{geo} (explanation see text).

For the Au target, the radius parameters are similar for all projectiles. These findings lead to the conclusion that the whole target nucleus is involved in the reaction, even in proton induced reactions.

Summary and conclusions

The data on p and π production in the target rapidity region are in general agreement with the limiting fragmentation picture. It is important that rescattering phenomena including pion absorption are properly incorporated into the event generators, as it was shown that VENUS has difficulties in describing the data.

The importance of pion absorption in excited target matter can be demonstrated from analyzing azimuthal correlations. It was found that protons are emitted back-to-back, while pions are observed rather side-by-side due to absorption effects.

Cumulative particle production is seen in both peripheral and central collisions, and also for light systems. This suggests that proton emission into the backward hemisphere may be linked to resonance decay.

The increase of source size extracted with the help of pp correlations for increasing target nucleus size leads to the conclusion that the whole target nucleus is involved in the reaction.

References

[1] A. Baden et al., Nucl. Instr. and Meth. **203** (1982) 189.
[2] K. Werner, P. Koch, Phys. Lett. **B 242** (1990) 251.
[3] H. Sorge et al., Nucl. Phys. **A 498** (1989) 567C–576C.
[5] T. Awes et al., Nucl. Instr. and Meth. **A 279** (1989) 479-502.
[6] G. Young et al., Nucl. Instr. and Meth. **A 279** (1989) 503-517.
[7] H.R. Schmidt et al., Nucl. Phys. **A 544** (1992) 449c.
[8] S. Fredriksson, G. Eilam, G. Berlad, L. Bergström, Phys. Rep. **144** (1987) 187.
[9] A. Baldin et al., Yad. Fiz. **18** (1973) 79.
A. Baldin et al., Sovj. Journ. Nucl. Phys. **18** (1973) 41.
[10] S. E. Koonin, Phys. Lett. **B 70** (1977) 43.
[11] C. Blume, Diploma thesis, Univ. of Münster (1993).

LIFETIME EFFECTS IN TWO-PROTON CORRELATIONS IN HEAVY ION COLLISIONS

M.A. Lisa, C.K. Gelbke, W. Gong, S. Pratt, N. Carlin, P. Decowski, R.T. deSouza, E. Gualtieri, S. Hannuschke, Y.D. Kim, R. Lacey, T. Li, W.G. Lynch, T. Murakami, G. Peaslee, G. Poggi, T. Reposeur, M.B. Tsang, A.M. Vander Molen, G.D. Westfall, H.M. Xu, J. Yee, and S.J. Yennello
Michigan State University, East Lansing, MI 48823

K. Kwiatkowski, V.E. Viola, Jr., and S.J. Yennello
Indiana University, Bloomington, IN

Abstract: Directional cuts in two-proton correlation measurements are used to disentangle the effects of size and lifetime of the emitting source. The importance of proper identification of the rest frame of the moving source is discussed. Longitudinal and transverse correlations for the reactions $^{36}Ar+^{45}Sc$ at E/A=80 MeV and $^{129}Xe+^{27}Al$ at E/A=31 MeV are presented. The method is shown to be sensitive to timescales consistent with fast decay as well as statistical evaporation.

Two-proton correlations have recently seen much use in the study of heavy ion collisions at bombarding energies ranging from a few MeV to a few GeV per nucleon [1-29]. These correlations are used as a tool to map out the spatio-temporal structure of the hot nuclear zone from which the protons are emitted. This information can in turn be used to study the equation of state, in-medium nucleon-nucleon cross section, energy density, and lifetime of excited residues [18-21,25,28,29]. However, for many purposes, it is important to distinguish between spatial and temporal effects, and, until now, attempts to make this distinction with protons have been unsuccessful.

Two protons emitted independently from a hot zone of nuclear matter (the "source") will mutually interact *en route* to a detector through the nuclear and Coulomb forces. These so-called final state interactions, along with the quantum-mechanical requirement that the two-proton wavefunction be antisymmetric (Pauli principle), modifies the observed final two-particle phase space density, as compared to the scenario in which the protons are distinguishable and do not interact [see, e.g. 17,30]. The degree to which the phase space distribution is modified is quantified by the correlation function, and is a function of the relative spatial separation of the protons upon emission. The attractive S-wave nuclear interaction leads to a pronounced maximum at a relative momentum of $q \approx 20$ MeV/c; this maximum decreases for larger sources. The Coulomb repulsion and Pauli principle lead to a suppression of the correlation function for $q \approx 0$.

The experimental two-proton correlation function 1+R(q) is defined in terms of the two-proton coincidence yield $Y_2(\mathbf{p}_1,\mathbf{p}_2)$ and a "fake" coincidence yield $Y^*_2(\mathbf{p}_1,\mathbf{p}_2)$:

$$\Sigma\, Y_2(\mathbf{p}_1,\mathbf{p}_2) = C\,[1+R(q)]\, Y^*_2(\mathbf{p}_1,\mathbf{p}_2), \qquad (1)$$

where q is the (invariant) magnitude of the relative momentum four-vector. For a given experimental gating condition, the sums on each side of Eq. (1) extend over all proton energies and detector combinations of the detector system corresponding to each q-bin. The normalization constant C is determined by the requirement that R(q) vanish for large q. The "fake" coincidence yield $Y^*_2(\mathbf{p}_1,\mathbf{p}_2)$ is intended to contain all detector biases and correlations aside from those due to quantum effects and final state interactions; it may be determined by mixing protons from different singles or coincidence events [31].

Figure 1 shows calculated correlation functions for protons emitted from hypothetical sources (characterized by the emission probability g) with varying spatial and temporal extent. The upper panel shows the effect of increasing the size of a source with negligible lifetime, while the lower shows the correlation function for a fixed source size and increasing lifetime. Clearly, an increase in either source size or lifetime has a similar effect on the correlation function. Indeed, these angle-integrated correlations cannot distinguish between size and lifetime. In the literature, the practice is to assume that the source has negligible lifetime and to fit the observed correlation function by varying the source size. Several systems above a bombarding energy of about 50 A·MeV have been measured, with extracted source sizes on the order of 3-8 fm [1-13]. However, application of this method to measurements of the correlation function at lower bombarding energy [14,16,22-24] or at backward angles in the laboratory [16] leads to unphysically large extracted source sizes, on the order of 10-100 fm. In these cases, a source of reasonable spatial dimensions (on the order of the compound nuclear system) is assumed, and the source lifetime is varied to fit the correlations. Lifetimes on the order of 100-2000 fm/c have been extracted.

So, we have a rather schizophrenic approach to interpreting the data: for the high energy measurements, we assume zero lifetime and extract a size, while at lower energies, we assume a source size and extract a lifetime. Clearly, it would be more satisfying to extract both size and lifetime from a single correlation measurement.

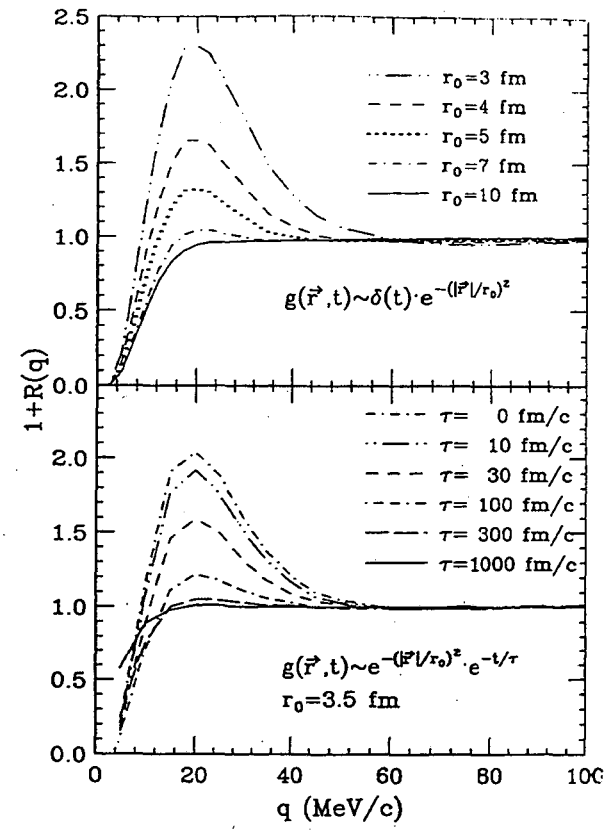

Figure 1. Calculated two-proton correlation functions corresponding to spherical Gaussian sources. Top panel: the source is assumed to have negligible lifetime and the size is varied. Bottom panel: The source radius is fixed at 3.5 fm, and the lifetime is varied.

In Figure 2a, the phase space distribution corresponding to proton emission from a long-lived source is shown. The detector sits at 38° (in the direction of v_{emit}). The finite lifetime of the source produces an elongation of the phase space distribution (the apparent source) along the direction of the total momentum ($\mathbf{P}=\mathbf{p}_1+\mathbf{p}_2$) [11,20]. Sensitivity of the correlations to this elongation would allow the determination both spatial and temporal extents. The nuclear and Coulomb final state interactions between the emitted protons are both dominated by S-wave components, so the magnitude of correlations due to these effects depends only on the relative separation of the protons, and not on the orientation of the separation. On the other hand, the Pauli principle leads to the suppression of the correlation function over the range $q_x \lesssim 1/R_x$, where q_x and R_x are the components of the relative momentum and the spatial separation of the proton pair in the x-direction, respectively. Therefore, the correlation function constructed when **q** is oriented along the short dimension of the phase space distribution ($\mathbf{q}\perp\mathbf{P}$, the transverse correlation function) will be more suppressed than when **q** lies along the long dimension ($\mathbf{q}\parallel\mathbf{P}$, the longitudinal correlation function).

Directional cuts as a means to disentangle the effects of size and lifetime were discussed by Koonin in his seminal 1977 paper on two-proton correlations [30]. Since then, several groups have searched for the effect [13,15,18,21,22,26], and no clear signal has been seen until now. This has led physicists to come to one of two conclusions: 1) proton-emitting sources created in heavy ion collisions really do have negligible lifetime, or, more likely, 2) some other effect is obscuring the predicted difference between longitudinal and transverse correlation functions.

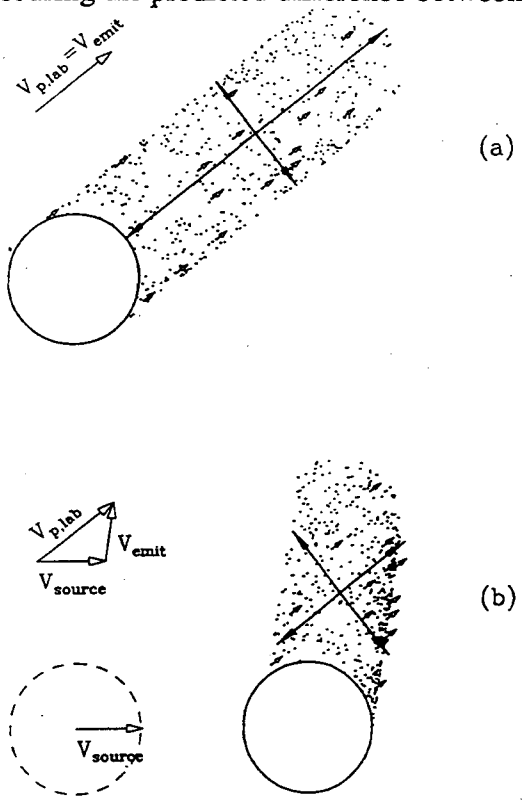

Figure 2. Schematic illustrations of phase space distributions at a time t=70 fm/c, as seen by a detector at θ_{lab}=38°, for a spherical source of radius 3.5 fm emitting protons of laboratory momentum 250 MeV/c. (a) Source is at rest in the laboratory. (b) Source moves with velocity v_{source}=0.18c. Laboratory velocities of the emitted protons $v_{p,lab}$, are depicted by small arrows, and the directions perpendicular and parallel to $v_{p,lab}$ are indicated by the double-headed arrows. (From Ref. [28])

Figure 2b illustrates a major complicating factor. Here, the source shown in Figure 2a is given a velocity relative to the laboratory frame. In this case the direction of elongation no longer lies along **P** as measured in the lab, but along **P** as defined in the source rest frame. Indeed, the extent of the apparent source parallel to and perpendicular to $\mathbf{P}_{lab}$, indicated by the double-headed arrows, are quite similar, and correlations cut on $\Psi_{lab} = \mathrm{Cos}^{-1}(\mathbf{P}_{lab}\cdot\mathbf{q}/(P_{lab}\cdot q))$ would not reveal the lifetime. This may explain why previous measurements, which compared correlations cut on Ψ_{lab}, observed no clear effect [26,28].

Proper identification of the source velocity is essential to extract the effects of a finite lifetime [28]. In heavy ion reactions, the source velocity can be a function of impact parameter. To extract both spatial and temporal dimensions of the source created in a heavy ion reaction, we performed a high statistics measurement of the two-proton correlation function with impact parameter selection [35]. The experiment was performed at the National Superconducting Cyclotron Laboratory at Michigan State University. A beam of ^{36}Ar ions at E/A=80 MeV incident energy bombarded a ^{45}Sc target. Charged particles were measured in the MSU 4π Array [32], which consisted of 209 plastic ΔE-E phoswich detectors covering polar angles between 7° and 158° in the laboratory frame. To measure proton pairs with high resolution, one of the hexagonal modules of the 4π Array, located at 38° in the lab frame, was replaced by a 56-telescope high-resolution hodoscope [33,34]. Each ΔE-E telescope of the hodoscope consisted of a 300-μm-thick Si detector backed by a 10-cm-long CsI(Tl) detector.

In Figure 3, we show the measured longitudinal and transverse correlation functions for proton pairs with total momentum P_{lab}=400-600 MeV/c emitted from central collisions. In a geometrical picture [35,36], the applied cuts correspond to impact parameters [36] of b/b_{max} = 0 - 0.36. Longitudinal (solid points) and transverse (open points) correlation functions were

defined by cuts on the angle $\psi = \cos^{-1}(\mathbf{q}\cdot\mathbf{P}/qP) = 0°\text{-}50°$ and $80°\text{-}90°$, respectively. (The normalization constant C in Eq. 1 is independent of ψ [21]) The top panel shows correlation functions for which the angle ψ was defined in the center-of-momentum frame of projectile and target ($\psi = \psi_{source}$); for central collisions of two nuclei of comparable mass, this rest frame should be close to the rest frame of the emitting source. The bottom panel shows correlation functions for which the angle ψ was defined in the laboratory frame ($\psi = \psi_{lab}$).

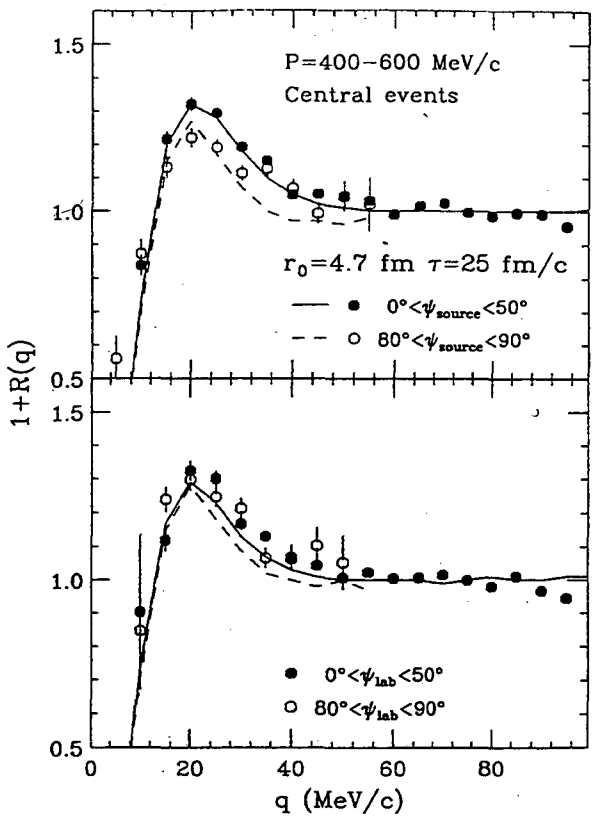

Figure 3. Measured longitudinal and transverse correlation functions for protons emitted in central $^{36}Ar+^{45}Sc$ collisions at E/A=80 MeV. The proton pairs have laboratory momentum between 400 and 600 MeV/c and are detected at $\langle\theta_{lab}\rangle$=38°. Longitudinal and transverse correlation functions (solid and open points, respectively) correspond to $\psi = \cos^{-1}(\mathbf{q}\cdot\mathbf{P}/qP) =$ 0° - 50° and 80° – 90°, respectively. Solid and dashed curves represent longitudinal and transverse correlation functions predicted for emission from a spherical Gaussian source with r_0 = 4.7 fm and τ = 25 fm/c, moving with v_{source} = 0.18c. Upper panel: **P** and ψ are defined in the rest frame of the presumed source moving with v_{source} = 0.18c. Lower panel: **P** and ψ are defined in the laboratory frame. (From Ref [28])

The data in Figure 3 represent the first clear experimental evidence of the predicted lifetime effect. The solid and dashed curves in the figure indicate calculated longitudinal and transverse correlation functions corresponding to a spherical Gaussian source of radius r_0 = 4.7 fm and lifetime τ = 25 fm/c moving at the center of momentum velocity of the system. As with the data, the signal revealing the finite lifetime in the calculation is strongest when cuts are performed in the proper frame.

We have calculated longitudinal and transverse correlations for a family of moving spherical Gaussian sources with systematically varying size and lifetime. The calculated correlations are compared to the data, and agreement is quantified by calculating the chi-squared per degree of freedom (χ^2/ν) in the peak region, q = 15 - 30 MeV/c.. The sensitivity of the correlation function to the extracted size and lifetime parameters is illustrated in Figure 4, which shows a contour plot of χ^2/ν for varying source parameters. Good agreement between calculations and data is obtained for source parameter values of roughly r_0=4.5-4.8 fm and τ = 20-40 fm/c. These extracted emission timescales are qualitatively consistent with those predicted by microscopic transport calculations [19-21].

Clear identification of the source frame was critical; for the case of no impact parameter selection, as well as for peripheral events, no difference between longitudinal and transverse correlations was seen in any rest frame [36].

The ability to disentangle the effects of size and lifetime for a quickly-decaying source through two-proton correlations prompted us to re-analyze a two-proton data set [21] for the reaction $^{129}Xe+^{27}Al$ at E/A=31 MeV [29].

While event characterization was critical for source frame identification in the nearly symmetric $^{36}Ar+^{45}Sc$ case, for the very asymmetric $^{129}Xe+^{27}Al$ system, the range of likely source velocities is small, even without impact parameter selection. For the extreme case of complete fusion, $\beta_{source} = 0.209$, while emission from an excited projectile would lead to $\beta_{source} = 0.251$. In our analysis, we assume a source velocity consistent with complete fusion.

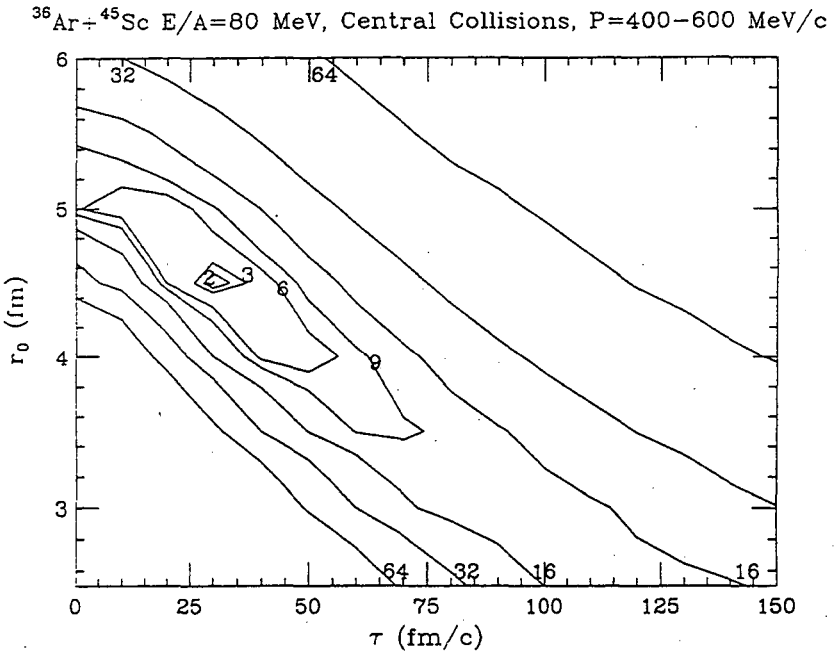

Figure 4. Contour diagram of χ^2/ν, which quantifies the agreement between theoretical longitudinal and transverse correlation functions and the Ar+Sc data shown in the upper panel of Figure 3. χ^2/ν is shown as a function of the size and lifetime of a moving spherical Gaussian source. Details are discussed in the text. (From Ref. [28])

In Figure 5, we show longitudinal and transverse correlations for proton pairs with lab momentum P>480 MeV/c measured in $^{129}Xe+^{27}Al$ collisions at E/A=31 MeV. In the middle panel, a clear suppression of the transverse correlation function (open points) is seen relative to the longitudinal correlation function (solid points), consistent with emission from a long-lived source. When the cuts on the relative angle between **P** and **q** are

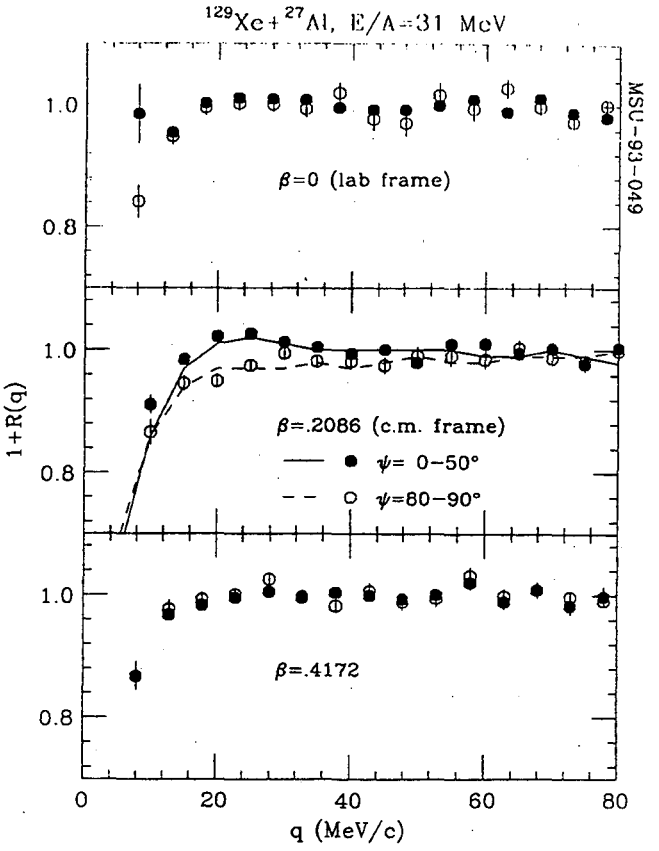

Figure 5. Longitudinal (solid points) and transverse (open points) correlation functions are shown for proton pairs with total laboratory momentum above 480 MeV/c emitted from the reaction $^{129}Xe+^{27}Al$ at E/A=31 MeV. Cuts on the angle $\psi = \cos^{-1}(\mathbf{q}\cdot\mathbf{P}/qP)$ were performed in three rest frames: the laboratory frame (top panel), the center-of-momentum frame of the entrance channel (center panel), and a frame moving with twice the velocity of the center-of-momentum frame. The solid and dashed curves shown in the center panel represent theoretical calculations of the longitudinal and transverse correlation function corresponding to surface emission from a moving spherical source with radius R=3 fm and lifetime τ=1700 fm/c. (From Ref. [29])

performed in the lab frame (top panel), or in the unphysically fast frame moving with twice the system center-of-momentum frame (bottom panel), the signal vanishes. The solid and dashed curves in the center panel correspond to calculated correlation functions for surface emission from a spherical source with R=3.0 fm and τ=1700 fm/c. Such timescales are qualitatively consistent with statistical model calculations [37], while the source size is somewhat smaller than expected for emission from a compound system.

In conclusion, we have clearly observed for the first time the predicted directional dependence of the two-proton correlation function for emission from long-lived nuclear sources. We have discussed the importance of proper identification of the rest frame of the moving source, and have extracted reasonable source sizes and lifetimes for two very different systems. The exploitation of this technique, which is sensitive to lifetimes spanning a range of more than an order of magnitude, adds a new degree of freedom to an already-useful tool in the study of heavy ion collisions.

References

1. F. Zarbaksh et al., Phys. Rev. Lett. **46**, 1268 (1981).
2. W.G. Lynch et al., Phys. Rev. Lett. **51**, 1850 (1983).
3. H. A. Gustafsson et al., Phys. Rev. Lett. **53**, 544 (1984).
4. C.B. Chitwood et al., Phys. Rev. Lett. **54**, 302 (1985).
5. J. Pochodzalla et al., Phys. Lett. **B174**, 36 (1986).
6. A. Kyanowski et al., Phys. Lett. **B181**, 43 (1986).
7. J. Pochodzalla et al., Phys. Rev. **C35**, 1695 (1987).
8. Z. Chen et al., Phys. Rev. **C36**, 2297 (1987).
9. Z. Chen et al., Phys. Lett. **B186**, 280 (1987).
10. Z. Chen et al., Nucl. Phys. **A473**, 564 (1987).
11. S. Pratt and M.B. Tsang, Phys. Rev. **C36**, 2390 (1987).
12. P. Depieux et al., Phys. Lett. **B200**, 17 (1988).
13. T.C. Awes et al., Phys. Rev. Lett. **61**, 2665 (1988).
14. P.A. DeYoung et al., Phys. Rev. **C39**, 128 (1989).
15. D. Ardouin et al., Nucl. Phys. **A495**, 57c (1989).
16. P.A. DeYoung et al., Phys. Rev. **C41**, R1885 (1990).
17. D.H. Boal et al., Rev. Mod. Phys. **62**, 553 (1990).
18. W.G. Gong et al., Phys. Lett. **B246**, 21 (1990).
19. W.G. Gong et al., Phys. Rev. Lett. **65**, 2114 (1990).
20. W.G. Gong et al. Phys. Rev. **C43**, 781 (1991).
21. W.G. Gong et al., Phys. Rev. **C43**, 1804 (1991).
22. D. Goujdami et al., Z. Phys. **A339**, 293 (1991).
23. B. Erazmus et al. Phys. Rev. **C44**, 2663 (1991).
24. M. Korolija et al., Phys. Rev. Lett. **67**, 572 (1991)
25. W. Bauer et al., Annu. Rev. Nucl. Part. Sci. **42**, 77 (1992).
26. D. Rebreyend et al., Phys. Rev. **C46**, 2387 (1992).
27. M.A. Lisa et al., Phys. Rev. Lett. **70**, 3709 (1993).
28. M.A. Lisa et al., Phys. Rev. Lett. **71**, 2863 (1993).
29. M.A. Lisa et al., submitted to Phys. Rev. C.
30. S.E. Koonin, Phys. Lett. **B70**, 43 (1977).
31. M.A. Lisa et al., Phys. Rev. **C44**, 2865 (1991).
32. G.D. Westfall et al., Nucl. Instr. and Meth., **A238**, 347 (1985).
33. W.G. Gong et al., Nucl. Instr. and Meth., **A268**, 190 (1988).
34. W.G. Gong et al., Nucl. Intstr. and Meth., **A287**, 639 (1990).
35. M.A. Lisa, Ph.D. Thesis, Michigan State University, (1993).
36. L. Phair et al., Nucl. Phys. **A548**, 489 (1992).
37. W.A. Friedman and W.G. Lynch, Phys. Rev. **C28**, 16 (1983).

Pion "flow" in relativistic heavy-ion collisions

Bao-An Li[1]

Hahn-Meitner-Institut, Glienickerstr.100, D-14109 Berlin, Germany

Using a hadronic transport model for relativistic heavy-ion collisions, we analyse simultaneously the average transverse momentum of nucleons and pions in the reaction plane as a function of rapidity. The transverse momentum distributions of nucleons and pions are correlated to each other in central collisions, indicating the flow effect of baryon resonances. While in peripheral collisions the two distributions are anti-correlated due to the strong shadowing effect of the spectators.

The endeavor of studying properties of hot and dense hadronic matter pioneered at Berkeley is now continued at SIS/GSI with relativistic heavy-ion beams of energies upto about 2 GeV/nucleon. At these beam energies about one half of nucleon-nucleon collisions are inelastic, mainly through the excitation of baryon resonances. The possibility of forming resonance matter transiently in these reactions has been actively discussed recently[1,2,3]. The dominating decay modes of the resonance matter are the pion emission and the resonance reabsorption. Pions are therefore useful tools for studying properties of the hot and dense hadronic matter, particularly that of the resonance matter.

However, pion observables (e.g. multiplicity, energy spectrum and angular distribution) are sensitive to the dynamics of pion production, propogation as well as the geometry of the reaction. The correct treatment of

[1]Address starting Jan. 1994: Department of Physics and Cyclotron Institute, Texas A&M University, College Station, Texas 77843, USA
e-mail: BALI@TAMCOMP.BITNET

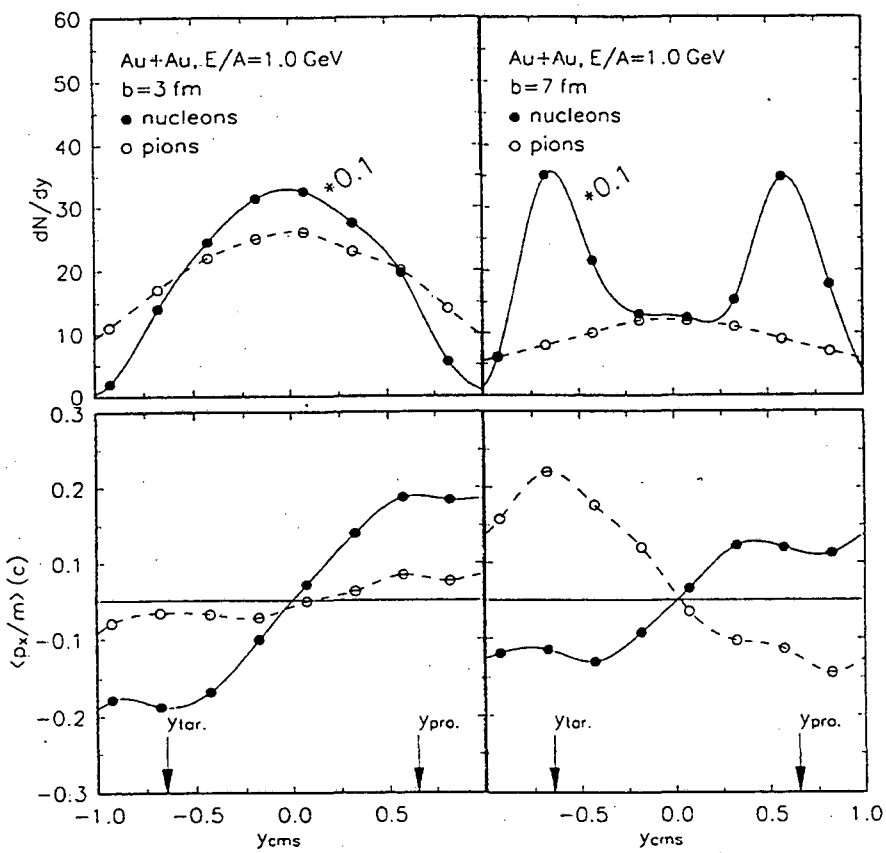

Figure 1: Rapidity and average transverse momentum distributions for nucleons and pions from the reaction of Au+Au at E/A=1.0 GeV at an impact parameter of 3 and 7 fm respectively.

pion dynamics is therefore a prerequisite of inferring properties of hadronic matter using pion observables. Moreover, the frequently advised, more clean probes of the hadronic matter, e.g. dileptons and kaons, are vitally affected by the $\pi, \Delta(N^*), N$ dynamics. Here we report some results of our study on the pion dynamics and properties of the hot and dense hadronic matter by analysing the transverse momentum of pions and nucleons in the reaction plane as a function of rapidity. The model we used to simulate relativistic heavy-ion collisions is the hadronic transport model detailed in ref.[4,5,6].

The transverse momentum analysis was first proposed by Danielewicz and Odyniec to identify the nuclear collective flow in relativistic heavy-ion collisions[7]. Searching for collective flow signatures among final state pions the method has also been applied to pions from relativistic nuclear reactions[8,9]. Typical results of our calculations on the transverse momentum distributions for nucleons and pions are shown in Fig. 1. To characterize the transverse momentum analysis use is usually made of the so-called

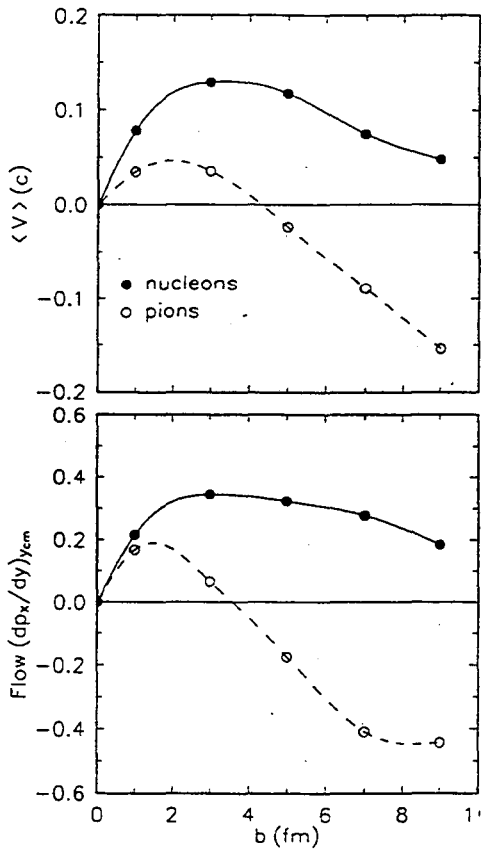

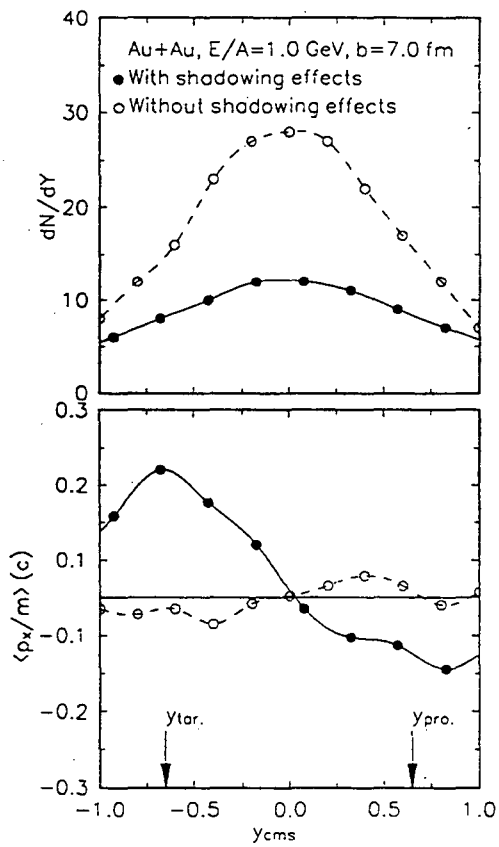

Figure 2: Average transverse velocity and flow

Figure 3: Shadowing effect.

flow parameter F and the average transverse momentum at forward or backward rapidities. The flow parameter F is defined as

$$F = (\frac{d < p_x >}{dy})_{y=y_{cms}}. \tag{1}$$

For ease of comparisons between nucleons and pions, we define the average transverse velocity (rather than the average transverse momentum) as

$$< v >= \frac{1}{\Delta y}\int_0^{\Delta y} \frac{< p_x >}{m} dy, \tag{2}$$

and we have used $\Delta y = 1$ for the Au+Au reaction at E/A=1.0 GeV. The two quantities are displayed in Fig. 2 as a function of the impact parameter. The transitian from the correlation in central collisions to the anti-correlation in semicentral and peripheral collisions is obvious. It is also interesting to notice that the average transverse velocity of pions is only about one third of that of nucleons in central collisions. From the upper windows of Fig. 1, it is seen that the transition is accompanied by the appearance of projectile-like and target-like fragments shown as peaks at projectile and target rapidities. It should be mentioned that the anti-correlation between transverse momentum distributions of nucleons and

pions was also found in a recent BUU model calculation for the reaction of Au+Au at E/A= 2 GeV and an impact parameter of 6 fm[10].

Why the average transverse momentum of pions has the same sign as that of nucleons in central collisions, but opposite sign in semicentral and peripheral collisions ? From the reaction dynamics of baryon resonance productions and the decay kinematics one would expect that the average transverse momentum of pions has the same sign as that of nucleons at both backward and forward rapidities. This is indeed true for central collisions for the following reasons. First, baryon resonances flow together with nucleons with positive (negative) average transverse momentum at forward (backward) rapidities. Therefore, pions emitted along the flow direction of nucleons have higher momenta due to the boost of the collective motion of baryon resonances. Moreover, the Pauli blocking for nucleons from the decay of baryon resonances unfavours more nucleons to be emitted to the flow direction of other nucleons. The momentum conservation of the decay will consequently favours more pions to be emitted to the flow direction of nucleons. In addition, in central collisions most of nucleons participate in the reaction and there is no distinct spectator existing as seen from the rapidity distributions. Whereas in semicentral and peripheral collisions, distinct spectators exist and the size of the spectators grows as the impact parameter increases. Therefore, pions emitted with positive (negative) transverse momenta at forward (backward) rapidities are likely to be rescattered or reabsorbed by the spectators there. While pions emitted with negative (positive) transverse momenta at forward (backward) rapidities can easily fly out without much interaction with the spectators. The net result is that pions with postive (negative) rapidities have negative (positive) average transverse momenta in semicentral and peripheral collisions.

To evaluate the magnitude of pion reabsorptions and quantify our above discussions on the shadowing effect, calculations have also been done by turning off the follwing reaction channels

$$\pi + N \rightarrow \Delta(N^*), N + \Delta(N^*) \rightarrow N + N, \tag{3}$$

as well as

$$N + \Delta(N^*) \rightarrow N + \Delta(N^*) \tag{4}$$

so that the shadowing effect plays no role.

In Fig. 3 we compare the rapidity distributions (upper window) and average transverse momentum distributions of pions calculated with and without the shadowing effect for the Au+Au reaction at b=7.0 fm. From the difference in normalizations of the two rapidity distributions, it is seen that about 50% of primordial pions are reabsorbed. It is interesting to see that without the shadowing effect pions have a transverse momentum distribution similar to that observed in central collisions and can be understood

similarly. The opposite behaviour of the average transverse momentum distributions in the two calculations demonstrate clearly the shadowing effect of the spectators.

In summary, the transverse momentum distributions of nucleons and pions are analysed simultaneously. A transition from correlation to anti-correlation is observed as the reaction goes from central to semicentral collisions. More detailed discussions on the nuclear shadowing effect and pion dynamics can be found in ref.[11,12].

References

[1] V. Metag, Prog. Part. Nucl. Phys. **30** (1993) 75; Nucl. Phys. **A553** (1993) 283c.

[2] E. Grosse, In: Proceedings of the International Workshop on Gross Properties of Nuclei and Nuclear Excitations XXI; Ed. H. Feldmeier, p1.

[3] W. Ehehalt, W. Cassing, A. Engel, U. Mosel and Gy. Wolf, Phys. Rev. C**47** (1993) R2467.

[4] B.A. Li and W. Bauer, Phys. Lett. **254B**, 335(1991); Phys. Rev. C**44**, 450 (1991).

[5] B.A. Li, W. Bauer and G. F. Bertsch, Phys. Rev. **C44** (1991) 2095.

[6] B.A. Li, Nucl. Phys. **A552** (1993) 605.

[7] P. Danielewicz and G. Odyniec, Phys. Lett. **B157** (1985) 146.

[8] D. Keane et. al. in: Proceedings of the 4th Nucl. Dynamics Workshop, Copper Mountain, Colorado, 1986, ed. V. Viola (Indiana University Report CONF-860270, UC-34C, INC-40007-37, 1986).

[9] J. Gosset et al., Phys. Rev. Lett. **62** (1989) 1251.

[10] S.A. Bass, R. Mattiello, H. Stöcker, W. Greiner and Ch. Hartnack, Phys. Lett. **B302** (1993) 381.

[11] B.A. Li, Phys. Lett. **B** (1993) in press.

[12] Nuclear shadowing effect in relativistic heavy-ion collisions, B.A. Li, Nucl. Phys. **A** (1994) in press.

Summary and Epilogue

Heavy ion collisions between 1 GeV/N and 10 GeV/N*

J. Aichelin
Laboratoire de Physique Nucléaire, Université de Nantes,
2, Rue de la Houssinière, 44072 Nantes Cedex 03, France

This contribution focuses on some aspects of heavy ion reactions between 1 GeV/N and 10 GeV/N. It has four parts. In the first part we demonstrate that the long standing goal, to measure the nuclear equation of state, can most probably not be completed without measuring the excitation function of several observables up to several 1 GeV/N. In the second part we show that, besides the increase of the flow, the spectator matter remains rather unaffected by an increase of the beam energy beyond 1 GeV/N. In part three we present results from calculations which show that experimental cross section up to 10 GeV/N can be well described using hadronic models. In the fourth part we report about a new idea to measure density isomers if present, as predicated by some theories, at densities above 2.5 ρ_0. There, too, a measurement of the excitation function up to several GeV/N is required.

1 Can we determine the nuclear equation of state with beam energies below 1 GeV/N?

The theoretical investigations of how to reveal the compressibility (or more generally, the nuclear equation of state (EOS)) started two decades ago with hydrodynamical simulations of heavy–ion collisions [1]. These calculations predicted two collective effects which depend on the EOS: the in-plane "bounce-off" and the out-of-plane "squeeze-out" [2]. Both phenomena have been observed in different experiments. Later it was conjectured that the total production cross sections of particles like π, γ, K^+, and η carry information about the EOS, but calculations showed that only the K^+ may be a sensitive probe. However, it most probably probes more the momentum dependent part of the potential than the density dependent part. For a detailed discussion we refer to the third section and to Ref. [3].

It is beyond the scope of hydrodynamical calculations to give a quantitative description of these phenomena because the system is not in equilibrium and the predicted values depend more on the viscosity, which is also an input parameter in these calculations as is the EOS. In principle, quantitative predictions became possible with the advent of BUU calculations [2].

According to the nuclear equation of state, the compressional energy W or the pressure is a function of two variables, the temperature T and the density ρ. Thus in principle we

are looking for the difference

$$\Delta W = W(T, \rho) - W(T = 0, \rho = \rho_0)$$

where ρ_0 is the normal nuclear matter density, the central density of the nucleons at the beginning of the reaction. The calculations show that the time scale for thermalization is of the order of the mean free path divided by the average relative velocity and is, therefore, small compared to the time which is required to reach the highest compression (20 fm/c). Therefore at 800 MeV/N, the compression of the system takes place at an almost constant temperature, which is, in our case — in agreement with experiment — 110 MeV. Hence the physics is determined by the difference

$$\Delta W = W(T = 110 \text{ MeV}, \rho) - W(T = 110 \text{ MeV}, \rho = \rho_0)$$

There are two contributions to the compressional energy: The change of the kinetic energy of the Fermi gas and the change of the potential energy. The first can be safely neglected because the compressional energy of a Fermi gas for the density we obtain is about 3 MeV/N, and it is taken into account in the dynamics due to Liouville's theorem. Hence the important quantity which determines the observables is the compressional energy stored in the potential.

To be able to calculate the compressional energy built up in a heavy-ion reaction, and hence to do a detailed investigation of what compression may be reached in these reactions and what causes the transverse momentum transfer requires a simulation of heavy ion reactions which conserves energy better than 2%. This is neither the case in BUU or VUU calculations, nor in the early versions of QMD. The version of QMD employed for this investigation achieves this goal by employing a high-order numerical integration.

In order to investigate the question of whether an appreciable compressional energy is built up we investigate a system which is, due to its size, most suitable for displaying compressional energy; i.e. an $Au+Au$ collision. Since the compression should increase with energy, we have chosen an energy of 800 MeV/N which is close to the highest beam energy presently available for heavy projectiles. We performed calculations at b = 3 fm for 3 different EOS's which cover the region of EOS's expected from microscopic calculations [4]. We report here on the results only. For the details of the QMD program we refer to Refs. [3, 4].

We investigate the time evolution of total, kinetic and potential energy as well as of the density. The results are displayed in Fig. 1. On the left hand side of the figure we display these quantities averaged over all nucleons, on the right hand side we average over the nucleons of the high density zone only. There the only nucleons considered are those which are, at the time of highest density ($\approx$ 22 fm/c), in a sphere of radius R = 3 fm around the point of highest density. About 35 of the 394 nucleons are in this sphere. Those nucleons are compressed most and should therefore display effects of the different EOS's most clearly. We start the discussion with the left column. The energy conservation for all static EOS's is better than 2% as can be seen from the top row. The momentum dependent EOS (SM) is slightly worse. This is due to the free mass scattering description

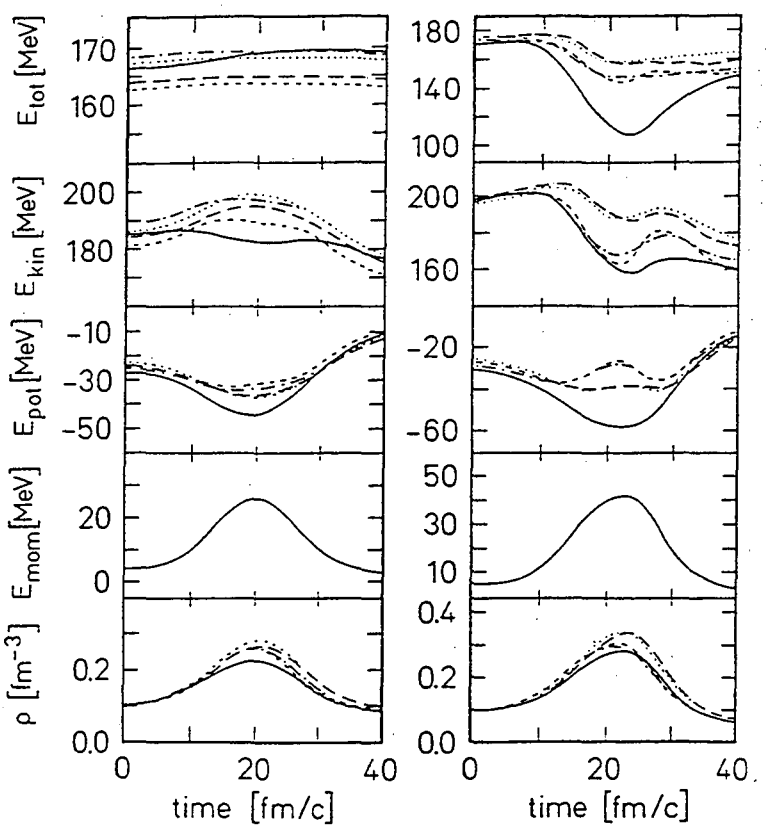

Figure 1: Time evolution of the average total, kinetic and potential (static and momentum dependent) energies as well as of the average density of nucleons of two colliding Au-nuclei at 800 MeV/N. The soft, hard, and soft momentum depended EOS correspond to the dashed, dashed-dotted and full line, respectively. We averaged over all nucleons (left) and the central region (right).

employed in these calculations [3] which slightly violates energy conservation in the case of momentum dependent potentials.

The second and third rows display the kinetic and potential energy, respectively. It was argued that due to the compression the potential energy increases and hence less energy is available for particle production [5]. In contradiction to this intuitive picture the potential energy does not increase but decreases and the kinetic energy increases. Thus compressional energy is not built up — at least on the average. The reason is quite obvious and can be seen from the bottom row. The combined system has a smaller surface. The average density at the center of the nucleons (center of the Gaussians) which is initially well below normal nuclear matter density, increases. According to the EOS this causes a lowering of the potential energy. For static potentials this means an increase in the kinetic energy, in the case of a momentum dependent potential the energy is stored in the momentum dependent part of the potential.

The right hand column displays the time evolution of energies and densities of the nucleons belonging to the high density region. Of course their total energy is not a conserved quantity, and indeed they lose about 20 MeV/N. This energy is transferred to the surrounding fellow nucleons. We will come back to this point later. We see that also the potential energy of these nucleons is lowered at the beginning of the reaction. Only later (around the time of highest compression) we see a slight increase in the potential energy due to compression. It reaches about 15 MeV/N and the difference between the different EOS's is even lower! Thus even in the most central collisions of the heaviest projectiles the nucleons of the most dense regions see compressional energies only of the order of 15 MeV at 1 GeV and it will be an extremely complicated task to find observables which measure the difference of the compressional energy of the different EOS's unambiguously. However, all calculations indicate that the density, the compressional energy, and also the flow, increases with increasing beam energy. The larger the flow the higher the beam energy is certainly the change to pin down the nuclear equation of state and therefore experiments between 1 GeV/N and 10 GeV/N will certainly be highly appreciated, if not mandatory. Whereas a quantitative prediction is still plagued by the problems of relativistic Hamiltonian dynamics, this qualitative tendency is predicted by all models.

What causes this small compressional energy? Due to the dynamics of the reaction the system is able to avoid high compression. Instead of piling up matter, which costs compressional energy, particles are diverted and energy is transferred to the surrounding fellow nucleons. Therefore the total energy of the central nucleons becomes lower. One effective way to do this is the transverse momentum transfer. Based on hydrodynamical calculations it was assumed that the bounce–off is due to the (isotropic) release of the compressional energy. This is not true according to our calculation. Quantifying the bounce–off by the quantity $\langle p_x^{dir} \rangle = \sum_i sign(y_i) p_x^i / A$ [3] we find that the nucleons from the central high compression zone have finally gained only a small average transverse momentum. A much higher average transverse momentum is gained by those nucleons which have not been part of the high compression region. These nucleons gained their momentum transfer while passing the surface of the high density region (and feeling the strong potential gradient). They do not really take part in the compression. Thus the bounce is a quite indirect measure for the compressional energy. It measures the gradient

of the compressional energy and not the compressional energy itself, as was believed earlier, and therefore does not test really the high density / high compression region, but still yields information on the EOS.

2 Spectator matter at beam energies beyond 1 GeV/N

The flow is predicted to increase with increasing beam energy. However, of the observables which measure properties of the spectator matter, this seems to be the only one which changes beyond a beam energy of 2 GeV/N. Hence one may conclude that the spectator matter bounces off collectively and the disintegration into fragments and single nucleons takes place only later.

In this section we would like to show that the transverse and parallel momentum spectra of protons in the target spectator domain do not change beyond an energy of 1 GeV/N. This behaviour is expected in the participant-spectator model. Beyond 1 GeV/N the velocity of the participant zone is so fast that nucleons with a average velocity of the order of the Fermi motion can hardly cross the border between participants and spectators during the time they are close together in coordinate space. Hence the only interaction between spectators and participants are elastic collisions (inelastic collision would place the reaction partners well in forward rapidity). The average transverse momentum transfer in elastic collisions is around 300 MeV/c and changes little with energy. Due to the constant transverse momentum transfer we do not expect that the transferred momentum changes substantially between Bevalac (E = 2 GeV/N) and CERN energies (E = 200 GeV/N). There was, however, the hope that some participants may enter the spectator matter and hence the spectator matter may act as an detector for these particles. This hope was based on the fact, that at low beam energies (and here even 200 GeV/N are low) a clear separation of the target and the midrapidity regime cannot be established and some rescattered particles show up at target rapidity. But it is an open question whether not only in momentum space but also in coordinate space rescattered particles and spectator particles overlap. Thus the physics at target rapidity is quite interesting for the understanding of the space-time evolution of the reaction.

The data at 2.1 GeV/N and at 200 GeV/N display striking similarities but also seemingly large differences in the target rapidity regime. Aleklett et al. [6] found that the yield of specific Na and Sc isotopes does not change above 1 GeV/N. This points towards a similar reaction mechanism as far as the target (spectator) fragmentation, the most probable source of these heavy ions, is concerned. This observation was confirmed by Brechtmann et al. [7, 8], who measured the production cross section of fragments with charges between 6 and 15. Also the dn/dy distribution of shower particles, measured in emulsion experiments, points towards an energy independence of the observables in the target rapidity region[9].

The baryons and light clusters, however, seem to show dramatic differences in the target rapidity domain. The slope of the transverse kinetic energy spectrum of protons has been reported to be 66 MeV for O (200 GeV/N) + Au as compared to 123 MeV for the Ne (2.1 GeV/N) + Au reaction[10]. Also the rapidity distribution differs significantly.

This is remarkable for a rapidity region ($y_{lab} < 0.2$) where we do not expect to see

nucleons which have suffered inelastic collisions. The least inelastic process is the creation of a Δ-resonance. The change of a target nucleon into a Δ goes along with a rapidity shift of $\Delta y \approx 0.2$ at large beam energies and of $\Delta y \approx 0.4$ at 2.1 GeV. Thus on the average the nucleon created in the decay of the Δ is not observed in the investigated rapidity window. At beam energies of several GeV/N on the average there are many particles produced and thus the inelasticity is even higher. In any case nucleons involved in an inelastic nucleon nucleon collision should not be observed in the considered rapidity window.

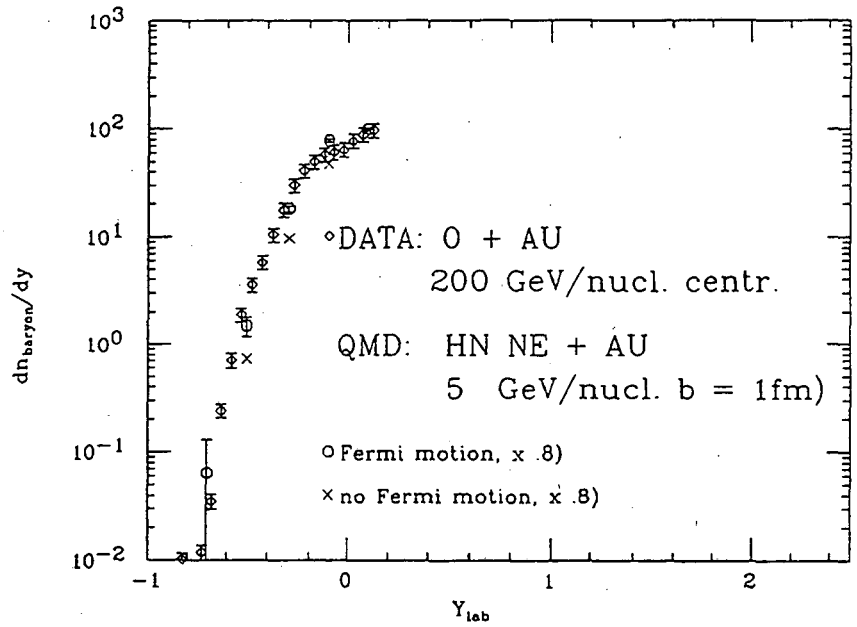

Figure 2: The theoretical rapidity distributions for the reaction of neon on gold at beam energies of 2.1 and 5 GeV/N as compared with experimental data of the reaction of oxygen on gold at 200 GeV/N.

Theoretically the baryon spectra in the target rapidity domain at 200 GeV/N and 1 GeV/N have not been analyzed so far with the same theoretical models. As mentioned in section 1 energies at 1 GeV/N are clearly the domain of Boltzmann Uehling Uhlenbeck (BUU) or "Quantum" Molecular Dynamics (QMD) models [2, 3]. In these models the nuclear interaction is treated as a sequence of nucleon nucleon collisions. Between the collisions the nucleons interact via an attractive field. Being of importance at that energy, great care has to be taken to simulate the Fermi momentum, the binding energy, and the Pauli suppression of possible collisions sufficiently accurately. The cross section for nucleon nucleon collisions can either be taken from experiment or can be calculated in the one boson exchange model. These models agree very well with the existing data up to 2 GeV/N. Energies of 200 GeV/N are the realm of string models [11, 12]. These models have been employed to investigate the baryon rapidity and transverse energy distributions. They were designed to describe observables which depend on inelastic

nucleon nucleon collisions i.e., the meson spectra, and little effort has been made to describe the dependence of the observables on elastic collisions.

How is it possible to compare reactions at 1 GeV and 200 GeV with the same theoretical tool? I think that the above mentioned experiments as well as the theoretical considerations allow the conjecture that in the target rapidity domain little changes between 1 GeV and 200 GeV. Participants and spectators do not mix. Whereas the physics of the participants is strongly energy dependent that of the spectators is independent of the energy.

In order to investigate this question [13], we applied the experimental cuts (300 MeV $> E_{kin}/N >$ 20 MeV and $-1.7 < \eta < 0.6$) to our theoretical baryon (all singles and clusters with $Z \leq 2$) rapidity distribution at 2.1 GeV/N and 5 GeV/N and compared them in Fig. 2 with the experimental results for O (200 GeV/N) + Au. We observe that the experimental results are almost in complete agreement with both calculations, although the calculations are performed at an energy 40 times lower than the experimental energy. The large difference between the rapidity distributions at 2.1 GeV and 200 GeV for $y < -0.4$ is due to the acceptance cut in the total energy ($E_{kin}/N <$ 300 MeV). For positive y-values the yield is reduced due to the cut in η. We would also like to mention that about 40% of the nucleons are bound in larger clusters and are not counted here.

In Fig. 3 we compare the experimental transverse energy distribution for Ne (2.1 GeV/N) + Au for different rapidity windows and that of O (200 GeV/N) + Au with the calculations at 2.1 GeV/N and 5 GeV/N for neon on gold. We start with the top row, where we compare experiment and theory at 2.1 GeV/N for the rapidity window $0.065 < y < 0.443$. The average experimental $\langle E_t \rangle$ is 123 MeV [10]. The theoretical results are filtered with the Plastic Ball filter routine SIMDAT. The QMD calculation reproduces the slope quite well for energies larger the 120 MeV. Below that there are discrepancies. They may be due to the insufficient treatment of small clusters in QMD or due to a not perfect acceptance filter. The same result we obtain when comparing theory and experiment in the rapidity window $0.1 < y < 0.2$ in the middle figure. Again the slope is well reproduced above E_t = 120 MeV. In the energy interval between 200 MeV and 425 MeV, where almost all particles are detected and therefore the influence of the acceptance filter is small, we find an $\langle E_t \rangle$ of 105 MeV for the experiment and an $\langle E_t \rangle$ of 97 MeV for the QMD calculations. Please note that the slope is steeper here as compared to the larger rapidity bin. The bottom figure displays our results for 2.1 and 5 GeV filtered with the above mentioned CERN Filter as well as the experimental data of WA80 group for 200 GeV/N O + Au. A closer inspection reveals that the CERN filter changes the spectra at $E_t < 100$ MeV (due to the cut in η) and at $E_t > 250$ MeV (due to the cut in E_{tot}). In between theory and experiment agree quite well above E_t =100 MeV, although the calculation is done at a 100 times lower energy. The calculations at 2.1 GeV/N give an $\langle E_t \rangle$ = 86 MeV as compared with the experimental value of $\langle E_t \rangle$ = 75 MeV at 200 GeV/N.

Thus the different rapidity distributions and the different slopes of the transverse energy distribution published for the reactions Ne (2.1 GeV/N) + Au and O (200 GeV/N) + Au can be attributed to different experimental set ups, which is sensitive to different parts of the phase space. The small differences in $\langle E_t \rangle$ of 15% may be due to a change of the elastic nucleon-nucleon cross section between these energies. Both spectra can be

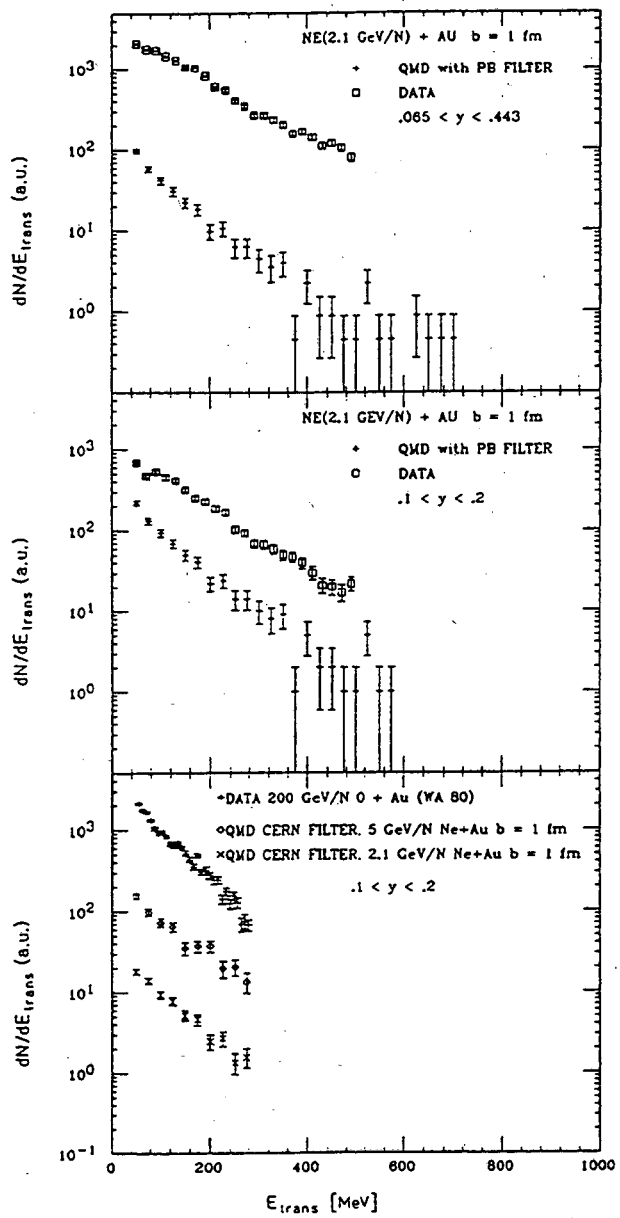

Figure 3: The calculated transverse kinetic energy spectra as compared with experiment. The theoretical calculations are filtered with the Plastic Ball filter SIMDAT (top and middle) and with the CERN Filter (bottom).

generated from the same primordial distribution if one applies the different experimental filter. It turns out that both distributions do not change by more than 50% in the energy range between 1 GeV/N and 200 GeV/N. Thus also the single particle distribution show the scaling features observed a while ago for the fragments above a beam energy of 1 GeV/N.

Our results confirm the conjecture, based on very general arguments, that nucleons observed at backward rapidity are only rarely involved in inelastic collisions. Only elastic collisions led to an excitation of the spectator matter. The momentum transfer in these collisions is constant and make the beam energy independence of the results plausible. Baryons having suffered inelastic collisions can contribute only if they have secondary collisions. The results and the agreement with experiment indicate that inelastic collision products contribute very little to the investigated spectra.

3 When do quark degrees of freedom become important?

At energies below $E = 1$ GeV/N the experimental double differential cross section $\frac{d\sigma}{d\Omega dE}$ for protons and pions observed in heavy ion reactions can be quite well described by models (called cascade models) which start from the assumption that a heavy ion collision can be viewed as a sum of individual nucleon nucleon collisions [14] which interact be the free elastic or inelastic cross section.

The free pp cross section in this energy domain has been described quite well in the framework of the one boson exchange (OBE) model, in which a σ, ρ, π, or ω meson is exchanged between the baryons [15]. The higher order contributions are phenomenologically incorporated by effective form factors which are usually adjusted to elastic scattering data. This limits the predictive power to the inelastic cross sections.

With increasing energy and hence larger momentum transfer this mesonic description of the scattering of nucleons has to break down. A larger momentum transfer probes a smaller length scale and therefore the substructure (quarks) of the nucleons becomes important. Due to the asymptotic freedom the collision will ultimately take place between free quarks.

Recent calculations have shown that up to beam energy of 10 GeV elementary reactions like $p + p \rightarrow \Lambda(\Sigma) + K^+ + p$ [16] as well as $p + p \rightarrow \Delta + N$ and $p + p \rightarrow \Delta + \Delta$ [17] can be described in the one boson exchange model. For energies larger then 10 GeV no data exist. Figure 4 displays the calculations of the last two reactions in comparison with the world data. Thus in the energy domain of concern, we are still able to describe the cross section on the hadronic level.

At 200 GeV/N, a very good agreement between data and theory has been obtained in the above mentioned quark based string models. This raises the question where the transition between the OBE and the string models takes place. A clear answer is not at hand yet because:

- The complexity of diagrams even in the one boson exchange model increases fast due to the many nuclear resonances and their complicated decay modes. Their properties and decay probabilities are little known and hence any theoretical calculation has

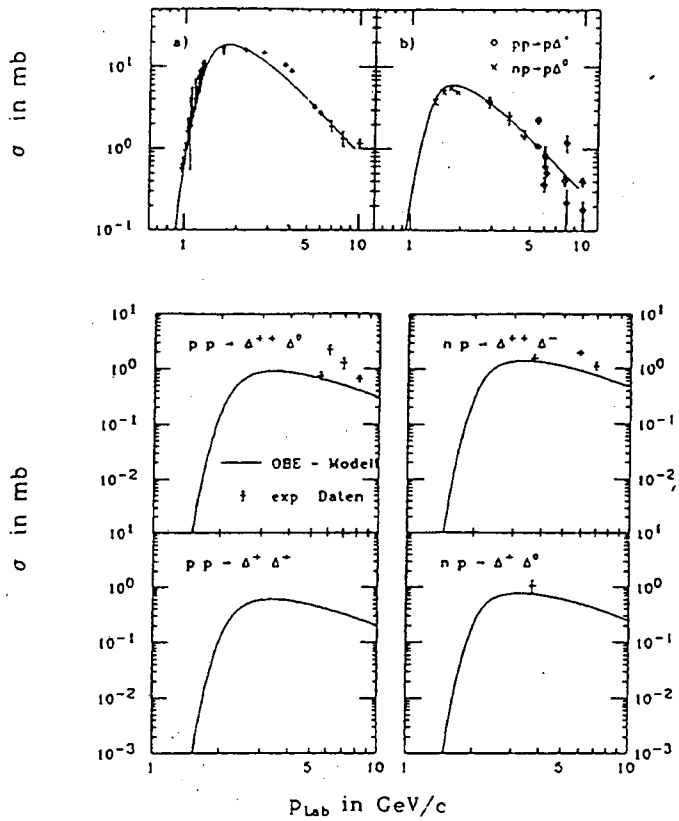

Figure 4: Calculation of the total cross section for Δ and double Δ production in comparison with the world data.

large error bars. Furthermore, the evaluation of the Feynman diagrams requires the calculation of the trace over many γ-matrices. For complicated processes these manipulations exceed the power of present trace manipulation programs.

- Effective form factors as required in the OBE model can simulate some quark effects.
- Data which allow verifing the validity of the calculation are very rare even for simple decay modes and the few which exist have large error bars.

The success of both the string based models as well as the hadron based models in explaining the AGS data at 14 GeV/N may suggest that in this region the transition takes place. However, this conjecture deserves an experimental verification.

4 Density isomers

It has been argued by several authors [19], that the nuclear equation of state may have a second minimum at densities higher than $2\rho_0$. The reason for this may be nonlinear scalar meson terms in the Lagrangian or collective excitations of zero frequency spin-isospin modes in nuclear matter, called pion condensation. Although it should be noted that up to now the existence of such a density isomer is still speculative a positive knowledge would limit several theoretical considerations. Unfortunately, up to now it is not clear at which energy and by which observables they would be revealed.

Motivated by these theoretical considerations we have investigated how the presence of density isomers would influence the production of particles. We will argue here, that the kaons may be a valuable tool for their detection. However, if the isomer is at a density larger than 2.5 ρ/ρ_0 energies above 1 GeV/N are required. This is the result of microscopic Boltzmann Uehling Uhlenbeck (BUU/VUU) calculations [20]. The details of the numerical solution can be found in Ref. [2].

Figure 5 displays the three different equations of state we use in our calculations. Up to a threshold which is higher than $2\rho_0$, all these EOS are identical and follow the hard equation of state (Eq. 1). The EOS's with a density isomer start to deviate from the hard EOS at $2.4\rho_0$ (Hisom 1) resp. $2.6\rho_0$ (Hisom 2). The density isomer has a depth of 2 MeV at $\rho = \rho_{thres} + .3\rho_0$. Above $\rho_{thres} + 0.6\rho_0$ we have

$$E/N_{Hisom}(\rho/\rho_0) = E/N_{Hard}(\rho/\rho_0 - 0.6).$$

Before coming to the results of the calculation it is instructive to discuss qualitatively our expectations. Below threshold kaon production is concentrated at central collisions where the density is high. At 1 GeV Au + Au the average density at the point of the kaon production is around $2\rho_0$, the maximal value about $3\rho_0$ [21].

Thus, in contradistinction to the flow the kaons test the high density zone itself. Only there are there a sufficient number of collisions that some baryons can gain a substantial increase of their momenta what is necessary to overcome the threshold. The Fermi motion alone is not able to provide the additional required energy. Most of the kaons are produced in a two step process

$$N_1 + N_2 \rightarrow N_1 + \Delta, N_3 + \Delta \rightarrow N_3 + \Lambda + K$$

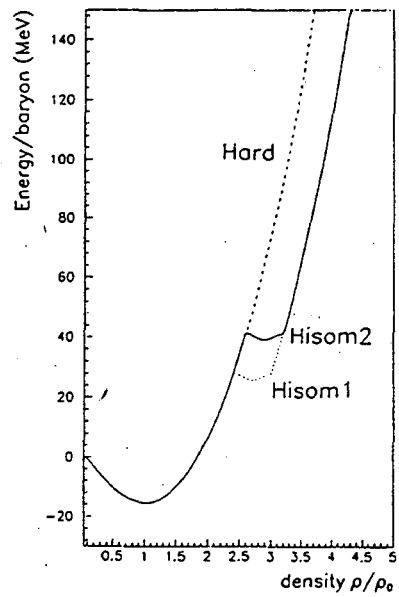

Figure 5: The three equations of state employed in the calculation.

Due to kinematical reasons this channel is much more effective than the channel

$$\pi + N \rightarrow \Lambda + K$$

which counts for not more than 20% of the produced kaons[22]. A decreasing mean free path of the Δ therefore enhances the kaon production because it reduces the probability that the Δ decays before it collides with another nucleon. A softening of the equation of state at high density allows the system to reach a higher density and hence a shorter mean free path and therefore favours the production of kaons. If a density isomer exists there is a region at which there is no additional energy is necessary to compress the system further. If the system enters this region in the course of a heavy ion reaction we expect a rather sudden increase of the density and consequently a increase of the kaons as well. Thus all depends whether the system reaches the required density. Below that density the system does not "notice" the fact that an isomer exists. Since the density is a monotonous function of the energy, we expect a jump appearing in the excitation function. Due to the increasing number of inelastic collisions we expect also a moderate dependence of the pion yield.

We come now to the numerical results. We performed calculations of the reaction Au + Au, b = 3 fm for the three different equations of state employing the BUU/VUU model. The details of this model can be found in Ref. [2]. Figure 6 displays the kaon yield. At 600 MeV/N the kaon yields of all three EOS are identical. At that energy the density of the system does not exceed $\rho/\rho_0 = 2.4$. At E_{beam} equal 700 MeV/N, the kaon yield for Hisom 1 is more than 1 order of magnitude higher than that of the other two.

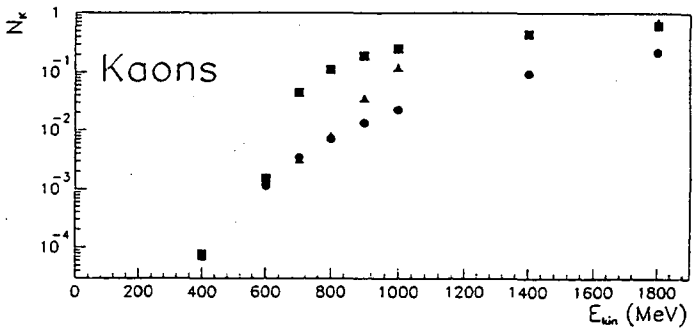

Figure 6: Kaon yield for the three equations of state.

The density of $\rho/\rho_0 = 2.6$ is reached around $E_{beam} = 1000$ MeV/N and consequently we observe now the jump in the kaon yield for Hisom 2. At still higher energies the difference between Hisom 1 and Hisom 2 becomes smaller because the density is now beyond $3.2\rho/\rho_0$ where both EOS become identical. Also the difference between the EOS's with isomer and the hard EOS becomes smaller. More and more kaons are produced now in peripheral reactions because the Fermi motion can provide the additional energy to overcame the threshold of 1.58 GeV. At still higher energies we expect that the majority of the kaons come from these peripheral reactions. Therefore the three curves merge and kaons are not suited anymore as a signal of a density isomer. However, if the isomer appears at a density which is not reached with beam energies below the kaon threshold, other processes which have a higher threshold may be used, like the production of $\bar{p}$'s or $\bar{\Lambda}$'s.

5 Conclusions

We have outlined several perspectives for heavy ion reactions in between 1 GeV/N and 10 GeV/N. As we have seen this is an exciting domain close to the borderline of conventional hadronic physics. We see strong evidence that this energy regime is still understandable in terms of conventional hadron physics. This helps a lot in analyzing the experimental results. The knowledge of the excitation function for particle production — like the enhancement of the strangeness — is certainly a prerequisit for the understanding of the AGS data. We expect a clear separation of spectators and participants with — beside the flow — little communication between the both. The compressional energy as well as the flow is expected to increase and therefore the measurement of the excitation function offers the perspective to pin down the nuclear equation of state with more precision than at low energies where the smallness of the effects renders conclusions difficult. But this domain may offer also exciting new phenomena like detection of possible density isomers.

* This talk is devoted to my father, whose death prevented an oral presentation.

References

[1] H.G. Baumgardt, J.U. Schott, Y. Sakamoto, E. Schopper, H. Stöcker, J. Hofmann, W. Scheid and W. Greiner, Z. Phys. **A273** (1975) 359;
J. Maruhn and W. Greiner in: Treatise on Heavy Ion Physics, ed. A. Bromley, Plenum Press NY

[2] H. Stvcker and W. Greiner. Phys. Rep. **137** (1986) 277 W. Cassing et al., Phys. Rep. **188** (1990) 361

[3] J. Aichelin, Phys. Rep. **202**, (1991) 233

[4] J. Jaenicke and J. Aichelin, Nucl. Phys. **A547**, (1992) 542

[5] G. Peilert, A. Rosenhauer, J. Aichelin, H. Stöcker and W. Greiner, Mod. Phys. Lett. **A3** (1988) 459 and Phys. Rev. **C39** (1989) 1402

[6] K. Aleklett et al., Phys. Lett. B197 (1987) 34.

[7] C. Brechtmann, W. Heinrich, Z. Phys. A330 (1988) 407.

[8] C. Brechtmann, W. Heinrich, Z. Phys. A331 (1988) 463.

[9] L.M. Barbier et al., Phys. Rev. Lett. 60 (1988) 405.

[10] H.R. Schmidt and H.H. Gutbrod, Proc. Nato ASI on The Nuclear Equation of State (Peniscola, Spain, 1989) Plenum Press New York

[11] K. Werner, Z. Phys. **C42**,85 (1989)

[12] H. Sorge et al., Z. Phys. **47**, 629 (1990)

[13] J. Jaenicke and J. Aichelin, Phys. Lett. **B256**, (1991) 341

[14] J. Cugnon, A. Lejeune and P. Grange, Phys. Rev **C35** (1987) 861, J. Cugnon in: Proc. Nato ASI on The Nuclear Equation of State (Peniscola, Spain, 1989) Plenum Press New York

[15] R. Machleidt, Advanced in Nuclear Physics, ed. J.W. Negele and E. Vogt Plenum Press, New York 1989

[16] J.M. Laget, Phys. Let **B259** (1991) 24

[17] S. Huber and J. Aichelin, Nucl.Phys. in print

[18] B. Andersen, G. Gustafson and B. Nielsson-Almqvist, Nucl. Phys. B281, 289 (1987)

[19] E. Feenberg and H. Primakoff, Phys. Rev. 70 (1946) 980. A.R. Bodmer, Phys. Rev. D4 (1971)1601. A.B. Migdal, JETP 34 (1972) 1184. T.D. Lee and G.C. Wick, Phys. Rev. D9 (1974) 2291. W. Weise and G.E. Brown, Phys. Rep. 27C (1976) 1

[20] C. Hartnack,et al. submitted to Phys. Rev. Lett.

[21] C. Hartnack, GSI Report 93 - 05 and to be published

[22] L. Xiong, C.M. Ko and J.P. Wu, Phys. Rev. C42 (1990) 2231

QUO VADIS, BEVALAC PHYSICS ?

Wolfgang BAUER
National Superconducting Cyclotron Laboratory
and Department of Physics and Astronomy
Michigan State University
East Lansing, MI 48824-1321, USA

ABSTRACT

The current status of relativistic heavy ion science is reviewed.

1. Introduction

On Saturday, February 21, 1993, the BEVATRON was shut down permanently. This ended two decades of research on relativistic heavy ion physics, which had begun in 1974 when the SUPERHILAC was converted into an injector for the BEVATRON, thus creating the BEVALAC. From the beginning, heavy ion research at the BEVALAC has been an international effort with scientists from the GSI forming the most important coliaboration from abroad. One of the results of this collaboration has been the ongoing series of *High Energy Heavy Ion Study* conferences, a series of which the present one is the 9th edition. These conferences were alternatively held at the GSI and at LBL. With the retirement of the BEVALAC, it may well be that this format has come to an end as well. And since this is the last talk of what could be the last *High Energy Heavy Ion Study*, a critical summary of where we are and where we are going with the field of relativistic heavy ion science is in order.

In the following I have attempted to give an account of the most important developments in physics, both experimental and theoretical, resulting from the research effort at the BEVALAC. This account is not so much meant as a review, but rather as a personal perspective. I am also attempting to include the description or at least mentioning of important outstanding problems which have to be addressed in the future. And finally, I try to point out directions into which BEVALAC physics might go, and where this research could be carried out.

Since this present manuscript is not meant to be a comprehensive review, I should point out where reviews can be found. A short overview of the history of BEVALAC physics has recently been published in Physics Today[1]. Several reviews can be found in Annual Review of Nuclear and Particle Science[2–9], in Physics Reports[10–16], and elsewhere.[17–22]

2. Models of Nuclear Dynamics

The field of nuclear dynamics represents an intersection of quantum mechanics, relativity, field theory, many-body theory, particle physics, fluid-dynamics, and thermodynamics. It is thus unrealistic to expect *one definite theory* which explains all observed phenomena to be derived. Progress has rather been made in small incremental steps, resulting from an iterative interaction between theory an experiment.

A large impetus for the field of relativistic heavy ion physics had come form nuclear hydrodynamics calculations[25] in which nuclei are represented by basically incompressible fluids with their motion governed by fluid-dynamics equations. The postulation of nuclear shock waves as a result of these calculations has resulted in two decades of theoretical arguments and experimental searches with proponents and opponents both declaring victory.[26]

One of the first models to be introduced as a means of describing the experimental results obtained by the Plastic Ball group at the BEVALAC was the "Fireball"[23]. Here it was assumed that thermal and chemical equilibration had taken place in the early stages of the nuclear reaction, and that the population of different particle species and energy distributions were then governed by thermodynamics arguments.

At about the same time the first one-dimensional Time-Dependent-Hartree-Fock calculations were performed for nuclear collisions.[24] Motivated by the success of the nuclear shell model, it was assumed here that heavy ion collisions are dominated by the effects of the one-body interaction of individual nucleons with the nuclear mean field.

An opposite approach was taken by proponents of intra-nuclear cascade[27] calculations, neglecting the interaction with the mean field and assuming dominance of two-body interactions. Thus heavy ion reactions were visualized as a sequence of individual independent two-body collisions.

The one- and two-body approaches were synthesized in the so-called Boltzmann-Uehling-Uhlenbeck theory (BUU, otherwise also known by various acronyms such as VUU, BNL, LV, ...).[28,29,12,14,17,19,15,7,22] This theory solves a Boltzmann-like integral equation for the nucleonic phase space density distribution function by utilizing the test particle method.[30] With it, it was for the first time possible to investigate the interplay between kinetic pressure and mean field compressional effects. One of the motivations for this was to determine the compressibility for nuclear matter

$$\kappa = k_f^2 \left.\frac{\partial^2 E_{\rm bind}/A}{\partial k_f^2}\right|_{\rho=\rho_0} = 9\rho^2 \left.\frac{\partial^2 E_{\rm bind}/A}{\partial \rho^2}\right|_{\rho=\rho_0} . \tag{1}$$

This goal, however, proved to be very elusive as theorists began to incorporate more and more realistic interactions including their non-locality or momentum dependence, and relativistic generalizations. (See ref. 20 for a review.) Clearly, much more work is to be done here.

The BUU theory is a theory for the time evolution of the one-body Wigner function of nucleons. It is thus not able to properly include fluctuations in its original

formulation. Attempts to improve on this point were directed to include fluctuations into the same formalism.[31]

An alternate way was motivated by using the test particle method in the limit of one test particle per nucleon, resulting in a molecular dynamics-type simulation, QMD[32,16] and QPD.[33] These models were produced in order to describe nuclear fragmentation. At beam energies above E/A $\approx$ 200 MeV this prescription seems to work well. At lower beam energies, however, where there is a maximum in the yield of intermediate mass fragments, QMD does not seem to work as well as desired (see the contributions of G. Peilert, M. Begemann-Blaich, M.B. Tsang, and C. Sangster in this volume). This might be due to an improper dependence of the entropy on the excitation energy in these calculations, resulting from the fact that they basically use classical dynamics as their foundation.

A possible remedy for this may be found along the way of the Fermionic Molecular Dynamics (FMD)[34,21,35] where the many body wave function of the nuclear system is taken as a truncated Slater determinant of Gaussian wave packets representing individual nucleons. At present, the procedure to include nucleon-nucleon collisions is implemented in an ad hoc way, but seems to result in better agreement with data.

A wide array of investigations to improve the present state of modeling nuclear dynamics is underway. While the progress over the last two decades has been very impressive, many fundamental questions remain unanswered. These include the proper inclusion of fluctuations, of three- and more-nucleon interactions, of true quantum effects, of consistent inclusion of mesonic degrees of freedom and retardation effects, of consistency between mean field and two-body interaction in the models. As more and better experimental data arrive, theoretical models become more and more constrained, and it is possible to falsify some (or even all) of them, replacing them with better ones. Some of the data driving this development will be examined in the following sections.

3. Particle Production

The only observables from heavy ion collisions which are accessible to experiment are the asymptotic momentum states of outgoing particles. These particles can roughly be divided into two groups: Primary particles (protons, neutrons, deuterons, tritons, helium nuclei, and heavier fragments such as intermediate mass fragments, evaporation residues, or target and projectile like fragments) and secondary particles (pions and other non-strange mesons, kaons and other strange mesons, strange baryons, anti-protons and other antiparticles, photons, di-lepton pairs, ...).

The primary category consists of particles made up of neutrons and protons, building blocks already present in the two colliding nuclei. The minimum energy needed to emit these particles is therefore only of the order of the difference in the binding energies between the emitting nuclear system and the ejectile, $\Delta E/A \leq 8$ MeV.

The particles in the secondary category are all created during the heavy ion collision. The minimum energy needed for their creation is their rest mass, M_0, in cases where the production of a single meson is not forbidden by conservation laws (e.g.: pion). In cases where particles can only be produced in pairs, the energy cost is even higher. For example, to produce a K^+, the minimum energy needed is

$$E_{\min} = M_0(K^+) + M_0(\Lambda) - M_0(p) \tag{2}$$

in the center of mass of the emitting system. Therefore the production of these particles can be a signature for a very energetic event. This is even true for the production of photons or di-lepton pairs, where one can select high photon energies or large values of the invariant mass, $M_{\rm inv}^2 = (\hat{P}_1 + \hat{P}_2)^2$, of the pair.

3.1. Medium Effects and the Nuclear Equation of State

At beam energies above nucleon-nucleon threshold the production of secondary particles is dominated by production from individual two-nucleon collisions. One can ask which medium effects play a role in modifying the elementary production probabilities and lead to observable consequences distinguishing particle production in the nuclear medium from an incoherent superposition of nucleon-nucleon collisions.

The most elementary of these effects is the motion of nucleons inside ground state nuclei due to the effects of the Pauli exclusion principle, the so-called Fermi motion. The maximum relative momentum between two nucleons from two different nuclei is then not just the beam momentum, p_b, but $p_b + 2p_{\rm f}$, where $p_{\rm f} \approx 250$ MeV/c is the Fermi-momentum. However, in the process of particle production, the outgoing nucleons have to scatter into unoccupied regions of phase space, another consequence of the exclusion principle.[36]

Transport calculations show that it is too simple-minded, however, to represent the two colliding nuclei as two (possibly overlapping) Fermi spheres in momentum space. The acceleration of the two approaching nuclei towards each other as their surfaces touch leads to a depletion of phase space density in the central region and opens up the so-called Fermi-hole.[37] This was shown to cause the preferred emission of high energy particles during the early states of the heavy ion reaction and thus makes particle production a sensitive probe of the high-compression phase.

Other medium effects playing important roles are the rescattering and reabsorption of produced particles[38] as well a medium-modifications to the elementary scattering process. All of these medium effects make subthreshold particle production an important testing ground for models of nuclear collisions and fundamental probes of nuclear dynamics. (See the contributions of H. Gutbrod, S. Bass, C. Muentz and P. Senger in this volume).

A very important idea in the development of relativistic heavy ion physics was the attempt to determine the nuclear compressibility from pion multiplicities.[39] The underlying assumption is that the energy spent to compress nuclear matter is not available for particle production. By comparing the observed pion multiplicities to

intranuclear cascade calculations without compressional effects, it was thus hoped to extract the nuclear compressibility. Shortly thereafter it was shown, however, that this initial attempt was too simple-minded, and that better cascade calculations were indeed able to reproduce the observed multiplicities.[40]

However, this initial idea remained a powerful driving force for the development of nuclear transport theories sketched above. For example, the first BUU transport theory paper[28] studied the dependence of the calculated pion multiplicity on the stiffness of the nuclear equation of state by selfconsistently including mean field compressional effects into the calculation.

In a refined version of this idea one investigates particle production around the threshold region, where the elementary production cross section is a very steep function of the available center-of-mass energy, thus yielding a more sensitive probe. However, then the use of pions as a probe is not a viable option, because the beam energy region of E/A $\approx$ 200 MeV is not expected to result in high compressions. A better probe thus seems to be the threshold production of kaons (see the contributions of E. Grosse and G. Li in this volume).

However, I remain somewhat skeptical as far as the chances for success are concerned. First, one has to realize that a change in the numerical value of the nuclear compressibility does not entail a corresponding proportional change in compressional energy. Rather what happens in transport calculations is that the maximum density reached adjusts to largely compensate for the change in compressibility, leading to roughly the same fraction of the total available energy being stored in compression.

Another effect that further complicates this simple picture is that at higher beam energies the population of resonances increases drastically. This leads to the exciting new possibility of (primarily Δ-) resonance matter (see the contribution of R. Simon). However, the resonance matter introduces also new uncertainties into the calculations for particle production, because, for example, around E/A = 1 to 2 GeV beam energy the dominant contribution to kaon production comes from reactions like

$$N + \Delta \rightarrow K + X \quad \text{and} \quad \Delta + \Delta \rightarrow K + X. \tag{3}$$

The calculation of the kaon production process requires then knowledge of the above elementary cross sections, which cannot be independently extracted from experiment, and whose medium modifications are unknown.

3.2. Subthreshold Particle Production

Far below threshold, several nucleons have to pool their energies to provide for the particle production. This can be accomplished by several subsequent individual nucleon-nucleon collisions in the spirit of the Fermi acceleration, energy storage through resonance excitations (see above), or by a collective emission of the particle as first suggested by Heisenberg[41,42]. A recent BEVALAC study to find traces of this effect (see Fig. 1) was conducted by dividing the pion production cross section for heavy systems by that for light systems[43]. However, down to a beam energy of 183

MeV per nucleon, no collective pion production component was visible in the data - in agreement with the BUU calculations assuming non-collective production. In fact, as of today no experimental studies on pion production in the subthreshold region have conclusively discovered any signatures of a collective production.[3,6]

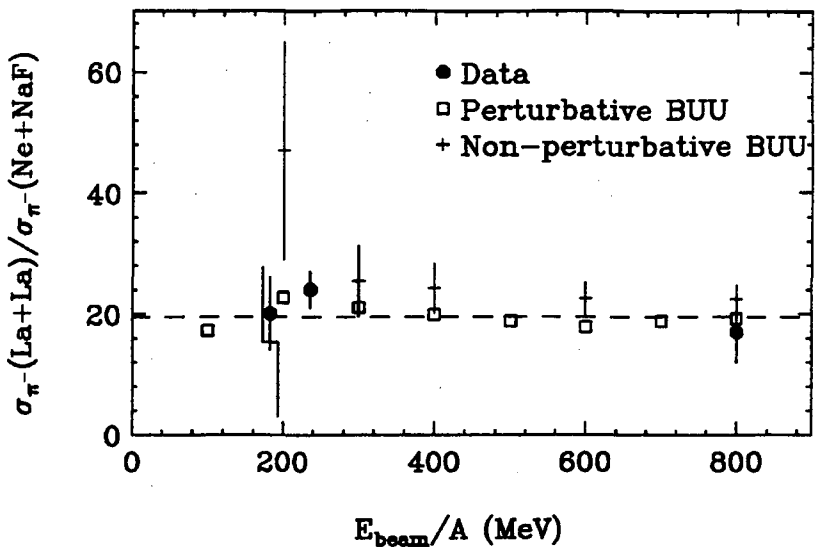

Fig. 1: Comparison between pion yield ratios from experiment (filled circles) and from two BUU calculations (perturbative - open squares; non-perturbative - crosses) (from ref. 43).

There are several open problems which warrant further study of subthreshold particle production. First, higher statistics studies of the kind described here have to be extended to lower beam energies to see if the heavy/light pion production ratio changes. Another way to address possible collective production is the impact parameter dependence of pion production by using 4π detectors as impact parameter filters. Similar studies can of course be conducted for the subthreshold production of other particles as well.

A further problem is the so-called 'slope anomaly' in pion production data. The energy spectra of produced secondary particles show a 'thermal' spectrum with an exponential fall-off conventionally parametrized via a constant T_0, called the 'temperature'. Naively, one would expect this temperature constant to be a monotonic (possibly even linear) function of the beam energy, with T_0 approaching 0 for the beam energy approaching 0.

This, however, does not seem to be the case. Instead, what is observed is a certain minimum apparent temperature in the pion spectra, $T_0(E_b) > 10$ MeV for all beam energies.[3,44] This present puzzle may have an intimate connection to a similar discrepancy between nuclear fragment energy spectra (which show a similar minimum 'temperature') and the nuclear temperature parameter as extracted from the measurement of population ratios of excited states relative to the ground state.[45] Interestingly enough this puzzle does not seem to exist for the slope parameters in high energy photon production.[15]

3.3. Electromagnetic Probes

With the current amount of activity devoted to studying high energy photon and di-lepton pair production from heavy ion collisions (see the contributions by W.K. Wilson, R.J. Porter, K. Haglin, C.M. Ko, and H. Specht), it seems appropriate to devote a separate section to these probes in this summary.

Electromagnetic probes derive the interest in them from the fact that they practically do not interact with the nuclear medium once they have been produced. They thus represent relatively clean probes of the hot and dense phase of the heavy ion collision.

From the study of high energy gamma production we have learned that (i) high energy photons are primarily produced in individual nucleon-nucleon collisions; (ii) meson-exchange currents play an important or even dominant role; (iii) high energy photons carry important information on the heavy ion reaction dynamics. Unfortunately, at higher beam energies, the decay of neutral pions into two gammas provides severe background problems. There may, however, be another source of high energy photons,[46] the decay $\Delta \rightarrow N + \gamma$, visible in the data (see R. Simon's contribution), shedding light on the exciting Delta-matter.

From di-lepton pair measurements we expect to learn about the pion-pion interaction in the nuclear medium and indirectly about the pion dispersion relation in nuclear matter. We can study the Dalitz-decay of mesons and baryons, investigate electromagnetic form factors, and learn about possible shifts of the masses and widths in the medium, with a possible glimpse at chiral restoration. All of these prospects are very exciting, but the current data do not constrain the models sufficiently. With the construction of the di-lepton spectrometer HADES at the GSI the available statistics for di-lepton pairs should increase by at least three orders of magnitude, however (see W. König's contribution).

4. Two-Particle Correlations

The information that can be extracted experimentally from one-body observables is limited. Fig. 2 illustrates this problem. On the left, we show schematically the expansion of a source in time, where the different shaded ovals are meant to represent snapshots of the source at different time instances. Particles emitted from this source will move on a straight trajectory (for simplicity we neglect the effects of bending magnets in spectrometers) to the detector. This detector can only record the asymptotic momentum state, $|\vec{p}(t \rightarrow \infty)\rangle$, of the detected particle. No coordinate space information on the emission point can be generated from this. Thus the measured single particle spectra represent an integration over the entire space-time extension of the emitting source.

The situation is different for correlated two particle observables. The final state interaction between the pair (represented by the oval containing the last directional change in the trajectories of the two particles) modifies their asymptotic momentum

states, and due to this correlation, the two-particle final state is not simply the direct product of the single particle states. This correlation can be expressed as

$$\mathcal{C}(\vec{p}_1, \vec{p}_2) = \frac{\langle \vec{p}_1, \vec{p}_2 | \vec{p}_1, \vec{p}_2(t \to \infty) \rangle}{\langle \vec{p}_1 | \vec{p}_1(t \to \infty) \rangle \langle \vec{p}_2 | \vec{p}_2(t \to \infty) \rangle} \tag{4}$$

And, since the interaction between the two particles in general depends on the separation of the two particles, so will the correlation function defined here. We can thus hope to extract information on the space-time extension of the emitting source from coincidence measurements of two (or more) emitted particles.

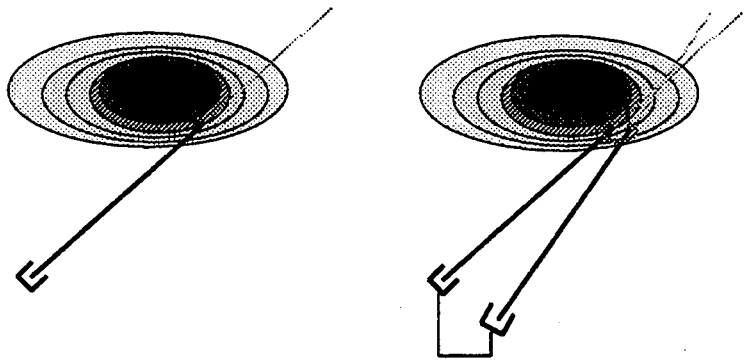

Fig. 2: Left: detection of a single particle emitted from an expanding source; right: simultaneous detection of two particles from the same source.

It has to be stressed that this volume information is essential for all attempts to make inferences about the nuclear equation of state. To obtain this information, it is not enough to perform simple global gaussian source fits to the data. Rather the data (and calculations) should in an ideal case be impact parameter binned. In addition, one has to differentiate between different pair velocities, $\vec{P}$, of the emitted particle pair, because the emission of high energy particles is more localized in time during a heavy ion collision, thus resulting in a smaller effective source 'radius' than that extracted for less energetic particles. Another cut providing very useful information is the distinction between longitudinal ($\vec{q} \| \vec{P}$) and transverse ($\vec{q} \perp \vec{P}$) correlations, where $\vec{q}$ is the relative momentum between the emitted pair (see M. Lisa's contribution). This information can be used to disentangle the contributions of life time effects and coordinate space extension of the source to the extracted effective radius.

The comparison of the results of transport calculations to experimental data has progressed enormously in the beam energy range around the Fermi energy during the last few years.[7,22] However, for relativistic energies this comparison is still in its infancy stage. Here I see a huge potential for future experiments and detailed calculations, providing possible additional narrowing down of the parameter windows for the nuclear equation of state.

As an example for the predictive power of present-day heavy ion transport theories Fig. 3 shows a comparison of data obtained by the DIOGENE collaboration[47] to the calculations for opposite sign pion correlations

$$R_{\pi^+\pi^-} = \frac{\sigma_2(\pi^+,\pi^-)}{\sigma_1(\pi^+)\sigma_1(\pi^-)} \tag{5}$$

as a function of the invariant mass of the pair. From this figure, we can clearly see an enhancement of the correlation function close to $M_{\rm inv} = 2m_\pi$ for the p+Pb case, whereas it is not present in the p+C case. In the calculations this is due to the effects of pion and delta resonance re-scattering and re-absorption, and the difference is caused by the fact the $R_{\rm Pb} \gg \lambda_\pi \approx R_{\rm C}$, where λ_π represents the mean free path of pionic excitations in nuclear matter.

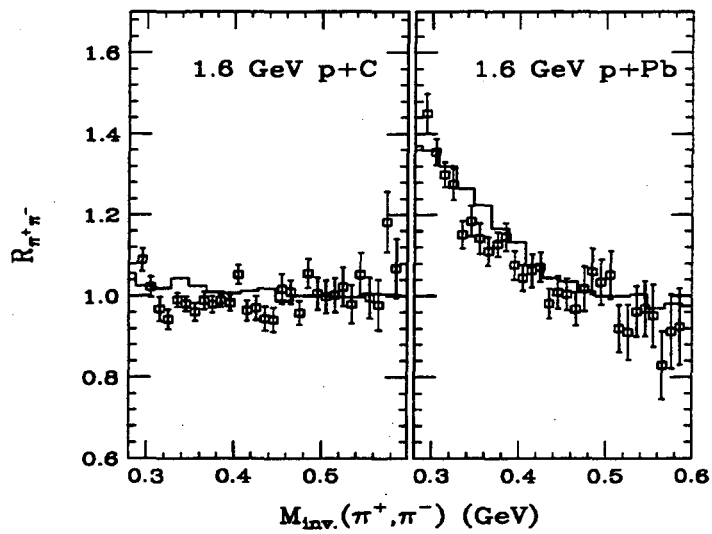

Fig. 3: Two-pion ($\pi^+\pi^-$) correlation function for 1.6 GeV proton induced reactions on C and Pb targets. The histograms represent the calculations, and the circles show the data of the DIOGENE collaboration.[47]

5. Collective Motion

Phenomena of collective motion of nucleons resulting from nuclear collisions are one of the most fascinating objects of study in relativistic heavy ion collisions, because they offer glimpses at true many-body effects not present in simple superpositions of individual two-body collisions. Early effects postulated were nuclear 'shock waves'[25,26] and 'blast waves'.[48]

The important effect of sidewards deflection in the reaction plane ('flow') was discovered by the Plastic Ball group at the BEVALAC.[49] Furthermore, a preferred emission out of the reaction plane around midrapidity was found by the Streamer Chamber group.[50] In addition, radial outward flow has been theoretically considered[51,52] and

observed in the data. This radial flow phenomenon may at lower energies even lead to the transient formation of hollow structures, bubbles, toroids,[53] or sheets.[54] (See also the contribution of E. Norbeck).

Again, the investigation of nuclear collective flow has largely been driven by the motivation to determine the nuclear compressibility and in turn has driven the development of transport theories (see the contributions of N. Herrmann, F. Rami, Y. Leifels, S. Bass, P. Senger, and H. Loehner).

Another exciting development are the new EoS TPC data (see the contribution of D. Keane) showing a non-viscous hydrodynamic scaling, a constant scale invariant flow of ≈ 0.35, for beam energies between E/A = 200 and 1200 MeV (see D. Keane's contribution).

At lower energies, E/A $\approx$ 50 to 100 MeV, the repulsive nuclear collective flow is balanced by the attractive nuclear surface interaction. The beam energy at which this happens was called the 'balance energy'.[55] It was shown that the projectile and target mass dependence of this quantity enables us to estimate the density dependent medium corrections of the nucleon-nucleon scattering cross section, with the best value suggesting a $\approx 20\%$ reduction as compared to the free value at nuclear matter density.[56,57] (See G. Westfall's contribution).

There are several challenges in this area remaining to be solved. Apart from a further determination of the parameters of the nuclear equation of state discussed above, we would like to see an experimental investigation into the postulated non-compact shapes; a continuation of the flow studies to higher energies to see how far upward the observed hydrodynamic scaling can be extended and to determine what the energy dependence of the different contributions (mean field compression and kinetic pressure) to the collective flow observable are; and finally a thorough investigation of the beam energy range between 50 and 200 MeV to determine at what energy hydrodynamic scaling breaks down and results in the disappearance of nuclear flow, an effect not predicted by this simple scaling picture.

6. Multifragmentation

The disintegration of excited nuclei into several smaller nuclei of light to intermediate mass is probably the most serious challenge to today's theoretical understanding of the nuclear many-body problem – as already discussed above.

Several 4π multiparticle detection systems are now delivering data of outstanding quality and statistics. The main objective is, in my opinion, to try to investigate the possibility of a first or second order phase transition of nuclear matter in these fragmentation events. Early studies on high-energy proton induced fragmentation reactions seemed to indicate the possible presence of this effect, but were not very useful because they were inclusive data, i.e. integrated over impact parameter and energy deposited.[58] Now exclusive experiments for reverse kinematics[59] and mass symmetric systems[60] have begun to map out the excitation function for the intermediate mass fragment production and seem to consistently indicate a critical excitation energy

per nucleon of about 8 MeV (see also contributions by M.B. Tsang, C. Sangster, M. Begemann-Blaich, G. Wozniak, and V. Lindenstruth).

New studies conducted with reverse kinematics and utilizing the EoS TPC have now confirmed the predicted[61] impact parameter dependence of the fragment production cross section. Much more important, for the same data set a moment analysis of fragment mass distribution[62,61] was conducted in an event-by-event manner. This enables one to determine the critical exponents of nuclear matter at the critical point (see contribution by A. Hirsch).

We have only begun to explore the vast possibilities of investigations into the nature of the phase transition. From the experience gained here there may also be a possible cross fertilization of methods with the future search for the quark-gluon plasma phase transition at much higher excitation energies. Possibly the most important contribution to physics in general is to be made by exploring how finite size effects wash out signatures of phase transitions in very small systems of only on the order of 100 constituents.

7. Summary

In the space allocated it was impossible for me to provide an adequate summary of the field, or even to mention (let alone discuss) everybody's contributions to this workshop. The whole area of radioactive secondary beam physics, for example, was not covered at all in my overview. However, what I hoped to convey is the multitude of exciting new results and future directions in relativistic heavy ion physics.

8. Quo Vadis, BEVALAC Physics?

On Saturday, February 21, 1993, the BEVALAC was retired. But the science of relativistic heavy ion physics has not died with it.

Fittingly, the bulk of the investigations started here will be carried on by the SIS accelerator at the GSI. The continuation to higher energies will be provided by the AGS accelerator at Brookhaven National Laboratory. At the low end of the BEVALAC's beam energy range, the NSCL at Michigan State University is currently operating the K1200 accelerator and is planning for an upgrade to be able to accelerate beams over the entire mass range up to energies of $E/A = 200$ MeV. Other accelerators around the world are also contributing valuable parts to the ongoing investigations into relativistic heavy ion science.

In the mean time, the field of relativistic heavy ion physics has also branched out to higher energies in the quest to discover positive evidence for the existence of the the quark-gluon-plasma. To a large degree this effort was and is driven by scientists having worked at the BEVALAC at one time or another during their career. Many of the ideas generated by the interaction of theorists and BEVALAC-experimenters have been propagated and extended into the subfield of ultrarelativistic heavy ion physics.

All of these ongoing efforts convince the observer that the shutdown of the BEVALAC does not constitute the end of relativistic heavy ion science. It is alive and well. I thus conclude with the words of Winston Churchill

"This is not the end.
It is not even the beginning of the end.
But it is, perhaps, the end of the beginning."

9. References

[1] S. Das Gupta and G.D. Westfall, Physics Today **46**(5), 34 (1993).
[2] D. Boal, Annu. Rev. Nucl. Part. Sci. **37**, 1 (1987).
[3] P. Braun-Munzinger and J. Stachel, Annu. Rev. Nucl. Part. Sci. **37**, 97 (1987).
[4] W.G. Lynch, Annu. Rev. Nucl. Part. Sci. **37**, 493 (1987).
[5] H. Nifenecker and J.A. Pinston, Annu. Rev. Nucl. Part. Sci. **40**, 113 (1990).
[6] U. Mosel, Annu. Rev. Nucl. Part. Sci. **41**, 29 (1991).
[7] W. Bauer et al., Annu. Rev. Nucl. Part. Sci. **42**, 77 (1992).
[8] J. Stachel and G.R. Young, Annu. Rev. Nucl. Part. Sci. **42**, 537 (1992).
[9] L. Moretto and G.J. Wozniak, Annu. Rev. Nucl. Part. Sci. **43**, 379 (1993).
[10] L.P. Czernai and J.I. Kapusta, Phys. Rep. **131**, 223 (1986).
[11] R. Stock, Phys. Rep. **135**, 259 (1986).
[12] H. Stöcker and W. Greiner, Phys. Rep. **137**, 277 (1986).
[13] B. Schürmann et al., Phys. Rep. **147**, 1 (1987).
[14] G.F. Bertsch and S. Das Gupta, Phys. Rep. **160**, 189 (1988).
[15] W. Cassing et al., Phys. Rep. **188**, 363 (1990).
[16] J. Aichelin, Phys. Rep. **202**, 233 (1991).
[17] P. Schuck et al., Prog. Part. Nucl. Phys. **22**, 181 (1989).
[18] H. Gutbrod et al., Rep. Prog. Phys. **52**, 267 (1989).
[19] W. Cassing and U. Mosel, Prog. Part. Nucl. Phys. **25**, 235 (1990).
[20] S.J. Wang et al., Ann. Phys. (N.Y.) **209**, 251 (1991).
[21] A. Ono et al., Prog. of Theoret. Phys. **87**, 1185 (1992).
[22] W. Bauer, Prog. Part. Nucl. Phys. **30**, 45 (1993).
[23] G.D. Westfall et al., Phys. Rev. Lett. **37**, 1202 (1976).
[24] P. Bonche et al., Phys. Rev. C **13**, 1226 (1976).
[25] W. Scheid et al., Phys. Rev. Lett. **32**, 741 (1974).
[26] "The Nuclear Equation of State", ed.: W. Greiner and H. Stöcker, NATO ASI Series B **216A** (Plenum, New York, 1989).
[27] J. Cugnon et al., Nucl. Phys. **A352**, 505 (1981).
[28] G.F. Bertsch et al., Phys. Rev. C **29**, 673 (1984).
[29] J. Kruse et al., Phys. Rev. Lett. **54**, 289 (1985).
[30] C.-Y. Wong, Phys. Rev. C **25**, 1460 (1982).
[31] W. Bauer et al., Phys. Rev. Lett. **58**, 863 (1987).

[32] J. Aichelin and H. Stöcker, Phys. Lett. **B176**, 14 (1986).
[33] D.H. Boal and J.N. Glosli, Phys. Rev. C **38**, 2621 (1988).
[34] H. Feldmeier, Nucl. Phys. **A515**, 147 (1990).
[35] A. Ono et al., Phys. Rev. Lett. **68**, 2898 (1992).
[36] G.F. Bertsch, Phys. Rev. C **77**, 713 (1977).
[37] W. Bauer et al., Phys. Rev. C **34**, 2127 (1986).
[38] B.A. Li and W. Bauer, Phys. Rev. C **44**, 450 (1991).
[39] R. Stock et al., Phys. Rev. Lett. **49**, 1236 (1982).
[40] Y. Kitazoe et al., Phys. Lett. **B166**, 35 (1986).
[41] W. Heisenberg, Z. Phys. **126**, 569 (1949).
[42] D. Vasak et al., J. Phys. G **11**, 1309 (1985).
[43] J. Miller et al., Phys. Lett. **314B**, 7 (1993).
[44] T. Suzuki, Nucl. Phys. A**538**, 113c (1992).
[45] W. Bauer, to be published in the proceedings of the Les Houches Winter School on Fragmentation Phenomena.
[46] W. Bauer and G.F. Bertsch, Phys. Lett. **229B**, 16 (1989).
[47] J. Pluta et al., Nucl. Phys. **A562**, 365 (1993).
[48] P.J. Siemens and J.O. Rasmussen, Phys. Rev. Lett. **42**, 880 (1975).
[49] H.A. Gustafsson et al., Phys. Rev. Lett. **52**, 1590 (1984).
[50] P. Danielewicz et al., Phys. Rev. C **38**, 120 (1988).
[51] P. Danielewicz and Q. Pan, Phys. Rev. C **46**, 2002 (1992).
[52] W. Bauer et al., Phys. Rev. C **47**, R1838 (1993).
[53] W. Bauer et al., Phys. Rev. Lett. **69**, 1888 (1992).
[54] L. Moretto et al., Phys. Rev. Lett. **69**, 1884 (1992).
[55] C.A. Ogilvie et al., Phys. Rev. C **42**, R10 (1990).
[56] G.D. Westfall et al., Phys. Rev. Lett. **71**, 1986 (1993).
[57] D. Klakow et al., Phys. Rev. C **48**, 1982 (1993).
[58] A.S. Hirsch et al., Phys. Rev. C **29**, 508 (1984).
[59] C.A. Ogilvie et al., Phys. Rev. Lett. **67**, 1214 (1991).
[60] T. Li et al., Phys. Rev. Lett. **70**, 1924 (1993).
[61] W. Bauer, Phys. Rev. C **38**, 1927 (1988).
[62] X. Campi, J. Phys. **A19**, L917 (1986).

List of Participants

Jorg Aichelin
Laboratoire de Physique Nucleaire
Université de Nantes
2, Rue de la Houssiniere
Nantes, Cedex
France F-44072

Daniel A. Ardouin
Université de Nantes
LPN-2, rue Houssiniere
Nantes, Cedex
France F-44072
(33) 40374955
(33) 40373176*

Steffen A. Bass
Universität Frankfurt
GSI Darmstadt
Postfach 11-05-52
Planckstr. 1
D-6100 Darmstadt
Germany

Wolfgang W. Bauer
NSCL
Michigan State University
East Lansing, MI 48824-1321
(517) 353-5965
(517) 353-5967

M. L. Begemann-Blaich
GSI Darmstadt
Postfach 11-05-52
Planckstr. 1
D-6100 Darmstadt
Germany
49-6151-359668
49-6151-359785

Walter Benenson
Michigan State University
Cyclotron Laboratory
Lansing, MI 48824
(517) 355-7432
(517) 353-5967

Paul Brady
Department of Physics
University of California, Davis
Davis, CA 95616
(916) 752-1793
(916) 752-4717

Harold C. Britt
National Science Foundation
1800 G Street NW, Room 520
Washington, DC 20550

Jim B. Carroll
University of California, Los Angeles
c/o Lawrence Berkeley Lab
1 Cyclotron Road
Berkeley, CA 94720
(510) 486-4507
(510) 486-7105

Daniel A. Cebra
University of California, Davis
Davis, CA 95616
(916) 752-4592
(916) 752-4717

A. Dean Chacon
Texas A&M University
c/o Lawrence Berkeley Lab.
1 Cyclotron Road, 50D-106
Berkeley, CA 94720
(510) 486-7650

Jerry L. Chance
University of California, Davis
Davis, CA 95616
(916) 752-5786
(916) 752-4717

Subal Das Gupta
Department of Physics
McGill University
3600 University Street
Montreal, Quebec
Canada H3A 2T8
(514) 398-6483
(514) 398-8434

Jürgen Friese
Technishe Universität München
Physik Department E12
James Franck Str. 1
Garching, 85747
Germany
49-89-3209-2439
49-89-3209-2297

Edmundo J. Garcia-Solis
Chemistry Department
University of Maryland
College Park, MD 20742
(301) 405-1853
(301) 314-9121

Harvey A. Gould
Lawrence Berkeley Laboratory
1 Cyclotron Road, 71-259
Berkeley, CA 94720
(510) 486-7777

Walter A. Greiner
Inst. fur Theoretische Physik der Universtat Frankfurt am Main
Postfach 11 19 32
D-6000 Frankfurt
Germany
798-2332
798-8350

Eckart H. Grosse
GSI Darmstadt
Postfach 11-05-52
Planckstr. 1
D-6100 Darmstadt
Germany
49-6151-359668
49-6151-359785

Hans H. Gutbrod
GSI Darmstadt
Postfach 11-05-52
Planckstr. 1
D-6100 Darmstadt
Germany

Kevin L. Haglin
Michigan State Univ., NSCL
East Lansing, MI 48824-1321
(517) 355-9671
(517) 353-5967

Luisa F. Hansen
Lawrence Livermore Nat'l Lab.
P. O. Box 808, L-289
Livermore, CA 94550
(510) 422-4512
(510) 423-8086

N. Herrmann
GSI Darmstadt
Postfach 11-05-52
Planckstr. 1
D-6100 Darmstadt
Germany
49-6151-359668
49-6151-359785

Andrew S. Hirsch
Department of Physics
Purdue University
West Lafayette, IN 47907
(317) 494-5192
(317) 494-0706

Eric L. Hjort
Purdue University
c/o Lawrence Berkeley Lab.
1 Cyclotron Road
Berkeley, CA 94720
(510) 486-6876

* Second telephone number in a listing is the fax number.

Marvin L. Justice
Kent State University
c/o Lawrence Berkeley Lab.
1 Cyclotron Road, 50D-106
Berkeley, CA 94720
(510) 486-6531
justice@lbl

Declan Keane
Department of Physics
Kent State University
Kent, OH 44242

Jessica C. Kintner
Department of Physics
University of California, Davis
Davis, CA 95616
(916) 752-5786
(916) 752-4717

C. M. Ko
Texas A&M University
Cyclotron Institute
College Station, TX 77843

W. Koenig
GSI Darmstadt
Postfach 11-05-52
Planckstr. 1
D-6100 Darmstadt
Germany
49-6151-359668
49-6151-359785

Yvonne Leifels
Universität Bochum
Universitatsstr. 152
Bochum 44780
Germany
49-6151-359785

Bao-An Li
Bereich Schwerionenphysik
Hahn-Meitner-Institute
D-14109 Berlin
Germany
49-30-8062-2313
49-30-8062-2097

Volker Lindenstruth
Lawrence Berkeley Laboratory
1 Cyclotron Road, 70A-3307
Berkeley, CA 94720
(510) 486-6460
(510) 486-7105

Michael A. Lisa
Lawrence Berkeley Laboratory
1 Cyclotron Road, 50D-119
Berkeley, CA 94720
(510) 486-7043

Herbert Löhner
University of Groningen, KVI
Zermikelaan 25
Groningen, 9747AA
Germany
31-50-63-3600
31-50-63-4003

William G. Lynch
Michigan State Univ., NSCL
East Lansing, MI 48824

Howard Matis
Lawrence Berkeley Laboratory
1 Cyclotron Road, 50D
Berkeley, CA 94720
(510) 486-5031
(510) 486-4818

Peggy McMahan
Lawrence Berkeley Laboratory
1 Cyclotron Road, MS 88
Berkeley, CA 94720
(510) 486-5980
(510) 486-7983

Alice C. Mignerey
Dept. Chemistry
University of Maryland
College Park, MD 20742
(301) 405-1852
(301) 314-9121

Jack Miller
Lawrence Berkeley Laboratory
1 Cyclotron Road
Berkeley, CA 94720

Christian Müntz
Inst. fur Kernphysik
Technische Hochschule
Darmstadt
Schlobgartenstr. 9
D-6100 Darmstadt
Germany
49-6151-359612
49-6151-359785

Edwin Norbeck
Department of Physics
University of Iowa
Iowa City, IA 52242
(319) 335-0903
(319) 335-1753

Grazyna J. Odyniec
Nuclear Science Division
Lawrence Berkeley Laboratory
1 Cyclotron Road
Berkeley, CA 94720
(510) 486-7128
(510) 486-4818

Douglas Olson
Lawrence Berkeley Laboratory
1 Cyclotron Road
Berkeley, CA 94720

Martin D. Partlan
University of California, Davis
c/o Lawrence Berkeley Lab.
1 Cyclotron Road
Berkeley, CA 94720
(510) 486-7129

Georg Peilert
Lawrence Livermore Nat'l Lab.
P. O. Box 808, L-397
Livermore, CA 94550

R. Jeff Porter
Lawrence Berkeley Laboratory
1 Cyclotron Road, 70A-3307
Berkeley, CA 94720
(510) 486-6083

Art Poskanzer
Lawrence Berkeley Laboratory
1 Cyclotron Road, 50D
Berkeley, CA 94720
(510) 486-5618
(510) 486-4818

Fouad Rami
Centre de Recherches Nucleaires
23, rue du Loess — B.P. 20
Strasbourg, France 67037
(33) 88.28.62.00
(33) 88.28.62.02

Jorgen Randrup
Lawrence Berkeley Laboratory
1 Cyclotron Road, 70A-3307
Berkeley, CA 94720
(510) 486-6157

John Rasmussen
Nuclear Science Division
Lawrence Berkeley Laboratory
1 Cyclotron Road, 70A-3307
Berkeley, CA 94720

Jörg Reinhold
Technishe Universität München
Physik Department E12
James Franck Str. 1
Garching 85747
Germany
49-89-3209-2439
49-89-3209-2297

Hans G. Ritter
Lawrence Berkeley Laboratory
1 Cyclotron Road, 50D
Berkeley, CA 94720
(510) 486-4138

Daniel E. Russ
Chemistry Department
University of Maryland
College Park, MD 20742
(301) 405-1853
(301) 314-9121

C. Sangster
Lawrence Livermore Nat'l Lab.
P. O. Box 808, L397
Livermore, CA 94550

Rolf P. Scharenberg
Physics Department
Purdue University
West Lafayette, IN 47907
(317) 494-5390
(317) 494-0706

W. Schwab
GSI Darmstadt
Postfach 11-05-52
Planckstr. 1
Darmstadt D-6100
Germany
49-6151-359668
49-6151-359785

Alan J. Scott
Kent State University
Kent, OH 44242

Peter Senger
GSI Darmstadt
Postfach 11-05-52
Planckstr. 1
D-6100 Darmstadt
Germany
49-6151-359652
49-6151-359785

Yiping Shao
Kent State University
c/o Lawrence Berkeley Lab.
1 Cyclotron Road, 50D-106
Berkeley, CA 94720
(510) 486-7129
(510) 486-4818

R. Simon
GSI Darmstadt
Postfach 11-05-52
Planckstr. 1
D-6100 Darmstadt
Germany
49-6151-359668
49-6151-359785

Wojtek Skulski
Nuclear Science Division
Lawrence Berkeley Laboratory
1 Cyclotron Road
Berkeley, CA 94720

Hans J. Specht
GSI, Darmstadt
Postfach 11-05-52
Planckstr. 1
D-64220 Darmstadt
Germany
49-6151-359-648
49-6151-359-991

K. Sümmerer
GSI Darmstadt
Postfach 11-05-52
Planckstr. 1
D-6100 Darmstadt
Germany
49-6151-359668
49-6151-359785

T. James Symons
Lawrence Berkeley Laboratory
1 Cyclotron Road, 70A-3317
Berkeley, CA 94720
(510) 486-4454
(510) 486-4808

Isao Tanihata
RIKEN
Inst. of Phys. & Chem. Res. 2-1
Hirosawa, Wako
Saitama, Japan 351-01

Mark L. Tincknell
Purdue University
1396 Physics
West Lafayette, IN 47907-1396
(317) 494-5510
(317) 494-0706

Betty Tsang
NSCL
Michigan State University
East Lansing, MI
48864

Kin Tso
Nuclear Science Division
Lawrence Berkeley Laboratory
1 Cyclotron Road, 71-259
Berkeley, CA 94720
(510) 486-7961
(510) 486-7981

Gary D. Westfall
Nat'l Superconducting Cyclotron Lab.
Michigan State University East Lansing, MI 48824-1321
(517) 353-8727
(517) 353-5967

Howard Wieman
Lawrence Berkeley Laboratory
1 Cyclotron Road, 70A-3307
Berkeley, CA 94720
(510) 486-6953

William K. Wilson
Nuclear Science Division
Lawrence Berkeley Laboratory
1 Cyclotron Road, 70A-3307
Berkeley, CA 94720
(510) 486-5708

Kevin L. Wolf
Texas A&M University
Cyclotron Institute
College Station, TX 77843
(409) 845-1411
(409) 845-1899

Gordon J. Wozniak
Lawrence Berkeley Laboratory
1 Cyclotron Rd., Bldg. 88
Berkeley, CA 94720
(510) 486-5071
(510) 486-7983
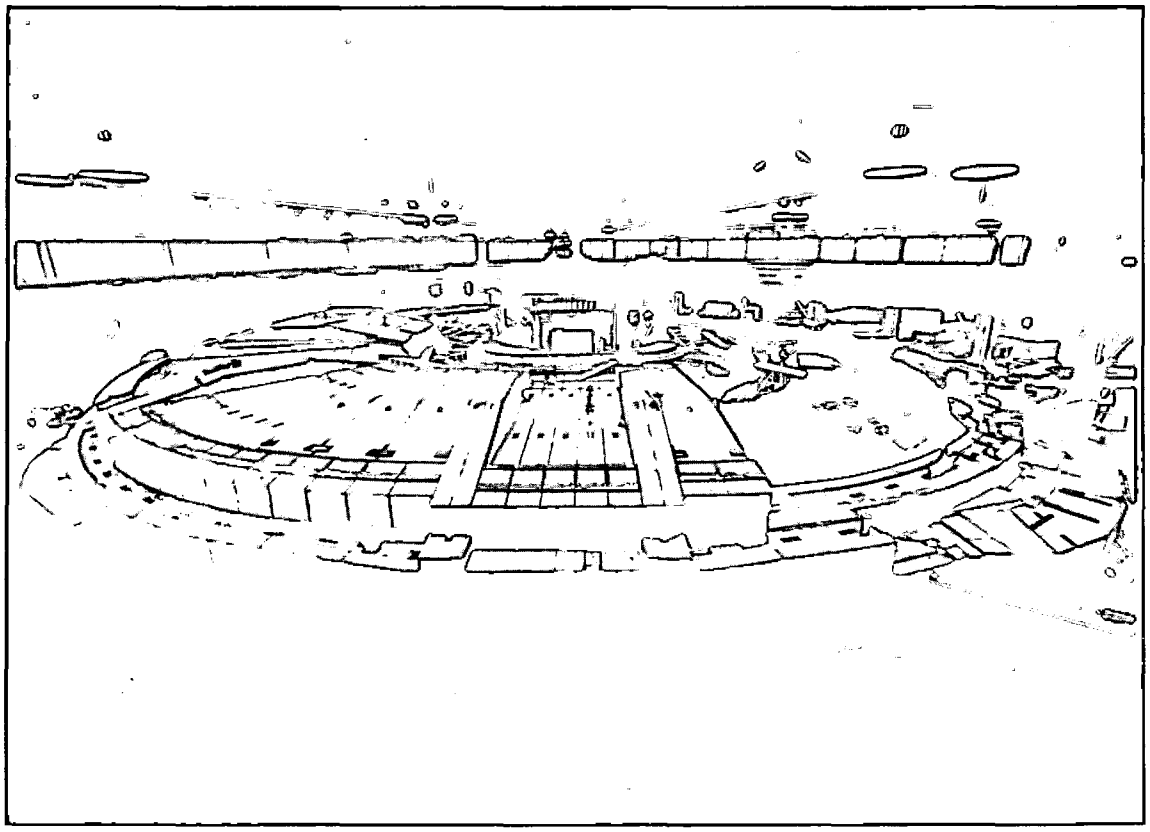
Lawrence Berkeley Laboratory
Technical and Electronic Information Department
University of California
Berkeley, California 94720